β-delayed neutron studies of $^{137-138}$I and $^{144-145}$Cs performed with trapped ions

By

Agnieszka Anna Czeszumska

A dissertation submitted in partial satisfaction of the

requirements for the degree of

Doctor of Philosophy

in

Engineering - Nuclear Engineering

in the

Graduate Division

of the

University of California, Berkeley

Committee in charge:

Professor Eric B. Norman, Chair
Dr. Nicholas D. Scielzo
Professor Karl A. van Bibber
Professor Daniel Kasen

Summer 2016

β-delayed neutron studies of $^{137-138}$I and $^{144-145}$Cs performed with trapped ions

Abstract

β-delayed neutron studies of $^{137-138}$I and $^{144-145}$Cs performed with trapped ions

by

Agnieszka Anna Czeszumska

Doctor of Philosophy in Engineering - Nuclear Engineering

University of California, Berkeley

Professor Eric B. Norman, Chair

The β-delayed neutron (βn) emission decay mode, prevalent in a vast number of neutron-rich nuclei, influences abundances calculated in the r-process nucleosynthesis models, affects nuclear reactor safety analysis calculations, and can illuminate aspects of nuclear structure. This thesis describes a newly developed recoil ion detection technique that was applied for high-precision βn branching ratio and neutron energy measurements of $^{137-138}$I and $^{144-145}$Cs. The recoil ion measurement approach avoids difficulties associated with direct neutron detection by instead detecting the daughter ion recoiling from neutron emission. The radioactive ions of interest are held in near-rest with the use of an ion trap, from which they leave the trap upon β or βn decay. The detector array surrounding the trap measures the time-of-flight of the recoil ion, as well as several associated decay products. Measuring the recoil ion's time-of-flight determines the recoil energy, from which the emitted neutron's energy can be deduced. Detecting other decay products gives rise to three different methods of measuring the βn branching ratio, which helps expose systematic effects. The technique builds upon a previous proof-of-principle experiment, and was expanded for the present measurements to include twice as many improved detectors, an upgraded ion trap, and a stronger source. This thesis also examines various backgrounds and detailed detector characterizations. The experimental campaign presented here serves to probe the limits of applying the recoil ion technique to explore further into the neutron-rich region.

To my parents and grandparents.

"Nothing in life is to be feared, only understood"
- Maria Skłodowska-Curie

Contents

List of Figures

List of Tables

Acknowledgments

This work was made possible thanks to the research staff at Lawrence Livermore National Lab and Argonne National Lab, and all the graduate students and postdoctoral scholars involved in the experiment. Nick Scielzo, the PI on this experiment, supervised the entire experimental effort, and worked with me on data analysis as well as this thesis. Nick has taught me an immense amount of experimental and analytical skills. With his attention to detail and scientific rigor, I could not imagine having a better supervisor. Rick Norman has been a wonderful advisor, and it was my privilege to be his student. He has cultivated my interest and appreciation of nuclear physics, and was very supportive of my research. Karl van Bibber and Dan Kasen offered interesting insights for the thesis as well as during my qualifying exam. Jason Clark and Guy Savard at ANL worked tirelessly to make the experiment happen. Shane Caldwell, a fellow graduate student involved in the experiment, contributed a tremendous amount of work into the experiment and data analysis, and in particular developed the TPM model. He taught me many experimental skills and the importance of showing up at the lab on a Saturday despite tornado warnings in nearby areas. Ryan Yee performed the proof-of-principle experiment, which the current experiment was build upon. Kevin Siegl and Sabrina Strauss contributed significantly to the data analysis. The experiment was also made possible thanks to Adrian Perez-Galvan, Scott Marley, Stephen Padgett, Ralph Segel, Ken Teh, Rodney Orford, Graeme Morgan, Mary Burkey, Jessica Harker, and Chris Chiara. Thank you.

I am indebted to my family and friends for providing the emotional support throughout my graduate school years. My parents, Wieslawa and Krzysztof, grandparents, Teresa and Jerzy, uncle Jarek, and brothers Lukasz and Mateusz always supported me in whichever path I chose to take and encouraged me to pursue the best education I could. Erika, Geoff and Stephanie provided support and camaraderie during my time in Chicago. I would have never made it without all the wonderful and caring friends: Sarah, Neil, Emily, Yvonne, Amelia, Anastasia, Zuzanna, Nathan, Carolyn, Katherine, Dave, Brian, Nicole, Sam, Maya, David, Tamara, Anna, Mady, Jonathan, Alisha, Josh, Moe, Dustin, Kay, Barbara, Tomi, and others - thank you so much for being there for me.

This material is based upon work supported by the Department of Energy, National Nuclear Security Administration, under Award Numbers DE-NA0000979 (NSSC), DE-AC52-07NA27344 (LLNL); Office of Nuclear Physics Contract DE-AC02- 06CH11357 (ANL), and grants DE-FG02-94ER40834 (University of Maryland), DE- FG02-98ER41086 (Northwest-

ern University); NSERC, Canada, under Application No. 216974; and the Department of Homeland Security. I would also like to acknowledge the support from the Lawrence Graduate Scholar Program at LLNL.

This dissertation was typeset using the ucastrothesis LaTeX template.

Chapter 1

Introduction

The discovery of nuclear fission in 1938 had revolutionary effects on the scientific landscape and the global politics [1]. What followed was the subsequent development and detonation of the nuclear weapons in Hiroshima and Nagasaki, profoundly affecting the outcome of World War II and ensuing changes in international relations, as well as the development of nuclear energy that could provide an entirely new way of energy production free from carbon emissions and politically-imbued resource dependancies.

The field of nuclear physics grew rapidly as observations of novel processes revised our understanding of atomic nuclei. In early 1939, Roberts *et al.* observed neutrons up to 1.5 minutes after bombarding uranium nitrate with deuterons [2]. They stipulated that the neutrons originated from direct emission from the excited fission fragments, or from photodisintegration of fission fragments by photons. In a follow-up experiment [3], Roberts *et al.* confirmed that the delayed neutrons were indeed emitted directly by the disintegrating nuclei. Later that year, Bohr and Wheeler published an article "The Mechanism of Nuclear Fission"[4], where they concluded that the emission of the delayed neutrons followed from the excited states in nuclei populated by the β decay of the fission fragments. It is important to note here that a crucial part of this discovery process was the observation that the neutron emission occurred on the same time-scale as the β decay. Since this process follows the β decay, these emitted neutrons are termed as β-delayed neutrons, or βn for short.

The β decay involves the weak interaction, the neutron emission is mediated by the strong interaction, and the γ-emission that competes with it is a product of the electromagnetic interaction. The interplay between these three forces makes the βn decay mode a particularly interesting subject of study. This introductory chapter contains an overview of βn emission physics, the general features of the processes involved in the βn decay mode, and discusses some important motivations for the study of βn emission.

1.1 β-delayed neutron emission

Neutron-rich nuclei that undergo β^- decay may populate excitation energies above the neutron separation energy of their daughter nuclei. In the process referred to as β-delayed

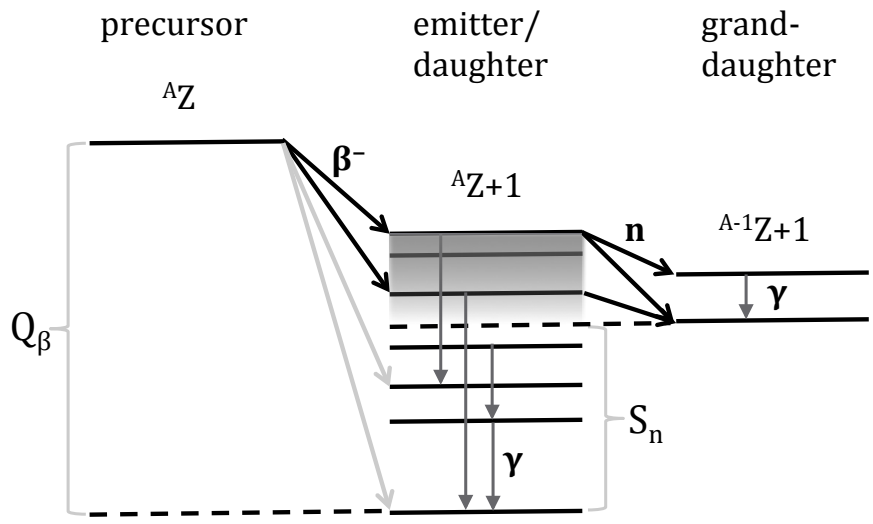

Figure 1.1: Schematic of a β-delayed one-neutron emission.

neutron emission (βn), the daughter de-excites via neutron emission with a probability, or branching ratio, of P_n. For the β^--decay of isotope ${}^AX$ into ${}^AX'$, the Q-value of the decay is defined as: $Q_{\beta^-} = [m({}^AX) - m({}^AX')]c^2$, where m are the atomic masses. The βn decay mode is energetically allowed when the daughter's Q_β value is larger than the daughter's neutron separation energy, $Q_\beta > S_n$, making it a prevalent decay mode in neutron-rich nuclei with 5-10 neutrons from the valley of stability. The diagram in Fig. 1.1 illustrates the basics of the delayed one-neutron emission.

Understanding of the general characteristics governing the βn decay necessitates a basic review of the applicable β decay theory. In the Fermi theory of β decay, the weak interaction treated as a perturbation on the system gives rise to the transition rate described by Fermi's Golden Rule [5]:

$$\lambda = \frac{2\pi}{\hbar}|V_{fi}|^2\rho(E_f), \tag{1.1}$$

where $\rho(E_f)$ is the density of final states. The V_{fi} matrix element describes the result of the interaction V between the final and initial states of the system: $V_{fi} = g\int[\psi_f^*\varphi_e^*\varphi_\nu^*]V_{V-A}\psi_i dv$, where the final state consists of the electron (φ_e) and neutrino (φ_ν) states in addition to the ψ_i nuclear state. Experiments have confirmed that the β decay is governed by the "vector minus axial-vector" interaction V_{V-A} [5]. Skipping through the details of the derivation, the total decay rate can be rewritten as:

$$\lambda = \frac{g^2|V_{fi}|^2}{2\pi^3\hbar^7c^3}\int_0^{p_{max}} F(Z',p)p^2(Q-T_e)^2dp. \tag{1.2}$$

The g in this equation is the interaction strength, $F(Z',p)$ is the Fermi function that accounts for the effect of the Coulomb field on the electron wave function, and $p^2(Q-T_e)^2$ is the

statistical factor derived from the accessible number of states of the emitted particles, where Q is the Q-value for the reaction and T_e is the kinetic energy of the electron.

The φ_e and φ_ν states can be described by the free-particle planar wave, $e^{i\mathbf{p}\cdot\mathbf{r}/\hbar}$. In the allowed approximation, the electron and neutrino don't carry away any orbital angular momentum l, and hence the expanded planar wave equation reduces to 1. As a result, the remaining matrix element only contains the contributions from the nuclear final and initial state, and retains the same parity. In a forbidden decay, the electron and neutrino carry away units of orbital angular momentum, though the resulting transition probability to such states is much smaller than for the allowed decays (a factor of $\sim 10^{-4}$ smaller).

In β decays where the transition to the ground state or low-lying excited states are inhibited because the initial and final states are of opposite parity or the total angular momentum change is greater than one (i.e. they do not satisfy the allowed beta decay selection rules), transitions to nuclear states at high excitation energies may be favored, despite the fact that the β phase space decreases with increasing excitation energy. When states above the neutron separation energy are populated, neutron emission becomes energetically possible. The excitation states may also de-excite via γ-emission. However, with an increasing excitation energy, neutron emission dominates over γ transition probability. In summary, the βn spectrum depends on three factors: (1) the β transition intensity into the highly-excited states above the S_n, (2) the γ decay competition from the populated states, and (3) the availability of the states in the grand-daughter accessible through the βn branch.

Conversely, the βn spectrum can be used to extract nuclear structure information. Since the neutrons are emitted at a specific energy, the energy of the excited state in the emitter can be derived (if the neutron decays into the ground state of the grand-daughter). The neutron spectrum is also proportional to the relative probability of the nuclear emission from different states in the emitter. This, in turn, depends on the average β decay intensity leading to the specific excited states, defined as the β-strength function S_β. The S_β can in turn provide information on the nuclear matrix elements. The accessible information serves as a motivation to study the βn emission, in addition to the many practical applications discussed in the next section.

1.2 Motivation for β-delayed neutron measurements

The β-delayed neutron decay mode has been observed in over 200 neutron-rich nuclei, and is energetically allowed in many more nuclei - the 2011 IAEA evaluation states that another $\sim$80 emitters were identified, but not yet characterized [6]. These numbers are expected to increase significantly as new facilities coming online (such as the Facility for Rare Isotope Beams at Michigan State University) will permit measurements in regions farther from stability. The characterization of the βn emission impacts nuclear physics research ranging from basic to applied [7]. Yet, despite the importance of βn measurements, existing branching ratio and neutron energy data is limited, and recent studies have also revealed discrepancies in published results [8, 9]. The lack of accurate data, combined with the increased need of βn

characterization for novel nuclear reactor designs, and the increases in capabilities due to new facilities coming online has reinvigorated βn studies, as exemplified by the 2011 IAEA report, and the ongoing IAEA Coordinated Research Activity started in 2013. These developments further motivate development of a novel, independent, measurement technique, which is the subject of this thesis.

To further motivate the study of β-delayed neutrons, the rest of this chapter details the impact of βn branching ratios and energy spectra in three research areas: nuclear energy, nuclear structure, and astrophysical nucleosynthesis. Of particular interest to this work are the applications to nuclear energy, motivating our measurements of ^{137}I and ^{138}I. The measurements of ^{144}Cs and ^{145}Cs, which can illuminate aspects of nuclear structure, are motivated by their importance to the stockpile stewardship mission.

1.2.1 βn role in a nuclear reactor operation

Early studies of βn's concentrated on their importance to nuclear reactor operation. Energy production in a nuclear reactor is achieved through fission chain reactions, where enough neutrons are produced in each fission to sustain a controlled chain reaction. On average, the ratio of neutrons produced in one generation of fission to the number of neutrons produced in the previous generation should be 1 (known as the multiplication factor k_{eff}). The βn emission from fission fragments supplies additional neutrons (delayed by the β decay half-life), thus impacting the neutron economics. Although the number of βn's constitutes less than 1% of total neutrons produced in a reactor, their presence is essential to reactor control safety. A reactor operated in prompt-subcritical state relies on the delayed neutrons to achieve criticality. The relatively long timescale of delayed neutron emission, ranging from a fraction of a second up to minutes, allows reactivity control with mechanical systems such as neutron-absorbing control rods.

The excessively large uncertainties in existing βn data result in overly conservative design and operation of reactors, increasing operation costs [6]. Novel Generation IV reactor designs require additional and/or more precise βn branching ratio and neutron energy spectra measurements [10] for reactor operation and safety analysis purposes. The new reactor designs employ novel fuel concepts that may, for example, utilize energetic (non-thermal) neutrons to sustain the chain reactions, or use different fissionable nuclei with not well characterized fission yields. As is the case of fast breeder reactors, where the fast spectrum of emerging neutrons is important, the existing approximations tailored for light water reactors are not applicable [11, 12].

The IAEA has recently proposed a set of "standard" βn precursors for the purposes of data evaluation and measurement [6]. These standards were selected based on the quality of available data and the number of independent measurements, as well as their large fission yields in the fission of nearly all actinides. Of particular interest is the case of ^{138}I, for which there exist two sets of discrepant data, summarized in Fig. 1.2. Six measurements are clustered around 5.4%, while three other measurements are clustered around 2%. The IAEA uses only the two most recent measurements in the P_n weighted average calculation, since

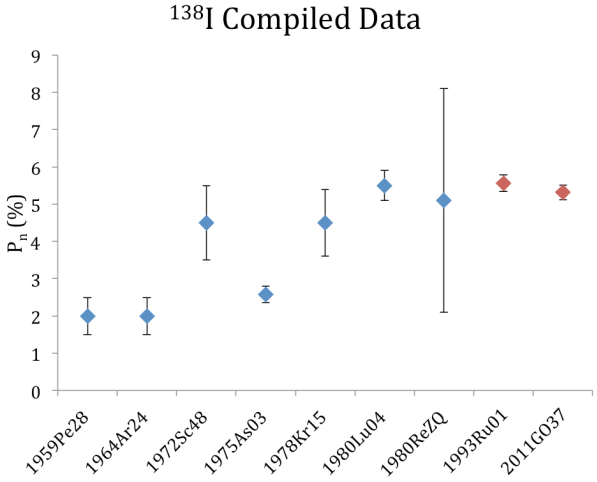

Figure 1.2: Compiled data of ^{138}I βn measurements. The two most recent measurements (1993Ru01 and 2011GO37, marked in red) were used in the weighted average calculation in the IAEA evaluation.

these data represent two independent measurements, and ignores the discrepant set around 2%. Using a different independent measurement technique could resolve this discrepancy. Another standard selected in the IAEA report is ^{137}I. It is a well-studied case, and it was the first βn precursor studied in the proof-of-principle experiment described in [13], upon which the current work is based on.

1.2.2 Constraining nuclear reaction rates

The neutron-capture reaction rates can serve a significant role in certain astrophysical nucleosynthesis scenarios, as some recent sensitivity studies have shown [14]. The neutron-rich environments present in explosive environments or during the nuclear reactor operation alter the fission product yields via neutron-capture reactions. Hence, neutron-capture cross-sections are needed for the stockpile stewardship mission [15, 16], and for calculations of criticality safety margins in nuclear reactors [10].

For isotopes far from the line of stability, it is not currently possible to measure neutron-capture rates directly. Several techniques have been used for indirect determination of the (n, γ) rates, where the experimentally found values for the γ strength function and the nuclear level density are combined with theoretical models to constrain the neutron-capture cross-sections. The relevant nuclear physics parameters can be extracted using the Oslo method [17, 18] applied to nuclei where the excitation states are populated by β decay [19]. In general terms, the β-Oslo method relies on a measurement of the γ-coincidence matrix, in which the total γ absorption spectrum (corresponding to the excitation energy of the state) is plotted against the primary γ-ray energy. The primary γ-ray matrix is proportional to the nuclear level density and the γ-ray transmission coefficient. The β-Oslo technique can

be used across a broad range of neutron-rich nuclei to extract or constrain neutron-capture reaction rates. In another method, the β-gated γ-ray spectra obtained using the Total Absorption Gamma Spectrometer (TAGS) are used to extract the β intensity distribution, $I_{\beta\gamma}$. Comparing the experimentally measured $I_{\beta\gamma}$ to the calculated one can estimate the values used for the γ-strength function or the neutron transmission coefficient [20]. Such a comparison performed for ^{94}Rb indicated that matching data to calculation would require a significant enhancement of the γ strength function, suppression of the neutron transmission coefficient, or combination of the two effects. Correspondingly, change in these values would modify the calculated (n, γ) cross-section values.

Conversely, as a different method for constraining the neutron-capture cross-sections, one can use the β-delayed neutron data. Nuclear structure information, such as β-strength function S_β or level densities $\rho(E)$, can be extracted from βn energy spectra [21, 22]. Such data can also provide constraints in modern nuclear-structure calculations and empirical models used to predict decay properties of nuclei far from stability, for which no data exist [23, 24, 25]. Furthermore, since neutron emission following the β^- decay may be interpreted as an inverse of neutron capture for the states where spin and parities match up, the nuclear structure information deduced from the βn data, coupled with theoretical models, can constrain neutron capture rates [26, 27]. To test the applicability of this approach to estimating capture rates, we were interested in measuring ^{144}Cs and ^{145}Cs, relevant to the stockpile stewardship mission. These nuclei have been studied previously [28], and have large fission yields, serving as a test case to gauge the achievable levels of detail applicable for the approach of estimating capture rates.

1.2.3 The r-process nucleosynthesis calculations

The origin of the naturally-occurring elements reflects the evolution of our universe. The first elements created during primordial nucleosynthesis, H, He, and Li, were the building blocks of the first stars. Stellar nucleosynthesis, in turn, is responsible for the creation of elements up to iron through fusion reactions. However, since the binding energy per nucleon (shown in Fig. 1.3) begins to decrease for elements heavier than iron, fusion (which proceeds to the right in the curve) is no longer energetically favorable.

The origin of elements heavier than iron has been identified as one of the greatest unanswered problems in physics [31, 32]. The process of production of these "heavy" elements is almost entirely attributed to successive neutron capture reactions, forming neutron-rich nuclei that decay back to stability and make up the solar abundance pattern of the heavy elements shown in Fig. 1.4. Roughly half these heavy elements are attributed to the s-process, where the neutrons are captured onto the nuclei on timescales much slower than their β decay half-lives. In this case, the successive neutron captures follow a production path close to stability. Alternatively, in a high neutron flux, the neutrons can be captured very rapidly on timescales smaller than the β decay half-lives, comprising the r-process path shown as a black line in Fig. 1.5. Through the r-process, very neutron-rich nuclei can be formed. After the neutron source is removed (after the "freeze-out"), the nuclei decay back to stability

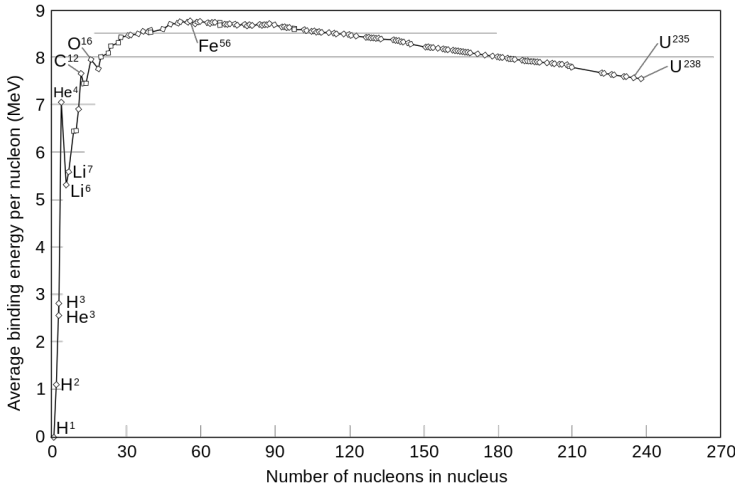

Figure 1.3: Binding energy per nucleon plotted against number of nucleons in the nucleus. Data from [29], plot via Wikimedia Commons.

through successive β^- decays. During the decay back to stability, βn emission may alter this path towards lower values of A, thus affecting the final abundances. The abundance pattern due to the r-process shown on the inset of Fig. 1.5 was calculated by subtracting abundances calculated due to the s-process (which is well characterized) from the observed solar abundance data.

The two main obstacles in theoretical studies of the r-process are the yet unidentified astrophysical site of the r-process, and incomplete nuclear data of neutron-rich isotopes far from stability. The r-process requires high neutron densities ($>10^{20}$ neutrons/cm^3) and temperatures above 10^9 [34]. Explosive neutron-rich environments, such as type II core-collapse supernova, have been proposed as plausible candidates for creating these necessary conditions. More exotic sites, such as neutron star mergers, have also been proposed [35]. Modeling the r-process itself requires nuclear input in the form of nuclear masses and β decay half-lifes [34], while the elemental abundance calculations also require accurate P_n data [36]. The impact of βn branching ratios on the final abundance pattern can be quite dramatic, as illustrated in Fig. 1.6. A sensitivity study described in [37] demonstrates how changing just one P_n value from 0 to 99% can shift the entire abundance peak. P_n values for many of the isotopes on the r-process path are still unknown, motivating further βn studies.

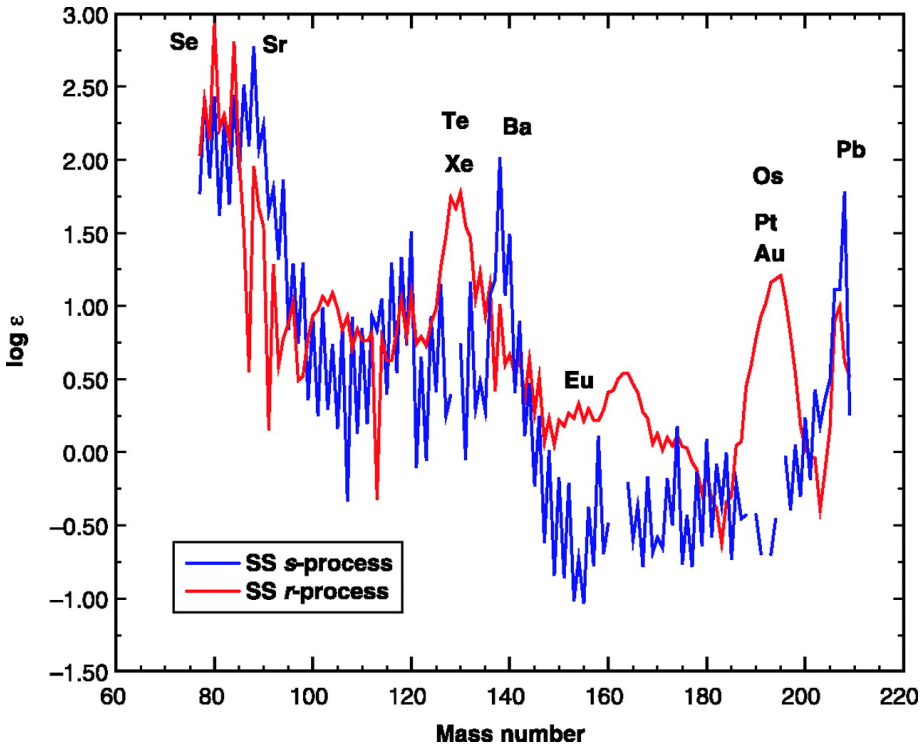

Figure 1.4: Relative solar system elemental abundances due to the r-process and s-process, from meteoritic abundance data[30]. The s-process peaks are shifted to the higher mass number, since the corresponding neutron shell closures occur near the region of the β stability, while in the r-process these neutron shell closures occur at lower proton numbers (and hence lower A). These paths are shown in Fig.1.5.

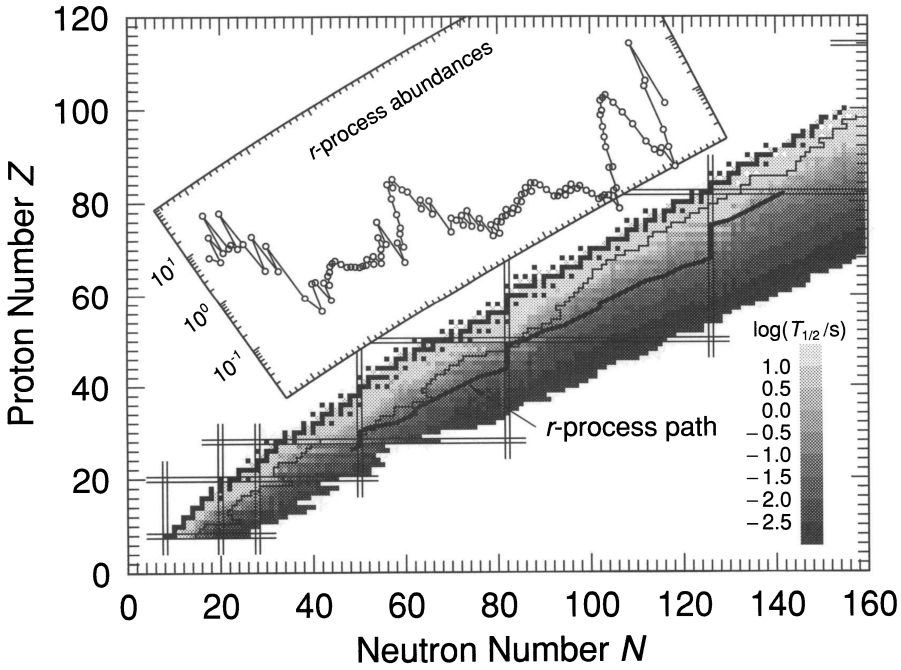

Figure 1.5: Chart of the nuclides with the r-process path marked as a dark line to the right of the β-stability region. Inset shows the solar abundance pattern resulting from the r-process nucleosynthesis [33]. The proton and neutron shell closures are marked with horizontal and vertical lines, respectively.

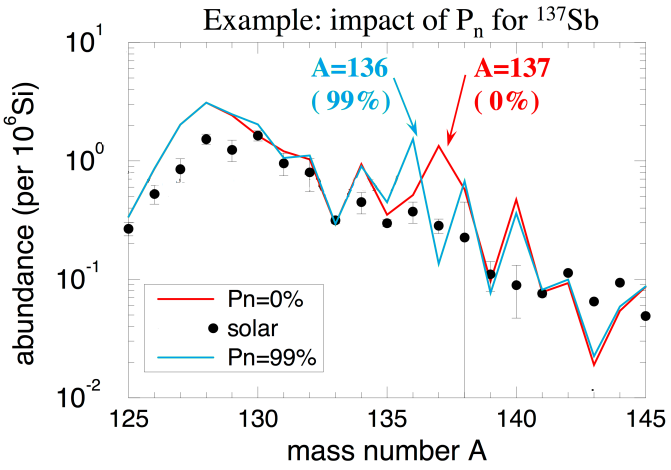

Figure 1.6: Impact of changing P_n of ^{137}Sb from 0% to 99% on the calculated elemental abundance pattern around mass A=137 [37].

Chapter 2

Techniques for characterizing β-delayed neutron emission

Existing methods for characterizing β-delayed neutron emission rely on direct neutron detection. Although improvement in detector technologies has allowed spectroscopic studies to be performed for a range of neutron emitters, a vast majority of the known βn precursors are yet to be measured. In this chapter, I review the most commonly used techniques for βn energy measurements, and compare them with a new indirect technique that has been developed to perform the measurements described in this thesis.

2.1 Existing techniques for spectroscopic measurements

Direct neutron detection mechanisms are based on the neutrons interacting in matter either via scattering or a nuclear reaction. Scattering off of light nuclei, such as hydrogen or helium that have masses closer to the mass of the neutron, induces a recoil of suitably large energy, which then ionizes the medium producing an electrical signal. In a scintillating material, the recoil can excite molecules along its path, producing a scintillation light that can be detected with a photo-multiplied tube. On the other hand, reaction products (such as protons or γ-rays) resulting from a neutron-induced nuclear reaction can be detected directly. However, the aforementioned methods suffer from low detection efficiencies or low energy resolutions of the measured neutron energy spectra, as well as contaminating backgrounds and complicated detector response functions.

2.1.1 ^{3}He ionization chambers

An ionization chamber, filled with ^{3}He gas, utilizes the exothermic $^3\mathrm{He}(n,p)^3\mathrm{H}$ reaction (with a Q value of 0.764 MeV) to directly detect neutrons. The cross section for this reaction is 5330 b for thermal neutrons, and falls off with energy proportionally to $1/v$, ranging from about 10 b to 1 b for the neutron energy range of 10-1000 keV. The proton and triton produced in the reaction readily ionize the surrounding gas. Collecting the resulting electrons and

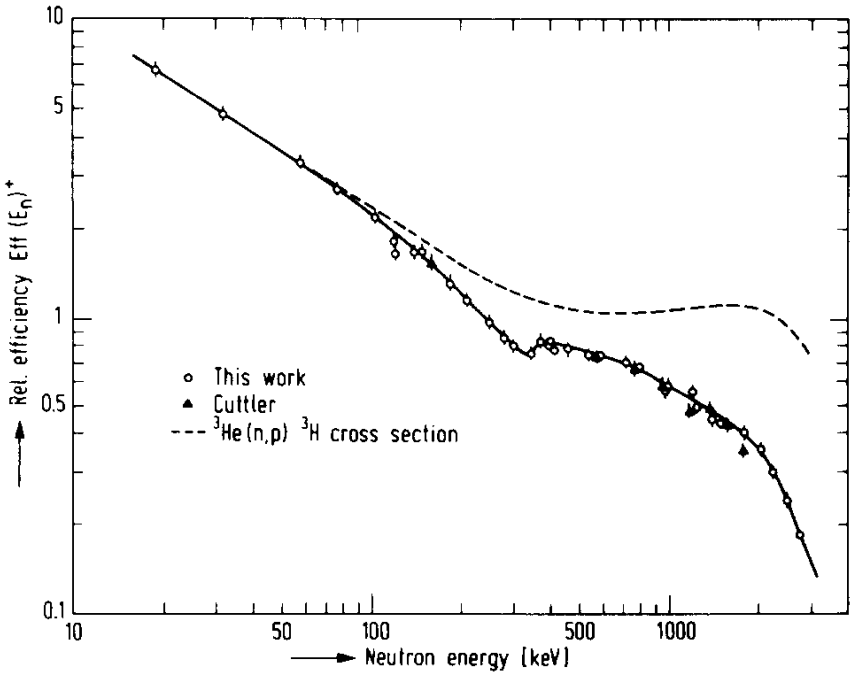

Figure 2.1: Relative efficiency of the ^{3}He fast neutron spectrometer in work of [42].

ions induces a detection signal. The resulting intrinsic detection efficiency ranges from 77% for thermal neutrons to 0.002% for MeV neutrons [38]. An example of an efficiency curve is plotted in Fig. 2.1. The amplitude of the full energy signal measured with by the charge collecting circuit corresponds to the energy of the neutron plus 0.764 MeV. The achievable energy resolution with the instrument configuration originally designed by Shalev and Cuttler is 20-40 keV FWHM over the energy range of 0-1 MeV [39, 40, 41]. Unfortunately, the neutrons can also scatter off of ^{3}He in the detector, producing a background continuum below the full energy peak. This background can also be induced from neutrons scattering off of dense gases that are added to the detector to reduce the path length of the charged reaction products depositing energy. Wall-effects resulting from incomplete energy deposition inside the detector volume may also be present as a background. These artifacts can be reduced with pulse-shape analysis. Many of the existing βn measurements employed this technique, such as spectroscopy of separated fission products in [42].

2.1.2 Proton-recoil proportional counters

Neutron energy measurements have also been obtained via measuring the energy of a proton recoiling from the neutron impact, detected in a proportional counter filled with hydrogen or methane gas or a scintillator. The energy transferred to the proton recoil follows a rectangular-like shape up to the full neutron energy transferred. This exact shape depends on the response of the detector material and its resolution. The total response to a spectrum

of neutron energies is then the sum of such response curves. Therefore, determination of the neutron energy spectrum requires very high statistics and complex unfolding techniques, as described in [43]. The γ's induce large backgrounds in these measurements, requiring pulse shape analysis [43]. The energy resolution obtained by this technique has reached 50 keV [44], though the low detection efficiency of about 0.001% deems it impractical for most βn spectroscopy measurements of nuclei far from stability, where the production of these nuclei in large amounts is difficult due to their short half-lives.

2.1.3 Neutron time-of-flight

The time-of-flight (TOF) of a neutron can be measured with fast scintillators by detecting the coincident β as the start of the TOF signal and neutron as the stop, as has been used in [45]. The neutron energy E_n can then be determined with the relation: $E_n = \frac{1}{2} m_n \left(\frac{d}{t_{TOF}}\right)^2$, where m_n is the neutron mass, d is the distance it traveled, and t_{TOF} is its time-of-flight. The β can be detected with a plastic scintillator, while the neutrons are counted with liquid or solid scintillators. Achievement of timing resolutions below 1 ns, and energy resolutions of 10% FWHM have been reported in literature. Large detection efficiency can be achieved with an increase in detector size. However, larger detector size decreases certainty of the exact event location and therefore compromises deduced energy resolution.

The major disadvantage of this technique is the scintillator sensitivity to γ's, and hence the presence of large backgrounds due to β-γ coincidences. These backgrounds can be reduced with pulse-shape discrimination or the difference in the TOF. The scintillator light resulting from a γ interaction decays more quickly than light produced by a recoiling proton (resulting from a neutron interaction). With appropriate electronics and signal processing, the γ background can be reduced up to 90% [45].

2.2 The recoil ion technique

By detecting the ion recoiling from neutron emission following the βn decay, measured in coincidence with the associated β-particle detection, neutron measurement can be achieved indirectly. The indirect measurement avoids many of the disadvantages of the methods described in Section 2.1, since a recoiling ion has electrical charge, and hence can be more easily detected. The energy of the recoil is deduced from the ion's time-of-flight, and is proportional to the neutron energy through conservation of momentum.

The technique relies on ion trapping to confine ions to a volume of $\approx$1 mm^3, from where they can decay nearly from rest and leave the trap undisturbed. Hence, accurate kinematic information can be obtained. At the low recoil energies involved, even the thinnest target foil would greatly distort the energy of the outgoing particle, making an accurate measurement impossible. Therefore, using the ion trap is crucial for this method to work. Ion traps have been widely used to collect nuclear data, such as nuclear masses [46], or β-ν correlations [47], and various types of ion traps exist to accommodate the specific experimental needs.

The open-geometry of the Beta-Paul Trap (BPT) used in the recoil ion technique enables placement of a detector array surrounding the trap.

The time difference between the β-particle detection and the recoil ion detection determines the time-of-flight (TOF) of the ion, and hence the recoil energy imparted by the decay. Using conservation of momentum, the neutron energy can be obtained from the nuclear recoil if the small contribution from the lepton and γ-ray emission is neglected. The TOF spectrum is also used to separate out recoils associated with neutron emission (with recoil energies on the order of a few keV) from those associated with β decay without neutron emission (with recoil energies of $\sim$100 eV). Decay products, such as γ-rays and β-particles are also measured, and provide additional methods of measuring the β-delayed neutron branching ratios, P_n.

The recoil-energy imparted by the β is much smaller from that imparted by the neutron. Therefore, the time-of-flight of the daughter recoil ion can be used to distinguish βn decays from the β decays without neutrons emitted. The recoil energy of the ion imparted by the neutron typically ranges from 1-10 keV. For a detector geometry where the flight path is on the order of 5 cm, this recoil energy translates to an ion's TOF on the order of 300-2000 ns, in what we refer in this work as "fast recoils." Conversely, recoil energy imparted by the β-particle averages around 100-300 eV, producing TOF's between 2000 and 5000 ns for the 5-cm flight path. We refer to these decays as "slow recoils." For the flight path of this size, the lowest energy neutrons can impart a recoil energy low enough that the ion's TOF is greater than 2000 ns, making it indistinguishable from the slow recoil ion distribution. In this case, the lowest energy neutrons that can be distinguished from the recoil ion TOF spectrum are at or above 100-keV, defining the neutron energy threshold for the particular experimental setup.

With the recoil ion technique, the branching ratios can be deduced using three methods by comparing the number of ions with short TOF's to: (1) the number of ions with longer TOF's, the "slow recoils," (2) the number of $\beta - \gamma$ coincidences deduced from the γ peaks, and (3) the number of detected β particles from the trapped species of interest. Comparison of the resulting branching ratios established with these three methods enables checks of systematic uncertainties.

In the recoil ion technique, the efficiency does not vary significantly with neutron energy, and the backgrounds are minimal due to the TOF of recoil ions being significantly longer than that of γ's. An intrinsic detection efficiency for the recoil ions of up to 60% is achievable, with energy resolutions of the reconstructed neutron of 10% FWHM. The neutron energy spectrum can be determined down to energies as low as 50-100 keV. Consequently, this method offers an excellent alternative for βn measurements, using a completely independent mode of detection.

The recoil ion proof-of-principle experiment conducted in 2012 demonstrated the promise of the recoil ion technique, and identified areas needing improvement, setting a basis upon which the work described in this thesis could be conducted.

2.2.1 The proof-of-principle experiment

The proof-of-principle experiment employing the recoil ion technique was conducted at the Argonne Tandem Linac Accelerator System (ATLAS) facility located at Argonne National Laboratory (ANL). The experiment was performed to measure the βn decay of ^{137}I, a well-studied βn precursor. The βn energy spectrum from the ^{137}I precursor was measured with ^{3}He ionization chambers [48, 42, 49, 21] as well as H_2 and CH_4 gas-filled proportional counters [50]. The ^{137}I ions were produced from the spontaneous fission of a 1-mCi ^{252}Cf source. The fission fragments were thermalized and extracted with a gas catcher [51]. Ions of mass 137 were then selected with a use of a timed deflection pulse and a He buffer gas-filled Penning trap [52]. In this configuration, the source provided a beam of $\sim$30 ions/s, and included the two nearest-neighbor isobaric contaminants: ^{137}Te and ^{137}Xe. The presence of the contaminants complicated the analysis, as the signal from these species had to be subtracted out of the slow-ion distribution and the β-singles counts, increasing uncertainties in the branching ratio numbers. In addition, ^{137}Te also has a βn decay branch, contaminating the neutron energy spectrum.

The Beta-decay Paul Trap used in the experiment has been previously built to perform precision β decay measurements [53], and was not optimized for the βn measurements. A plastic scintillator in a ΔE-E configuration was used to detect β's, while the recoil ions were detected using a microchannel plate (MCP). The MCP and the plastic scintillator were previously used for β-ν correlation studies [47]. Two high-purity germanium (HPGe) detectors, with 80% and 140% relative-efficiency, were placed on the re-entrant ports to measure the γ's. Fig. 2.2 shows the schematic of the experimental setup. A detailed description of the experiment can be found in [13]. Results of the experiment are summarized in Table 2.1 and Fig. 2.3. The proof-of-principle experiment was a successful demonstration of the recoil ion technique, and an opportunity to identify necessary improvements to the experimental setup.

Method	P_n(%)
(1) Low-energy recoil ions	6.80 $\pm$ 0.78 (sys) $\pm$ 0.41 (stat)
(2) β-delayed γ's	6.88 $\pm$ 0.79 (sys) $\pm$ 0.69 (stat)
(3) β-singles	6.95 $\pm$ 0.40 (sys) $\pm$ 0.65 (stat)
2011 IAEA evaluation [6]	7.33 $\pm$ 0.38

Table 2.1: Summary of the proof-of-principle results for P_n measurements, compared to the IAEA evaluation, as listed in [13].

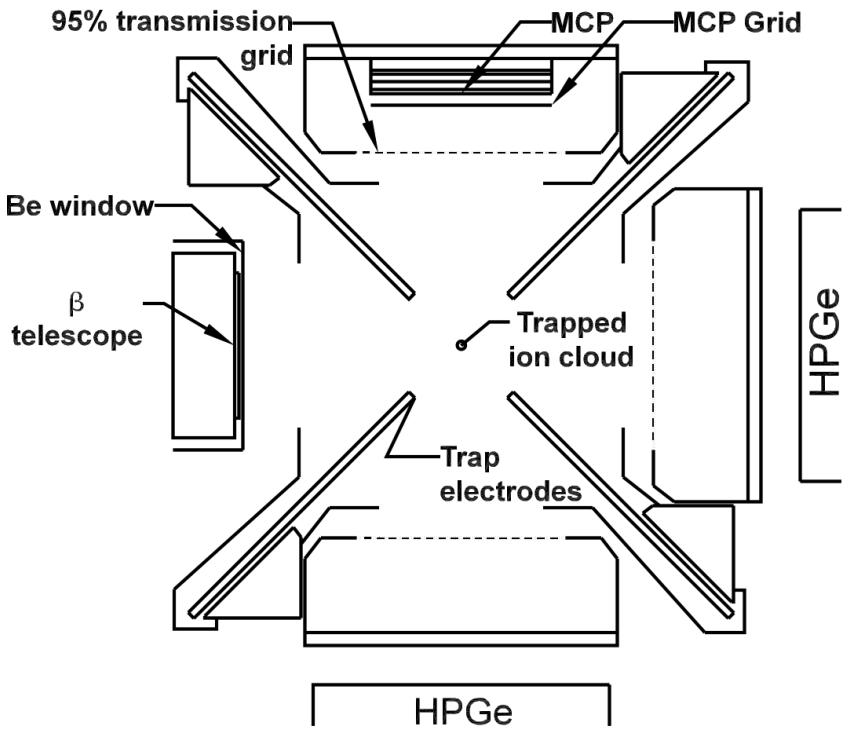

Figure 2.2: Experimental setup showing the trap and surrounding detectors for the proof-of-principle measurement, looking down the beam axis. Taken from [13].

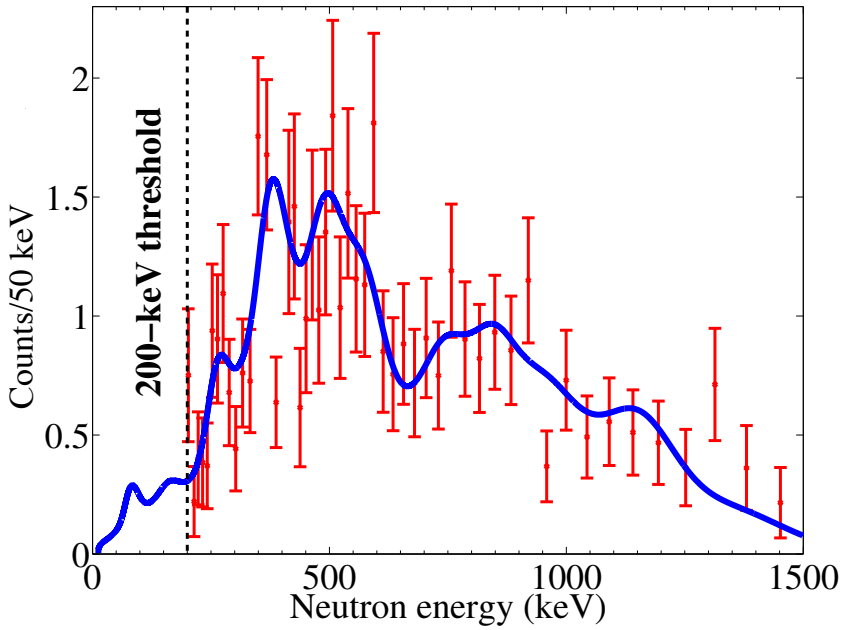

Figure 2.3: Neutron energy spectrum result from [13], compared to the spectrum of [21] convolved with the energy resolution of the proof-of-principle measurement (solid line).

Chapter 3

Experimental setup

The experimental apparatus used to perform the measurements described in this work expanded on the setup used in the proof-of-principle experiment, and employed several crucial improvements. The description of the experimental setup begins with the discussion of the beam production and trapping of the ions under investigation. The detector array consisting of two microchannel plate detectors (MCP's), two ΔE-E plastic scintillators, and two high-purity Germanium detectors (HPGe's) is described in detail, together with an overview of the detector calibrations. The basics of the signal processing and data acquisition are also outlined.

The experimental campaign conducted at the end of 2013 is the subject of this work, and builds upon the previously completed experiments. The improved trap and detector array used in the 2012 campaign was installed at the CAlifornium Rare Isotope Breeder Upgrade (CARIBU) facility, dramatically improving statistics with a 100 m-Ci ^{252}Cf source. Over the course of six weeks, data was collected on nine different isotopes (some for calibration purposes): $^{137-140}$I, $^{134-136}$Sb, and $^{144-145}$Cs. The focus of this thesis are the measurements of $^{137-138}$I and $^{144-145}$Cs, motivation for which was discussed in Chapter 1. Table 3.1 summarizes the datasets that were analyzed for this thesis, and includes estimates of the beam intensities achieved and basic information on the nearest-neighbor isobars. The run conditions (the cycle times) are also listed for completeness, and will be explained in the following sections.

3.1 Beam production and delivery

The experimental chamber was installed at the CARIBU hall at the ATLAS facility at Argonne National Laboratory (pictured in Fig. 3.1), taking advantage of its ∼100-mCi ^{252}Cf spontaneous fission (SF) source. The ^{252}Cf decays with a half-life of 2.645 years, and has a 3.09% spontaneous fission branch, resulting in an average activity of $\sim 10^8$ fissions/second. The resulting beam intensities, estimated in Table 3.1, provided an unprecedented level of statistics.

Cooled and extracted from the ^{252}Cf source via a gas catcher [51], the majority of ions emerge singly charged. The gas catcher thermalizes the fission fragments through collision

	Dataset				
	^{137}I.07	^{138}I.06	^{138}I.07	^{144}Cs.02	^{145}Cs.02
Species Z-1	^{137}Te	^{138}Te	^{138}Te	^{144}Xe	^{145}Xe
Species Z	^{137}I	^{138}I	^{138}I	^{144}Cs	^{145}Cs
Species Z+1	^{137}Xe	^{138}Xe	^{138}Xe	^{144}Ba	^{145}Ba
Z-1 half-life (s)	2.49(5)	1.4(4)	1.4(4)	0.388(7)	0.188(4)
Z half-life (s)	24.5(2)	6.23(3)	6.23(3)	0.994(6)	0.587(5)
Z+1 half-life (s)	229.08(78)	844.8(48)	844.8(48)	11.5(20)	4.31(16)
Z-1 fission yield	2.35×10^{-3}	5.43×10^{-4}	5.43×10^{-4}	1.16×10^{-4}	1.12×10^{-5}
Z fission yield	1.81×10^{-2}	1.06×10^{-2}	1.06×10^{-2}	5.60×10^{-3}	1.50×10^{-3}
Z+1 fission yield	4.33×10^{-2}	4.67×10^{-2}	4.67×10^{-2}	3.94×10^{-2}	2.19×10^{-2}
Total Runtime (h)	35.881	17.827	16.614	35.607	26.553
Cycle time (s)	246	60	90	9	5.6
Background time (s)	101	20.1	30.1	3.1	1.7
Capture time (s)	6	2	6	0.6	0.4
Obs. Z activity (Bq)	2.34×10^{2}	3.15×10^{2}	1.64×10^{2}	4.40×10^{2}	1.49×10^{2}
Avg. beam (ions/s)	8280	2830	1470	630	126
Avg. deadtime correction	1.071	1.077	1.065	1.096	1.058

Table 3.1: Summary of collected data and beam characteristics, including basic information on the nearest-neighbor isobars. The datasets are named after the precursor studied. The cumulative fission yields from the ^{252}Cf source are obtained from [54]. The observed activity is estimated from the observed number of β-singles counts and averaged over the data collection time.

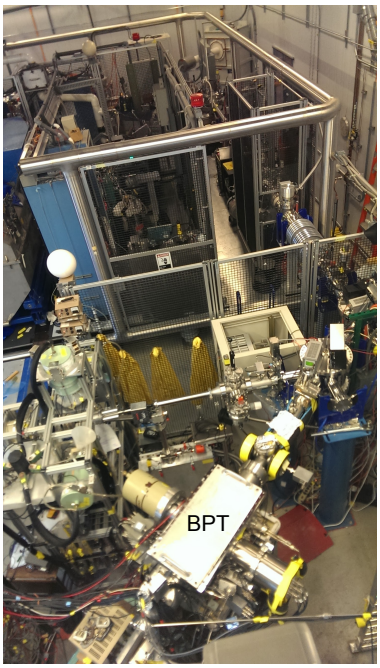

Figure 3.1: BPT experimental chamber placed in the CARIBU hall.

and ionization, and extracts them with a combination of DC fields, RF fields and gas flow. The DC gradient along the gas catcher axis pushes the ions towards the exit, and the RF field keeps the ions from hitting the walls and neutralizing. The ions exit through the nozzle with the help of the gas flow. The novel use of the RF focusing structure in the high-intensity gas catcher allows operation at high ion currents. The emerging ions are further cooled and focused in two radio-frequency quadrupole (RFQ) sections that form a differential pumping section where He gas is removed. The ions are then accelerated with an electrostatic 50 kV potential to form a beam, which is monitored with a silicon detector. Overall, the extraction via the gas catcher takes about 20 ms, and converts about 20% of total activity into the beam.

The beam transport is achieved with standard electrostatic ion optics components. The beam undergoes isobar purification and bunching with the use of a time-deflection pulse and an isobar separator [55]. The isobar separator has a mass resolution of about $\Delta M/M \sim 5000$ and is able to remove most isobars with the exception of some nearest neighbors (with +1 or -1 neutron). In case of a large fission yield of an isobaric contaminant, the beam may be tuned to favor one neighbor over the other. The tuning of the beam is achieved by choosing the mass of interest. Optimization of the transport is monitored with two sets of diagnostic detectors inserted into the beam path. Each set comprises of a micro channel plate for ion counting and a silicon surface barrier detector for β-counting. Following the beam purification stage, the ions are bunched with electrostatic potentials and enter the low-energy experimental area for measurements.

With the use of a DC potential set at the entrance of the experimental chamber, the

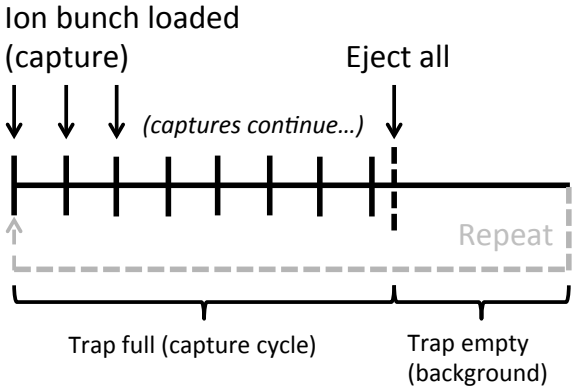

Figure 3.2: Diagram illustrating the trap loading cycle as a function of cycle time t_c.

transport of the ions could be finely controlled. The ions were loaded into the trap in bunches that could be quickly cooled and trapped, so as to minimize the disturbance of the existing trapped ion cloud. After several bunches, the entire population was ejected to assess the backgrounds. A schematic showing the trap loading and emptying events as a function of cycle time is shown in Fig. 3.2. The time between capture pulses, the number of injections, and the length of the background cycle was tailored to each isotope, depending on the presence of isobaric contaminants and the decay characteristics of the isotopes under study. Recording the cycle time also allowed analyzing the data in terms of temporal effects, such as radioactive decay.

The components of the beam were monitored with the Canadian Penning Trap Mass Spectrometer (CPTMS) [56]. The Penning trap uses a homogenous axial magnetic field to confine particles radially and a quadrupole electric field to confine the particles axially. The resulting trapping potential causes the ions to orbit around the trap axis with a motion characterized by the cyclotron frequency ω_c, which only depends on the charge to mass ratio of the trapped species and the well-known strength of the magnetic field. If a quadrupole RF excitation matching the ω_c in frequency is applied to the trap electrode, the trapped ions experience resonant excitation. To produce a mass measurement, the ions are released from the trap following the application of the RF excitation. The ions then drift towards a micro channel plate used to measure the time-of-flight of the ions, from which their energy can be deduced. The energy of the ions corresponds to the gain in orbital energy resulting from an RF excitation that matches ω_c. A spectrum is generated plotting the TOF of the ions vs. the applied frequency. The value that produces the shortest TOF determines the ω_c, from which the ion's mass can be derived. Further details of the CPT operation are described in [57]. The amplitude of the peak in the spectrum is roughly proportional to the amount of the isobar in the beam. By using the CPT, we were able to estimate relative amounts of various isobars in the beam at specific tuning conditions.

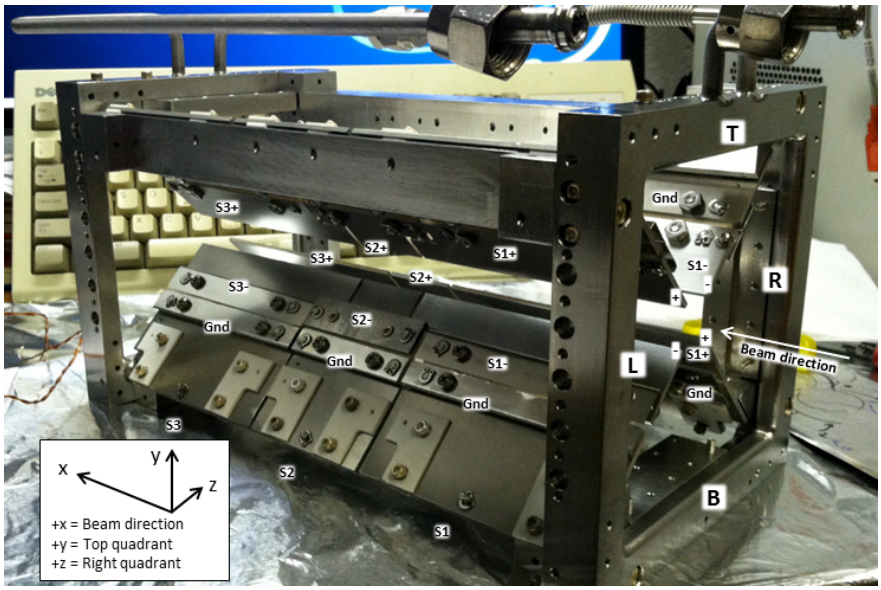

Figure 3.3: The BPT, with all the installed electrode blades labeled.

3.2 The Beta-Paul Trap (BPT)

To confine ions under study, we used an open-geometry linear radiofrequency quadrupole (RFQ) ion trap, to which we refer to as the Beta-decay Paul Trap, or BPT for short. The BPT was based on a design developed to perform precision β decay studies, and is described in detail in [53]. The trapping potential of the BPT is achieved with four flat stainless-steel electrodes placed concentrically around the trap center, with a trap radius (the distance between the tip of the electrode and the trap center) of 11 mm. Each electrode plate is segmented into three sections along the beam axis, so that a dc field can be applied to create an axial confinement. The trap, with all the electrodes labeled, is shown in Fig. 3.3. Changing the DC potential for the same segment in all the electrodes also controls the loading and ejection of the ions. The DC voltages applied to the electrodes are listed in Table 3.2. The radial confinement is achieved by having the two electrodes at opposite sides of each other held at the same potential, while the other two electrodes are held at an opposite potential. The potentials are then varied with a RF field of a sinusoidal-like form. This creates a "rotating saddle" potential pictured in Fig. 3.4.

For an ideal Paul trap that uses hyperbolic electrodes, the trapping potential gives rise to equations of motion for the charged particle described by the following Mathieu equations, rewritten with the dimensionless parameters a, q, and τ [58]:

$$\frac{d^2x}{d\tau^2} + (a + 2q\cos 2\tau)x = 0, \tag{3.1}$$

$$\frac{d^2z}{d\tau^2} - (a + 2q\cos 2\tau)z = 0. \tag{3.2}$$

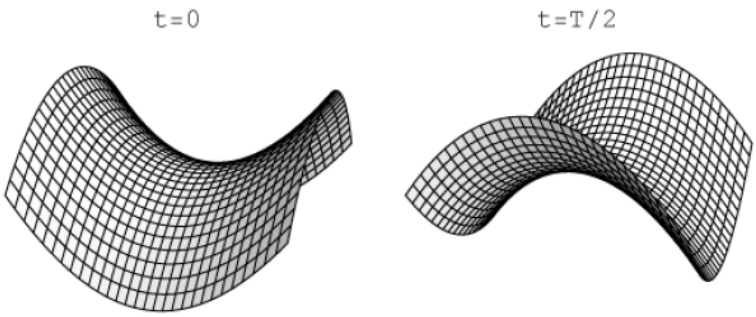

Figure 3.4: Graphic approximating the "rotating saddle" potential created by the RF fields in the BPT.

The dimensionless parameters are defined as:

$$a = \frac{4eU}{mr_0^2\omega^2}, q = \frac{2eV}{mr_0^2\omega^2}, \tau = \frac{\omega t}{2}, \tag{3.3}$$

where U is the DC potential, V is the RF potential with driving frequency ω, r_0 is the trap radius, m is the mass of the ion, and e is the electron charge. x and z are the coordinates perpendicular to the beam axis, where y points along the beam axis. The solutions to these equations yield a stability relation where motion in x and z directions are stable (the particles oscillate with limited amplitude), or unstable (amplitudes grow exponentially and particles are lost). Stability depends only on the a and q parameters, and is achieved for regions of overlapping x and z stability. The diagram showed in Fig. 3.5 illustrates the regions where a plotted vs. q gives the z and x stability for the two-dimensional quadrupole field. The lowest region of stability for overlapping x and z stability is shown in Fig. 3.6. The stability is achieved within the triangle. All ions with different charge to mass ratios lie along the operating line a/q = 2U/V = constant, for fixed values of r_0, U, V, and ω. This property gives rise to the Linear RFQ operated as a mass filter.

For the case of our open-geometry trap with flat electrodes, the trapping field can be approximated near the trap center as equivalent to that produced by the ideal trap with a radius of $r_{ideal} = 1.3 \times r_0$. In our experimental setup, the trap stability condition was chosen so that only 1+ ions would be confined. Upon β decay, the recoil ions emerge in 2+ (or higher) state and hence are no longer confined in the trap.

In order to minimize the size of the ion cloud, we injected helium acting as a buffer gas. Helium was chosen due to its high-ionization potential. The helium gas was sustained at a pressure around 5×10^{-5}. The resulting size of the ion cloud (the FWHM) was found to be around 2.5 mm. This was found by analyzing the leading edge of the slow ions in the time-of-flight spectrum, and comparing it to the simulations.

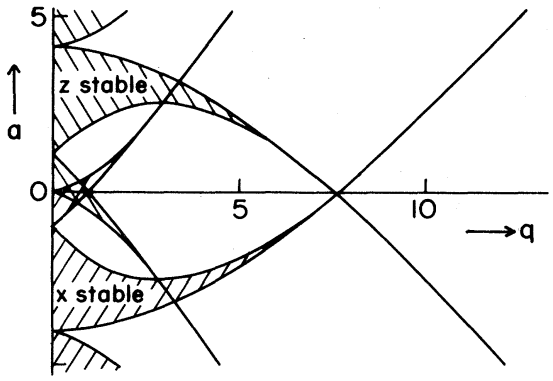

Figure 3.5: Paul trap stability diagram, adapted from [58].

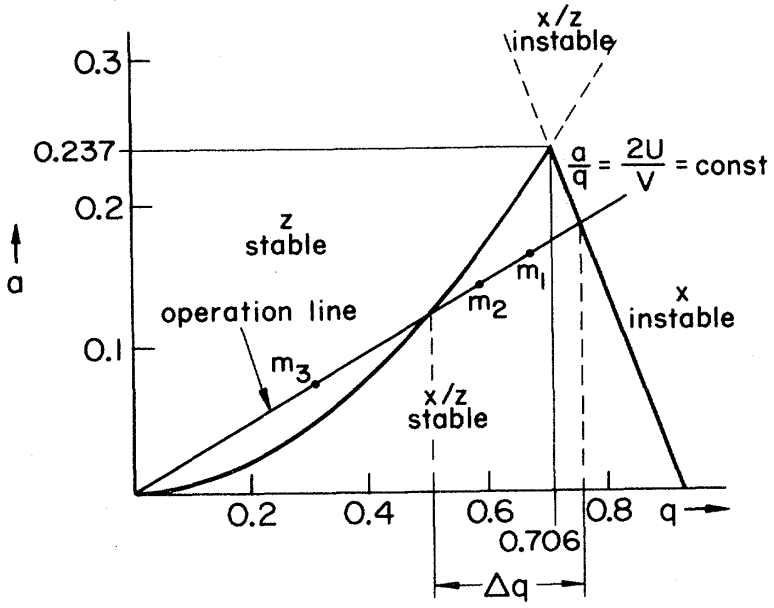

Figure 3.6: Lowest region of overlapping z and x stability, adapted from [58].

3.2.1 Characterizing the BPT RF fields

The RF field present on the electrodes can distort the trajectory of low-energy recoil ions. The simulation used to characterize this effect needs precise voltage and waveform information, and hence detailed calibrations were performed to measure the exact frequencies and amplitudes of the RF fields.

The RF fields were applied using a linear, resistive coupling circuit with balanced power-resistors and used a power amplifier operating at roughly 75W. The coupling circuit is shown in Fig. 3.7. The circuit used transformers with 8 windings on the primary coil and 3 on the secondary. The RF signal was tailored to each isotope, and separately measured for each dataset. We measured the signal on each electrode with an oscilloscope (using a 10X probe) and a high-precision digital multimeter.

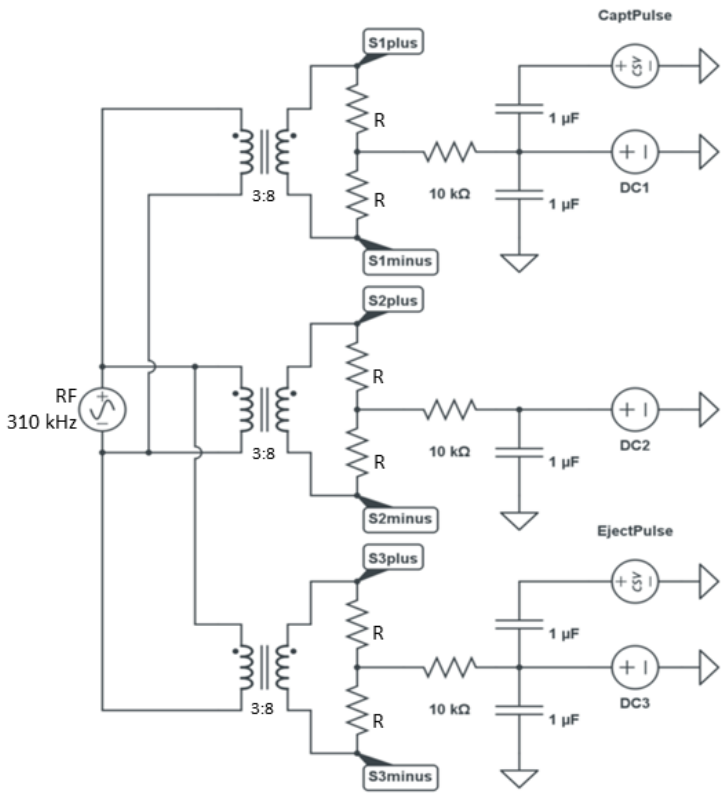

Figure 3.7: Coupling circuit used for applying voltages to the trap electrodes. The S1, S2, and S3 denote the three segments of each of the four electrodes, and the + or - indicates the sign of the amplitude. Each 'R' has a value of 470Ω. The CaptPulse and EjectPulse refer to the voltage pulses used to control the capture and ejection of species in the trap.

The oscilloscope measurements revealed that the applied waveform contained harmonics of the original sine signal. The waveform can be described with a sum of three sine waves

Electrode	Trapping	Capture	Eject
S1	+20 V	-15 V	+20 V
S2	-17 V	-17 V	-17 V
S3	+20 V	+20 V	-80 V
endplates	-30 V	-30 V	-30 V

Table 3.2: DC voltages applied to the electrodes for axial confinement.

as follows:

$$(V_{rf}/2)(t) = \sum_{i=1}^{3} A_i \sin[2\pi f_i(t - t_i)] \tag{3.4}$$

$$f_i = 310 \times i \text{ kHz}$$
$$t_1 = 1.461\mu s$$
$$t_2 = 1.840\mu s$$
$$t_3 = 1.945\mu s$$

The high-precision multimeter used to measure the amplitude of the voltage was calibrated with a digital function generator. The scaling between the multimeter and the peak-to-peak voltage was found to be 80.8 V_{pp}/V_{ac}, where V_{ac} indicates the multimeter reading. With the known scaling, the multimeter scaling with the individual harmonics' amplitudes was found to be as follows: 45.5 V/V_{ac} for A_1, 0.5 V/V_{ac} forA_2, and -9.1 V/V_{ac} for A_3. The amplitudes used for each isotope, scaled from ^{137}I values, are listed in Table 3.3.

Isotope	^{137}I	^{138}I,06	^{137}I,07	^{144}Cs	^{145}Cs
A1	109.3V	108.22	107.635	111.55	109.975
A2	1.15	1.138	1.1315	1.175	1.1575
A3	-8.9	-8.6864	-8.5707	-9.345	-9.0335

Table 3.3: Values calculated from the measured signal for the amplitudes of the individual RF harmonics

In addition to performing the electrode measurements, the probe itself was tested in case it had an effect on the measurement. By using an additional probe, no measurable change in the probe reading was found due to the presence of another probe. We also found uniformity in voltage across all the electrodes. The effect due to room temperature was found to account for a change of about 0.01 $V_{ac}/°F$, which is within the uncertainties of the voltage measurement. The correct waveform was then implemented in the simulations for each isotope. The waveform for ^{137}I is shown in Fig. 3.8.

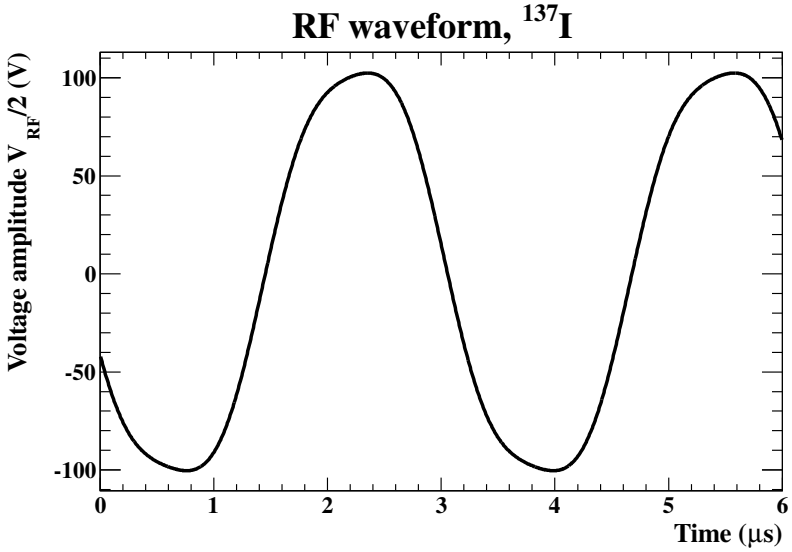

Figure 3.8: The shape of the RF amplitude as a function of time, applied to the electrodes in the positive (+) phase.

3.3 The detector array

The schematic of the detector array setup is shown in Fig. 3.9. The schematic is not drawn to scale, and omits the boundary of the chamber and various shielding in order to clarify the placement of the detectors around the trap electrodes. Overall, three sets of two detectors of each type were used to measure and characterize the decay products. The microchannel plate detectors and the plastic scintillator detectors were chosen due to their fast timing and high intrinsic efficiency, while the high-purity germanium detectors offer excellent γ-ray energy resolution. The diagrams containing the details of the electronics setup for each detector are described in Appendix C.

3.3.1 The plastic detectors

The two custom-made plastic scintillator detectors used for β-particle detection were placed in a ΔE-E telescope configuration, with the ΔE located 105 mm from the trap center. We refer to each of the detectors as Left or Bottom, referring to its position with respect to the trap center looking down the beamline. The scintillator material for the detectors was chosen to be EJ-204. The ΔE, a disk of 1-mm thickness, had a negligible sensitivity to γ-rays, while the E detector, a cylinder 13-cm long, could measure β's up to 20-MeV in energy. The diameters of the ΔE and E were 4.2" and 5.15", respectively. The telescope was placed behind a thin (8-μm thick) aluminized Kapton window to prevent the outgassing from the detector affecting the vacuum inside the trap volume. The plastic detectors were pumped with a separate turbopump vacuum system to retain integrity of the Kapton window and

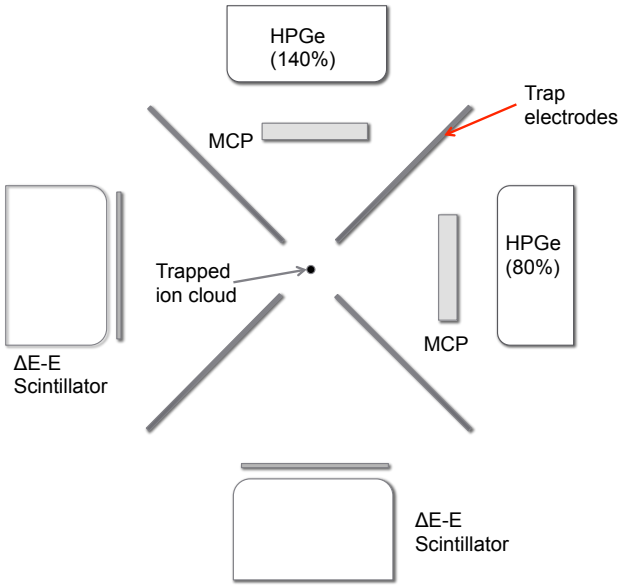

Figure 3.9: Schematic of the trap and detector placement, looking down the beam axis, not drawn to scale. Electrode and MCP shielding, as well as chamber re-entrant ports are omitted for clarity.

to minimize energy loss for the β-particles traveling between the Kapton window and the detector volume.

The E scintillator was coupled to a 5" photomultiplier tube (PMT) made by Electron Tubes Enterprises Ltd. (Part No. 9390KEB). The ΔE scintillator was surrounded by a light guide, wrapped in a Vikuiti reflective film, that channeled the light into two 1.5" Hamamatsu PMT's. We wrapped each of the PMT's in magnetic glass in order to prevent the strong magnetic fields present in the experimental area to affect their operation. The detector construction schematics are shown in Fig. 3.10 and Fig. 3.11. A photograph in Fig. 3.12 shows the improvements we made to the detectors in form of wrapping light guides with reflective tape and adding magnetic glass.

Each E scintillator PMT signal was split into two signals with a use of a passive splitter (Mini-Circuits SCP-2-1+). One of these outputs was wired through an Ortec 113 pre-amplifier, prior to being shaped with a Tennelec 244 amplifier. The output of the amplifier was then recorded with the 7164 Phillips Analog-to-Digital Converter (ADC) module. The other output of the splitter was fed through a Tennelec 455 constant-fraction discriminator (CFD) for accurate timing pick-off. This timing signal was recorded with a LeCroy 4208 Time-to-Digital Converter (TDC), and was also an input into the master trigger. The ΔE PMT signals were treated identically, with the exception of using a linear FIFO NIM module instead of a passive splitter, and amplifying the timing signal by 20 prior to feeding it into the CFD. The two ΔE PMT signals were treated independently and combined in software. The timing of ΔE was determined by averaging the two PMT signals (the difference had a variance of $\approx$ 1 ns).

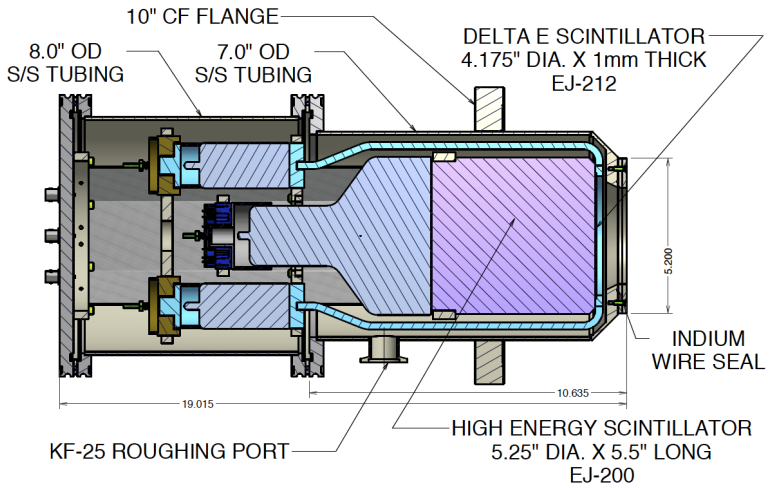

Figure 3.10: Schematic for the plastic detector assembly.

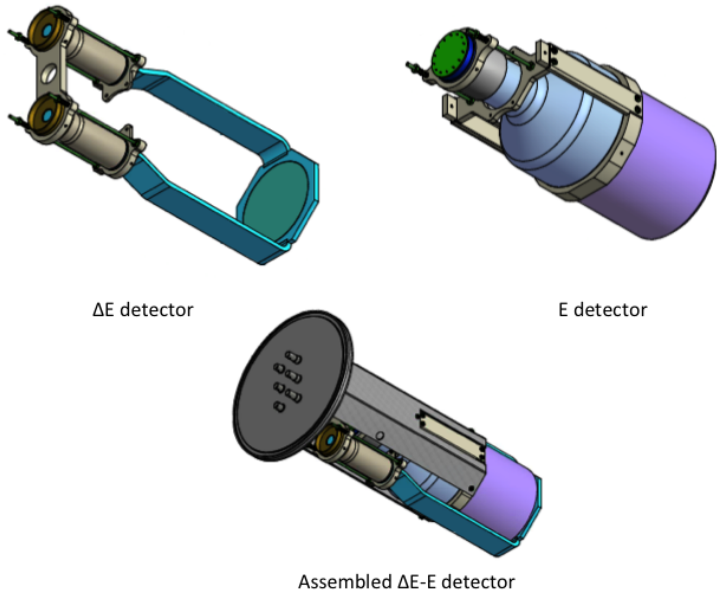

Figure 3.11: ΔE and E assemblies, separately and together.

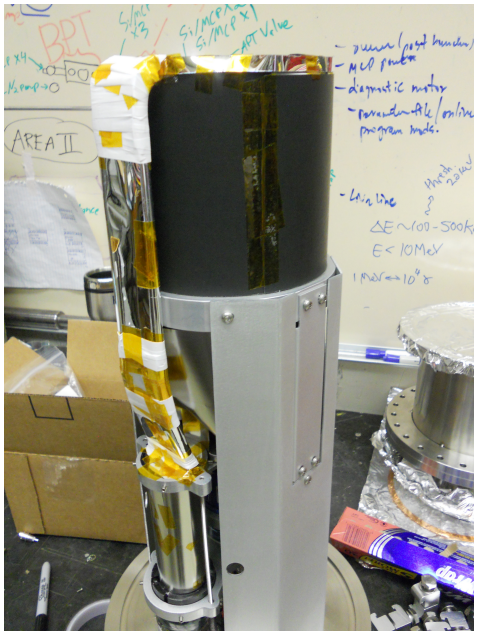

Figure 3.12: Uncovered plastic detector assembly showing various improvements.

Scintillator β detection threshold and energy calibration

In theory, the Kapton window should allow β's above ≈30 keV to enter the detector. In practice, the actual energy detection threshold was found to be higher, since threshold also depends on the light collection and the PMT efficiency. Analysis of pulse-height distributions for low-energy conversion electrons from the ^{134}Sb dataset and β's from the ^{207}Bi calibration source reveled that the energy for each ΔE at which the detector efficiency drops to 50% is **76 ± 24 keV** for the Left ΔE and **62 ± 30 keV** for the Bottom ΔE. The energy calibration for the ΔE's was found to be:

$$E_{LEFT} = (0.54 \pm 0.08) \times C + (23 \pm 16) \text{ keV}, \tag{3.5}$$

$$E_{BOTTOM} = (0.57 \pm 0.08) \times C + (-9 \pm 20) \text{ keV}, \tag{3.6}$$

where C is the channel number, and E_D is the energy in keV for each ΔE detector D.

3.3.2 High-purity germanium (HPGe) detectors

Two coaxial single-crystal Ortec HPGe detectors were placed outside of the vacuum chamber on re-entrant ports. The Top detector (located on the BPT chamber top cover) was a 140%-relative-efficiency crystal, while the Right detector (placed to the Right of the trap center when looking down the beamline) was a 80%-relative-efficiency detector. The standard output of each detector was a timing and amplitude signal. The amplitude signal was split

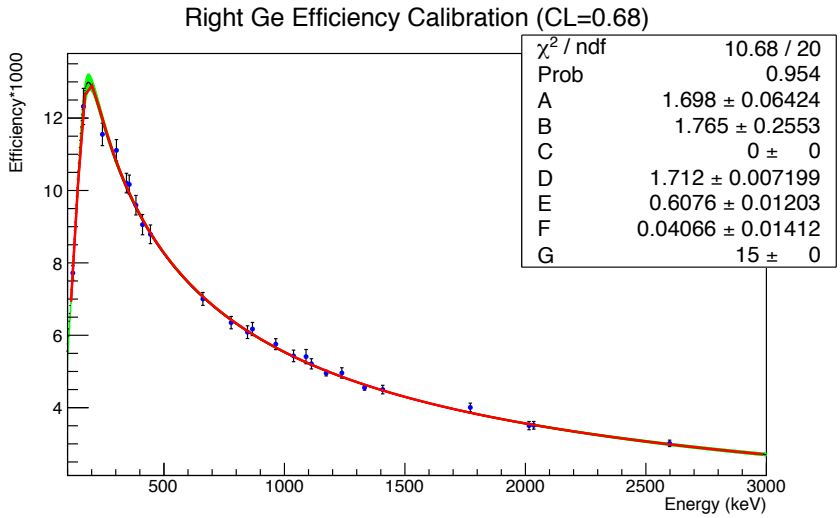

Figure 3.13: Right HPGe efficiency curve fit to the calibration points. The fit uncertainty is marked in green.

into two (with a Mini-Circuits SCP-2-1+ passive splitter), each amplified with an Ortec 572 amplifier by a different amount. Hence, each HPGe energy signal consisted of two spectra, one covering a range in γ energies up to 3 MeV, and the other up to 9 MeV. The timing signal of the detector was shaped and amplified with an Ortec 474Q Quad Timing Filter Amplifier (TFA) and then fed through an Ortec 473A CFD. The output of the CFD was split into two, with one recorded by a LeCroy 4208 TDC, and the other as an input into the master trigger.

HPGe calibrations

The energy and efficiency of the Right HPGe was calibrated before and after the main experimental data taking with standard γ-ray sources: ^{60}Co, ^{133}Ba, ^{137}Cs, and ^{152}Eu. Each of the sources was calibrated by NIST on March 31st, 2014, and had an activity of about 41 kBq. The sources were positioned within 0.25 mm of the trap center with the use of a custom-made source jig. With the Top detector attached, the insertion and removal of a source required lifting the entire BPT chamber cover with a lift. Due to limited time availability prior to the scheduled beam time, the Top detector was only calibrated with ^{152}Eu prior to the data taking. The detector then failed during the experimental run, and we were unable to calibrate it with other sources after the experiment.
The results of the efficiency analysis for the two detectors are shown in Fig. 3.13 and Fig. 3.14. The total efficiency curve for each detector was determined by fitting the results from the individual peaks in the calibration with Eqn. 3.7:

$$\varepsilon_\gamma = 0.001 \exp\{[(A + Bx + Cx^2)^{-G} + (D + Ey + Fy^2)^{-G}]^{-1/G}\}, \tag{3.7}$$

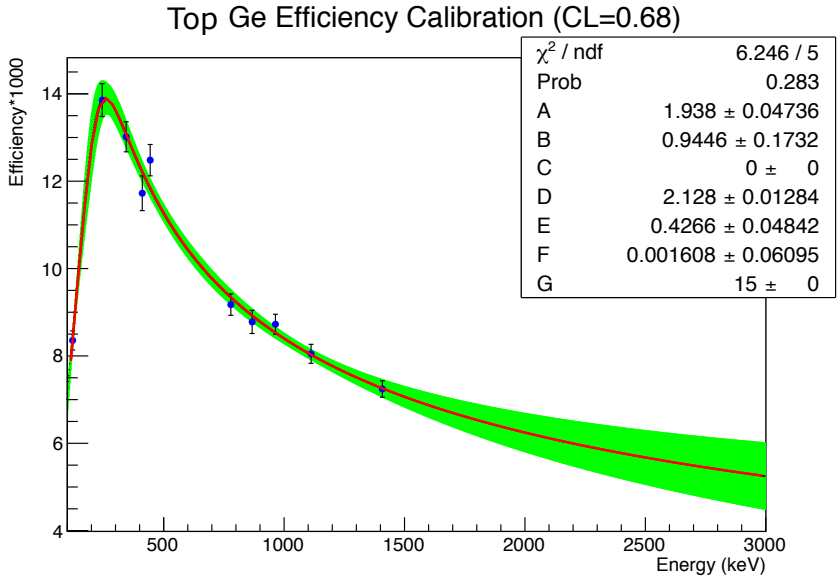

Figure 3.14: Top HPGe efficiency curve fit to the calibration points. The fit uncertainty is marked in green.

where x and y are defined as:

$$x \equiv \ln(E_\gamma/100 \text{ keV})$$
$$y \equiv \ln(E_\gamma/1000 \text{ keV}).$$

The parameters for the efficiency curve determined from fitting the calibration data are shown in each efficiency curve figure, and are summarized in Table 3.4. The effect of the ion cloud on the efficiency was estimated to be around 2% by comparing point source data to the Geant4 model.

3.3.3 Microchannel Plate (MCP) detectors

A microchannel plate detectors used in the experiment were made of slab of lead-silicate glass containing a regular array of tubes, each of diameter of about 10-μm, acting as an electron multiplier when placed under a strong electric field. A particle entering the channel strikes the wall inducing a secondary electron cascade, thus a channel can be considered a continuous dynode structure. In a Chevron configuration, two MCP's are stacked together, with the channels oriented at an angle from each other and relative to the surface plane, so as to increase the total electron yield [59]. The current resulting from the electron cascade is read out at the back of the detector. In a configuration where the information on the location of the impact is desired, one may use an an anode with uniform finite resistivity and circular boundary. By reading off the charge at the four corners (posts), it is possible

Parameter	Top Ge	Right Ge
A	1.938	1.698
B	0.9446	1.765
C	0.0	0.0
D	2.128	1.712
E	0.4266	0.6076
F	0.001608	0.04066
G	15.0	15.0

Table 3.4: Fit parameters to the efficiency curve.

to calculate the location of the impact based on the relative charge collected by each post. The resistive anode readout is based on the design by Lampton and Carson [60].

In the experimental setup, each MCP detector consisted of two 5 cm x 5 cm resistance-matched plates, sourced from Photonis, and installed in a Chevron configuration. A 89% transmission grid was placed in front of the MCP to create a uniform acceleration field for the recoil ions and to prevent the MCP bias voltage affecting the recoil ion trajectories inside the trap. The front plate was biased to -2500 V. The entire assembly, pictured in Fig. 3.15, was installed on a grounded ceramic plate, and covered with an aluminum grounding shield with a square hole covered by another 89% transmission grid. The MCP's were fixed to the trap frame, located at the Right and Top locations in front of the HPGe's. The distance from the trap center to the ground can was ∼42 mm, and ∼53 mm to the plate surface.

The MCP signal was read out from the four corners of the resistive anode. This configuration allows determination of the event location by comparing the amount of charge distributed among the four posts. To reconstruct the location of the ion, the charge collected at the posts (marked as A, B, C, and D) is weighted as in Eq. 3.8 to produce dimensionless coordinates ranging from -1 to 1:

$$x = \frac{C + D - A - B}{A + B + C + D} \tag{3.8a}$$

$$y = \frac{A + D - C - B}{A + B + C + D}. \tag{3.8b}$$

These coordinates are then converted to physical coordinates with a transformation characterized by the calibration data. The calibration was performed with a ^{238}Pu α source illuminating the MCP with a custom mask installed in front of the detector. The mask used is shown in Fig. 3.16. By fitting the calibration data to the known locations of the holes, we can obtain a scaling between the dimensionless and real coordinates. The best fit was found for the scaling values of 25.645 for the Top MCP and 25.728 for the Right MCP.

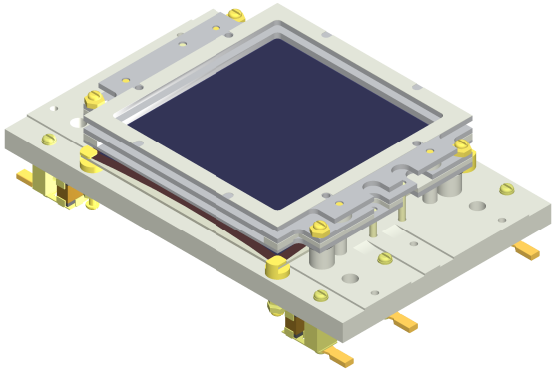

Figure 3.15: MCP assembly, without the ground can. Design by Quantar.

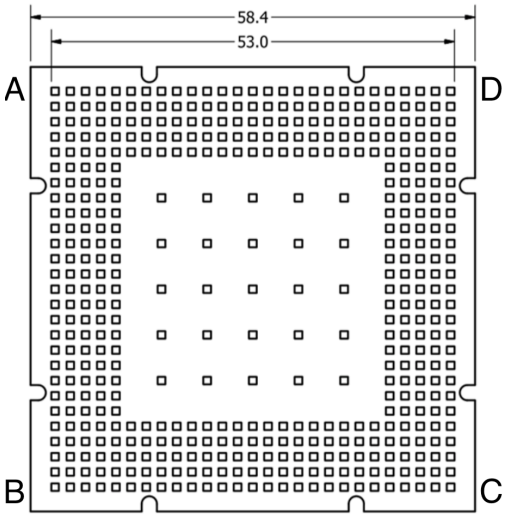

Figure 3.16: Mask design used for mapping the MCP's. The posts are labeled.

	Plastic Detector	
Measured quantity	Left ΔE	Bottom ΔE
Trap center to aperture (mm)	85.7(5)	84.8(5)
Aperture radius (mm)	41.15(13)	41.15(13)
Solid angle ($\Omega_\beta/4\pi$)	**4.927(56)%**	**5.017(57)%**

Table 3.5: Physical measurements and the resulting solid angles for the plastic detectors.

Bias voltage provided by the power supply was split in a voltage divider box to bias the resistive anode and the MCP plates. The bias used for the rear plate was capacitively read off to provide the event timing information. The timing signal was fed through two Ortec 820 fast amplifiers (each amplifying by 20X), and a Tennelec 455 CFD, before being recorded with the LeCroy 4208 TDC and input into the master trigger. A separate power supply fixed the grid voltage to 0 V. The grid could also be biased to other voltages to make it possible to select out specific charge states.

The four post signals of the MCP were shaped and pre-amplified using a commercially-available electronics from Quantar. The DC pedestal in the signal output was then removed with a transformer (Mini-Circuits T4-1+). The outputs were recorded with an ADC.

3.3.4 Solid Angle Measurements

The solid angles used in all the branching ratio calculations were found from the physical measurements performed after the experiment. The measurements were performed using a cylindrical gauges with diameters near 0.9000", inserted into the trap volume to fit in between the electrodes. The distances to the detectors were inferred by measuring the distance from the gauge, and adding back the gauge radius.

For the circular ΔE detectors, the solid angle can be easily calculated with $\Omega = 2\pi(1 - \cos\theta)$, where θ is the apex angle of the cone subtended by the detector, calculated from the distance to the detector and the radius of the detector aperture. The cone subtended by the detector is actually not just the diameter of the plastic detector. Rather, the size of the Kapton window opening defines the aperture size, as it is smaller than the ΔE diameter (as the β's cannot penetrate through the stainless steel supporting the Kapton window). The plastic detector physical measurements and the solid angles are summarized in Table 3.5.

The solid angle of the MCP can be calculated from equation 3.9:

$$\Omega_{MCP} = 4 \arctan \frac{W^2}{2d\sqrt{4d^2 + 2W^2}}, \tag{3.9}$$

where the solid angle is computed for a square of width W at a distance d. The width W corresponds to the width of the fiducial area of the MCP, and d corresponds to the distance

	MCP Detector	
Measured quantity	Right MCP	Top MCP
Width of fiducial area (mm)	46.00(34)	46.00(34)
Trap center to grid (mm)	48.26(25)	48.01(25)
Trap center to surface (mm)	52.87(25)	52.51(25)
Solid angle ($\Omega_{MCP}/4\pi$)	**5.09(12)%**	**5.14(12)%**

Table 3.6: Physical measurements and the resulting solid angles for the MCP detectors.

from the trap center to the surface of the MCP. The values used in computing the solid angle, as well as the resulting MCP solid angles, are listed in Table 3.6.

The HPGe efficiency calibration takes into account both detector solid angle and intrinsic detection efficiency, and therefore these values aren't separately determined.

3.4 Signal processing and data acquisition

The timing signals from the detectors were fed into two 24-bit LeCroy 4208 Time-to-Digital Converter (TDC) units with 1-ns timing resolution. Any detector timing signal initiated the time counting in the TDC unit. Appendix C contains the diagrams with the electronics setup for all the detectors, as described in this chapter. The data was stored only if the TDC Common received input from the master trigger (the logical OR of all timing signals). Hence, we recorded the β-singles, γ-singles and MCP singles along with the coincidence data. The trigger configuration is shown in Fig. 3.17. The pulse amplitudes were recorded by 12-bit Phillips 7164 ADC's. The ADC data acquisition timing gate of length 22.25 μs was initiated by the master trigger. The master trigger rate varied between 500 and 1000 Hz for the different measurements, and the deadtime per event was 142μs. The singles data for all detectors and the RF phase was recorded by two scalers, one reset by the capture and the other by the eject pule, hence allowing event measurement as a function of time in the trap cycle. The Scarlet data acquisition system [61] was used to read off all the CAMAC modules. A sort code then records all the event variables and creates a ROOT tree, as well as multiple histograms created with appropriate cuts on detector or timing amplitudes.

The experimental setup described in this chapter introduces some unique challenges to the analysis of the system's performance and interpretation of data. The next chapter describes the basic methods we use to analyze the dataset and calibrate the system.

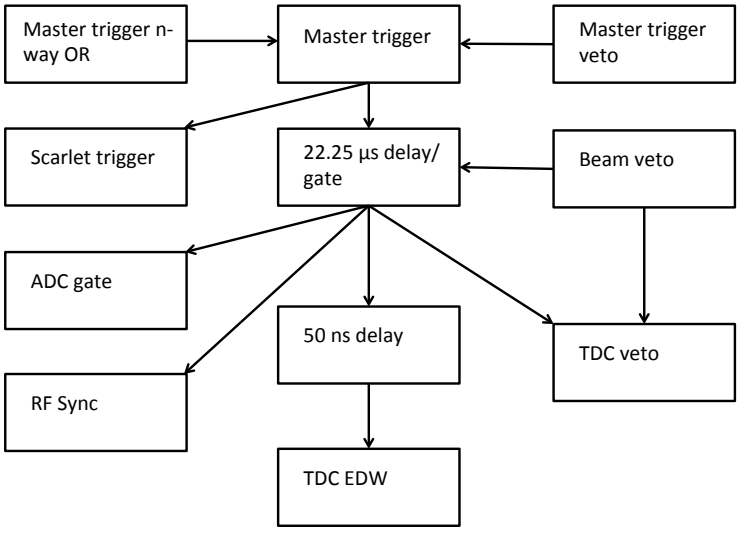

Figure 3.17: Diagram illustrating the data acquisition trigger setup.

Chapter 4

Methods and system characterization

Each recorded event consists of singles or coincidence data, and contains timing and amplitude for each detector that received a pulse, and the information on the event's occurrence during the measurement cycle as well as the phase that the RF field was in. From this information, we can derive the time-of-flight of the recoil ion, the build up and decay of activity inside of the trap, location of the event on the MCP, and even the charge-state distribution of the recoil ions, among other information. The rich amount of information provided gives a lot flexibility permitting various systematic effects to be studied.

Section 2.2 discusses the basis of the recoil ion technique. In this chapter, I focus on discussing the analysis methods and how the main challenges were addressed to extract the needed data employed in obtaining the branching ratio and neutron energy spectra results. The procedure of obtaining the resultant neutron energy spectra is discussed in Chapter 5, and the branching ratio analysis and results are presented in Chapter 6.

The recoil ion technique relies on the measurement of the recoil ion time-of-flight (TOF), defined as the time difference between the β detection in the ΔE scintillator and the recoil ion detection in the MCP. Due to its importance to the analysis, and since a lot of auxiliary information can be extracted from the figure (i.e. amount of slow recoils vs. fast, the ion cloud size, presence of high charge-states or conversion electrons, presence of backgrounds), it is fitting for the analysis discussion to begin by presenting the TOF spectra obtained in the experimental campaign. The accidental-subtracted TOF's from the sum of four ΔE and MCP detector combinations for the $^{137-138}$I and $^{144-145}$Cs isotopes are shown in Figures 4.1, 4.2, 4.3, 4.4, and 4.5.

The β-γ or β-β coincidence peak features at 0 ns, which defines the "zero-timing peak". It results from a β triggering the ΔE detector, coincident with a γ or a scattered β triggering the MCP. At longer TOF's, the neutron-recoil events are visible ($<$2000 ns). The large number of counts above 2000 ns is then attributed to the β recoils without neutron emission, or the slow recoils.

Several other types of figures crucial in the analysis are shown throughout this chapter. However, the gathered raw data undergoes detailed treatment prior to their use in determining the branching ratio and neutron energy spectra. In this work, two main challenges

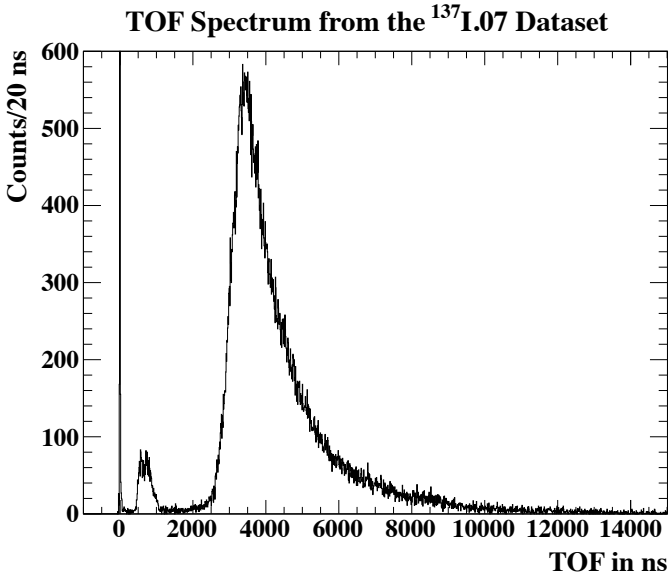

Figure 4.1: ^{137}I TOF spectrum with accidental background subtracted.

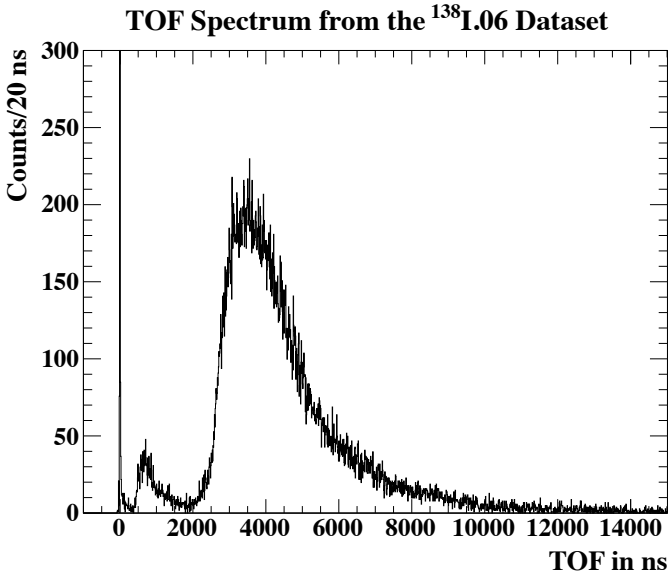

Figure 4.2: ^{138}I TOF spectrum from dataset 06, with accidental background subtracted.

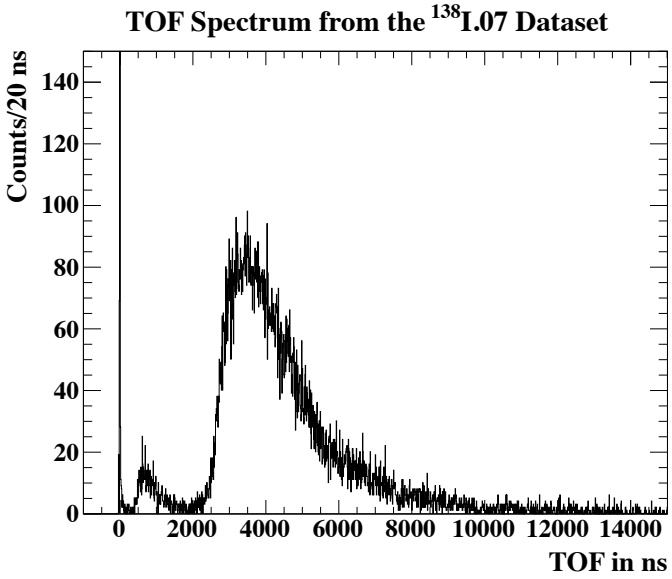

Figure 4.3: ^{138}I TOF spectrum from dataset 07, with accidental background subtracted.

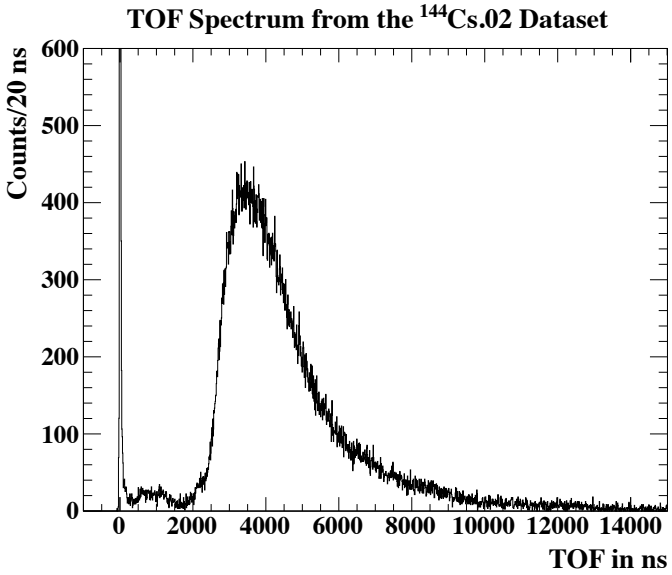

Figure 4.4: ^{144}Cs TOF spectrum with accidental background subtracted.

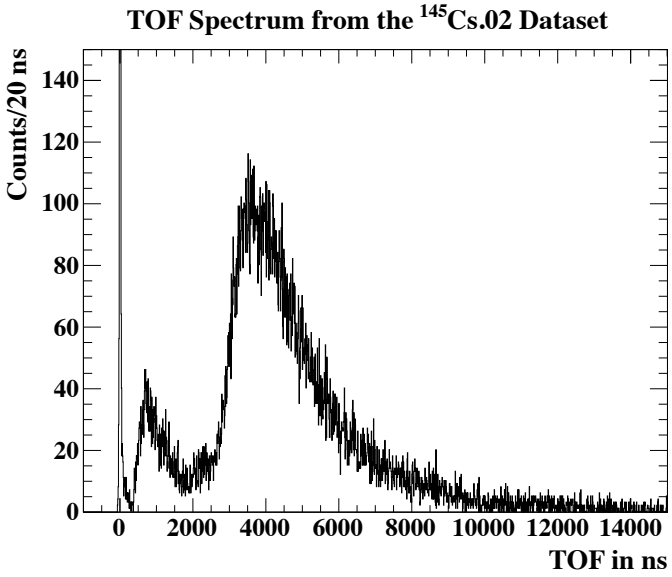

Figure 4.5: ^{145}Cs TOF spectrum with accidental background subtracted.

to interpretation of results were addressed in high detail. These challenges are:

1. Isolating the decays from the trapped isotope of interest in the presence of isobaric contamination and backgrounds from untrapped isotopes.

2. Determination of the efficiency for detecting the emitted decay products. In particular, the determination of intrinsic MCP efficiency was identified as a high priority.

Presence of an isobaric contaminant can be excluded for the cases where its ^{252}Cf fission yield is much smaller than the precursor, or it's half-life is much longer, and hence activity low (for the datasets under study, this information is compiled in Table 3.1). The largest effect of the isobaric contaminants is seen in the β-singles analysis, which also suffers from large backgrounds due to the untrapped species. The end goal of eliminating these backgrounds is to extract a number of trapped precursor data, as its detection efficiency can be accurately assessed and applied. We have developed a method where the model of the trap population can be used to extract the species of interest. The Trap Population Model and its application to determine the signal from the trapped species of interest is discussed in Section 4.1.

The efficiency for detecting β particles, γ rays, and recoil ions depends not only on the solid angle and intrinsic efficiencies of the detectors used, but also on effects such as β particle scattering, RF electric fields influencing the paths of low-energy recoil ions in varying charge states, and the properties of the decay scheme. In order to characterize detection efficiency values, we used a set of simulations performed to emulate the system. The resulting relative coincident efficiency values that modify the solid angle values are termed the ω values. They vary for each type of coincidence and between different isotopes, and rely on careful comparison of data to simulation. The derivation of the ω values is described in Section 4.2.

Lastly, the MCP intrinsic efficiency is needed in branching ratio calculations. Analysis revealed that the intrinsic (or absolute) efficiency ε_{MCP} is smaller than the open-area ratio of ∼60%. To estimate the efficiency, we collected data on the β decay of ^{134}Sb serving as a calibration case, due to its similar mass to the studied isotopes, and the relatively simple decay scheme which allowed reliable simulations to be made.

The methods described here were used to solve the three main challenges encountered in analyzing data obtained from the recoil ion technique. These methods and the ensuing results will be referred to during the discussion on obtaining neutron energy spectra and the branching ratio results in the following chapters.

4.1 Background elimination

Each event contained information on when it occurred during the measurement cycle. Referring back to the discussion on loading ions into the trap (illustrated in Fig. 3.2), the time in the measuring cycle determines the time during the trapping period or background measurement. By studying the buildup and decay of the activity, we can deduce the presence of isobars and the amounts of untrapped species. In addition, the data needs to be corrected for deadtime and accidental coincidences.

4.1.1 Deadtime corrections

Since the rate of events changes as the trap population evolves, the deadtime correction is not constant in time during the measurement cycle. Our data acquisition system produced a non-paralyzable deadtime of 142μs ± 1μs. In a non-paralyzable model, each trigger induces a constant deadtime, during which any additional triggers are lost and do not affect the length of the deadtime [62]. The true event rate r_{true} can be deduced from:

$$\frac{r_{true}}{r_{obs}} = \frac{1}{1 - r_{obs}\tau_d}, \tag{4.1}$$

where r_{obs} is the observed trigger rate, and τ_d is the deadtime-per-trigger. The resulting deadtime correction at each cycle time bin is used to multiply the observed rate to correct it. Deadtime per cycle time for ^{137}I dataset is shown in Fig. 4.6. Average deadtime correction applied to the total counts in the dataset are listed in Table 3.1.

In addition to the effect of deadtime, the beginning of each run was not synchronized with the beginning of the cycle. As a result, the data requires a "coverage correction" to account for fact that parts of the cycle received more measurement time. This correction is also multiplied by the counts in each bin in the cycle time. The correction is negligible for all the isotopes under study expect for the ^{137}I.07 dataset, which had a long cycle time and hence was more affected. The coverage correction for ^{137}I.07 is shown in Fig. 4.7.

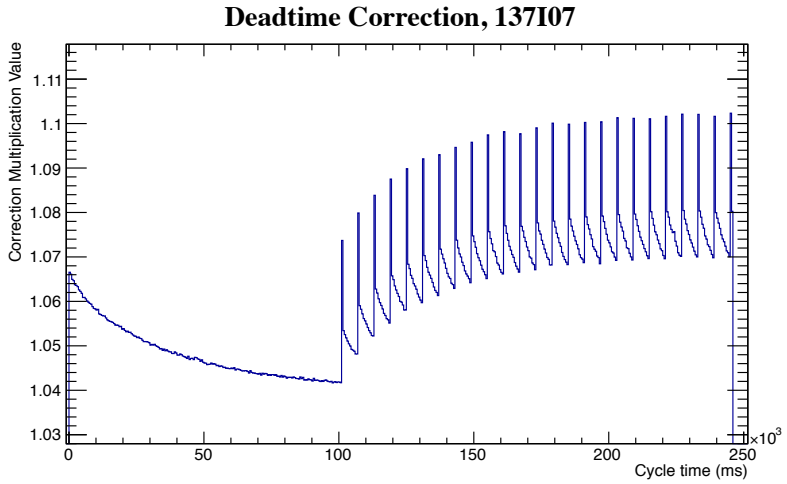

Figure 4.6: Data correction plotted as a function of cycle time for the ^{137}I.07 dataset.

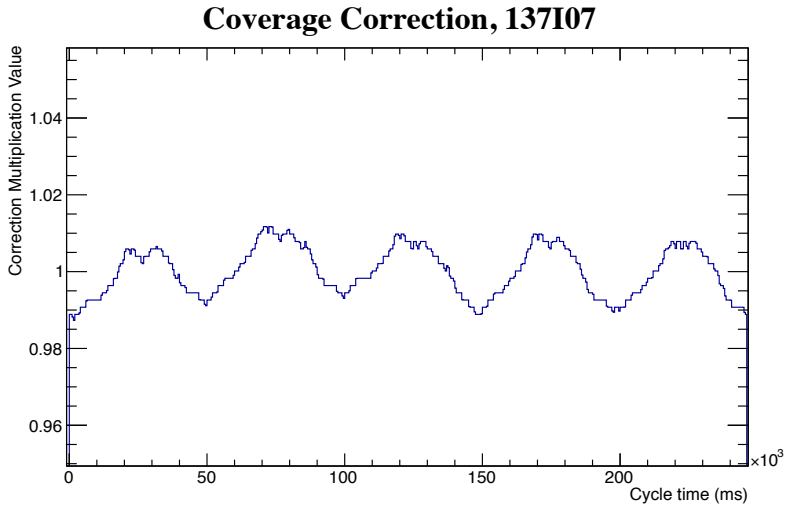

Figure 4.7: Coverage correction plotted as a function of cycle time for the ^{137}I.07 dataset. The histogram was rebinned and scaled back accordingly to shown the effect more clearly.

4.1.2 The Trap Population Model (TPM)

The data in the cycle time histogram, corrected for deadtime and coverage, can be analyzed according to the presence of isobars and untrapped species. For this purpose, the Trap Population Model was developed to take into account the growth and decay of the activity in the trap chamber, and the relationships between the species in the trap. The main factors complicating the analysis are:

1. Presence of isobaric contaminants: due to the limitations of the isobar separator used in the setup, up to nearest-neighbor isobaric contaminants were present in the dataset, depending on the ^{252}Cf yield and beam tuning.

2. Imperfect capture efficiency of the trap: some of the ions injected into the trap are not captured, and instead may end up on the surface of the BPT and/or the experimental chamber and produce activity.

3. Finite trap lifetime: a vacuum leak that went undetected during the experiment caused an imperfect trap storage lifetime. Trapped ions were continuously removed from the trap by neutralizing through charge-exchange reactions with contaminant molecules. Untrapped species contribute to the background.

4. β's emitted by untrapped species: daughters of the β decay recoils from the trapped populations end up on surfaces within the BPT chamber, and contributed to the untrapped backgrounds with unknown efficiencies. The decay chain is followed for each species, whether trapped or not.

These factors were taken into account in the model through modifying the source and decay terms of each trapped and untrapped species, for all the species present. The derivation and implementation of the TPM is described in great detail in Shane Caldwell's thesis [63]. For the convenience of the reader, an introductory summary of the model description is included in Appendix B of this thesis.

4.2 Simulations and their role in obtaining effective detection efficiency values

Numerous simulations were performed to study the effects of various systematics, such as scattering, ion cloud size and the effect of RF fields on ion trajectories. To model the β decay kinematics, we used a custom β decay generator, BD2, a code originally developed to study β-ν angular correlations [64, 47]. The code was later modified to accommodate the study of βn-decay channels [53]. The code models the distribution of decay products' 4-momenta vectors following the β or βn decay, for use as an input for SimIon and Geant4 simulation packages. The SimIon software computes electric fields based on the electrode geometry and voltages applied to determine ion trajectories, while the Geant4 models the energy loss

Detector	Interacting particle(s)	Energy cut value
Left ΔE	e^-, γ	76.0 $\pm$ 24 keV
Bottom ΔE	e^-, γ	62.0 $\pm$ 30 keV
Left ΔE	neutron	368.0 $\pm$ 71 keV
Bottom ΔE	neutron	368.0 $\pm$ 71 keV

Table 4.1: Summary of energy cuts applied in the simulation for particles interacting in the ΔE plastic scintillators, corresponding to energy thresholds for detected particles. Details on how these values were obtained are discussed in Section 3.3.1 (for electrons), and Section 5.36 (for neutrons).

and scattering for the emitted electrons, γ-rays, and neutrons. The details of the simulation packages are described in more detail in the rest of this section.

The BD2 code assumes an allowed β decay spectrum and incorporates the known β decay transitions to excited states in the daughter nucleus to generate the decays. The user can adjust the charge-state distribution for the recoil ions, size of the ion cloud, as well as the β-ν angular correlation coefficient, $a_{\beta\nu}$. These input parameters are adjusted so that the simulation results best reproduced the observed data. The size of the ion cloud was found by fitting the leading edge of the slow-ion TOF spectrum of ^{134}Sb to the simulated distribution. The size of the ion cloud was assumed to be the same for each species measured. Sections 4.2.4 further describe the determination of the charge state distribution and $a_{\beta\nu}$, respectively, as related to the analysis of the slow-ion data.

SimIon is a commercial software platform used for modeling electric fields and charged particle trajectories. The electrodes are modeled with a 0.5-mm resolution. The simulation outputs the location, time-of-flight, and impact velocities of the recoil ions that hit the MCPs. Hence, the effective solid angle of the MCPs can be studied for various charge states, along with many of the systematic effects discussed.

The Geant4 open-source platform enables the study of scattering and energy loss of β's, γ's, conversion electrons (CE's), and neutrons. The output of the simulation is energy deposited in the plastic detectors due to each particle. Thus, the efficiency of detecting β's undergoing scattering in the BPT chamber and energy loss in the Kapton foil can be determined. Although the energy loss inside the detector material is modeled to reflect the physics accurately, the amount of scintillation light produced and subsequently detected by the PMT to produce a signal above a threshold is not. To remedy this, a threshold is set while analyzing the simulation data, informed by the threshold found from calibration and experimental data. The thresholds for detecting electrons and neutrons in the ΔE plastic scintillator are listed in Table 4.1.

Outputs of the Geant4 and SimIon simulations, as well as auxiliary files produced by the BD2 code that contains the input information, are all combined to form one master ROOT file. The file contains a data tree, much like the trees produced with the sort code used for

building ROOT files containing the experimental data. The user can impose threshold values for each variable, or cuts, to control the selection of events in producing various histograms. The MCP relative efficiency correction (which depends on the ion impact velocity and the impact location on the MCP) can be applied on event-by-event basis with the use of a subsort routine. The subsort incorporates the analysis results from Section 5.4 by taking each recoil ion event, and assigning a probability of the event being detected. The subsort does not take into account the intrinsic MCP efficiency ε_{MCP}, which is independent of ion energy.

The simulations were used for determining the effects of the experimental setup (i.e. detector thresholds or the BPT RF fields) on detection efficiencies. In order to define the detection efficiency in relation to the solid angle efficiency, a new variable ω is used, referred to as the "relative detection efficiency". The ω value encapsulates the modification to the detection efficiency for a specified decay product or coincidence from the solid angle value. Equation 4.3 describes this relation for the case of detection of β particles:

$$\omega_\beta = \left(\frac{n_\beta}{N_\beta}\right)_{sim} \frac{1}{\Omega_\beta}, \tag{4.2}$$

where the $(n_\beta/N_\beta)_{sim}$ ratio represents the observed events in the simulation, produced by applying appropriate spatial and energy cuts, to the total emitted decays. The ratio is divided by the detection solid angle, in this case the ΔE plastic scintillator solid angle Ω_β. In the remainder of this section, I describe in more detail how each of the ω values was determined for each isotope and for various decay products or coincidences. The ω values presented in this chapter do not list uncertainties, since each P_n calculation depends on the ratio of two ω values, for which the systematic uncertainties are inter-dependent.

4.2.1 $\omega_{\beta R}$ value

The $\omega_{\beta R}$ value as a function of neutron energy is effectively calculated when obtaining the correction to the neutron energy spectrum, as described in Section 5.6.4. By applying the same cuts to the simulation file, weighted by the appropriate neutron energy spectrum and charge state distribution, we obtain the energy-averaged value of $\omega_{\beta R}$, listed in Table 4.2. The cuts applied consist of the MCP efficiency correction, fiducial area MCP cut, plastic detector energy cut for β's and neutrons (see Table 4.1), and a neutron energy threshold cut of 100 keV. The average $\omega_{\beta R}$ is determined with:

$$\omega_\beta = \left(\frac{n_{\beta R}}{N_{\beta R}}\right)_{sim} \frac{1}{\Omega_{MCP}\Omega_\beta}, \tag{4.3}$$

where the ratio of detected βn events $n_{\beta R}$ to the total emitted βn events $N_{\beta R}$ is divided by the product of the detector solid angles involved in observing the coincidence.

	$\omega_{\beta R}$			
Detector Combination	^{137}I	^{138}I	^{144}Cs	^{145}Cs
Left ΔE-Right MCP	1.27	1.11	0.96	1.14
Left ΔE-Top MCP	0.93	0.76	0.72	0.88
Bottom ΔE-Right MCP	1.03	0.82	0.81	1.00
Bottom ΔE-Top MCP	1.12	0.91	0.77	1.07

Table 4.2: Average $\omega_{\beta R}$ values for each isotope and each detector combination.

	ω_{β}			
Detector	^{137}I	^{138}I	^{144}Cs	^{145}Cs
Left ΔE	1.31	1.35	1.35	1.44
Bottom ΔE	1.31	1.36	1.36	1.46

Table 4.3: ω_β values found for each isotope for each plastic ΔE detector, found with the simulations.

4.2.2 ω_β value

The ω_β value is obtained for the efficiency of detection of all β-singles, including β's associated with the neutron emission (fast recoils), and β's associated with β decay without neutron emissions (slow recoils). The detection efficiency depends on the decay scheme and the total decay Q value. Therefore, the ω_β value is different for each isotope. There are also contributions from the ΔE scintillator detecting γ's, conversion electrons (CE's), and neutrons, that need to be taken into account.

The ω_β value used in the P_n calculation is for all the decays. Since in the simulation the slow and fast recoils are run separately, the total ω_β is then the sum of the individual ω_β's associated with either slow or fast recoils weighted by the P_n value obtained from literature:

$$\omega_\beta = (1 - P_n)\omega_\beta(r) + P_n\omega_\beta(R). \tag{4.4}$$

Although the P_n value obtained in literature might have a large uncertainty, its effect on the resulting total ω_β value is negligible compared to the other systematic effects. The total ω_β's for all the isotopes are listed in Table 4.3.

Enhancement of the efficiency above the solid angle value (i.e. $\omega_\beta > 1$) is caused by scattering of β's into the detector and the detection of conversion electrons. Presence of conversion electrons measurably increases the ω_β value for transitions where the internal conversion coefficient is large (as in the low-lying states of ^{144}Cs and ^{145}Cs). The effect of β-scattering gets larger with an increasing Q value, which is associated with higher energy β

	$\omega_{\beta\gamma}$			
Detector	^{137}I	^{138}I	^{144}Cs	^{145}Cs
Left ΔE+Bottom ΔE	1.35	1.37	1.39	1.38

Table 4.4: $\omega_{\beta\gamma}$ values found for each isotope, for the sum of the plastic detectors.

particles. Moreover, the simulation also takes into account β decays that populate excitation states of the daughter that de-excite through γ emission or undergo internal conversion.

4.2.3 $\omega_{\beta\gamma}$ value

The $\omega_{\beta\gamma}$ value quantifies the modification to the efficiency for detecting β's associated with the emission of a specific γ-ray. The γ of interest is usually the transition with the largest intensity for each isotope. Imposing an association with the γ constrains the number of detected decays by altering the effect of conversion electrons on total detection efficiency. Specifically, emission of a γ-ray for the specific transition determines that no conversion electron was emitted. Hence, the resulting $\omega_{\beta\gamma}$ value will depend on the specific γ selected and the international conversion coefficients.

The simulations incorporate information on γ cascades and internal conversion coefficients. The $\omega_{\beta\gamma}$ is obtained by selecting only the events where the γ of interest was emitted in the γ cascade. The β particles associated with the γ emission are selected for energy deposition above the threshold value, as in the ω_β determination. The $\omega_{\beta\gamma}$ value is then defined in the usual way:

$$\omega_{\beta\gamma} = \left(\frac{n_{\beta\gamma}}{N_{\beta\gamma}}\right)_{sim} \frac{1}{\Omega_\beta}. \tag{4.5}$$

For the cases where the conversion coefficient is large for the γ transition of interest, the $\omega_{\beta\gamma}$ may be smaller than the ω_β value for that isotope. On the other hand, the value may become larger if the γ of interest is emitted in decays that emit, on average, higher-energy β particles. The values of $\omega_{\beta\gamma}$ for each isotope is listed in Table 4.4. In measuring the β-γ coincidences, either ΔE plastic scintillator is used. Hence, the $\omega_{\beta\gamma}$ values encompass the sum over both of the plastic detectors.

4.2.4 $\omega_{\beta r}$ value

Since recoil ions associated with β decay without neutron emission have low recoil energies (typically below 300 eV), their trajectories are significantly perturbed by the RF field of the BPT. Correspondingly, the kinematic effects associated with the specific decay have a significant impact on the low-energy ions. In contrast, these perturbations produce negligible

effect on the high-energy ions recoiling from neutron emission. Furthermore, in the case of ^{144}Cs and ^{145}Cs, $\omega_{\beta r}$ value is increased by the detection of conversion electrons.

The simulation inputs important for determining the $\omega_{\beta r}$ value are: (1) the decay scheme, (2) the charge-state distribution, and (3) the β-ν correlation coefficient $a_{\beta\nu}$ value. The decay scheme available in the literature gives the β energies and corresponding intensities. For many isotopes, the decay scheme may lack higher-lying excitation states (a result of the Pandemonium effect [65]), though its effect has not been found to greatly alter the deduced $\omega_{\beta r}$ value. The effects due to γ cascades and the conversion electrons are also included in the simulation through the inclusion of RIPL files. The next two subsections describe how the charge state distribution and the $a_{\beta\nu}$ value are determined by matching data to the simulations, but first I describe the general features of the decay kinematics affecting the detection efficiency.

The ratio of the slow-recoils detected at the 180° detector combination to the slow-recoils detected at the 90° detector combination is affected by the average $a_{\beta\nu}$ value for the decay, as well as the kinematic focusing that enhances the measured number of coincidences at the 180° detector combination. The kinematic focusing arises since the momentum of the β particle strongly affects the direction of the slow-recoil. The number of coincidences at the 180° detector combination can be 5-10 times larger than at the 90° detector combination. Hence, the 180/90 ratio is an important tool in matching the data to simulations, and deriving the average $a_{\beta\nu}$ value. The $a_{\beta\nu}$ influences the decay phase space by specifying the momenta distribution of β and ν via the relation: $1 + a_{\beta\nu}\frac{v_\beta}{c}\cos\theta_{\beta\nu}$, i.e. for $a_{\beta\nu}$= -1, the β and ν momenta vectors are more likely to point in opposite directions, while for $a_{\beta\nu}$= +1, the momenta are more likely to be aligned in the same direction. The momentum of the recoiling ion will therefore be influenced by the $a_{\beta\nu}$ value. The $a_{\beta\nu}$ will differ for each transition, and since we generally measure the decay of all transitions, we refer to the average $a_{\beta\nu}$ value as the "effective" a_{eff}. The simulations use this a_{eff} as an input.

The first step to establishing the correct average $a_{\beta\nu}$ value is to determine the possible range of charge state distributions. The signature of the charge state distribution can be seen by plotting the number of detected slow-recoil ions against the trap RF phase, since the RF fields have a larger effect on higher charge-state ions. The specific curve shape that fits the pattern of ions in each charge state vs. RF phase can be reproduced with the simulation. In general, the number of events follows a sinusoidal shape, with the higher charge states having a larger peak-to-trough ratio. The fit function $f(t_{RF})$ is created by adding the curves for the first three charge states ($f^{2+}(t_{RF})$, $f^{3+}(t_{RF})$, and $f^{4+}(t_{RF})$), weighted with the charge base B according to a power-law distribution:

$$f(t_{RF}) = \frac{f^{2+}(t_{RF})}{1+B+B^2} + \frac{B\cdot f^{3+}(t_{RF})}{1+B+B^2} + \frac{B^2\cdot f^{4+}(t_{RF})}{1+B+B^2}. \tag{4.6}$$

An example of this fit is shown in Fig. 4.13. The mean charge state C_D is then determined

as:

$$C_D = \frac{2 + 3 \cdot B + 4 \cdot B^2}{1 + B + B^2}. \tag{4.7}$$

For completeness, the inverse of this equation for calculating B is:

$$B = \frac{(C_D - 3) + \sqrt{-23 + 18 \cdot C_D - 3 \cdot C_D^2}}{2 \cdot (4 - C_D)}. \tag{4.8}$$

The fit function $f(t_{RF})$, and hence the resulting mean charge state C_D, is largely independent of which $a_{\beta\nu}$ was used in the simulation. To produce the range of all possible charge state distributions, the data is first fit to the $f(t_{RF})$ produced for $a = +1$ and $a = -1$, corresponding to the physically possible range of $a_{\beta\nu}$ values. The $a = -1$ favors lower recoil momentum, and the resulting mean charge from the $a = -1$ fit is always lower than the $a = +1$ fit. The average charge base is obtained by taking the mean between the values fit with $a = -1$ and $a = +1$ functions.

The mean charge obtained this way is used to weight the coincidences in the simulation:

$$N_c = \frac{N^{2+}}{1 + B + B^2} + \frac{B \cdot N^{3+}}{1 + B + B^2} + \frac{B^2 \cdot N^{4+}}{1 + B + B^2}, \tag{4.9}$$

where N_c stands for a number of coincidence counts, for example for the 180° detector combination for the $a = +1$ simulation.

The a_{eff} can then be obtained by matching the weighted coincidence counts in the simulation at a specific average $a_{\beta\nu}$ value to the data. This is achieved by regressing the linear combination of the simulated counts at $a = +1$ and $a = -1$ to the ratio of the 180/90 slow-ion counts in the data (R_D):

$$a_{eff} = 2 \times \frac{R_D \cdot N_{90}^{a=-1} - N_{180}^{a=-1}}{(N_{180}^{a=+1} - N_{180}^{a=-1}) + R_D \cdot (N_{90}^{a=-1} - N_{90}^{a=+1})} - 1. \tag{4.10}$$

R_D is obtained by fitting the slow recoil ion coincidences plotted as a function of cycle time with the TPM code, as described in Section 4.1.2, or simply by counting the TOF spectrum in cases where no isobaric contaminants are expected (see Section 6.4 for details on each isotope). The N_D^a values represent the simulated coincidences, where D is the detector combination (at 180° or 90°) and a is the $a_{\beta\nu}$ value.

The a_{eff} value can then be used to obtain the new coincidence counts N_D and hence the new charge base value to weight these counts:

$$N_D^{a_{eff}} = N_D^{a=-1} \cdot (1 - a_{eff})/2 + N_D^{a=+1} \cdot (a_{eff} + 1)/2 \tag{4.11}$$

This process is repeated until the a_{eff} value converges, and the B value stops changing.

The $\omega_{\beta r}$ value is defined as the ratio between the slow recoil ion coincidence counts $N_D^{a_{eff}}$ and the total counts, divided by the product of solid angles of the combination of detectors involved. The correct $\omega_{\beta r}$ value is obtained by weighting the N_D counts with the charge-state

	$\omega_{\beta r}$			
Detector Combination	^{137}I	^{138}I	^{144}Cs	^{145}Cs
Left ΔE-MCP$_R$	3.84	2.85	4.59	2.92
Left ΔE-MCP$_T$	0.48	0.72	0.54	0.61
Bottom ΔE-MCP$_R$	0.58	0.86	0.70	0.80
Bottom ΔE-MCP$_T$	3.16	2.33	3.80	2.33

Table 4.5: $\omega_{\beta r}$ values for each detector combination and each isotope.

distribution and the a_{eff} as determined in this analysis. Results for each isotope and each detector combination are listed in Table 4.5.

4.3 MCP intrinsic efficiency from ^{134}Sb calibration data

The total detection efficiency of the MCP to recoil ions depends on the MCP solid angle Ω_{MCP} (measured directly), the ion impact energy and the impact location (due to the spatially-varying gain and charge-collection efficiency), the discriminator threshold, and the open-area ratio. For the convenience of the analysis, the MCP efficiency is split into a product of energy-dependent and energy-independent factors. The intrinsic MCP efficiency, defined in this work as ε_{MCP}, is independent of the ion's impact energy or any effects due to the detection threshold imposed by the electronics, and is the subject of this section. The energy-dependent MCP efficiency, measured relative to the intrinsic efficiency, is discussed in Section 5.4.

The intrinsic efficiency here represents the fraction of ions that are detected out of the total number of ions that impact the MCP, and encompasses the effect due to the two transmission grids placed in front of the MCP, as well as any remaining intrinsic detection effects. The value of ε_{MCP} can be deduced by comparing results between data and simulation of a calibration case with a well-known decay scheme, ensuring that the simulation can accurately represent the data. This intrinsic efficiency does not depend on effects due to the electronics readout that may also affect the number of observed events.

The total number of β decays occurring, N_β, can be written in terms of the observed number of β-singles, n_β, or β-recoil coincidences, $n_{\beta r}$. Equating the N_β number from Eq. 6.2 and Eq. 6.4, and canceling out the common $\Omega_\beta \varepsilon_\beta$ terms, results in:

$$\frac{n_\beta}{\omega_\beta} = \frac{n_{\beta r}}{\Omega_{MCP}\varepsilon_{MCP}\omega_{\beta r}(1-P_n)}. \tag{4.12}$$

Rearranging this equation as a ratio of observed numbers of β-recoils to β-singles yields:

$$\frac{n_{\beta r}}{n_\beta} = \Omega_{MCP}\varepsilon_{MCP}(1 - P_n)\frac{\omega_{\beta r}}{\omega_\beta}. \tag{4.13}$$

If a calibration case is picked where no β-delayed neutron emission occurs, the P_n value is equal to 0. Assuming that the simulation properly treats the ω values (meaning that the decay scheme is well known), the only difference between the simulated and measured ratio $n_{\beta r}/n_\beta$ is the unknown intrinsic MCP efficiency ε_{MCP} (since in the simulation, this value is assumed to be 1). The intrinsic MCP efficiency is then found with the following relation:

$$\varepsilon_{MCP} = \frac{[n_{\beta r}/n_\beta]_{data}}{[n_{\beta r}/n_\beta]_{simulation}}. \tag{4.14}$$

In order to calibrate the efficiency of the MCP under the experimental conditions, it is important to use an isotope similar in mass to the nuclei measured, and with a simple and well-known decay scheme, such that the simulation inputs are well-defined. Unfortunately, fission fragments in the high-mass fission peak usually have complicated β decay schemes. For these reasons, we used the case of ^{134}Sb, where the decay is quite simple despite the presence of an isomer. ^{134}Sb decays into the ground state of ^{134}Te via a 1st forbidden transition (0^- to 0^+) with a branching ratio of 97.6% [54]. For the 0^- to 0^+ transitions, the first-forbidden β-decay theory predicts $a_{\beta\nu} = 1$ [66]. The decay scheme is shown in Fig. 4.8.

The presence of a long-lived ^{134}Sb^m isomer ($t_{1/2} = 10.07$ s) complicates the analysis (its more complex decay scheme is shown in Fig. 4.9). However, the isomer can be identified and subtracted from the ground state decay due to the presence of its characteristic γ-rays, conversion electrons, and the decay half-life, as described in the next section.

4.3.1 Results from the ^{134}Sb data

The analysis tools mentioned in this section are described in much more detail in the Chapters 5 and 6. This section rather concentrates on showing the relevant results and the interpretation of them to deduce the intrinsic MCP efficiency.

We collected 44 hours of data on ^{134}Sb, of which 37.9 hours consist of the `134sb01` and `134sb03` datasets that were optimized to measure the ground state decay, whereas the `134sb02` dataset (consisting of the remaining 6.1 hours) was optimized for measurement of the isomer. The optimization to measure the isomer was achieved by using a longer time interval between ion captures, so that most of the ground state would decay away between successive captures. The characteristics of the three datasets that were collected are summarized in Table 4.6.

Isomer subtraction

The number of ground state $n_{\beta r}$ and n_β decays is determined by taking the number of decays found in the `134sb01` and `134sb03` datasets, and subtracting the properly scaled

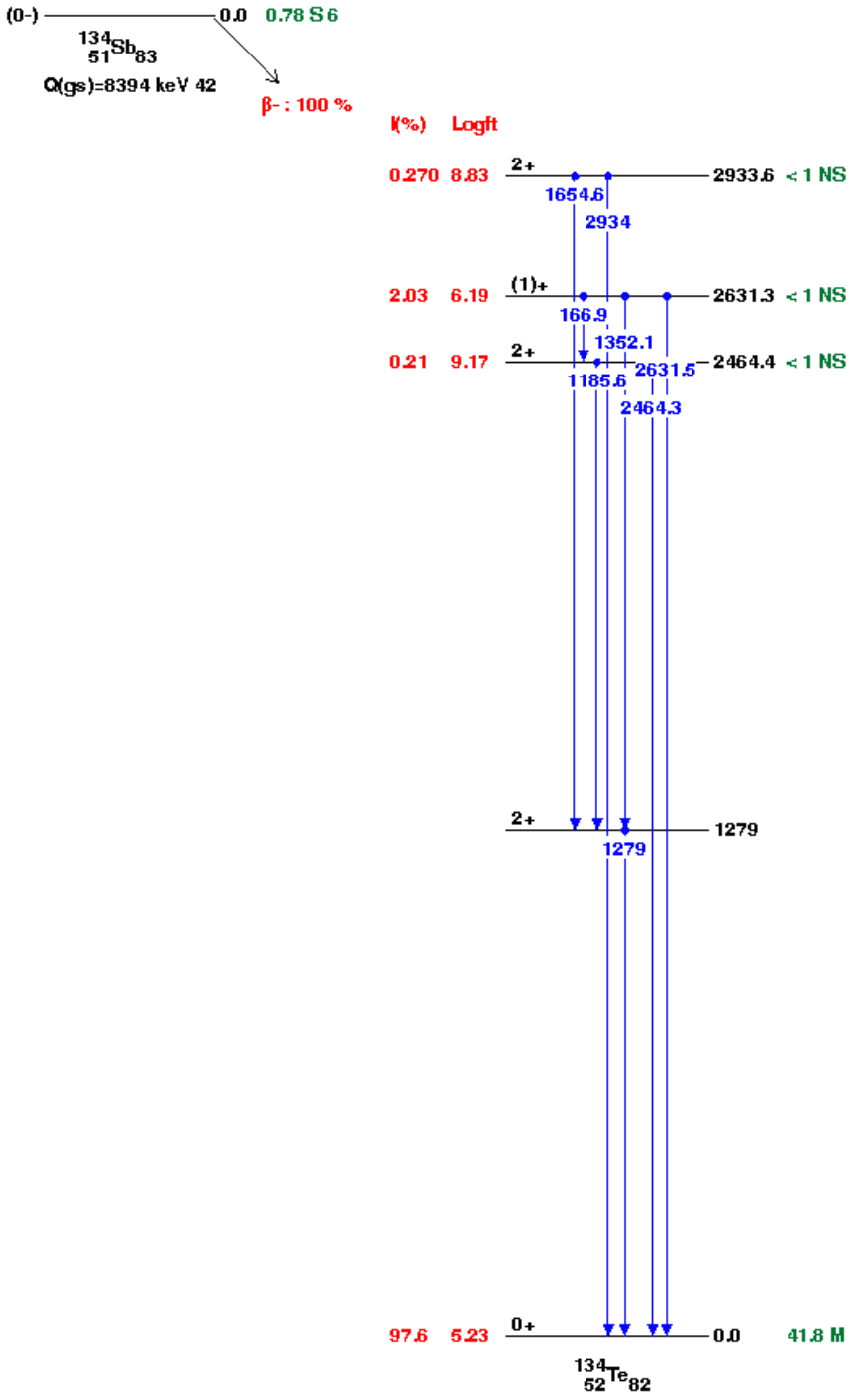

Figure 4.8: ^{134}Sb decay scheme from NNDC.

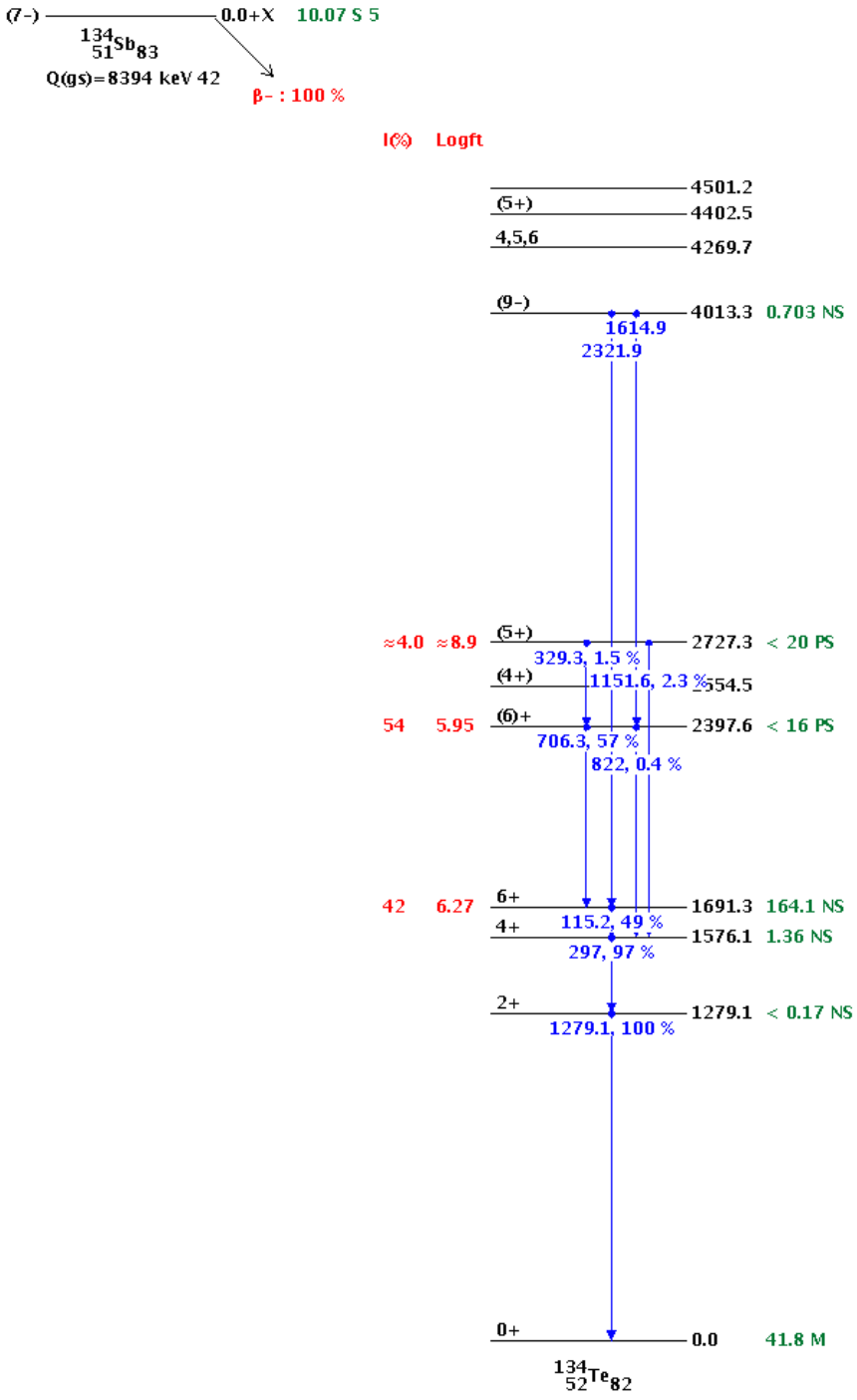

Figure 4.9: ^{134}Sb^{m} decay scheme from NNDC.

	Dataset		
Dataset characteristic	`134sb01`	`134sb02`	`134sb03`
Runtime (hrs)	21.1	6.1	11.5
Capture interval (s)	0.6	6.0	0.6
Background interval (s)	4.3	30.1	4.3
Cycle time (s)	10.2	90.0	10.2
Total triggers	21,614,361	7,302,592	13,965,179

Table 4.6: Summary of datasets collected on ^{134}Sb and ^{134}Sb^m for MCP efficiency calibration.

isomer decays from the `134sb02` dataset. The scaling factor y is defined as the isomer subtraction factor, and was obtained by comparing the amount of the isomer decay present in each dataset with five different methods:

1. γ-singles from the isomer decay
2. β-singles
3. β-γ coincidences from the isomer decay
4. β-recoil coincidences
5. Conversion electrons (CE) from the 1619-keV to 1576-keV highly-converted ($\sim$50%) transition in the isomer decay

The γ-singles and β-γ coincidences were obtained by counting under the 297-keV peak in the HPGe spectra. The β-singles, β-recoils, and the β-CE coincidences were counted by fitting counts vs. cycle time histograms, which enabled subtraction of untrapped species and the ground state decay from the isomer decay counts. The conversion electron counts were detected in coincidence with β's, with a TOF gate of 10-1000 ns. The activity due to the conversion electrons as a function of cycle time was consistent with the half-life of the 1619-keV state ($t_{1/2}$ = 162 ns), from which the conversion electrons originate. The fits produced with the `BFit2` program are shown in Figures 4.10, 4.11, and 4.12. The numbers found for the isomer decay in the `134sb02` dataset, the combined `134sb01` and `134sb03` dataset, as well as the resulting isomer subtraction factors are listed in Table 4.7.

β-singles and β-recoil coincidence counts

The number of counts for the ^{134}Sb ground state decay, n_β and $n_{\beta r}$, was determined per detector combination with the `BFit2` program. Presence of isobaric contaminants in the fit was ruled out, since the beam was determined to be free of ^{134}Sn (through CPT data and γ-ray analysis). On the other hand, the ^{134}Te is long-lived and therefore gives few trapped

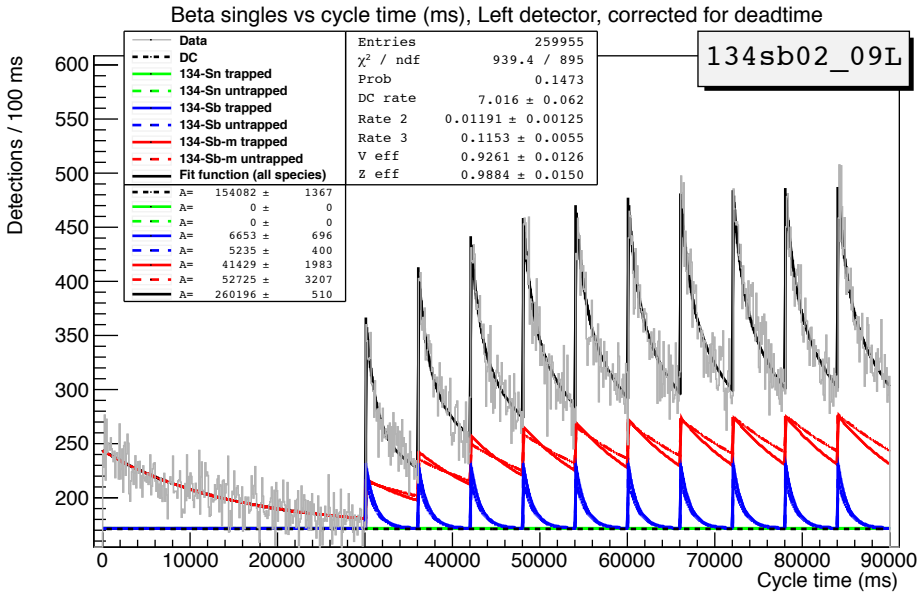

(a)

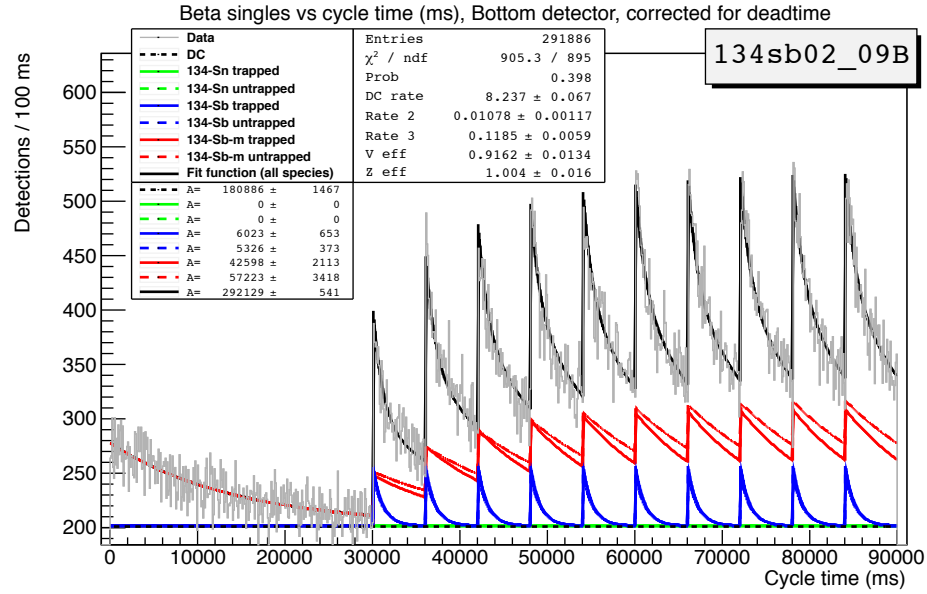

(b)

Figure 4.10: β-singles fits.

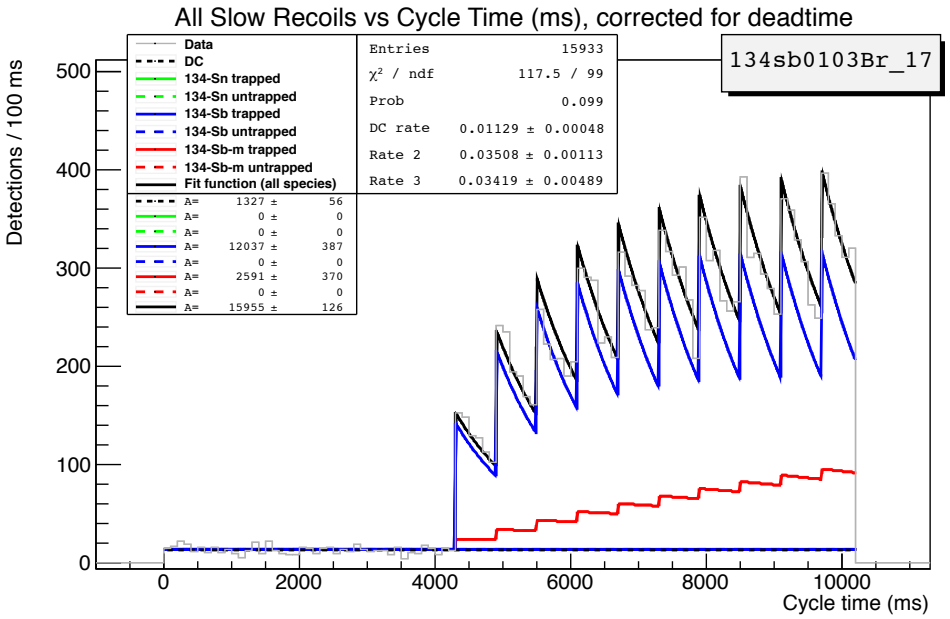

(a)

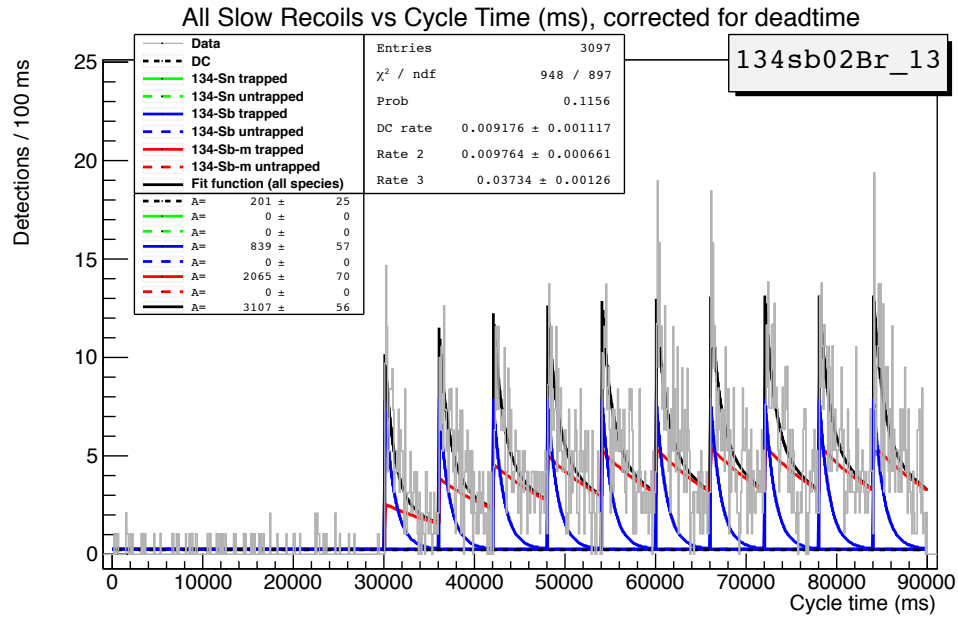

(b)

Figure 4.11: β-recoil (slow ion) fits.

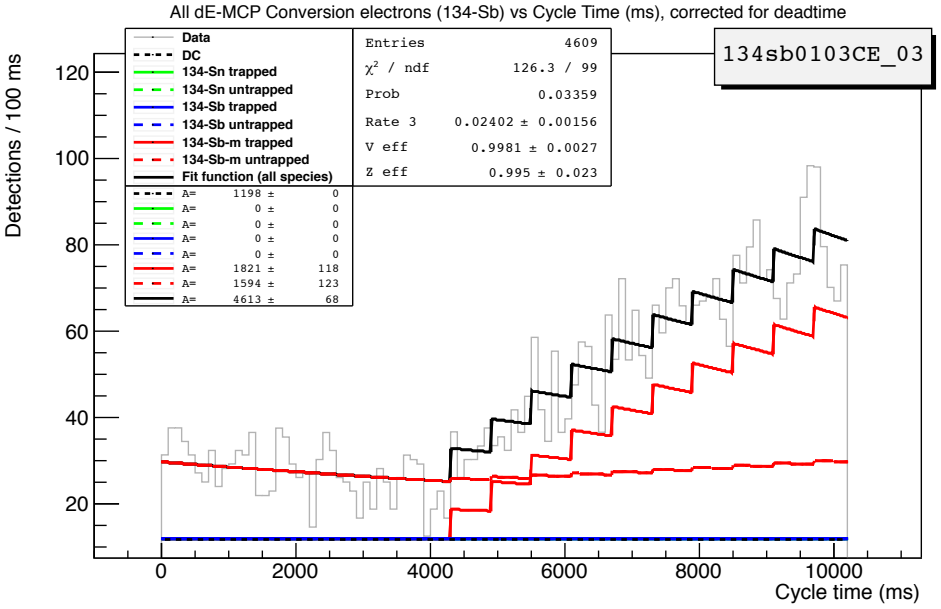

(a)

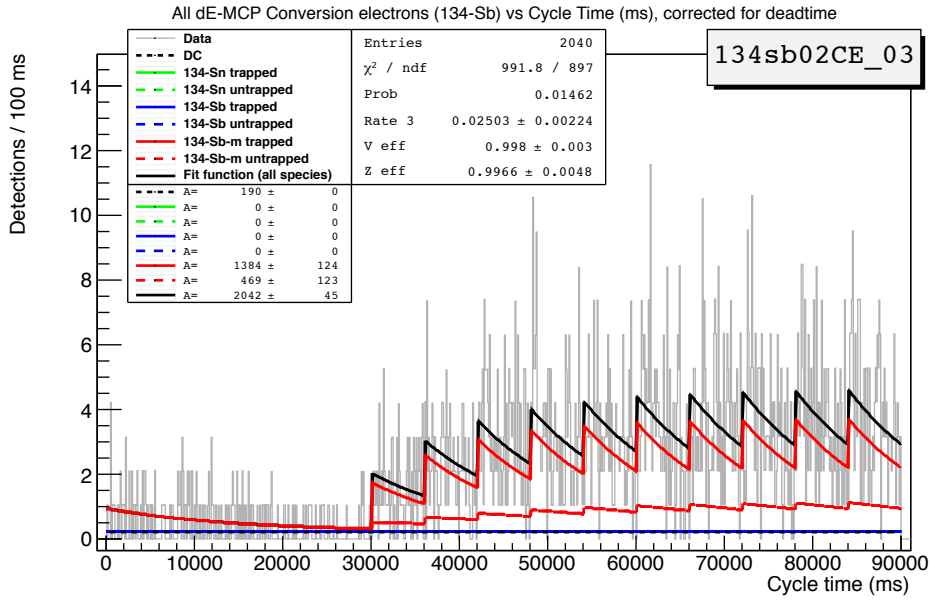

(b)

Figure 4.12: Fits to the β-conversion electron coincidence vs. cycle time.

Method	Counts from the dataset		Subtraction factor
	`134sb01+134sb03`	`134sb02`	
γ-singles	541,662(72,745)	352,138(55,043)	1.54(32)
β-singles	108,053(8,911)	84,019(6,394)	1.29(13)
β-γ's	95,125(10,914)	67,846(8,425)	1.40(24)
β-recoils	2,350(443)	1,914(110)	1.23(21)
β-CE's	1,821(125)	1,384(198)	1.32(21)
Final result			**1.32(12)**

Table 4.7: Results of the isomer subtraction factor analysis, determined with five different methods. The final result is the average between γ and β singles, with the other three methods serving as a check.

ion decays. Moreover, the ^{134}Te's β decay background from the untrapped ions doesn't vary much over the cycle time and looks like a DC component. The trap-lifetime, identical for both the isomer and the ground state, was determined with the `134sb02` dataset, due to its longer cycle time. The results are presented in Table 4.8.

Detector	Number of counts	Uncertainty in counts
Left n_β	102950	2291
Bottom n_β	103889	2586
Left-Top $n_{\beta r}$	284	107
Bottom-Right $n_{\beta r}$	509	129
Bottom-Top $n_{\beta r}$	4043	264
Left-Right $n_{\beta r}$	5457	300

Table 4.8: Number of observed ground state ^{134}Sb decays determined from fits to data.

4.3.2 ^{134}Sb Simulation results

In order for the simulation to yield physically correct results, the $\omega_{\beta r}$ must accurately reproduce the observed slow-ion TOF spectrum. The TOF spectrum is compared to the isomer-subtracted spectrum from the data. In the procedure outlined in Section 4.2.4, the data from the slow recoil ions vs. RF phase and the 180°/90° ratio are used to determine the charge-state distribution and the effective $a_{\beta\nu}$ respectively. In addition, the simulation results for the recoil ions also incorporated the efficiency correction due to the electronic

threshold, as described in Section 5.4. The charge state distribution, obtained from fitting the recoil vs. RF phase shown in Fig. 4.13, was: 68.7% for 2^+, 23.3% for 3^+, and 8.0% for 4^+. For the transition to the ground state of ^{134}Te, $a_{\beta\nu} = +1$. However, since the average $a_{\beta\nu}$ was found to be 0.48, it is expected that up to ∼15% of transitions occurred to higher-lying excited states. The procedure for determining the average $a_{\beta\nu}$ and the charge state distribution is outlined in Section 4.2.4.

Values for the β-singles and β-recoils found by running the simulation under the conditions with correct charge state distribution and $a_{\beta\nu}$ value are listed in Table 4.9.

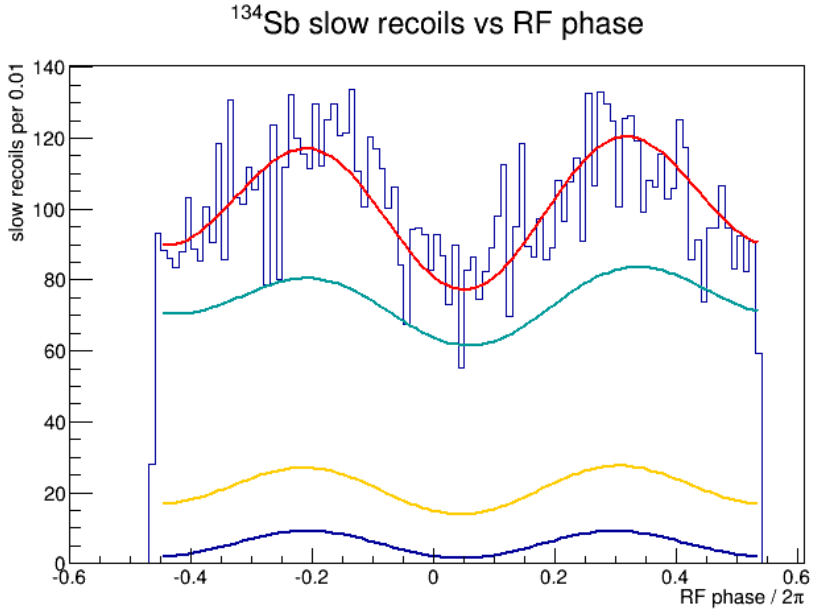

Figure 4.13: ^{134}Sb slow-recoils vs. RF phase from the 134sb01+134sb03 datasets. Each curve, corresponding to a specific charge state, was produced by the simulation, with the greatest contribution from charge state 2^+, and lowest from 4^+. The red curve is a linear combination of the three charge states regressed to the data.

4.3.3 MCP intrinsic efficiency results

Combining the results from the simulation and the data, the MCP intrinsic efficiency can be obtained. This value is used in calculating the branching ratio from β-singles and β-γ's. The uncertainty in this value is dominated by the uncertainties in the fits to the data. The resulting MCP intrinsic efficiency encompasses any effects due to the open-area ratio and the transmission grids, yet is surprisingly low. In addition, one would expect the Top and Right MCP intrinsic efficiency to be similar. Additional MCP characterization may be required to determine the cause of the low efficiency observed in our dataset.

Detector	Number of counts	Uncertainty in counts
Left n_β	68096	252
Bottom n_β	68096	252
Left-Top $n_{\beta r}$	1331	36
Bottom-Right $n_{\beta r}$	1581	40
Bottom-Top $n_{\beta r}$	12178	110
Left-Right $n_{\beta r}$	14121	118

Table 4.9: Number of simulated ground state ^{134}Sb decays.

Detector(s)	ε_{MCP}	Uncertainty
Right MCP	**0.249**	0.025
Top MCP	**0.268**	0.027

Table 4.10: MCP efficiency calculated with Eq. 4.14 and numbers from Tables 4.8 and 4.9.

Chapter 5

Neutron energy spectra measurements

This chapter summarizes the general procedure for obtaining the neutron energy spectra from the available recoil ion data. The various corrections implemented in the analysis are enumerated, with special emphasis on accidental subtraction, background reduction, and the detection effects encapsulated in the $\omega_{\beta R}$ correction value found through simulations (as described in Section 4.2.1).

The neutron energy spectrum is deduced from the recoil ion's time-of-flight, which in turn is determined by the recoil energy (E_r) imparted by the neutron through conservation of momentum, if the small contributions from the β^-, $\bar{\nu}$, and any γ's are ignored. Hence, with $\mathbf{p_n} \approx -\mathbf{p_r}$, the neutron energy is given by:

$$E_n = \frac{M_r E_r}{m_n} = \frac{\frac{1}{2} M_r^2 (d/t_{TOF})^2}{m_n}, \tag{5.1}$$

where t_{TOF} is the measured time-of-flight of the recoil ion, and d is the distance the ion travels from the center of the trap to the MCP, determined from the location of the impact on the MCP surface.

Since there are different timing delays between the various detector combinations (due to cable lengths, for example), the TOF of each combination has to be corrected to measure the exact timing difference from the β-γ coincidence peak that is referred to as the "zero-timing peak". The TOF is derived from subtracting ΔE detector timing from the MCP timing, and from subtracting the additional correction accounting for the delays. The corrections for each detector combination are listed in Table 5.1.

As the ions pass through the grounded grid in front of the MCP, they are accelerated by the electric field resulting from the 2.5 kV bias on the surface of the MCP. We are interested in the ion's velocity as it strikes the grid, which determined the initial recoil energy. However, the MCP measures the time of the ion's impact at the MCP surface, after the ion undergoes the acceleration. Hence, to obtain the unperturbed TOF we need to correct for this acceleration. The correction can be derived analytically, since the force on the ion due to the approximately uniform electric field is known.

Using polar coordinates, we label (t_1, s_1, z_1) as the event of the ion crossing the grid, where

Detector Combination	TOF Subtraction (ns)
Left ΔE and Top MCP	-72.244±1.2
Left ΔE and Right MCP	-7.255±1.0
Bottom ΔE and Top MCP	-63.855±1.0
Bottom ΔE and Right MCP	1.930±1.1

Table 5.1: Timing subtraction from the TOF values in each detector combination, from the zero-timing peak determined through calibrations. The uncertainty is given by the σ value in the Gaussian fit to the zero-timing peak.

t_1 is its time-of-flight from the trap center to the grid, s_1 is the radial distance from the center of the grid to the ion's impact location on the grid (pointing along the surface of the grid), and z_1 is the distance from the center of the trap to the grid, pointing perpendicular to the grid's surface. Similarly, the (t_2, s_2, z_2) coordinates mark the event impacting the MCP: z_2 is the distance from the trap center to the MCP surface, s_2 is the radial distance from the MCP center to the ion impact location on the MCP that is known from the measurement, and, finally, t_2 is the total time-of-flight of the ion, which we measure. The z_1 and z_2 values are known from physical measurements of the apparatus.

The acceleration of an ion of charge q and mass m_i in the z direction, due to a uniform electric field is $\mathbf{a} = a\hat{\mathbf{z}} = \left(\frac{qE}{m_i}\right)\hat{\mathbf{z}}$. The field is given by $E = -V_{bias}/(z_2 - z_1)$, where $-V_{bias}$ is the voltage difference between the grid and MCP plate (given by the bias voltage of 2.5 keV, since the grid is grounded), and $z_2 - z_1$ is the distance between the grid and the MCP. Using the equations of motion and the fact that the s component of the velocity vector is constant and drops out (since all the force points in the z direction), the required t_1 can be calculated with:

$$t_1 = \frac{1}{6}\left[4t_2 - \left(\frac{6z_2 + at_2^2}{(A^2+B)^{1/6}} + \frac{(A^2+B)^{1/6}}{a}\right)\left(\cos(\theta/3) - \sqrt{3}\sin(\theta/3)\right)\right]. \tag{5.2}$$

For details of the derivation, the reader is referred to Shane Caldwell's thesis [63], Appendix D. Over the fast ion TOF range, the TOF correction ranges from ∼0.6% to ∼4.6%, which results in energy corrections of 1.2% to 9.3%.

The neutron energy spectrum obtained from this TOF still needs to be corrected for various systematic effects that can affect the shape of the neutron spectrum. First, the accidental background is subtracted, and the energies are shifted to account for the small effect from the lepton recoil. In addition, there are also neutrons detected by the plastic detector, and in the case of ^{137}I, β-delayed neutron signal from ^{137}Te is present as a contaminant. Finally, the energy dependance of the efficiency of the detectors is applied to correct the spectrum. All these corrections are discussed further in the remainder of this chapter.

5.1 Subtraction of accidentals

Before applying the corrections, the accidentals have to be subtracted out of the neutron energy spectrum. The accidentals are assumed to have a flat distribution in the TOF spectrum, and hence also the inverse velocity spectrum. Using the inverse velocity spectrum is preferable to the TOF spectrum since the correction due to the acceleration of ions entering the MCP is already taken care of within the sort code.

In the inverse velocity distribution (denoted as $k = 1/v_r$), the region between 0.3 and 0.4 $\mu s/\text{mm}$ appears flat (which can also be verified by fitting a line to the distribution). Defining the number of accidentals as N, and noting that the accidentals within the background region are a constant as a function of k yields the following relation, where a is a constant:

$$a = \tfrac{dN}{dk},$$

where a is found by integrating the counts in the region of interest, and dividing by the inverse velocity interval of that region. For a small bin width ΔE_n, the number of accidentals at a specific neutron energy E_n can be approximated as:

$$\Delta N \approx \frac{dN}{dE}\Delta E = \frac{dN}{dk}\frac{dk}{dE}\Delta E = a\frac{dk}{dE}\Delta E \tag{5.3}$$

Defining the recoil energy E_r as a function of k:

$$E_r = \tfrac{1}{2}m_r(1/k)^2,$$

and converting E_r into E_n with the conservation of momentum yields:

$$k = \sqrt{\tfrac{m_r}{2E_r}} = \sqrt{\tfrac{m_r^2}{2E_n m_n}}.$$

Taking a derivative with respect to E_n results in:

$$dk = \sqrt{\tfrac{m_r^2}{8m_r E_n^3}}dE_n.$$

Plugging in the dk/dE into Eq.5.3 results in:

$$\Delta N = a\sqrt{\frac{m_r^2}{8m_r E_n^3}}\Delta E_n. \tag{5.4}$$

The equation can now be used to translate the accidental spectrum from inverse velocity into neutron energy bins. Using a obtained from the flat region of the inverse velocity spectrum (divided by the size of the bin), the size of the accidental contribution can be calculated at each neutron energy bin. The accidental contribution is shown as the smooth curve overlaying the neutron energy spectrum in Fig. 5.1. The accidental subtraction does not eliminate the entire background seen at the low neutron energies, subject of the investigation in the proceeding Section 5.2.

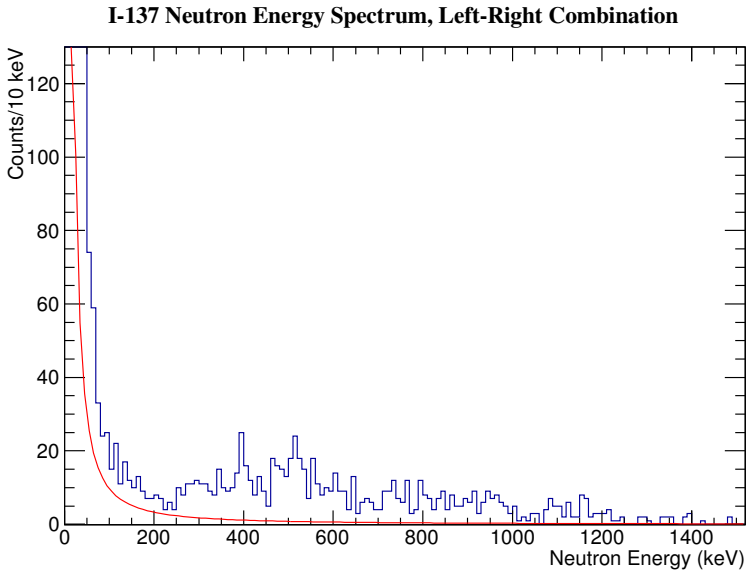

Figure 5.1: Neutron energy spectrum from the ^{137}I precursor decay, in the Left-Right detector combination. The smooth curve represents the accidentals, derived from the flat accidental region in the inverse velocity spectrum.

5.2 Background in the TOF region between 50-1000 ns

The TOF spectrum during the cycle time when the trap is empty is expected to be flat for TOF's longer than 50 ns, beyond the contribution from the zero-timing peak (defined by the β event in ΔE coincident with another scattered β or a γ-ray triggering the MCP). However, Fig. 5.2 illustrates a background extending out to 1000 ns in the TOF spectrum, referred to in the following discussion as the "low-TOF background". This background is most pronounced for the ^{144}Cs dataset since its beam intensity is high, and this isotope was measured for the longest time relative to the other isotopes (the ^{144}Cs P_n is on the order of 3%, requiring a large amount of statistics to complete the measurement). This background is also seen during the trap-full time in measurement cycle, when the trap is capturing ions. However, since the highest-energy/shortest TOF recoil ions arrive around 300 ns, the interval over which the low-TOF background can be characterized in the trap-full time period is limited only to the 50-300 ns region. Below 50 ns, the signal is overwhelmed by the zero-timing coincidence peak.

Detailed analysis could not reach a conclusive explanation for the source of the background. During the trap-empty measurement cycle, the entire signal in the low-TOF region is solely due to untrapped species as well as any other β-particle coincidences aside from recoil ions. The short TOF indicates that the background could be due to recoil ion decays originating at much shorter distances than the trap center, such as from the surface of the MCP shield or the electrode plates. The signal may also result from β-γ coincidences, where

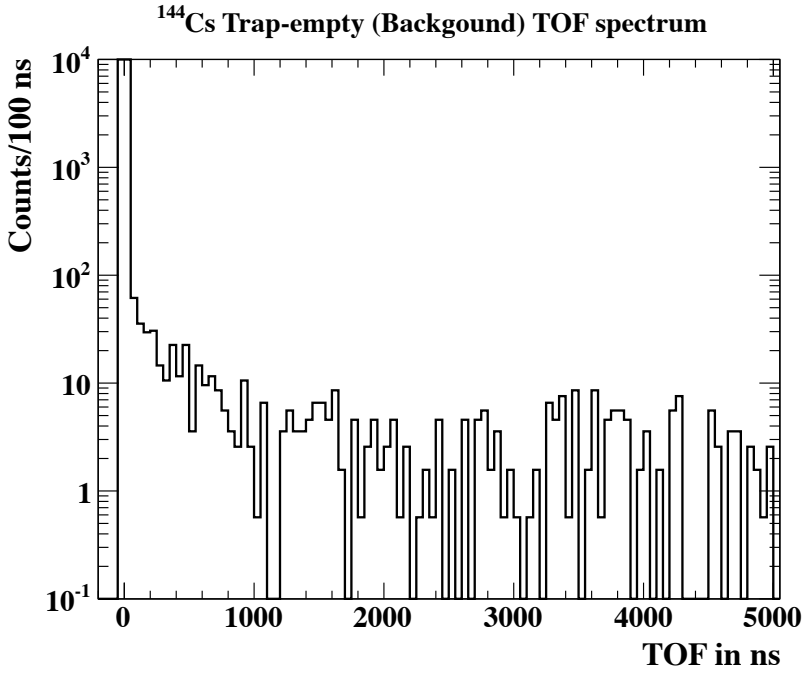

Figure 5.2: TOF spectrum during the trap-empty cycle of ^{144}Cs. The excess of counts at TOF's longer than 50 ns constitutes the "low-TOF" background.

the γ triggers the MCP, as opposed to a recoil ion. The MCP timing signal observed on the oscilloscope indicated presence of ringing, and hence a trigger from the second or third harmonic from the γ could lead to triggers at low TOF's, but beyond the 0 ns peak. Despite the unknown source of the background, a consistent procedure for its subtraction was accomplished. The low-TOF background was characterized with the trap-empty spectrum, and subtracted from the trap-full spectrum with an appropriate subtraction factor determined for each dataset.

The inverse velocity spectrum during the trap-empty cycle served as the best platform for characterizing the low-TOF background. The inverse velocity spectrum was fit between 0.005 and 0.03 μs/mm, which corresponds to the inverse velocity range of the neutron-recoil events. The best fit was achieved with a sum of two exponential functions, which reasonably describes a contribution from a slower-decaying component at longer TOF's, that one exponential would underestimate. The fit for ^{144}Cs is shown in Fig. 5.3. The spectrum is the sum from all four ΔE-MCP detector combinations.

Fits were performed for all the other isotopes, and it was found that using the same fit function shape as for ^{144}Cs yielded satisfactory results. The amplitude of the second exponential was fixed as a fraction of the amplitude of the first exponential, leaving the amplitude of the first exponential as the only free-floating parameter.

The fit function was then transformed into the energy spectrum, and compared with the trap-empty energy histogram, resulting in a satisfactory agreement even outside the fit

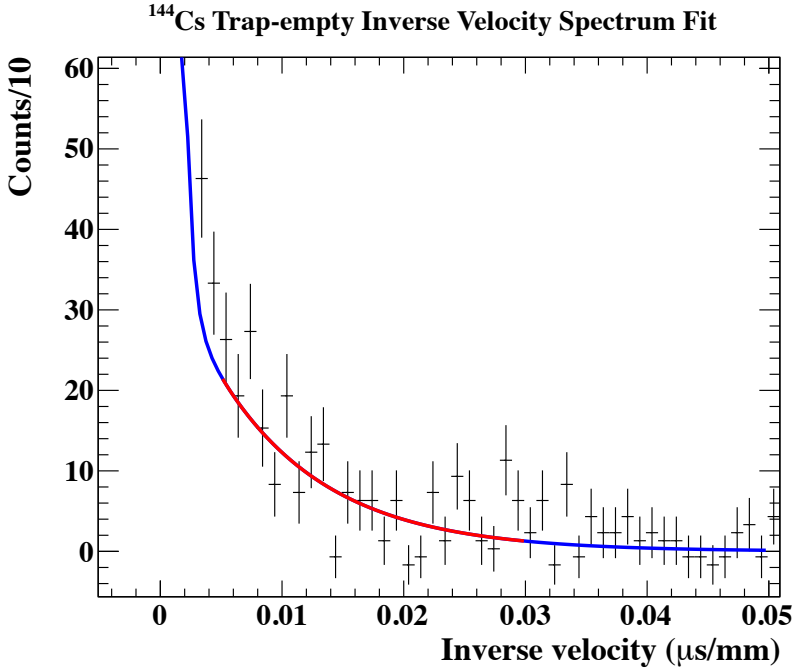

Figure 5.3: Fit to the trap-empty inverse velocity spectrum of ^{144}Cs. Fit was performed over the range marked in red (0.005-0.03) with a sum of two exponentials, using the log-likelihood method.

range. This transformed function is the basis for the background subtraction, but still needs to be scaled properly to the trap-full energy spectrum prior to subtraction, by what I refer to as the **subtraction factor**.

One of the ways the subtraction factor can be deduced is from taking the ratio of the counts in the trap-empty spectrum to the trap-full spectrum, over a region where no inferred neutron-recoil events are expected, i.e. 2000-4000 keV. This method can be implemented in an improved way by fitting the trap-empty spectrum. The fit function from the trap-empty spectrum is then scaled iteratively to match the trap-full spectrum in the region where no recoils are expected. The subtraction factor is then determined as the scaling factor that produces the best fit to the trap-full spectrum (i.e. where the standard deviation is lowest). This procedure was repeated for each isotope. The uncertainty in this method encompasses the standard deviation from the fit integrated over all the bins. The resulting subtraction factors from the simple counting and from the improved scaling method are listed in Table 5.2, in the columns titled "Counts ratio" and "From scaling fit", respectively.

Another method of deducing the subtraction factors is to look at the low-TOF background between 50 and 200 ns as a function of time in measurement cycle. After correcting for deadtime and subtracting accidentals, the resulting histogram is fit according to a simplified Trap Population Model (described in Section 4.1.2). In this simplified treatment, only the contributions from the precursor and its daughter are included in the fit, with contributions of both trapped and untrapped populations. The fit to the ^{144}Cs precursor low-TOF background is shown in Fig. 5.4.

During the trap-empty cycle (the first 3000 ms), the untrapped species decay starting with the amplitude built up during the trap-full cycle, with a decay half-life consistent with the daughter decay. This is marked with the red line in the fit of Fig. 5.4 and Fig. 5.5. Hence, the remaining counts above the background in the trap full cycle are due to the trapped species, and the fit to these counts is consistent with the precursor half-life. These figures illustrate that the subtraction factor cannot be simply deduced from the scaling in cycle time, due to the presence of the trapped species. Rather, the subtraction factor is the ratio of the counts in the trap-full to the trap-empty regions counted under the fit. The uncertainty in this subtraction factor encompasses the standard deviation of data compared to the fit.

The three methods yielded subtraction factors, listed in Table 5.2, that were consistent with each other for the ^{144}Cs.02, ^{145}Cs.02, and ^{137}I.07 datasets. Due to very low statistics in both of the ^{138}I datasets, the subtraction factors were inconsistent, though since in these cases the low-TOF background is small, the large uncertainty in the subtraction factor did not dramatically affect the uncertainty in the background-subtracted fast-ion numbers.

The fully characterized subtraction function is valid for the sum of the four detector combinations. However, since each detector combination has its own energy spectrum, the subtraction function needs to be scaled from the 4-detector sum, to 1-detector spectrum. To characterize the low-TOF background in an energy spectrum from a single detector combination, the fit to the 4-detector combination is scaled down using the ratio in the total counts in the trap-empty energy spectrum for the two histograms.

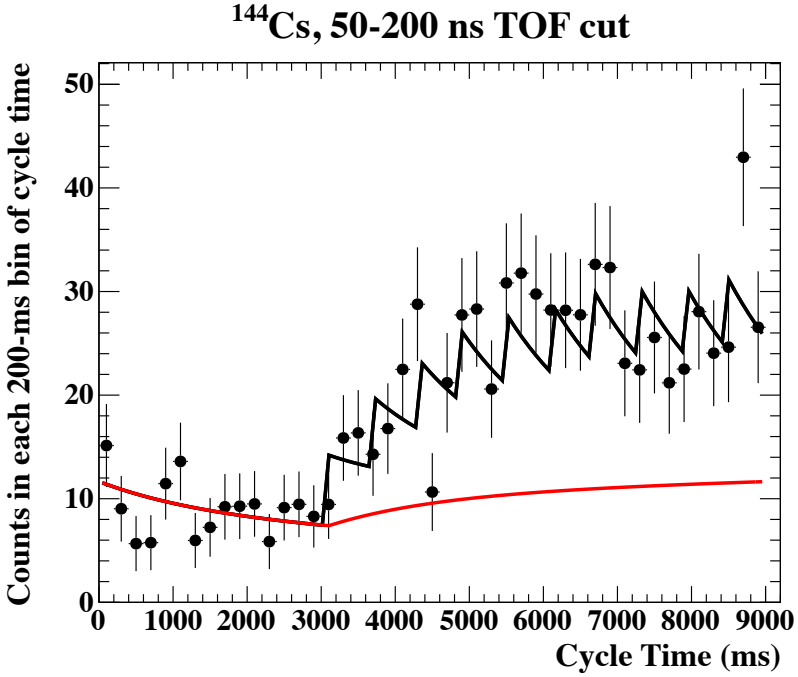

Figure 5.4: Fit to the counts with TOF between 50 and 200 ns vs. cycle time, for the ^{144}Cs precursor decay. Fit uses a combination of two species in both untrapped and trapped state. The contribution of trapped species in the low-TOF background is shown to be significant.

Dataset	From scaling fit	From cycle fit	Counts ratio	Weighted Avg.
^{144}Cs.02	4.49(35)	5.24(66)	5.64(54)	4.90(27)
^{145}Cs.02	5.62(72)	4.93(120)	4.55(74)	5.07(48)
^{137}I.07	5.51(86)	10.24(140)	10.03(370)	6.98(72)
^{138}I.06	6.06(100)	8.61(460)	7.68(210)	6.46(91)
^{138}I.07	15.53(380)	7.57(620)	6.86(350)	10.44(240)

Table 5.2: Subtraction factors used for scaling trap-empty background that is then subtracted from the trap-full spectrum, reducing contribution from the low-TOF background. Subtraction factors were obtained with three different methods. The weighted average of the three values constitutes the subtraction factor used in the background subtraction.

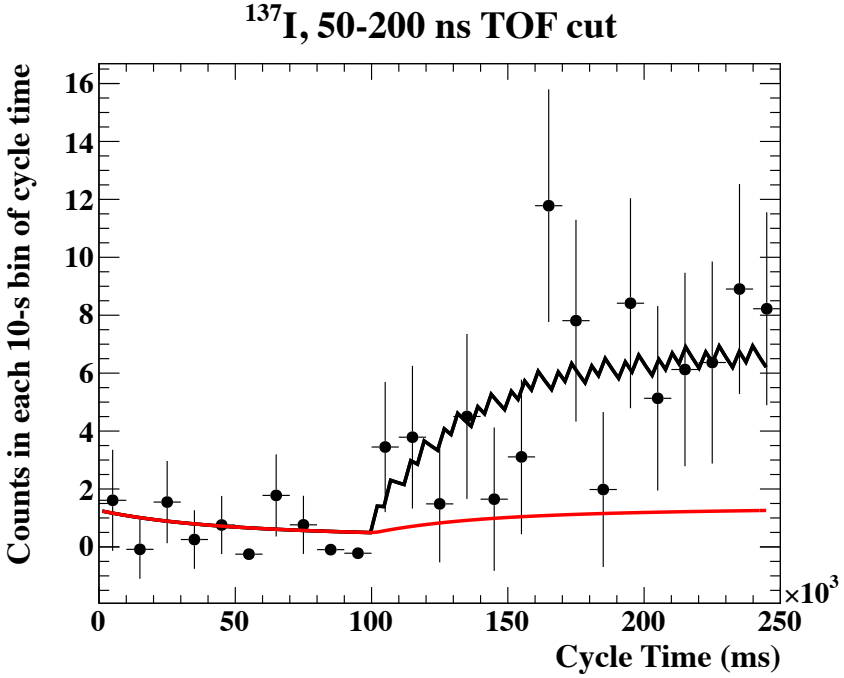

Figure 5.5: Fit to the counts with TOF between 50 and 200 ns vs. cycle time, for the ^{137}I precursor decay. Fit uses a combination of two species in both untrapped and trapped state. The contribution of trapped species in the low-TOF background is shown to be significant.

Dataset	Low-TOF counts	Uncertainty	Size of correction (%)
^{144}Cs.02	747.6	41.2	31.1
^{145}Cs.02	344.1	32.6	11.2
^{137}I.07	211.8	21.9	6.8
^{138}I.06	155.8	21.9	7.2
^{138}I.07	47.9	10.9	5.6

Table 5.3: Number of counts attributed to the low-TOF background above 100 keV for the sum of four detector combinations, and the size of the correction relative to the total counts.

In summary, the steps for subtracting the low-TOF background are:

1. Obtain a function describing the trap-empty energy spectrum using a transformed fit to the trap-empty inverse-velocity spectrum. Use a spectrum that's a sum of four detector combinations.

2. Scale the function down to match the spectrum from each detector combination separately, using the ratio of counts in the one detector combination spectrum to the sum spectrum.

3. Scale the fit function to match the trap-full cycle using the subtraction factor from Table 5.2.

4. Subtract the scaled background from the trap-full energy spectrum.

5. Vary the subtraction factor within its associated error to deduce systematic uncertainty from the background subtraction

The relevant histograms and fit functions for the ^{144}Cs are shown in Fig. 5.6. Fig. 5.7 shows the low-TOF background subtraction for all the other datasets.

The resulting correction varies between 6-31%, and is largest for the ^{144}Cs dataset. The uncertainties associated with the low-TOF background subtraction contribute to the systematic uncertainty in the branching ratio calculations.

5.3 Correcting for lepton recoil

The sort code takes each event and calculates the neutron energy based on the recoil ion time-of-flight and the MCP position, as described in Equation 5.1. In addition, the sort code corrects the time-of-flight of the recoil ion for the acceleration due to the electric field between the grid and the face of the MCP (see Equation. 5.2). The accuracy of the energy reconstruction was verified by simulating mono-energetic neutrons at known energies, and

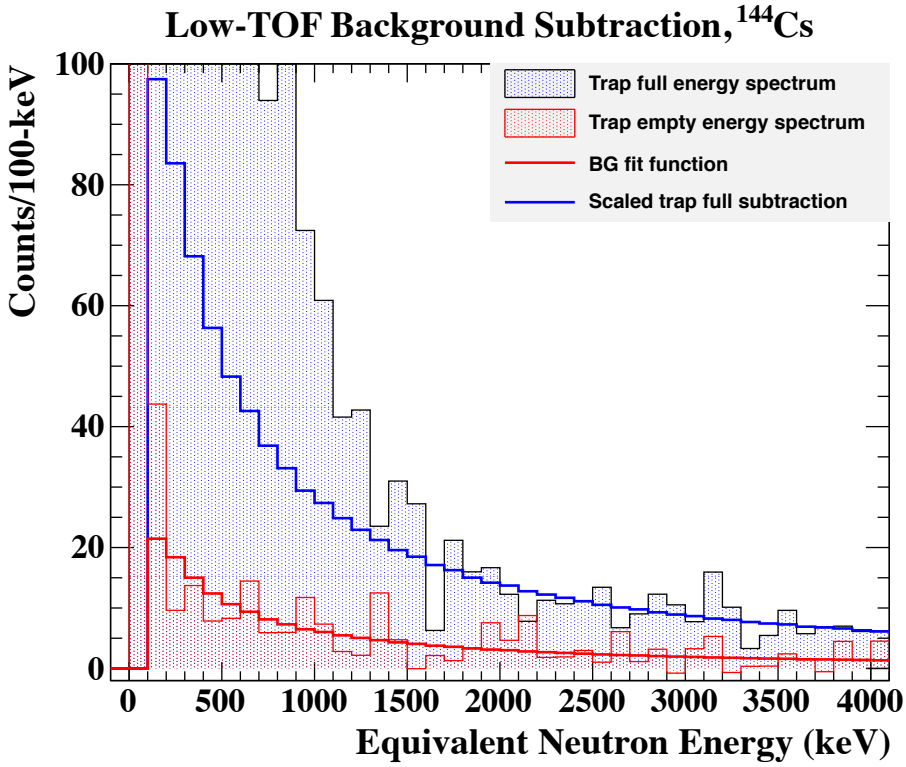

Figure 5.6: Low-TOF background subtraction from the neutron energy spectrum (sum of four detector combinations). The red line is the fit to the trap-empty spectrum, and the blue line is the fit scaled by the subtraction factor from Table 5.2. The low-TOF background subtraction is performed with the blue fit.

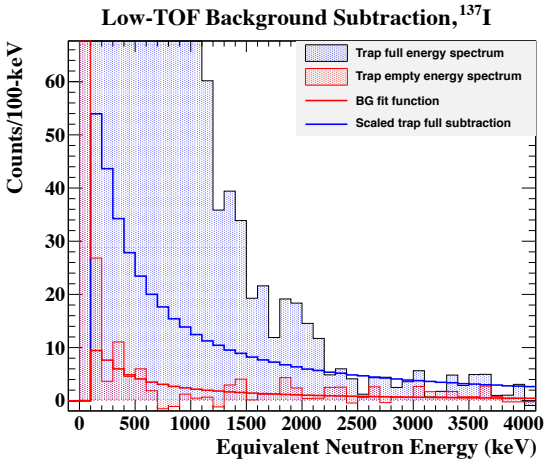

(a) ^{137}I.07 dataset.

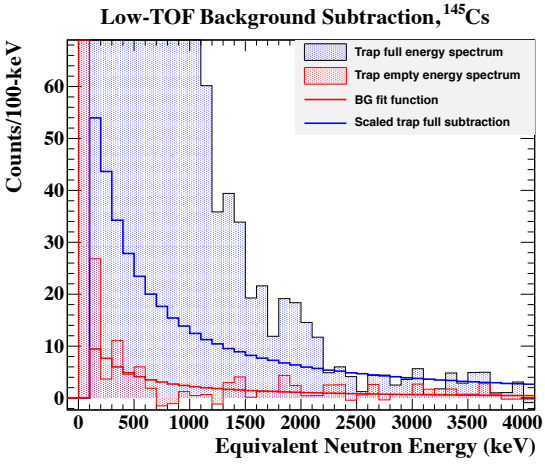

(b) ^{145}Cs.02 dataset.

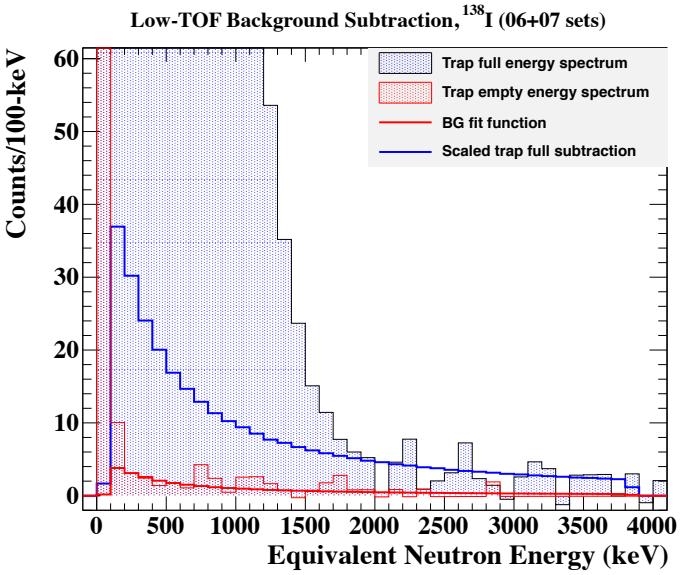

(c) Sum of ^{138}I.06 and ^{138}I.07 datasets.

Figure 5.7: Low-TOF background subtraction.

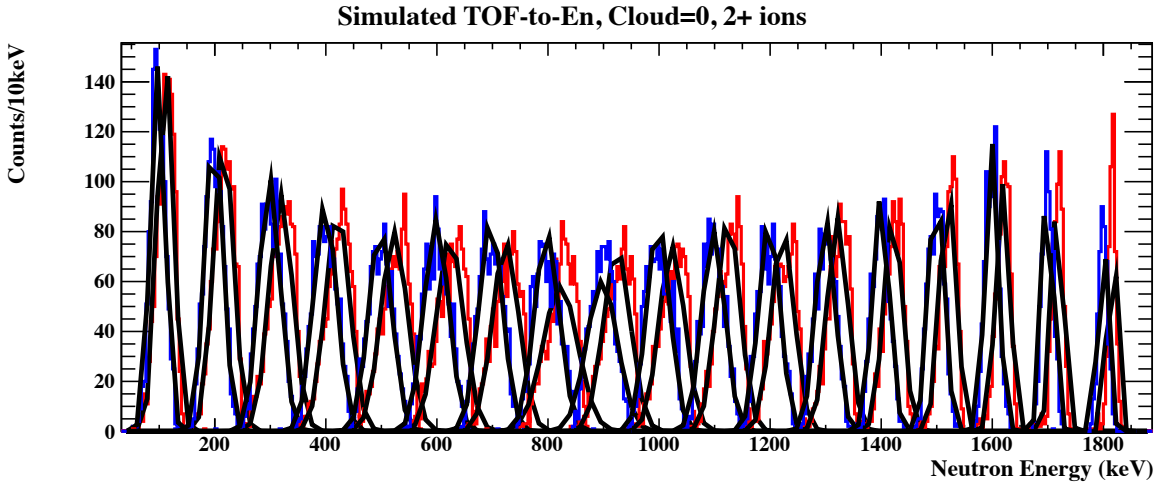

Figure 5.8: ^{137}I simulated mono-energetic neutron spectrum for 2^+ recoil ions, with a TOF-to-E_n reconstruction code implemented. Blue line is for the 90° detectors combination, and red is for 180°. The cloud size was 0.001 mm.

calculating neutron energy from the resulting recoil ion time-of-flight. The simulation was done using an ion cloud with a Gaussian distribution of 2.5 mm (FWHM) in all three spatial directions and for a point source. The reconstructions of the neutron energy with these two different ion cloud sizes are shown in Fig. 5.8 and Fig. 5.9. The energy shift for the 180° detector pair is evident. The culprit of the energy drift is due to lepton recoil being ignored in the energy reconstruction. The effect of the lepton recoil would indeed be most pronounced at the 180° detector pair combination.

For the events detected in the 180° detector combination, the recoil ion and the β have momenta vectors pointing in opposite directions. The recoil ion momentum is largely due to the neutron, and hence the neutron momentum also points opposite to the recoil ion's momentum, in about the same direction as the β momentum. Ignoring momentum due to the neutrino, and rewriting the momentum relation from Equation 5.1, the magnitude of the neutron momentum is: $p_n = p_r - p_\beta$. Using the non-relativistic momentum definition for the recoil ion, the neutron kinetic energy is:

$$E_n = \frac{(M_r v_r - p_\beta)^2}{2 m_n c^2}, \tag{5.5}$$

where p_β can be measured with the plastic detector. Finding the energy of the neutron from the recoil TOF in the simulation results in a neutron energy spectrum that slightly over-corrects the energy shift, since the neutrino momentum is ignored (since no experimental setup would allow its direct measurement). Comparison between the Gaussian fit's FWHM for the uncorrected spectrum and the spectrum corrected with the equation (event-by-event) is shown in Fig. 5.10. The figure also illustrates the effect due to the ion cloud size, which is a larger than the size of the over-correction due to the event-by-event lepton correction.

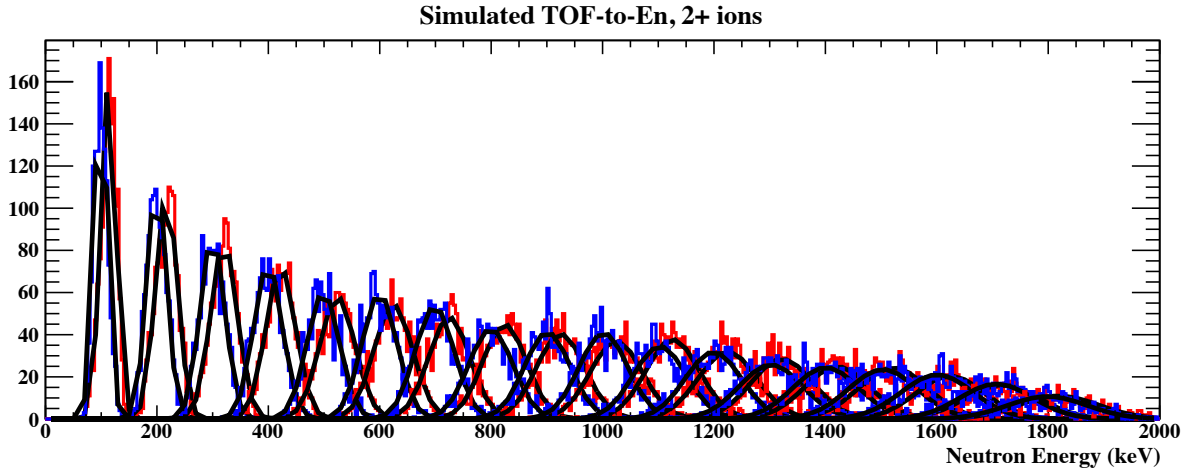

Figure 5.9: ^{137}I simulated mono-energetic neutron spectrum for 2^+ recoil ions, with a TOF-to-E_n code implemented. Blue line is for the 90° detectors combination, and red is for 180°. The cloud size was 2.5 mm FWHM, which results in the decreasing neutron energy resolution with increasing higher neutron energies.

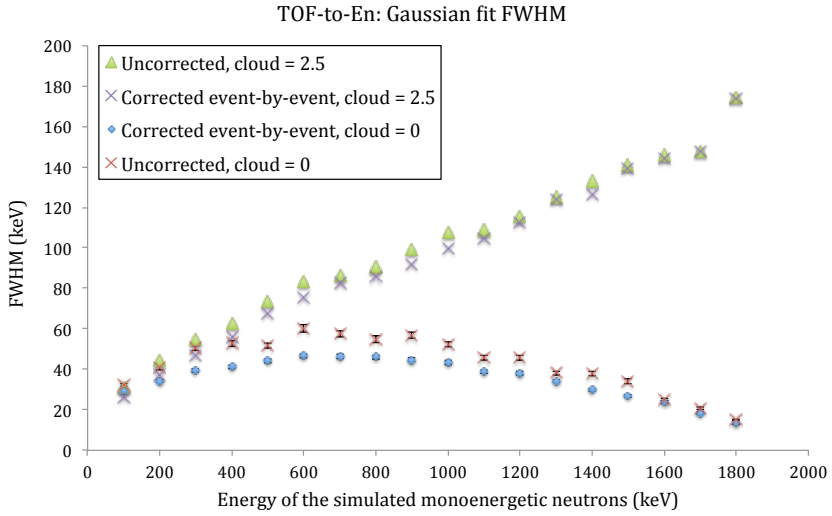

Figure 5.10: FWHM of the Gaussian fit to the corrected and uncorrected energy spectra reconstructed from simulated ^{137}I recoil ion TOF.

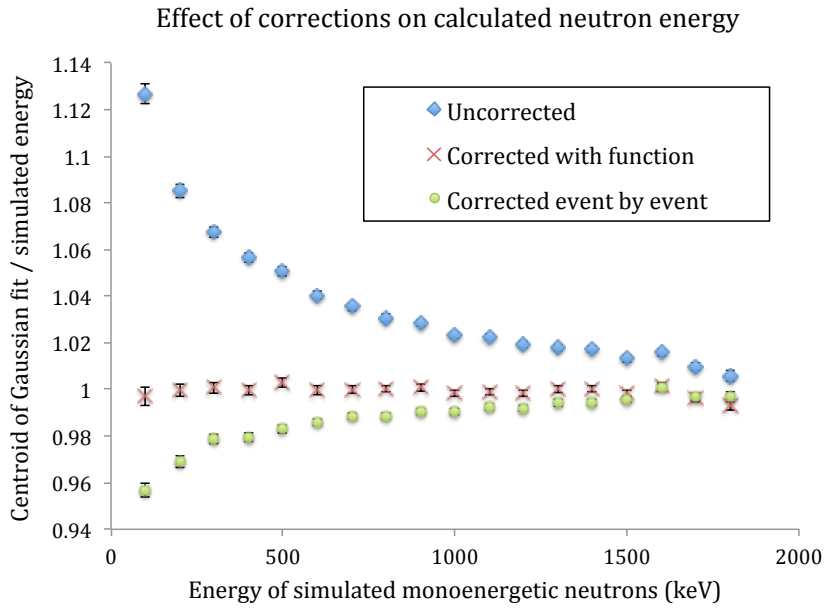

Figure 5.11: ^{137}I energy shift for the 180° detector combination, defined as the ratio between the centroid of the Gaussian fit to the reconstructed TOF-to-E_n energy peak and the simulated mono-energetic neutron energy. The comparison shows the difference between the uncorrected spectrum, spectrum corrected with an empirical function, and spectrum corrected event-by-event with Eq. 5.5, as described in this section. The latter method over-corrects the spectrum at low energies, since the antineutrino momentum is ignored.

A simpler and more direct way to correct for the lepton recoil is to fit the simulated reconstructed neutron energy spectrum from monoenergetic neutrons at each 100 keV (a flat spectrum). In the reconstructed spectrum, these monoenergetic neutrons result in a Gaussian, with a peak shifted from the original energy. By deriving a relation between the reconstructed peak and the original energy of the neutron, an empirical correction is found. This correction can then be applied to the spectrum obtained from data, and the energy can be shifted appropriately.

Comparison between these two ways of correcting the spectrum for ^{137}I are shown in Fig. 5.11. The empirical function correction method has been used to correct the experimentally obtained neutron energy spectra for the 180° detector combination. An energy shift function was derived for each isotope separately, based on the individual simulations. The effect of the lepton recoil on real data can be seen for the ^{137}I dataset in Fig. 5.12.

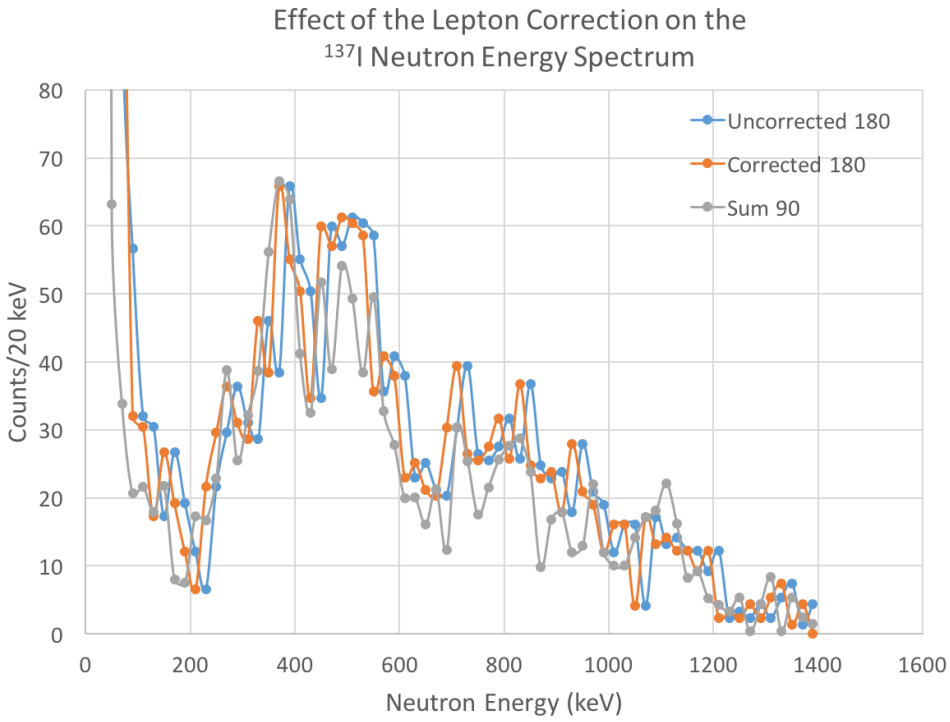

Figure 5.12: Effect of correcting the ^{137}I neutron energy spectrum for the lepton recoil.

5.4 MCP energy-dependent efficiency correction

The neutron energy spectrum derived from the recoil ion time-of-flight relies on the recoil ion signal imparted on the MCP. Ideally, the MCP should have a response independent of the ion impact velocity, and an intrinsic efficiency approaching the open-area ratio. In reality, the MCP gain may affect the fraction of detected events, and hence exhibit an energy-dependent detection efficiency [67, 68]. In the data collected during the experiment, it was observed that the Top MCP detected fewer low-energy ions than the Right MCP. This section details the analysis performed to derive an energy-dependent correction to the relative efficiency of the MCP. This efficiency correction does not take into account the intrinsic efficiency of the MCP, which was measured with the ^{134}Sb calibration data using slow-recoil ions. However, this efficiency correction is crucial for correcting the neutron energy spectrum shape, as the efficiency for detecting the recoil ions changes with the recoil ion (and hence neutron) energy.

Due to the Poisson nature of the electron multiplication process in the MCP [69], the Pulse Height Distribution (PHD) from a single ion impact can be described with a Gaussian distribution. This has been observed in previous experiments [70]. The centroid and standard deviation of this Gaussian are a function of the MCP gain, as well as the ion mass, its charge state and energy [67]. Therefore, the first step towards a consistent characterization of the MCP is to look at the response due to ions grouped by similar impact velocity.

The ion impact energy (and therefore velocity) can be calculated from the measured ion time-of-flight (TOF), distance traveled (d) calculated from the deduced impact position on the MCP, and the addition of energy imparted by the acceleration due to the MCP bias:

$$KE_{impact} = qV_0 + KE_{recoil}, \tag{5.6}$$

where q is the charge state, V_0 the MCP bias (in this case, 2500 V), and $KE_{recoil} = \frac{1}{2}m_{ion}(\frac{d}{TOF})^2 = \frac{1}{2}m_{ion}v_{recoil}^2$. The resulting impact velocity is dominated by the qV_0 term, except for recoil ions following neutron emission. For these fast recoils, the KE_{recoil} term is comparable to the qV_0.

Hence, the ion impact velocity is defined as:

$$v_{impact} = \sqrt{v_{recoil}^2 + \frac{2qV_0}{m_{ion}}}. \tag{5.7}$$

Since gain can change across the face of the MCP, we need to account for the ion's impact location. In the analysis that follows, the fiducial area of the MCP was subdivided into 16 equally-sized "pixels", each 5.75 by 5.75 mm. The resulting pixel grid with the labeled pixel names, posts, and the defined coordinate axis, is drawn in Fig. 5.13. The choice of this number of pixels was a compromise between spatial resolution and the available statistics in each pixel. Furthermore, only 4-post events were taken into account in the efficiency analysis, as only these events have a well-defined PHD, which is the sum of the charge collected by the four posts.

The electronic threshold imposes a lower limit on the measured PHD, and attenuates data causing efficiency to drop depending on the centroid and standard deviation of the PHD.

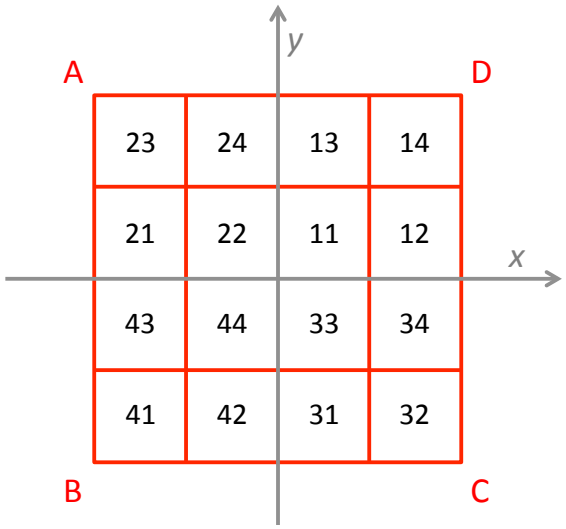

Figure 5.13: MCP pixel grid naming conventions.

Therefore, the MCP efficiency is expected to vary with position and ion impact velocity.

For a Gaussian distribution with mean μ and standard deviation σ, the area between the threshold at a and the highest channel on the ADC at b can be calculated with:

$$\frac{1}{\sqrt{2\pi}\sigma}\int_a^b e^{\frac{-(x-\mu)^2}{2\sigma^2}} = \frac{1}{2}\left[\mathrm{erf}\left(\frac{b-\mu}{\sqrt{2}\sigma}\right) - \mathrm{erf}\left(\frac{a-\mu}{\sqrt{2}\sigma}\right)\right]. \tag{5.8}$$

Essentially, this is what defines the relative efficiency at a single ion impact velocity for a specific MCP gain.

5.4.1 Determining the discriminator threshold

The timing signal on the MCP travels through a TC 455 Constant Fraction Discriminator (CFD) NIM module. The CFD threshold level was set to optimize the signal-to-noise ratio. However, the discriminator causes some of the events to be lost below the threshold level. The first step in determining the effect of the discriminator threshold is to precisely determine the location of the threshold on the MCP's Pulse Height Distribution (PHD) histogram for each pixel.

In order to determine the threshold, single events (as opposed to coincidences) from the ^{137}I dataset were used due to the high statistics. The PHD of these events consists of pulses induced by ions, γ's, and β's. Although each type of particle may induce a different PHD shape, the threshold is a constant.

Effect of the threshold on PHD data can be seen in Fig. 5.14a and Fig. 5.14b, for pixel 21 on the Right detector, and pixel 22 for the Top detector. These pixels were chosen as representative, since most pixels have very similar response with the exception of the corner

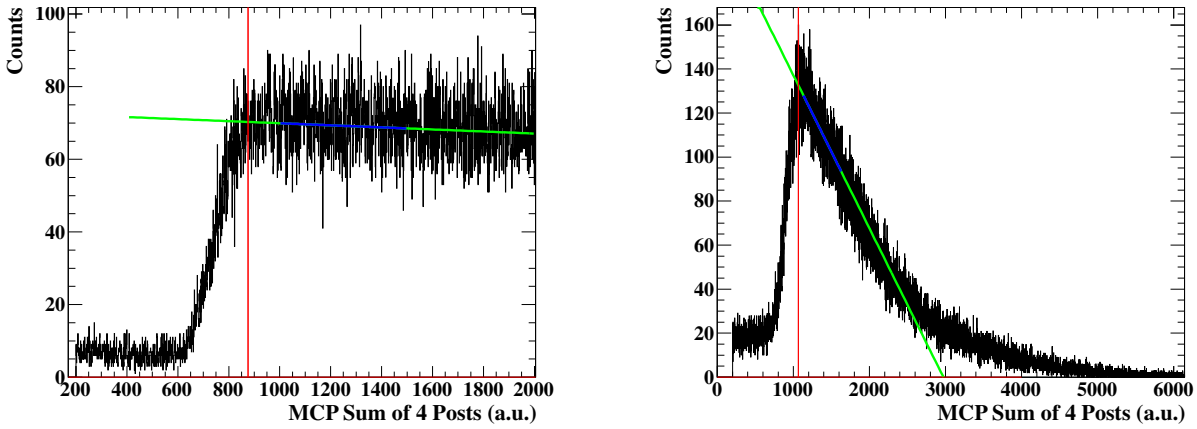

(a) Right MCP PHD, Pixel 21

(b) Top MCP PHD, Pixel 22

Figure 5.14: Linear fit (blue) to the ^{137}I singles MCP PHD data. Green line is the extension of fit. Red vertical line marks the threshold

pixels. First, the histogram mean is found, and a linear fit is applied from the histogram mean to 500 channels out (represented with the blue line). Although the PHD form may more closely resemble an exponential, the local linear approximation is appropriate, and independent of any nonlinear effects that could affect the PHD shape. By plotting the ratio of the data to the linear fit extended over the range of the PHD (green line), the discriminator cutoff can be more easily defined. These ratios are plotted in Fig. 5.15a and Fig. 5.15b. The threshold is then defined as the point where the ratio of data to fit, rebinned by 10, crosses the value of 0.98, resulting in a conservative threshold value. The procedure was repeated to find threshold at each pixel over the face of each MCP. The threshold values vary across the location of the MCP despite identically applied discriminator threshold. The variation may therefore be explained by the behavior of the anode itself.

5.4.2 Positional dependence of the MCP response

Ions recoiling from β decay without neutron emission all initially have kinetic energies on the order of $\sim$100 eV. The ions get accelerated between the grid and the MCP plate with a force proportional to the ion's charge state. The PHD of ions with the same initial KE (and hence the same TOF) but in different charge states will end up with different impact velocities, each defined as in Eq. 5.7. Therefore, selecting slow ions at each pixel, where the impact energy can be approximated as uniform, the resulting PHD can be described as the sum of Gaussians, each corresponding to a different charge state.

Assuming a linear relation between centroid of the Gaussian distribution and ion impact velocity [70, 67], the ratio of centroids between charge states 3^+ and 2^+ can be defined as

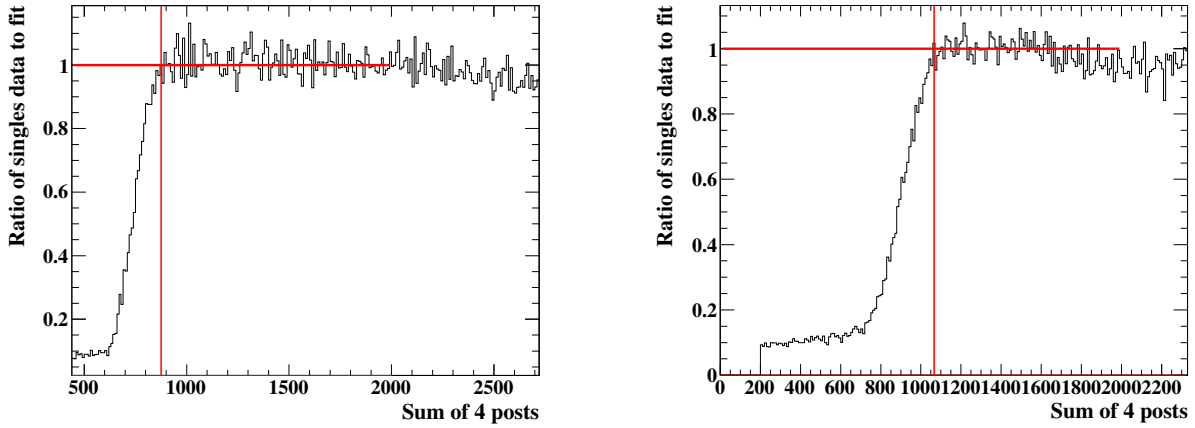

(a) Right MCP (b) Top MCP

Figure 5.15: Ratio of ^{137}I singles PHD to linear fit. Threshold is marked with a vertical red line.

follows:

$$\frac{x_0^{3+}}{x_0^{2+}} = \sqrt{\frac{T_r + q_3 \times V_0}{T_r + q_2 \times V_0}}, \tag{5.9}$$

where x_0^{3+} is the centroid of the Gaussian distribution of the ions in charge state 3^+, while x_0^{2+} of the ions in charge state 2^+. T_r is the kinetic energy of the ions imparted by the recoil, q_3 and q_2 are charge states, and V_0 is the MCP bias (2500 V in the current case). For the purposes of this analysis, only three charge states for ^{137}I are considered, with distribution consistent with the analysis described in 4.2.4, and predictions in literature [71, 72].

Slow ion data per pixel was fit above the thresholds found in Sec. 5.4.1. The upper limit of the fit is set a couple hundred channels below highest non-empty bin, to avoid any nonlinearity effects (such as pileup) that could skew the fit. The first fit uses a sum of three Gaussians at specified centroid and amplitude ratios, each with identical variance. The relative amplitudes are set by the relative amounts of each charge state present, which is known from the analysis (the procedure for obtaining the charge state distribution is described in Section 4.2.4).Therefore, the only free parameters of the fit are the variance, amplitude, and centroid of the Gaussian representing the the 2^+ charge state, with 3^+ and 4^+ Gaussian values set relative to it. The second fit uses a single Gaussian with amplitude, mean, and variance as free-floating parameters.

As can be seen in Fig. 5.16a and 5.16b, the difference between the 3-Gaussian and 1-Gaussian fit is negligible, and hence for the purposes of the analysis, PHD at a single velocity per each pixel can be fit with a single Gaussian. The slow ion fits for each pixel of each MCP are shown in Figures 5.25 and 5.27 for the Top MCP, and Figures 5.28 and 5.30 for the Right MCP. The locations of the plots correspond to the physical location of the pixel on the MCP.

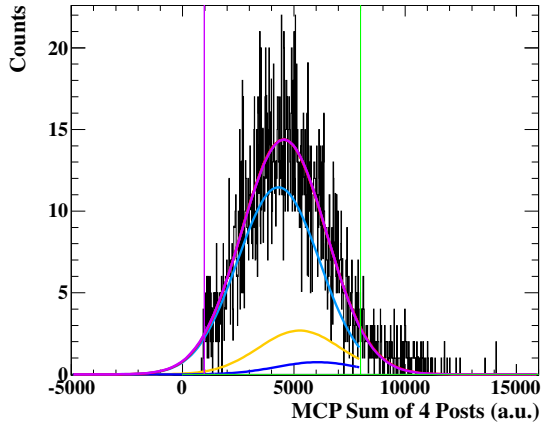

(a) Typical PHD from a pixel in the Right MCP (pixel 33).

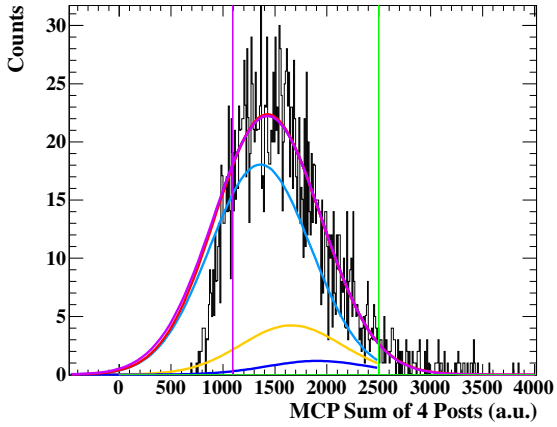

(b) Typical PHD from a pixel in the Top MCP (pixel 11).

Figure 5.16: Fit to ^{137}I slow ion data. The fit is performed between the vertical purple line around 1000 (the threshold) and the vertical green line (upper fit limit). The 1-Gauss fit to the data is the violet line. The 3-Gauss fit is the sum of blue, yellow and navy Gaussians shown, and is marked with a red line, essentially indistinguishable from the 1-Gauss fit on these plots.

5.4.3 Centroid as a function of ion impact velocity

By summing up the Gaussian fits from all the pixels, a total function can be found which describes the PHD over the entire MCP area. The total fit function consists of 16 Gaussian curves, with their amplitudes and centroids set as a ratio relative to pixel 11 values (but any other representative pixel with sufficient statistics would work). The variance of each Gaussian is fixed to the values found for in each pixel fits, as the variance was assumed not to change with ion impact velocity based on results from literature: [70, 67]. Hence, in the whole-MCP fit consisting of the sum of the 16 Gaussians, there are only two parameters that vary - the amplitude and centroid of the pixel 11 Gaussian. The total fit function was applied to PHD's of slow ions (for the entire fiducial area of the MCP) of ^{137}I, ^{138}I (two different datasets), and ^{134}Sb. The resulting fits are shown in Fig. 5.17.

The total function can be applied to fit fast ion data, enabling determination of the centroid dependence on ion impact velocity. To produce PHD's of a specified impact velocity cut, equal velocity bin widths and spacings are used. The impact velocity bin width found to be optimal with respect to statistics and narrowness of the velocity cut is 0.018 mm/ns. The average impact velocity is weighted by the counts in each 1/v bin within the cut area. As was done with all PHD data, accidentals are removed by taking events at high TOF values where the spectrum is flat, and subtracting them from the cut area, scaled by the ratio of velocity windows.

Fits to fast ion data from four different datasets, ^{137}I, ^{138}I (dataset 06 and 07), and ^{135}Sb, produced PHD centroids at 14 different impact velocity bins, in addition to the four

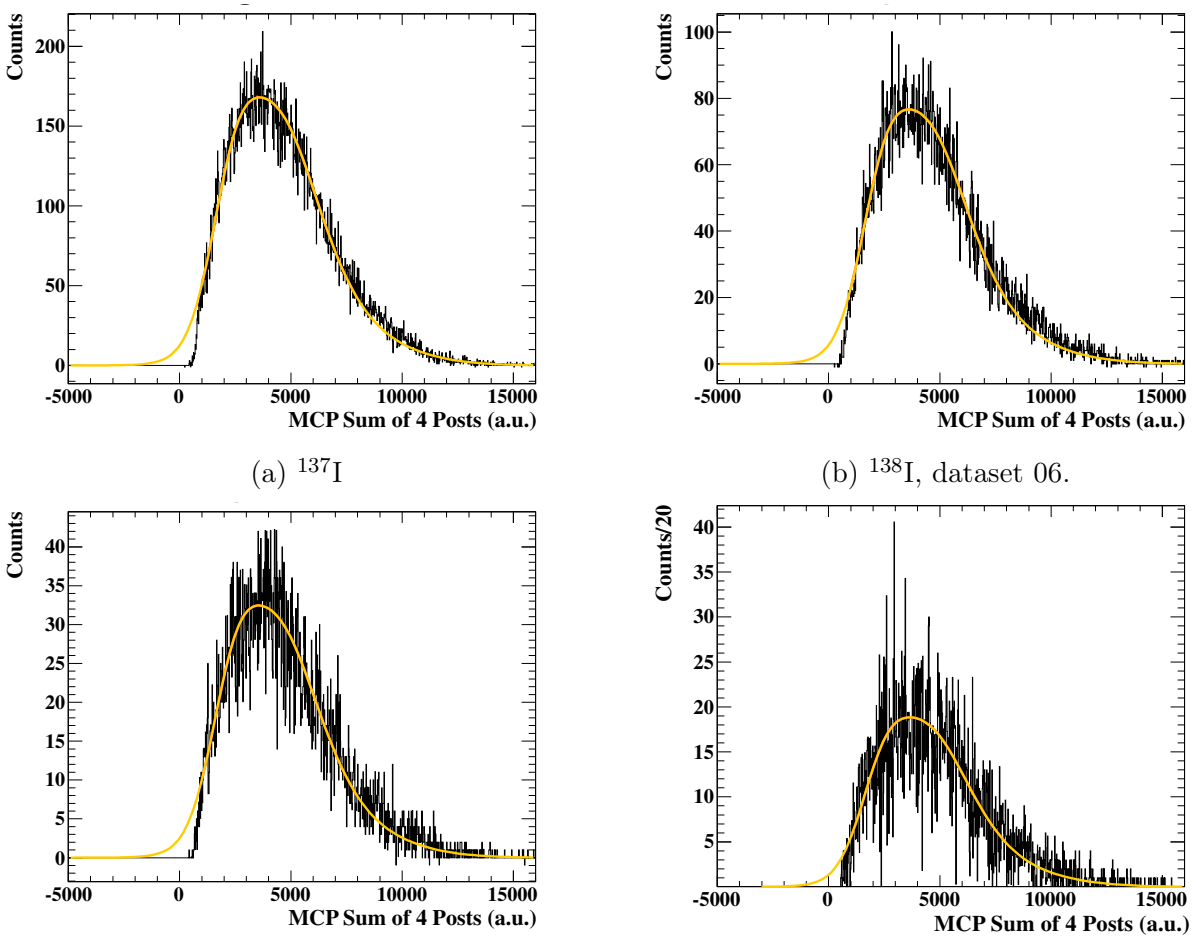

(a) ^{137}I

(b) ^{138}I, dataset 06.

(c) ^{138}I, dataset 07.

(d) ^{134}Sb, isomer subtracted

Figure 5.17: Fit to slow ion data PHD over the entire Right MCP fiducial area.

data points from fits to slow ion data. The results are summarized in Fig. 5.19, with a superimposed linear fit (continuous red line). The upper and lower bounds of the fit (dashed lines) were produced by refitting the original fit with the slope fixed to original fit parameter value, plus or minus the parameter's uncertainty. The resultant parameter values are listed below:

$$x^{11}_{Top} = 12520.6 \times v_{impact} + 393.188 \tag{5.10}$$

$$x^{11}_{Right} = 27293.5 \times v_{impact} + 1729.81 \tag{5.11}$$

Centroids for all the other pixels can then be easily calculated by multiplying the value from pixel 11 by appropriate ratio, listed in 5.4 and Table 5.5. These equations give the centroid for the single Gaussian approximation of the more accurate multi-Gaussian fit that

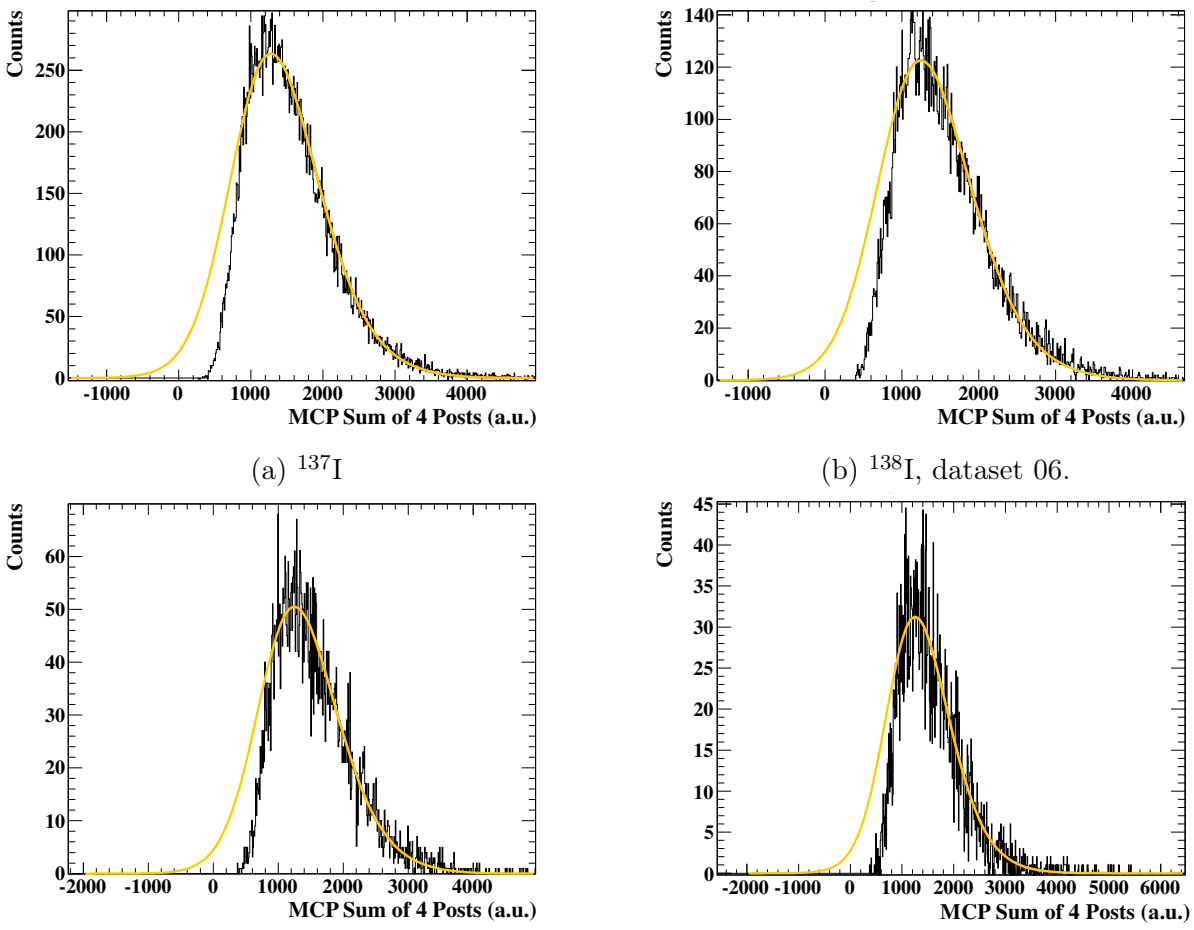

(a) ^{137}I

(b) ^{138}I, dataset 06.

(c) ^{138}I, dataset 07.

(d) ^{134}Sb, isomer subtracted

Figure 5.18: Fit to slow ion data PHD over the entire Top MCP fiducial area.

consists of a few charge states (as can be seen in Fig. 5.16a and Fig. 5.16b). Since the relationship between the 2^+ centroid and the single Gaussian approximation is known, the 2^+ centroid can be simply obtained:

$$\mu_{Top} = x_{Top}^{11,2+} = 0.9466 \times x_{Top}^{11} + 3.3906 \tag{5.12}$$

$$\mu_{Right} = x_{Right}^{11,2+} = 0.9461 \times x_{Right}^{11} + 4.8786 \tag{5.13}$$

The σ for charge state 2^+ PHD is listed in Table 5.4 and Table 5.5. Together with the threshold value, these parameters fully describe the fraction of the Gaussian above the threshold for each MCP pixel according to Eq. 5.8. The final step of converting this fraction into MCP efficiency is to correct it by the entries below the threshold, which increase the fraction slightly.

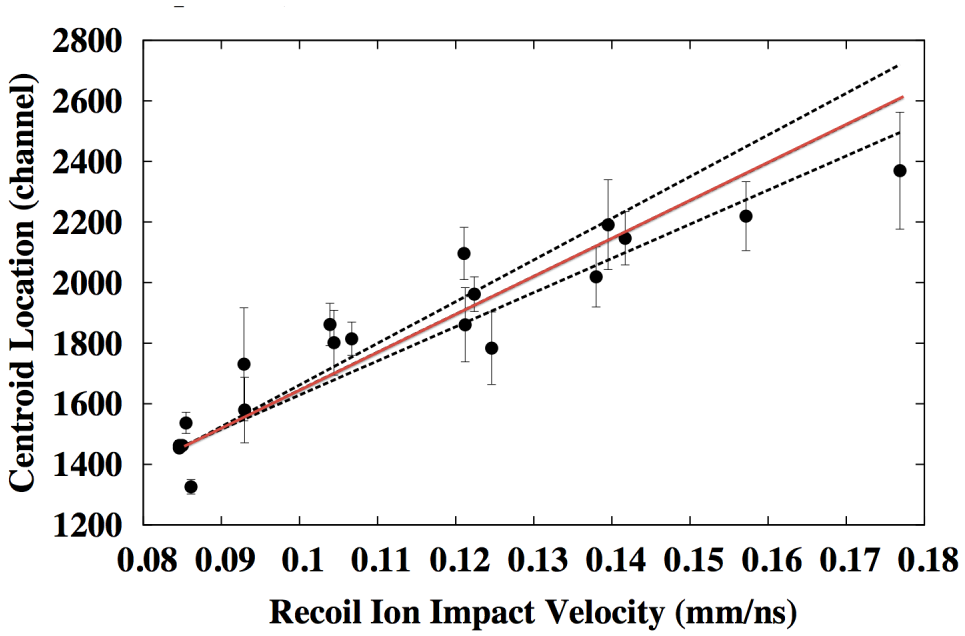

(a) Top MCP.

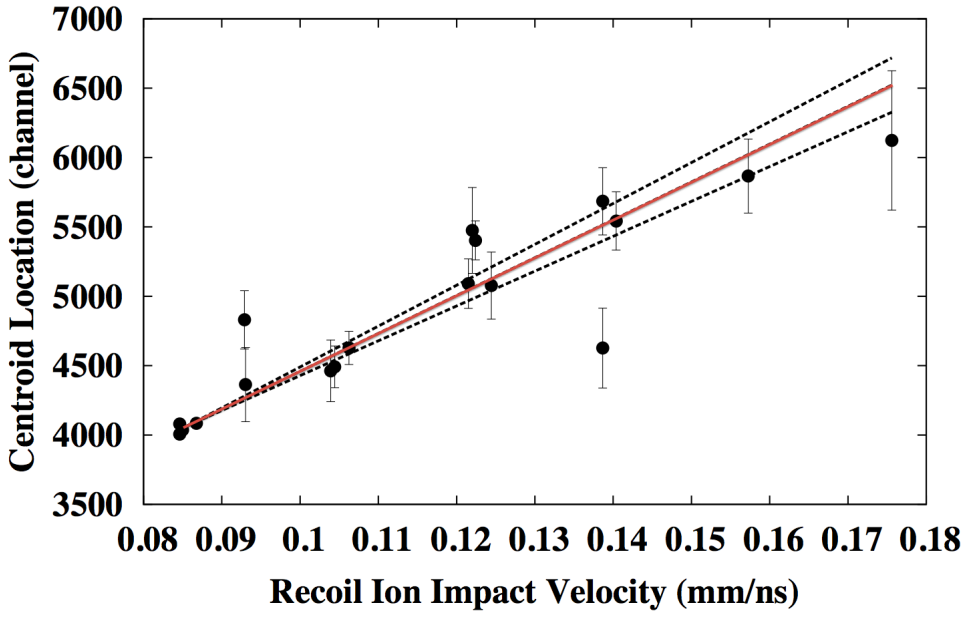

(b) Right MCP.

Figure 5.19: Linear fit to the centroid values of the the MCP PHD of pixel 11 vs. ion impact velocity. The data include fast and slow ion data from multiple isotopes, split into equal bin width of ion impact velocity. The data points around ion impact velocity of 0.085 mm/ns represent slow-ion data (hence their small uncertainties due to the large available statistics).

Top MCP

Pixel	Threshold	Relative Amplitude	Relative μ	σ	σ_{2+}
11	1095	1.0	1.0	518.985	485.91
12	915	0.606	0.763	400.559	381.899
13	875	1.048	1.015	599.509	576.640
14	755	0.799	0.675	515.726	502.958
21	885	0.650	0.716	430.899	410.753
22	1065	0.972	0.980	497.150	464.835
23	705	0.714	0.657	447.009	431.876
24	855	1.077	1.030	631.819	605.832
31	845	1.190	1.202	861.185	839.113
32	715	0.849	1.221	841.279	818.464
33	1095	1.096	1.078	621.275	591.189
34	935	0.865	0.860	565.768	545.761
41	765	0.830	0.643	580.544	571.117
42	925	1.105	1.055	800.806	780.730
43	915	0.674	0.724	418.544	400.136
44	1085	1.114	0.944	574.931	549.793

Table 5.4: Top MCP values used for fitting each pixel PHD with a single Gaussian which represents sum of three Gaussians for charge states 2^+, 3^+ and 4^+. Relative amplitude and μ are relative to pixel 11. Last column has values for σ of a Gaussian for charge state 2^+.

Right MCP					
Pixel	Threshold	Relative Amplitude	Relative μ	σ	σ_{2+}
11	945	1.0	1.0	1489.26	1435.69
12	945	0.679	0.579	905.060	869.95
13	845	0.995	1.077	1723.68	1665.94
14	775	0.741	0.545	1081.38	1052.38
21	875	0.701	0.897	1414.93	1362.6
22	925	0.999	1.181	1779.90	1726.95
23	705	0.684	1.075	1775.98	1728.23
24	785	0.982	1.371	2210.07	2136.33
31	795	0.934	1.667	2744.00	2665.99
32	755	0.701	0.979	1764.58	1716.45
33	975	0.986	1.161	1907.30	1844.26
34	915	0.637	0.650	1055.32	1018.66
41	705	0.653	1.301	2533.36	2469.06
42	775	0.821	1.825	3053.69	2963.48
43	865	0.680	0.974	1639.62	1589.89
44	925	0.896	1.273	1917.23	1864.18

Table 5.5: Right MCP values used for fitting each pixel PHD with a single Gaussian which represents sum of three Gaussians for charge states 2^+, 3^+ and 4^+. Relative amplitude and μ are relative to pixel 11. Last column has values for σ of a Gaussian for charge state 2^+.

5.4.4 Correction for events below the threshold

The fraction of the Gaussian below threshold calculated in the previous section does not take into account that there remain entries below the threshold due to the slow roll-off of the discriminator. In order to take these entires into account, which increases the efficiency, an algebraic manipulation is performed that takes into account the entries recorded and the areas calculated from the fits. Applying the correction value C_{val} to the fraction yields formula for the efficiency:

$$\varepsilon = C_{val} \times f = \left(1 + \frac{B}{f}\right) \times f \tag{5.14}$$

where f is the area of Gaussian fit above the threshold calculated using Eq. 5.8 and B is the entries below the threshold. The entries below the threshold can be modeled by studying the slow ion data, also per pixel, as was done with the PHD above the threshold. Plotting the ratio of the data to the Gaussian fit below the threshold can illuminate any trends that could then be generalized in full efficiency description. Due to gain that is about a factor of three higher, the correction to Right detector's efficiency is much smaller than the Top detector's, and hence the treatment of the entries below threshold is simplified. The correction to the Top detector efficiency can be quite large and hence requires more detailed modeling described further in this subchapter.

Correcting Top MCP

Data from each pixel from ^{137}I dataset cut on slow ions and its corresponding Gaussian are used to produce the ratio plots. Ratio of data to fit below threshold for pixel 24 is shown in Fig. 5.20.

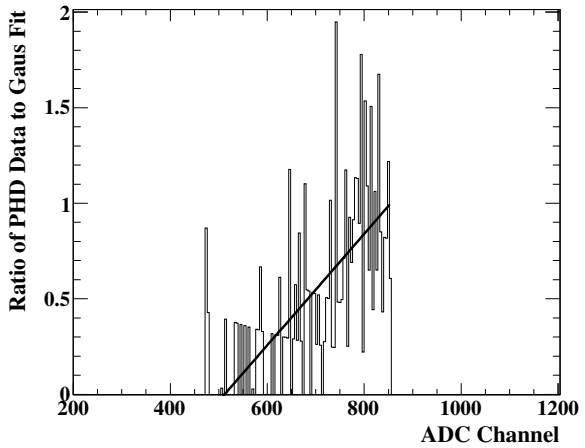

Figure 5.20: Modeling correction for entries below threshold for pixel 24. Only data below the threshold is plotted.

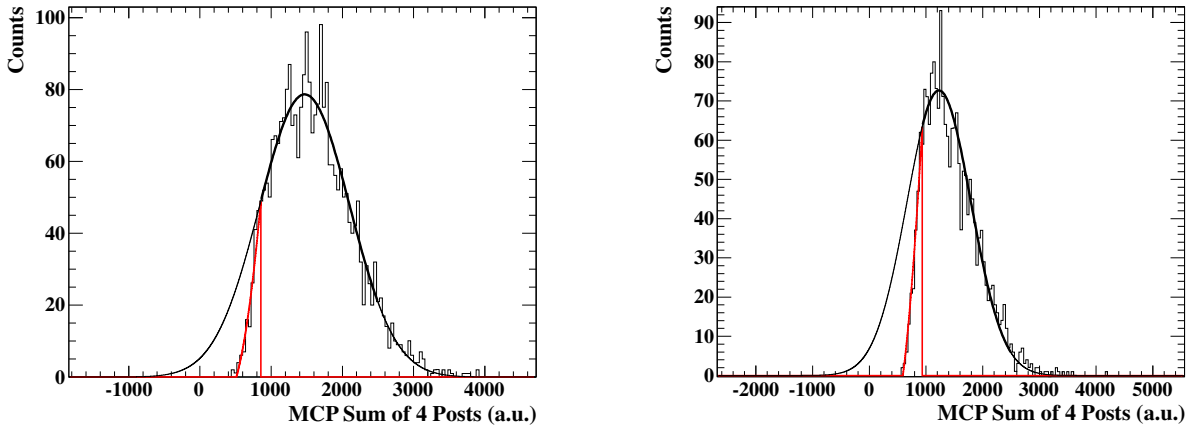

(a) Pixel 24 (b) Pixel 34

Figure 5.21: Fit to Top MCP PHD and corresponding correction below threshold calculated using Eq. 5.15, marked in red.

A linear fit is applied to each ratio, revealing that the slope is nearly the same in all cases, and hence set to 0.002915599. The corresponding intercepts of the linear fit were found for each pixel: -2.19258, -1.66777, -1.55115, -1.20128, -1.58031, -2.10511, -1.0555, -1.49284, -1.46368, -1.08465, -2.19258, -1.72609, -1.23043, -1.69693, -1.66777, -2.16342 (listed in the same pixel order as in Table 5.4).

Entries below threshold can be analytically calculated by taking the value of the Gaussian fit (function g for pixel i) at each bin x, and multiplying by the corresponding value found with the linear function at that bin $(m_i x + b_i)$:

$$B = \sum_{x=0}^{threshold} = g_i(x) \times (m_i x + b_i). \tag{5.15}$$

The entries are calculated until threshold for that pixel is reached. Fit to ^{137}I slow ion data for pixels 24 and 34, which includes analytically calculated correction for entries below threshold, is shown in Fig. 5.21. In the code, this correction was tabulated for several ion impact velocities at all the pixels, and interpolated during efficiency calculation.

Correcting Right MCP

There are relatively few entries below threshold for the Right MCP. Instead of following the procedure outlined for Top MCP above, the ratio of total entries below threshold to the Gaussian area below threshold was found for all pixels instead of a using a linear relationship. The resulting correction is sufficiently small that a more complex procedure (as was used to the Top MCP correction) would yield the same answer within statistical uncertainties. The average value of the ratio R of total entries below threshold to the Gaussian area below

threshold is 0.125 ± 0.065. The correction value is then calculated with:

$$C_{val} = 1 + \left(\frac{R \times (1 - f)}{f} \right) \tag{5.16}$$

Characterizing corrections for Top and Right MCP were found for PHD of slow ions, which in reality consists of a sum of PHD's from several charge states. However, the correction calculation is valid for any charge state PHD individually. This was confirmed by calculating correction for each charge state separately, summing them up, and comparing the number to the number obtained from data.

5.4.5 MCP efficiency results

Putting together the pieces of the analysis, it is possible to calculate MCP efficiency for any ion impact velocity at any position of the MCP. The code calculating the efficiency is implemented by using bilinear interpolation over the MCP area at a specific ion impact velocity. Interpolation occurs over four points surrounding the impact position corresponding to the centers of the pixels used in analysis. For areas at the edge of the MCP, beyond the centers of the edge pixels, a linear extrapolation is used. In this case, it is assumed that the efficiency will follow a linear trend from two preceding pixels, extending from the center of the MCP. For the corners, the value is extrapolated over the preceding diagonal pixels. This assumption results in valid average values for the efficiency at the edge pixels.

The efficiency value at each pixel is calculated for the specified ion impact velocity (given directly in the simulation). Using Eq. 5.10 or Eq. 5.11, and multiplying the result by the relative μ value given in Table 5.4 or Table 5.5, one obtains a parameter x. The x parameter is related to the PHD Gaussian centroid μ via Eq. 5.12 or Eq. 5.13. This μ value is then used in Eq. 5.8, together with the proper threshold and σ_{2+} values listed for each pixel in Table 5.4 or Table 5.5. The value calculated with Eq. 5.8 is then corrected as was described with Eq. 5.14, Eq. 5.15, and Eq. 5.16.

Following the procedure outlined in this section, efficiency values were tabulated for impact velocities in the range of 0.07 to 0.22 mm/ns. The resultant efficiency curves are drawn in Fig. 5.22 and Fig. 5.23. From these figures, it is evident that the Right MCP, as expected from data, is quite a bit more efficient (efficiency above 90%) than the Top MCP (below 70% at lowest efficiency pixel for slow ions). The result of interpolating the efficiencies at low ion impact velocity for ^{137}I is mapped out in Fig. 5.24.
MCP Efficiency correction is applied to the simulation output, event by event, and wrapped up into the $\omega_{\beta r}$ and $\omega_{\beta R}$ values.

5.5 Neutron-recoil coincidence correction

Neutrons emitted in the decay may trigger the plastic detectors at 180° from the MCP, and hence can be mistaken as a coincidence between β and a recoil ion in the fast TOF range.

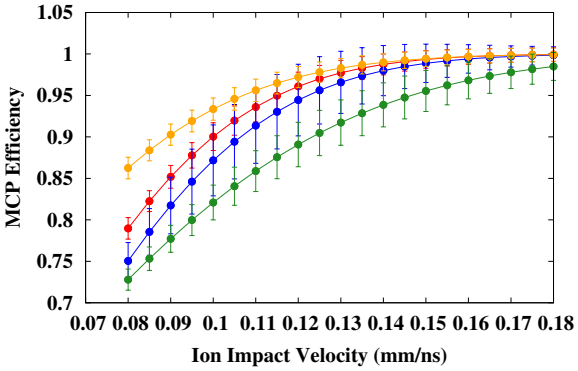

(a) Pixels 11 (red), 12 (blue), 13 (orange), 14 (green)

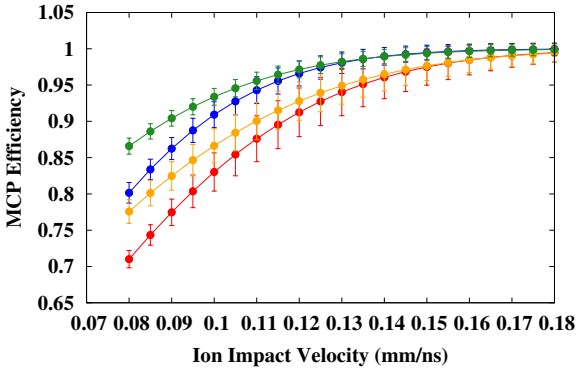

(b) Pixels 21 (red), 22 (blue), 23 (orange), 24 (green)

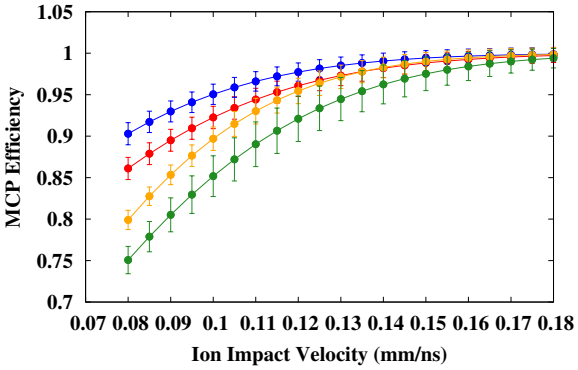

(c) Pixels 31 (red), 32 (blue), 33 (orange), 34 (green)

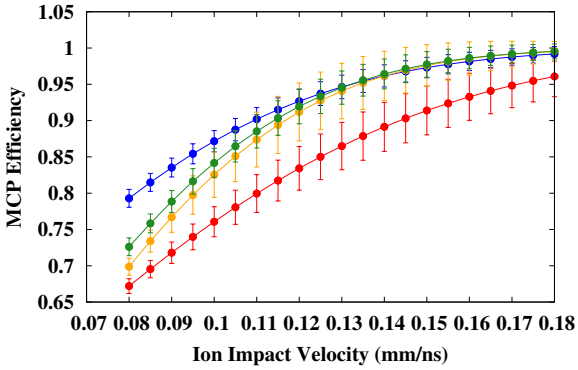

(d) Pixels 41 (red), 42 (blue), 43 (orange), 44 (green)

Figure 5.22: Tabulated efficiency curves for Top MCP, per pixel.

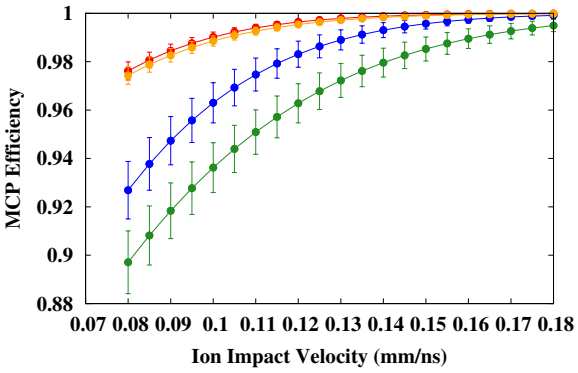

(a) Pixels 11 (red), 12 (blue), 13 (orange), 14 (green)

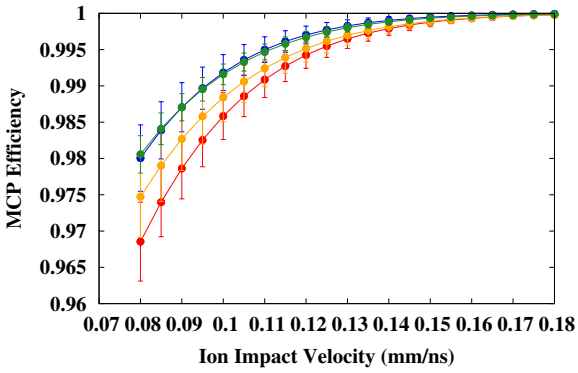

(b) Pixels 21 (red), 22 (blue), 23 (orange), 24 (green)

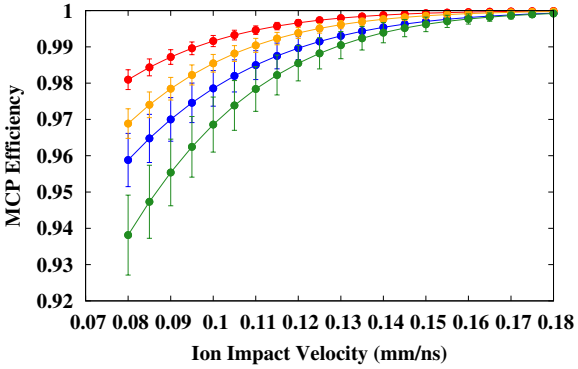

(c) Pixels 31 (red), 32 (blue), 33 (orange), 34 (green)

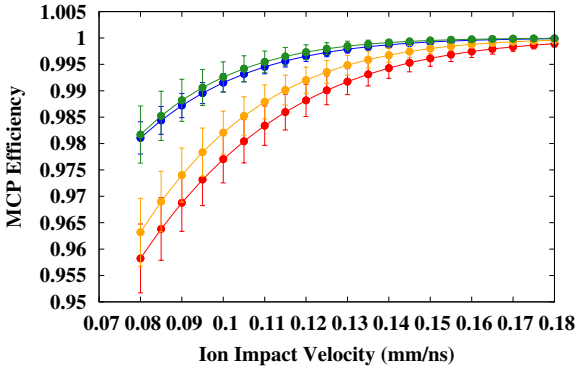

(d) Pixels 41 (red), 42 (blue), 43 (orange), 44 (green)

Figure 5.23: Tabulated efficiency curves for Right MCP, per pixel.

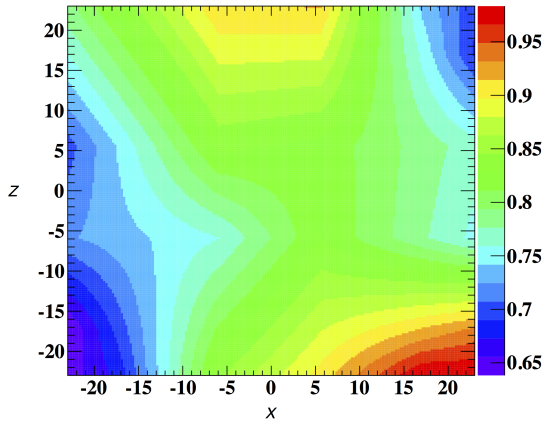

(a) Top MCP

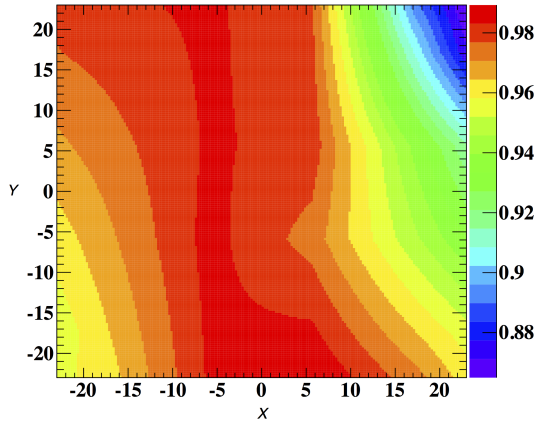

(b) Right MCP

Figure 5.24: Map of MCP efficiency response at slow ion impact velocity for ^{137}I (0.08 mm/ns). Map coordinates are the global coordinates used in the simulations.

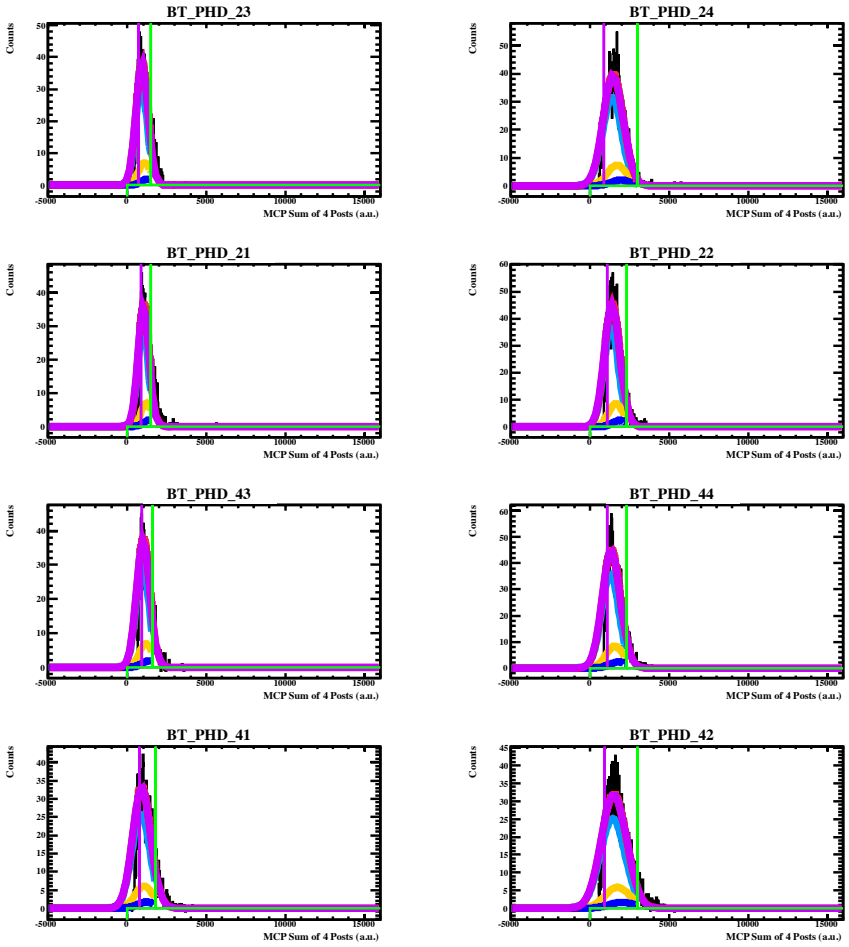

Figure 5.25: Slow ion fits for pixels in quadrants 2 and 4 of the Top MCP for the ^{137}I.07 dataset.

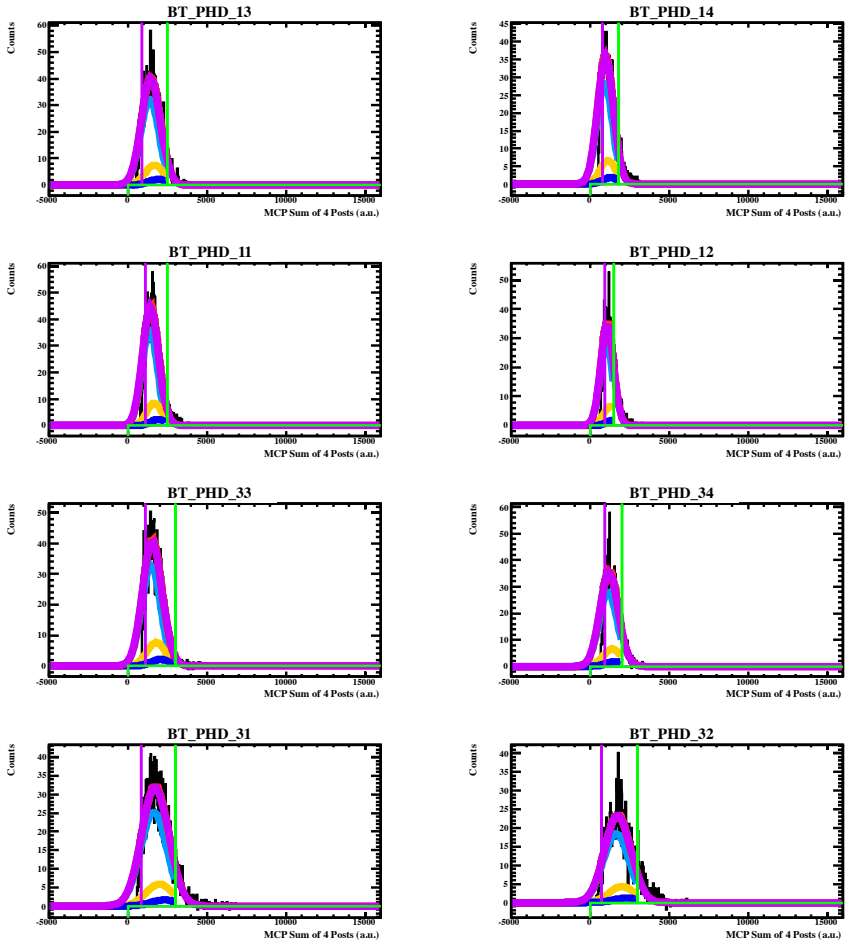

Figure 5.26: Pixels in quadrants 1 and 3.

Figure 5.27: Slow ion fits for pixels in quadrants 1 and 3 of the Top MCP for the ^{137}I.07 dataset.

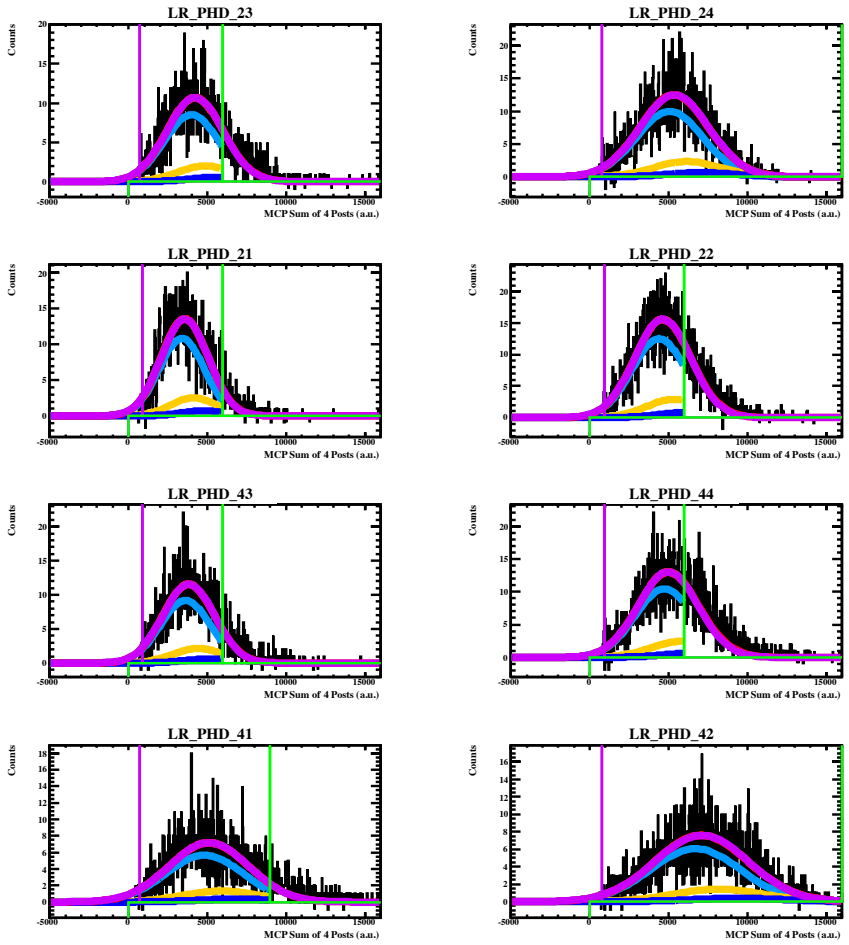

Figure 5.28: Slow ion fits for pixels in quadrants 2 and 4 of the Right MCP for the ^{137}I.07 dataset.

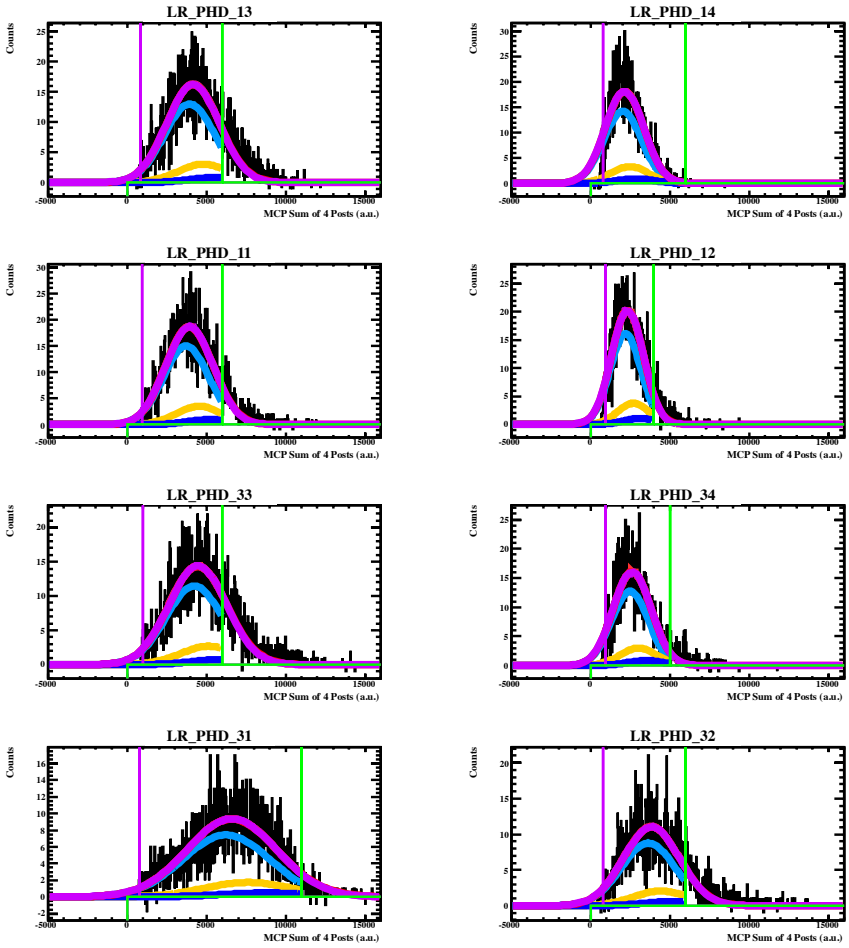

Figure 5.29: Pixels in quadrants 1 and 3.

Figure 5.30: Slow ion fits for pixels in quadrants 1 and 3 of the Right MCP for the ^{137}I.07 dataset.

These events are defined as neutron-recoil coincidences, or N_{nR}. Since the absolute efficiency of these events is not well known, it is easiest to correct the detected coincidences at 180° detector combination by a correction factor to obtain the number of true β and recoil ion coincidences, or $N_{\beta R}$. Ignoring the effects due to conversion electrons and γ-rays on the plastic detectors, one can define the total detected coincidences in the 180° Plastic-MCP detector combination as a sum of the $N_{\beta R}$ and N_{nR} coincidences, defined here as "doubles", or N_D. Therefore, the correction due to neutrons, or C_n, can be defined as the number by which the detected coincidences N_D are divided to extract $N_{\beta R}$:

$$C_n = \frac{N_{\beta R} + N_{nR}}{N_{\beta R}} = 1 + \frac{N_{nR}}{N_{\beta R}}. \tag{5.17}$$

In this chapter I describe the methodology for determining the C_n correction factor with simulations and available data.

5.5.1 Response of the plastic scintillator to neutrons

A charged particle passing through an organic scintillator produces flourescent light by exciting molecules along its path. For electrons above 125 keV, the light yield increases linearly with the initial particle energy [73]. For heavier charged particles, such as protons, the light yield is always smaller than that for electrons due to quenching resulting from higher ionization along the particle's path [62]. Since the plastic response to neutrons is mediated through proton recoil, we expect the resulting light yield from a recoil proton to be smaller than for the same energy deposited due to a β particle. Fig. 5.31 shows the scintillator response to electrons vs. protons. Although the data is plotted for the NE-102 scintillator, the ratio of the response is similar for different kinds of scintillators [62].

Using this ratio from the data given in [74], one can calculate the equivalent proton recoil energy that would be necessary to produce the same light output as the electron at a specific energy. This comparison is plotted in Fig. 5.32. If a neutron were to transfer all of its energy into the proton, it would still need an initial energy of at least 200 keV to produce the same light output as an electron at 60 keV.

The electronic threshold for the β's which was determined to be 76 keV (left ΔE) and 62 keV (bottom ΔE) corresponds to roughly $\sim$350 keV and $\sim$200 keV, respectively. This derivation serves only as an estimate, however, and more detailed analysis was performed to obtain the neutron detection threshold value, as is described later in this section.

In the simulation, Geant4 lists energy deposition due to each particle interacting within the detector material. To correctly infer simulation results, a threshold needs to be applied in the analysis of the simulation data. Since the neutron detection threshold has not been measured directly, an approach consisting of iteratively comparing data to simulation at varying thresholds can offer an insight into this value.

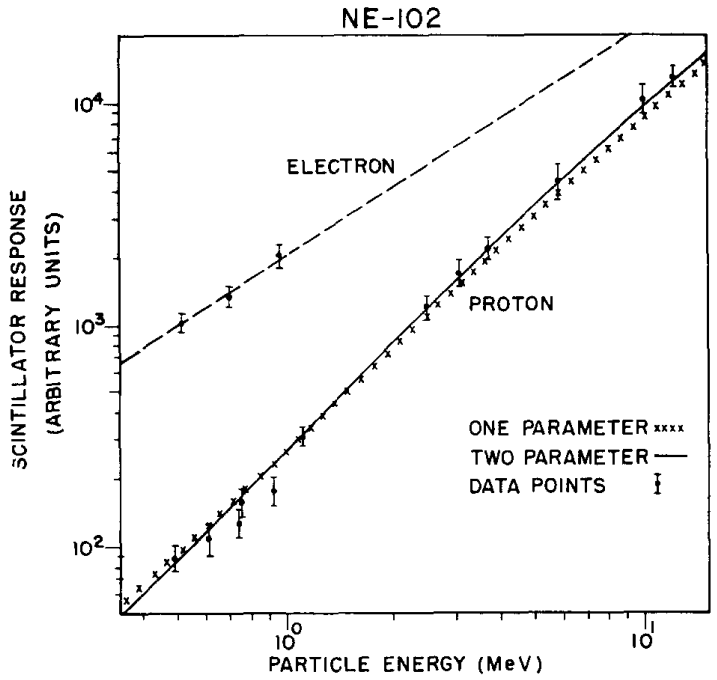

Figure 5.31: Scintillator response for electron and proton recoils, adapted from [74].

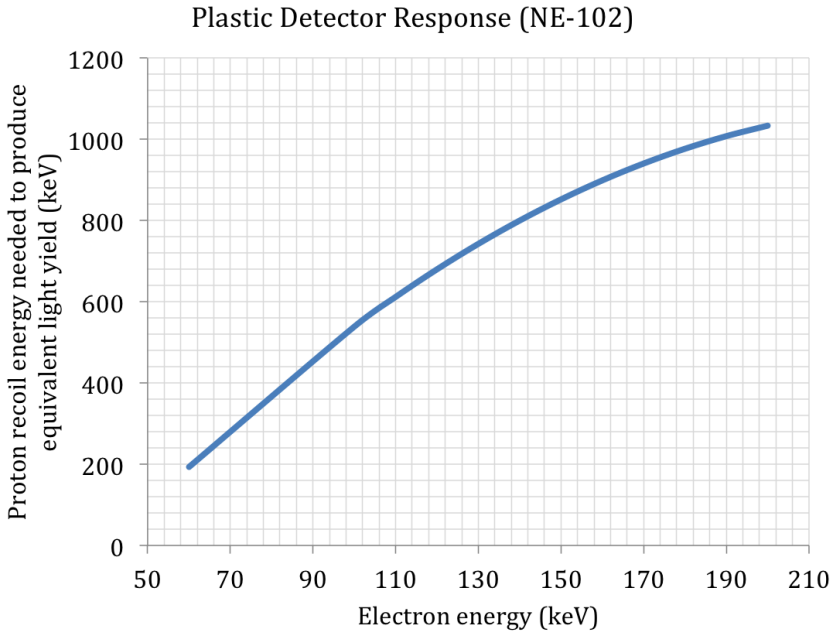

Figure 5.32: Comparison of particle energies inducing equivalent light output in a plastic scintillator, using data from [74].

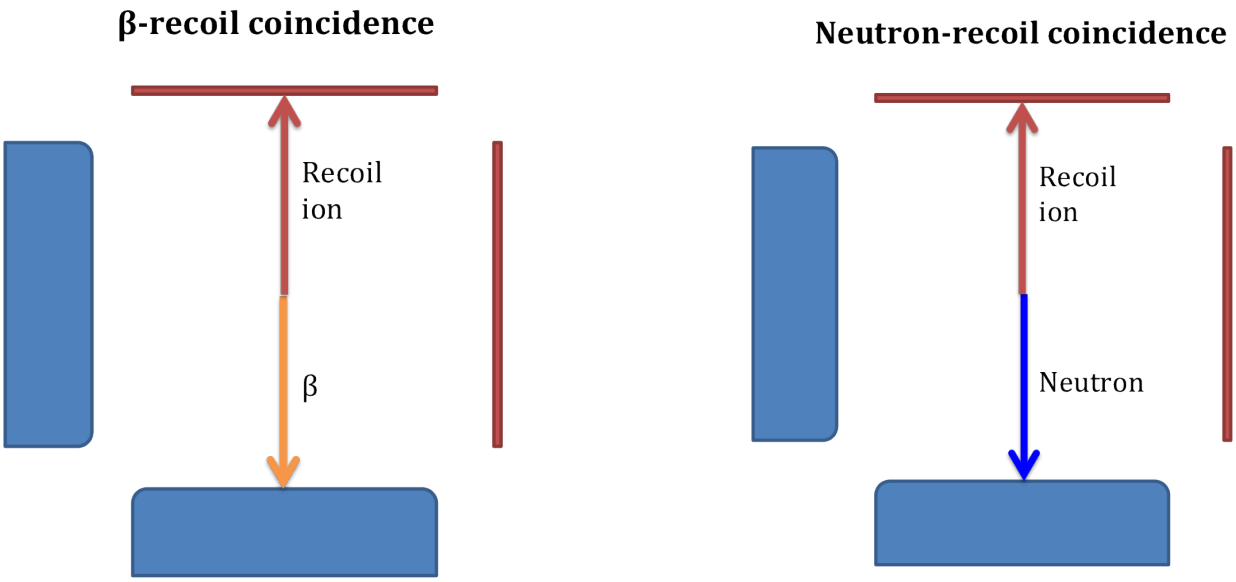

(a) β-recoil coincidence, $N_{\beta R}$

(b) Neutron-recoil coincidence, N_{nR}

Figure 5.33: Diagrams illustrating coincidences in the experimental detector setup, not drawn to scale.

5.5.2 Determining the neutron detection threshold

Comparison of data to the simulation can provide constraints on the threshold. However, it is difficult to separate out pure neutron-recoil contribution from the dataset, since both β-recoil and neutron-recoils can produce pulses of the same height. The only way to extract the neutron events is to look at the triple coincidences between the two plastic detectors and an MCP detector.

Fig. 5.33 demonstrates the various situations where either neutron or β trigger the plastic detector in coincidence with a recoil. In a triple coincidence, β triggers one plastic, a neutron trigger the other plastic detector, and both are in coincidence with a recoil ion detected by the MCP at 180° from the neutron-triggered plastic (shown in Fig. 5.34). Since neutrons nearly exclusively will trigger the plastic detector at 180° from the MCP, one may assume with high certainty that the coinciding trigger in the other plastic detector at 90° from the MCP is a β-particle associated with the same decay event. Furthermore, the 90° combination is not dependent upon any kinematic focusing effects. Therefore, the ratio of the triple coincidences to the β-recoils at 90° gives a good estimate of the neutron detection efficiency, only dependent upon neutron energy distribution and the neutron energy threshold in the plastic detector:

$$\varepsilon_n \approx \frac{N_{\beta nR}}{N_{\beta R}^{90}}. \tag{5.18}$$

The triple coincidences extracted from the data also take into account a timing difference

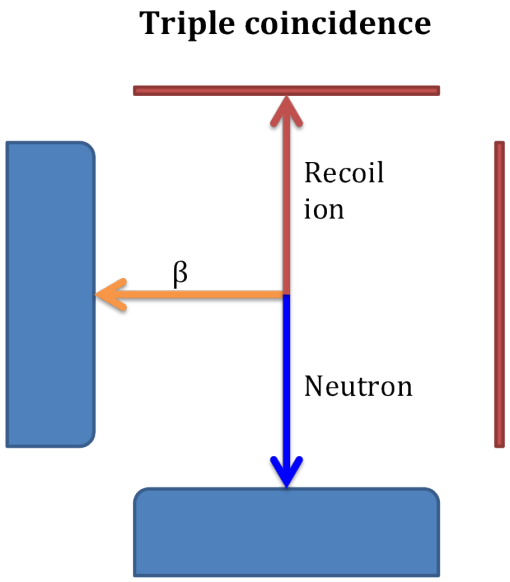

Figure 5.34: Triple coincidence for the recoil ion triggering the top MCP, β triggering the left plastic, and neutron triggering the bottom plastic. The alternative configuration would have the recoil ion trigger the right MCP, with β in the bottom plastic and neutron in the left plastic. Not to scale.

cut between the two plastic detectors of -25 ns to 25 ns, so as to minimize contribution from accidental coincidences.

The threshold can therefore be found by comparing the ε_n from the data to the simulated ε_n value at varying neutron detection thresholds in the ΔE. The simulated value also compares the triples to doubles at 90° for consistency. The difference between the data and the simulated value found at various neutron thresholds for ^{137}I is shown in Fig. 5.35. The points are fit with a 3rd degree polynomial to find the threshold value where the difference is zero.

The threshold was found this way for ^{137}I, and both of the ^{138}I datasets, since these isotopes should not have data triples contaminated with conversion electrons. The neutron thresholds found, as well as their weighted average, is shown in Fig. 5.36. Hence, the weighted average of **368(71)** keV is implemented as the neutron threshold used in the simulations across all other isotopes.

Applying the neutron threshold to the simulation enables comparison of the simulation to the data across various observables. Specifically, comparing the simulated 180/90 ratio of fast ion counts can reveal any inconsistencies. The simulated ratio is derived by adding contributions from both the β-recoil and neutron-recoil coincidences, with respective detection thresholds applied. The data ratio is taken by applying time-of-flight cuts characteristic to the fast ion data, and subtracting the accidentals determined from the 15-20 μs time-of-flight region. Fig. 5.37 illustrates the comparison of the 180/90 ratios. The uncertainty in the data is simply calculated from the counting statistics. In the case of the simulated values, the

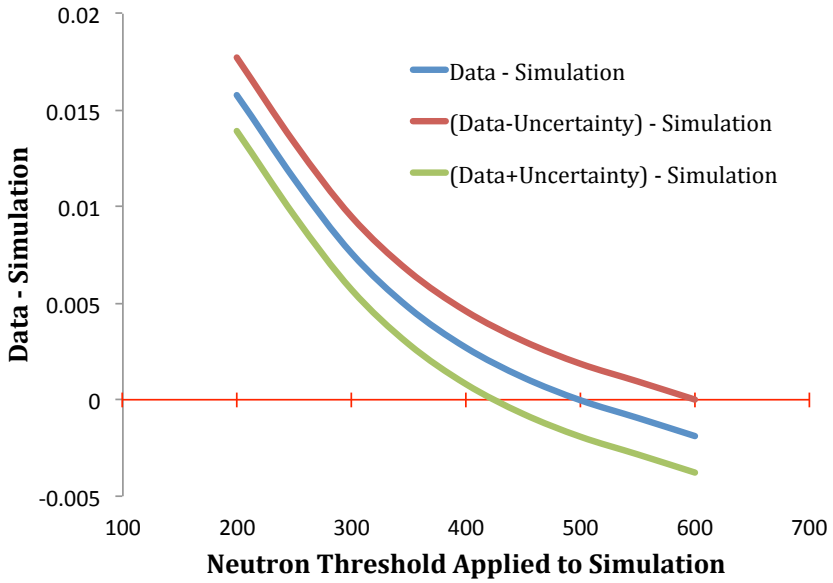

Figure 5.35: Difference between ε_n found in data and simulation

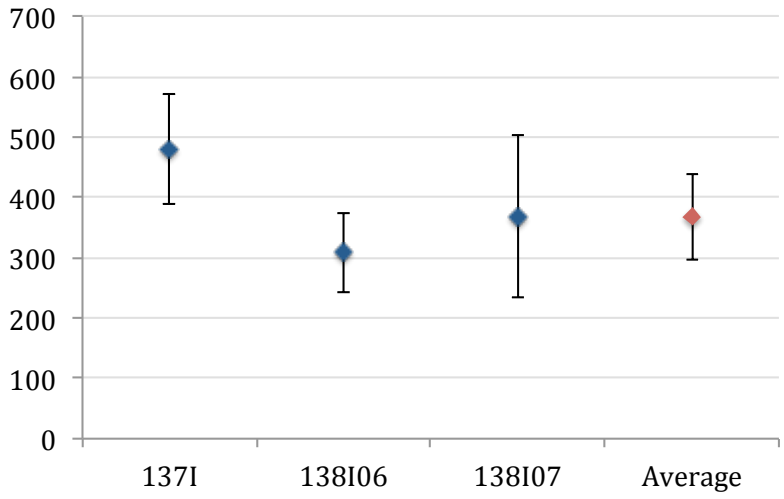

Figure 5.36: Neutron thresholds found for various isotopes

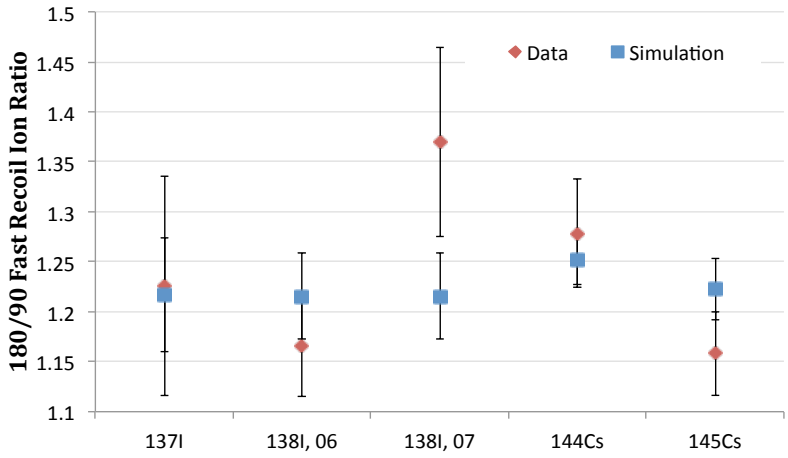

Figure 5.37: Comparison of the data and simulation for the 180/90 detector combination of the fast ion counts

applied neutron threshold is varied between its uncertainty values, producing bounds from the simulated 180/90 ratio value. The simulated ratio values are in good agreement with the observed ratios for all the isotope datasets, with the exception of 138I07, where there is a 1.5σ difference.

In addition to the detector response, the accuracy of the simulated 180/90 ratio also depends on the effects of the kinematic focusing and details of the decay scheme. These details are not completely known for all the isotopes studied in this work, and hence the comparison to data should be treated as approximate. However, given the observed good agreement for the well-studied ^{137}I dataset gives confidence to the determined neutron detection threshold.

5.5.3 Determining C_n

The value of C_n can either be determined directly from the simulation using Eq. 5.17 and the proper neutron threshold, or from data by substituting the N_{nR}^{180} with observable values:

$$N_{nR}^{180} = \varepsilon_n N_R = \varepsilon_n \left(\frac{N_{\beta R}^{180}}{\omega_\beta \Omega_\beta} \right), \tag{5.19}$$

where $\omega_\beta \Omega_\beta$ product is the detection efficiency of the plastic detector to β particles associated with fast ions (determined with simulations), and ε_n is determined from triple coincidences as discussed in Eq. 5.18. Combining these results into Eq. 5.17 yields the following equation for C_n calculated using the triples data:

$$C_n^{Triples} = 1 + \frac{N_{nR}^{180}}{N_{\beta R}^{180}} = 1 + \frac{\varepsilon_n}{\omega_\beta \Omega_\beta}. \tag{5.20}$$

The observed ratio of 180°/90° coincidences reflects the effect due to the β decay kinematics and the contribution from direct neutron detection in the 180° detector combination. I define

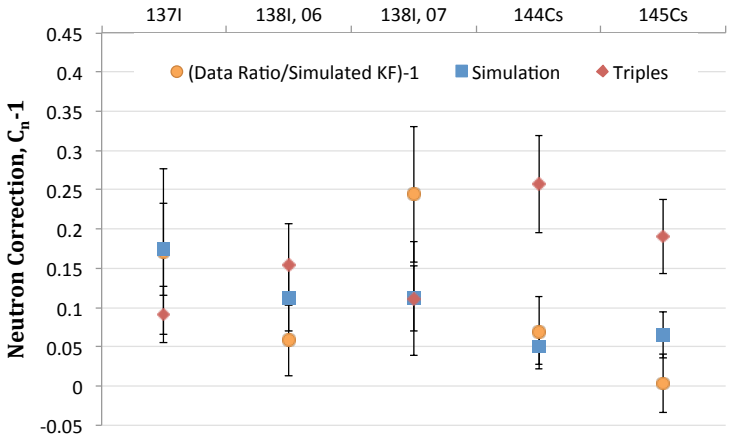

Figure 5.38: Comparison of C_n values obtained with three methods

the "kinematic focusing", K_f, factor that combines the effects of nuclear decay and β-particle kinematics which contribute to $180°/90°$ ratio of β-recoil coincidences greater than 1:

$$K_f = \frac{N_{\beta R}^{180}}{N_{\beta R}^{90}}. \tag{5.21}$$

Substituting the definition of C_n from Eq. 5.17 into this ratio, and assuming that no neutrons are detected in the 90° detector combination so that $N_{\beta R}^{90} = N_D^{90}$, results in the following relation:

$$C_n^{KF} = \frac{N_D^{180}}{N_D^{90}} \times \frac{1}{K_f}. \tag{5.22}$$

Therefore, the observed ratio $180°/90°$ divided by the K_f found in the simulation gives an estimate of the neutron contribution.

A comparison of the neutron correction found directly from the simulation, triples (as in Eq. 5.20) , and 180/90 ratio divided by simulated K_f (as in Eq. 5.22), is shown in Fig. 5.38. For easier comparison, the C_n-1 quantity is plotted instead of C_n. The disagreement of the $C_n^{Triples}$ with both C_n^{KF} and $C_n^{Simulation}$ for ^{144}Cs and ^{145}Cs datasets suggests that the triples data may be contaminated with conversion electrons that increase the ε_n value and hence the $C_n^{Triples}$. Since the other cases show a rather good agreement across the three values, the simulated $C_n^{Simulation}$ value is chosen as the correction applied to data. The resulting simulated $C_n^{Simulation}$ values for each isotope are summarized in Table 5.6.
The variation in C_n values across the different isotopes is due to the differences in the neutron energy distribution (i.e. if higher proportion of neutrons are at higher energies, the C_n is larger), as well as the degree of kinematic focusing. For larger values of kinematic focusing, more data will be affected at the 180° detector combination. The C_n correction is applied through the neutron threshold cut, and hence the differences in the individual C_n values are incorporated in the simulation for each individual isotope.

Isotope	Simulated C_n
^{137}I	1.17(6)
^{138}I	1.11(4)
^{144}Cs	1.05(2)
^{145}Cs	1.06(3)

Table 5.6: Summary of C_n values from simulations ($C_n^{Simulation}$).

The neutron-recoil correction is applied directly to the neutron energy spectrum by incorporating the neutron-detection threshold into the simulations that produce the $\omega_{\beta R}$ value. The neutron-recoil correction applied to neutron energy spectrum is discussed in more detailed in Section 5.6, together with all the other energy spectrum corrections.

5.6 Implementing energy-dependent corrections: deriving the $\omega_{\beta R}$ value

The neutron energy spectrum, obtained from the recoil ion time-of-flight, has to be properly corrected for various energy-dependent detector efficiency effects and contaminating backgrounds, as well as the recoil energy imparted by the leptons. A set of simulations was conducted to characterize these effects for all the isotopes studied. The product of these obtained corrections can be applied to the measured neutron energy spectrum by dividing events in each energy bin by the value of the correction at that energy, or more specifically by dividing the observed events by the $\omega_{\beta R}$ value at that energy. The discussion of the $\omega_{\beta R}$ values can be found in Section 4.2. This $\omega_{\beta R}$ value embodies the fractional change in the shape of the neutron energy spectrum due to various effects beyond the solid angle.

This section describes the corrections to the shape of the energy spectrum resulting from energy-dependent detector efficiency effects. These corrections encompass the MCP efficiency correction and the neutron-recoil coincidences seen in the 180° detector combination, as well as any other detector effects. Whereas the previous sections describe corrections where the background is subtracted or the energies are shifted (due to the lepton recoil correction), in this case the energy spectrum is modified by dividing it by the corrections due to the energy-varying detection efficiency effects, or the $\omega_{\beta R}$ value.

5.6.1 Corrections due to the plastic detector

The electronic threshold of the ΔE scintillator imposes an efficiency limit on the low-energy β-particles associated with high-energy neutron events. Analysis of the calibration data revealed the electronic threshold to be at 76.0±24 keV for the Left ΔE and 62.0±30 keV for the Bottom ΔE. The difference between the neutron energy spectrum produced with a cut

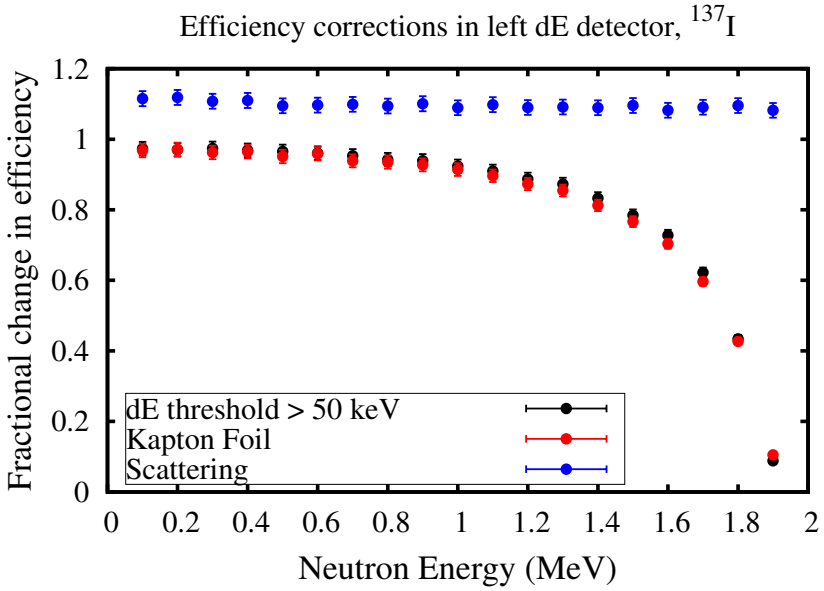

Figure 5.39: Left plastic detector fractional efficiency effects on the neutron energy spectrum for ^{137}I decay. Each effect is studied independently of the other effects (i.e. the effect of adding Kapton foil is determined by keeping the ΔE threshold at 0 and turning off the scattering). The response of the bottom plastic is nearly identical.

of 0 keV and the electronic threshold is shown in Fig. 5.39 (for demonstrative purposes, 50 keV was used as the threshold). The effect is most pronounced for low-energy β-particles, as the efficiency of detecting these events decreases dramatically with the imposed threshold.

The energy loss suffered by the β-particles passing through the thin Kapton window in front of the plastic detector alters the number of measured events. In a separate simulation, Kapton window was completely removed from the Geant4 geometry setup. The number of detected events (without any scattered events) depositing energy in the detector was compared to the events detected with the Kapton window in place. The energy loss through straggling in the Kapton is energy-dependent. Some low-energy β-particles do not make it through the Kapton layer. The overall correction due to the Kapton window is shown in Fig. 5.39.

Scattering of the beta-particles off of the electrodes and other material within the ion trap into the detector can increase the amount of detected events by up to 15%. The effect of the scattering is studied by taking the ratio between the events that have the initial momentum vector pointing within the solid angle of the detector (using 28°, which is larger than the pure solid angle since the ion cloud is not a point), and the number of events that deposit non-zero energy in the detector. The effect, also shown in Fig. 5.39, does not vary largely across the energy spectrum, and overall increases the detection efficiency, as β-particles are scattered into the detector.

The overall influence of each ΔE plastic detector on the energy spectrum of ^{137}I is shown

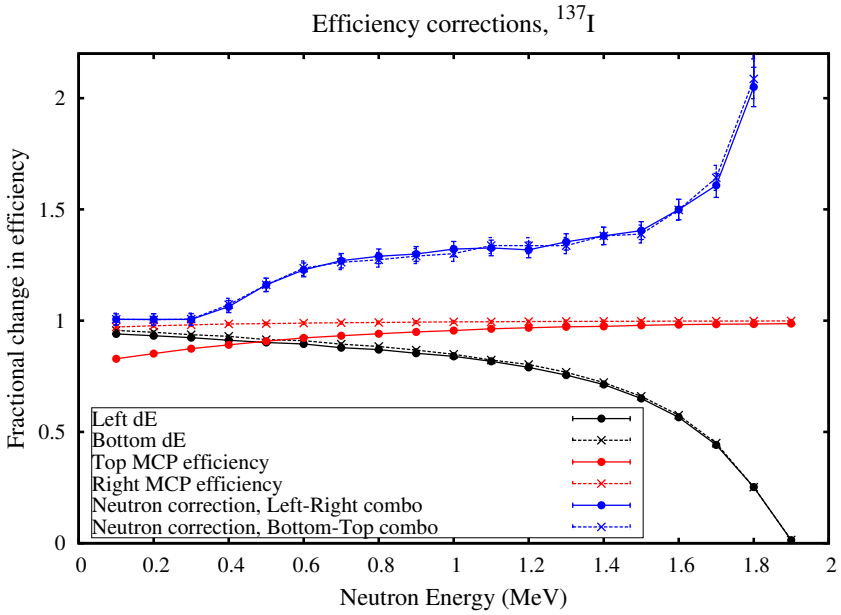

Figure 5.40: Fractional corrections to the neutron energy spectrum of ^{137}I due to detector effects.

in Fig. 5.40. The effect of the plastic detector for other isotopes follows a similar shape.

5.6.2 Applying the MCP detection efficiency effects

As was described in 5.4, the MCP efficiency depends on the impact velocity of the detected recoil ion, as well as the location of the event on the MCP. The effects of applying the MCP efficiency correction on the neutron energy spectrum are probed by taking a ratio of the spectrum simulated without the correction to the spectrum with the efficiency correction applied, on event-by-event basis. Since the detection efficiency of the Top MCP is ∼30% lower at low recoil ion energies (corresponding to low neutron energies), the correction for that detector is more pronounced than that of the Right MCP in that energy region, as shown in Fig. 5.40.

5.6.3 Correction due to neutrons triggering the plastic detector

Accounting for the detected neutrons can amount to up to a ∼15% correction for the ΔE-MCP detector pair separated by 180°. The threshold for detecting the neutrons in the plastic detector has been found to be around 360 keV, as described in more detail in Section 5.5. Applying this energy threshold cut to the simulation yields the correction curve shown in Fig. 5.40. This correction only applies to the Left ΔE-Right MCP and Bottom ΔE-Top MCP detector combinations of the ΔE plastic scintillator and the MCP.

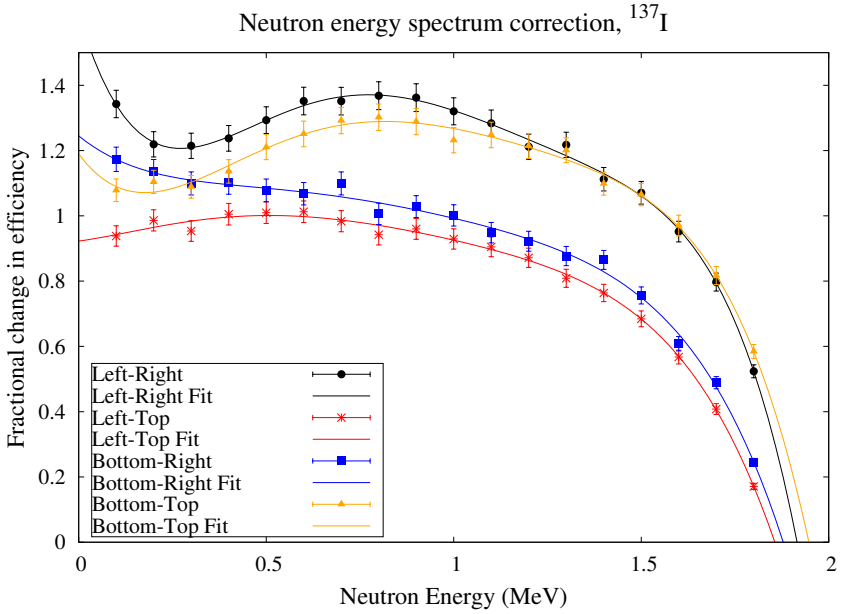

Figure 5.41: Total fractional corrections to the neutron energy spectrum of ^{137}I

5.6.4 Summary of the $\omega_{\beta R}$ corrections

Fig. 5.41 shows the total correction for each ΔE-MCP detector combination for the ^{137}I decay. The total curve is a product of the previously mentioned effects, and also includes any effects due to the kinematic focusing or electric fields of the MCP on the recoil ions. The total curve is constructed by drawing a mono energetic neutron energy spectrum with all the relevant cuts applied, and comparing it to the spectrum produced without the cuts. The resulting total correction is then fit with a 5th degree polynomial. The fits are also shown in Fig. 5.41. The largest discrepancy between the detector combinations results from the neutron correction at 180° (for the left-right and bottom-top), and the MCP efficiency correction being much larger for the Top MCP (especially at lower neutron energies). The corrections for the rest of the isotopes are shown in Fig. 5.42, 5.43, and 5.44.

5.7 Corrected neutron energy spectra

To sum up the procedure outlined in the preceding sections, the following steps are taken to arrive at the neutron energy spectra:

1. At each detector combination, the flat accidental background is subtracted from the neutron energy spectrum produced by the sort code.

2. The background at low-TOF is subtracted using a proper scaling.

3. Lepton correction is applied to the data from the 180° detector combination.

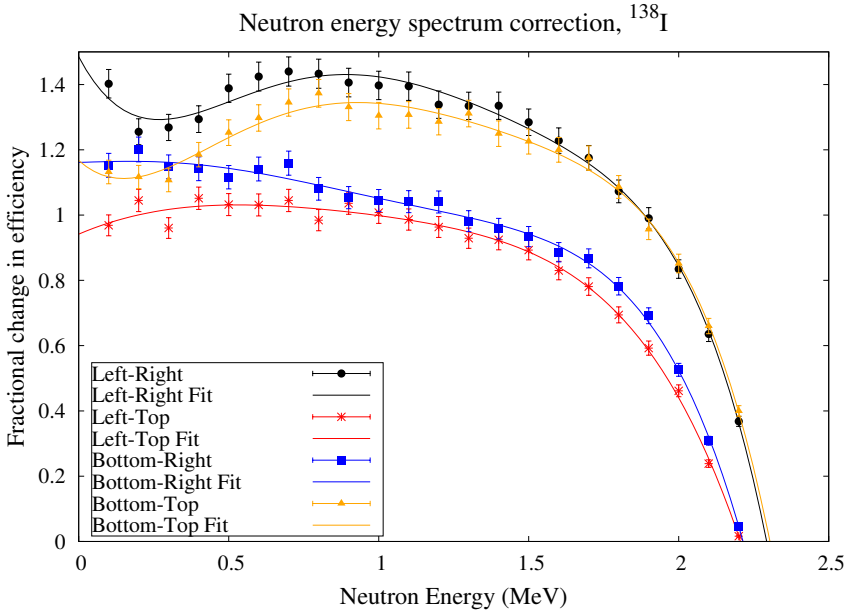

Figure 5.42: Total fractional corrections to the neutron energy spectrum of ^{138}I

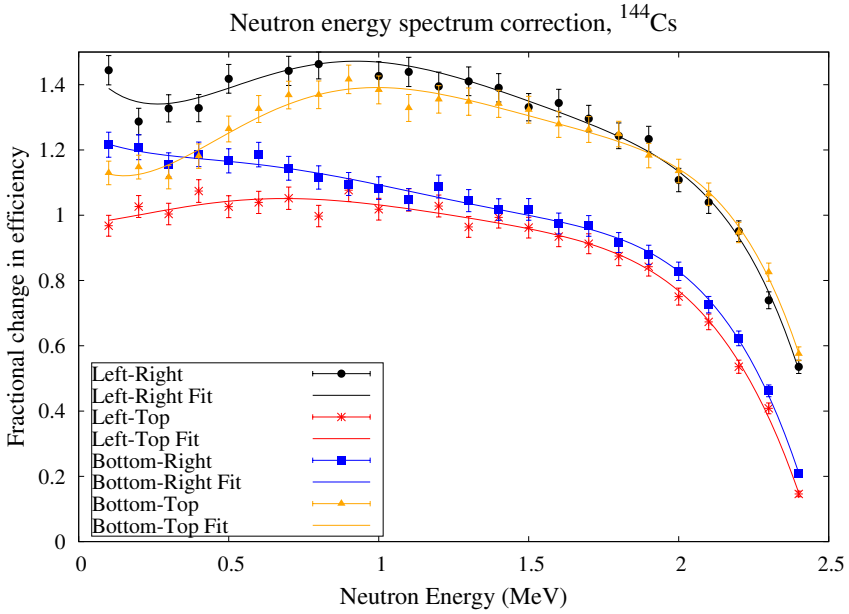

Figure 5.43: Total fractional corrections to the neutron energy spectrum of ^{144}Cs

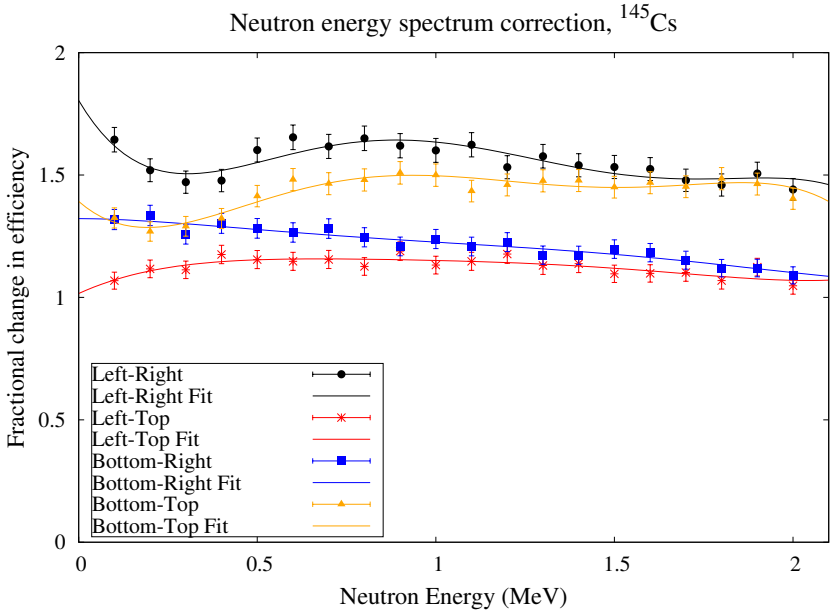

Figure 5.44: Total fractional corrections to the neutron energy spectrum of ^{145}Cs

4. The total efficiency correction is applied to the neutron energy spectrum by dividing the counts in each energy bin by the correction derived from the $\omega_{\beta R}$ curve as a function of energy, fit to a polynomial.

5. Neutron energy spectra obtained for each of the four detector combinations are added up to yield the total neutron energy spectrum for that isotope.

As is shown in Fig. 5.45, the resolution varies with energy from 30-keV to 270-keV FWHM (10%-50%). Therefore, a 10-keV bin size was chosen as an average value across all bins so as to reflect the energy resolution, yet kept small enough to illustrate the structure within the spectrum.

The resulting spectra are also used to count the fast-recoils associated with neutron events by counting between 100-keV and the upper energy cut for each isotope. The spectra are shown in Figures: 5.46, 5.47, 5.48, and 5.49. The spectra are compared to neutron spectra obtained from literature, measured with ^{3}He ionization chambers in the case of ^{137}I [21] and ^{138}I [48], and with proportional counters in the case of $^{144-145}$Cs [28]. The literature spectra are scaled to match the data.

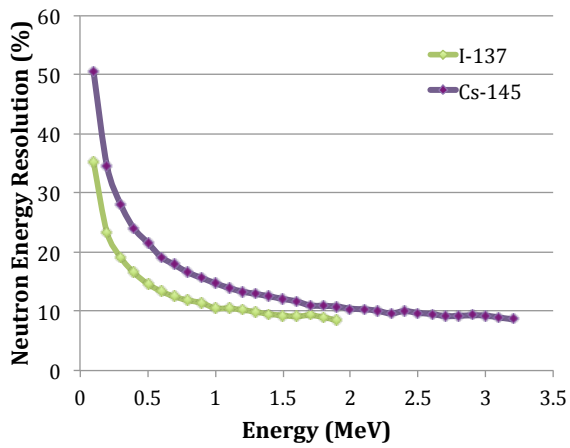

(a) Resolution plotted as a % of neutron energy.

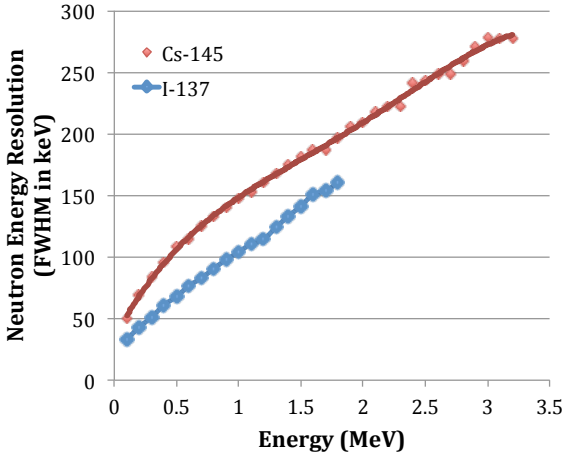

(b) FWHM resolution plotted in keV.

Figure 5.45: Simulated neutron energy resolution achieved with the current experimental setup. The simulation reflects an ion cloud size of 2.5 mm. The figure shows the lightest and heaviest of the isotopes studied in this thesis, with all the other isotopes falling in between the two trend lines.

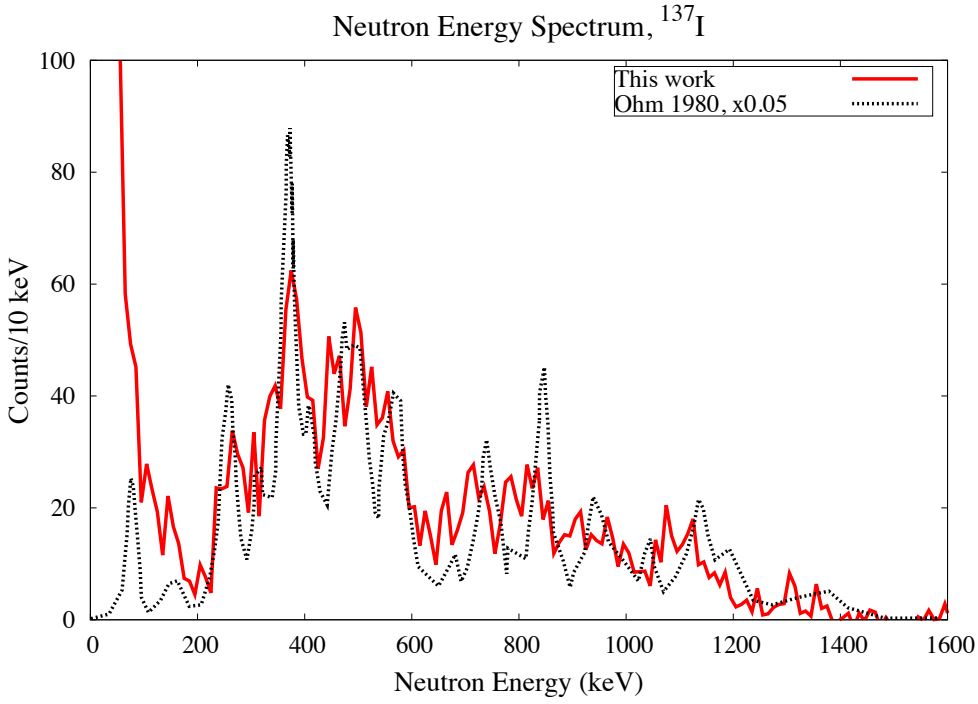

Figure 5.46: Corrected ^{137}I neutron energy spectrum, compared to literature result. Literature spectrum has been scaled down by a factor of 0.05 for easier comparison, and is in arbitrary y-axis units.

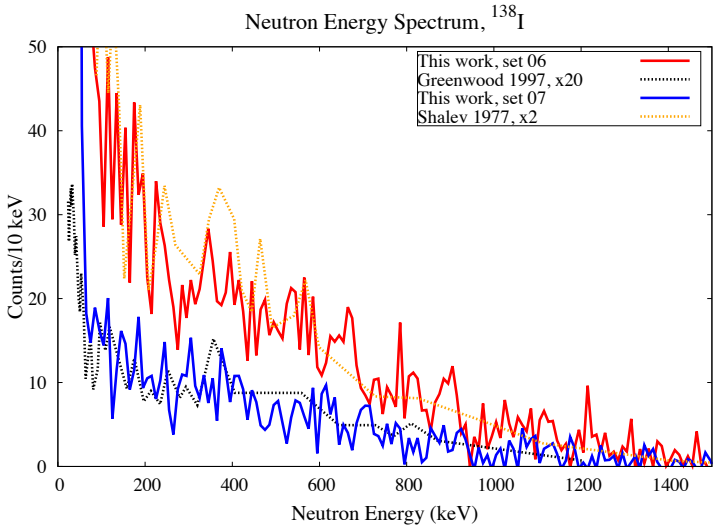

(a) Corrected ^{138}I neutron energy spectra from both datasets taken during this experimental campaign, compared with spectra found in previous literature. Data from set 06 contains about twice as many counts since that run was about twice as long as the 07 run. The two runs differ by their cycle time settings. The literature spectra have been scaled for comparison purposes by numbers indicated on the legend.

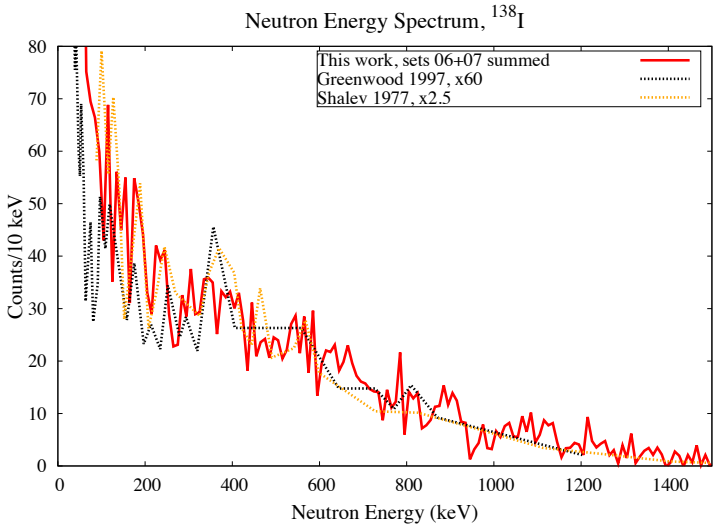

(b) ^{138}I neutron energy spectrum, summed over both 06 and 07 datasets, compared to literature results. The literature spectra have been scaled for comparison.

Figure 5.47

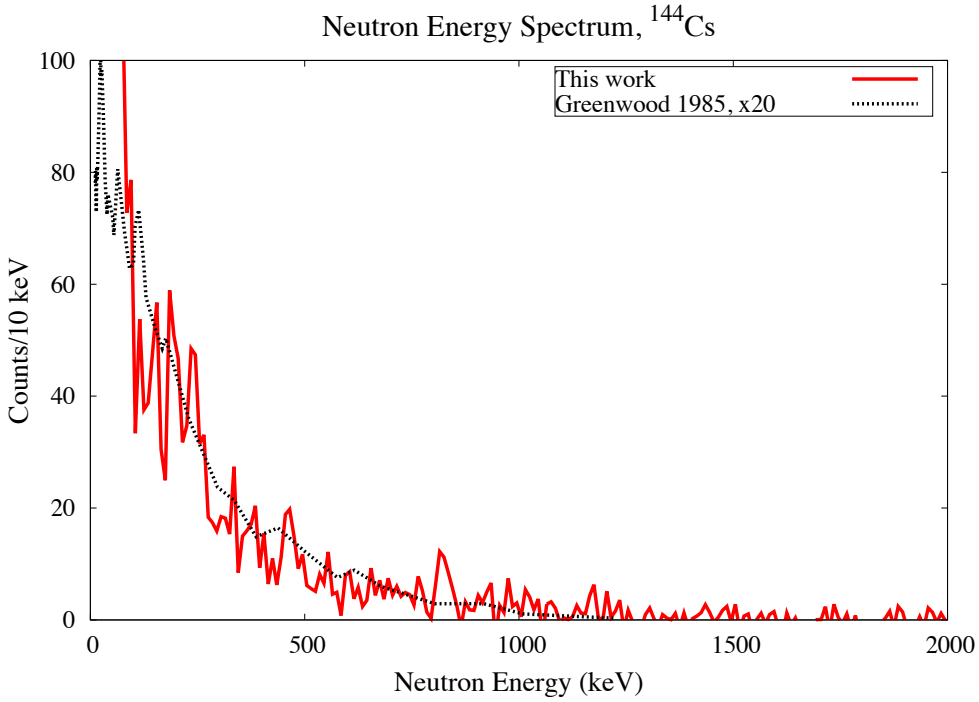

Figure 5.48: Corrected ^{144}Cs neutron energy spectrum, compared to literature result that was scaled by a factor of 20.

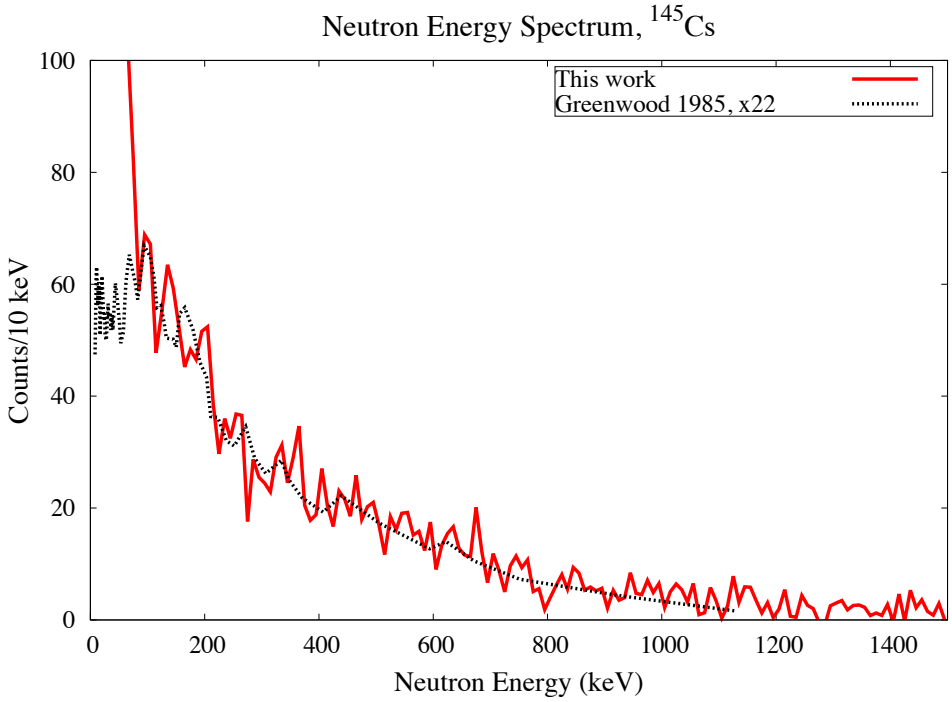

Figure 5.49: Corrected ^{145}Cs neutron energy spectrum, compared to literature result, that was scaled by a factor of 22.

Chapter 6

Deducing the P_n branching ratio values

The detector array in the experimental setup allows for three different methods of determining the branching ratio: (1) by counting the β-singles, (2) by counting the number of β-delayed γ-rays, (3) by counting the recoil ions not associated with the neutron emission (the slow recoils). The different detector combinations and detected observables of the three methods facilitate detailed studies of the systematic effects affecting the branching ratio results.The study of systematic effects relies on analysis of the data under various conditions that can be achieved with the variety of variables recorded: the timing and energy deposition information from each detector, time in measurement cycle, time in RF cycle, CPT beam line data, and the time-of-flight information.

6.1 Overview of the branching ratio measurements

The branching ratio P_n is defined as the fraction of the β decays that result in emitting a neutron: $P_n = \frac{N_{\beta n}}{N_\beta}$, where $N_{\beta n}$ is the number of βn events, and N_β is the number of all β decays. The number of βn events is measured as the plastic-MCP coincidence counts within the appropriate TOF window. The counts observed with the detector setup are related to the total emitted $N_{\beta R}$ events via:

$$n_{\beta R} = N_{\beta R} \cdot \Omega_\beta \cdot \Omega_{MCP} \cdot \varepsilon_{MCP} \cdot \omega_{\beta R} \cdot f, \tag{6.1}$$

where $N_{\beta R}$ is the number of β-delayed neutron decays occurring, $n_{\beta R}$ is the number of observed decays, Ω_β is the solid angle subtended by the plastic detector, Ω_{MCP} is the solid angle subtended by the MCP, and ε_{MCP} is the MCP detector intrinsic efficiencies. To account for our $n_{\beta R}$ measurement threshold equivalent to 100-keV in neutron energy, the f value is defined as the fraction of the neutron spectrum above our detection threshold. The fraction f is obtained from existing literature where a neutron spectrum has been measured. The $\omega_{\beta R}$ factor (described in detail in Section 5.7) encompasses all effects that modify the coincidence efficiency from the solid angle value, such as: intrinsic efficiency of ΔE (ε_β), β and recoil scattering, RF and DC effects on the ion trajectories, relative placement of the

detectors from each other, the effect of the MCP accelerating field on the ions, and the energy-dependent MCP efficiency correction (the relative detection efficiency), described in Section 5.4. The $\omega_{\beta R}$ factor is determined in the simulations for each isotope, and these effects are energy-dependent. The solid angles are listed in Tables 3.5 and 3.6. The MCP intrinsic efficiency is described in Section 4.3. In the proceeding equations, we denote R to represent recoils from β-delayed neutron emission (fast recoil ions), while r denotes the recoils where β decay occurs without neutron emission (slow recoil ions).

6.1.1 Using the number of β-singles

The observed number of β-singles in the plastic detector, n_β, is related to the total number of β decays decays N_β, via:

$$n_\beta = N_\beta \cdot \Omega_\beta \cdot \omega_\beta, \tag{6.2}$$

where in this case ω_β encompasses the modification to solid angle detection efficiency due to scattering and plastic detector threshold effects. The resulting P_n is:

$$P_n^\beta = \frac{n_{\beta R} \cdot \Omega_\beta \cdot \omega_\beta}{n_\beta \cdot \Omega_{MCP} \cdot \varepsilon_{MCP} \cdot \Omega_\beta \cdot \omega_{\beta R} \cdot f} = \frac{n_{\beta R} \cdot \omega_\beta}{n_\beta \cdot \Omega_{MCP} \cdot \varepsilon_{MCP} \cdot \omega_{\beta R} \cdot f}. \tag{6.3}$$

The number of β-singles counted in the plastic has to be corrected for contributions from contaminating isobaric species present in the trap. This is achieved with differing radioactive decay constants between the isotope of interest and its isobaric contaminants. The details of the analysis are discussed in Section 6.3 and the method is described in Section 4.1.2.

6.1.2 Using the ratio of recoil ions

The number of decays can also be obtained from the recoil ion counts observed in the TOF spectrum. The total is the sum of the fast and slow recoils, $N_\beta = N_{\beta R} + N_{\beta r}$, and so the relation between the observed $n_{\beta r}$ and the total number of emitted decays $N_{\beta r}$ is:

$$n_{\beta r} = N_\beta \cdot \Omega_\beta \cdot \Omega_{MCP} \cdot \varepsilon_{MCP} \cdot \omega_{\beta r} \cdot (1 - P_n). \tag{6.4}$$

The resulting P_n is:

$$P_n^{\beta r} = \frac{n_{\beta R} \cdot \Omega_\beta \cdot \Omega_{MCP} \cdot \varepsilon_{MCP} \cdot \omega_{\beta r} \cdot (1 - P_n)}{n_{\beta r} \cdot \Omega_\beta \cdot \Omega_{MCP} \cdot \varepsilon_{MCP} \cdot \omega_{\beta R} \cdot f} = \frac{n_{\beta R} \cdot \omega_{\beta r} \cdot (1 - P_n)}{n_{\beta r} \cdot \omega_{\beta R} \cdot f}. \tag{6.5}$$

Since the slow recoil ions have low energies (on the order of 100's of eV), the value of $\omega_{\beta r}$ is quite sensitive to the details of the decay scheme, as well as the charge state distribution following the β decay. The higher charge states are more strongly affected by the RF fields, and hence their detection efficiency diminishes. Details of the decay scheme important to the β-recoil coincidence detection are the β intensity to specific decay branches, and the β-ν correlation coefficient, $a_{\beta\nu}$. As the transitions to the low-lying states in the βn emitters are almost entirely first forbidden, the $a_{\beta\nu}$ will depend on the details of the matrix elements

involved. In the present experimental setup, the β-recoil coincidence can be detected at either 180° or 90° angle between the detectors. Since the β momentum strongly affects the slow recoil ion momentum, the 180° combination is strongly favored over the 90°, an effect we refer to as kinematic focusing. Although the $a_{\beta\nu}$ value for the different transitions are not known, the average value can be deduced by comparing the observed ratio of β-ion coincidences at 180° and 90°, to the simulated ratio, with varying average decay $a_{\beta\nu}$ value between -1 and +1. Section 4.2.4 details the analysis that goes into determining the $\omega_{\beta r}$, the average $a_{\beta\nu}$, and the charge state distribution.

6.1.3 Using the number of β-γ coincidences

For γ's of known intensity, it is possible to deduce the number of β decays by counting the β-delayed γ-rays from the precursor decay. In this case, the number of observed β decays can be expressed as:

$$n_{\beta\gamma} = N_\beta \cdot I_\gamma \cdot \varepsilon_\gamma \cdot \Omega_\beta \cdot \omega_{\beta\gamma}, \tag{6.6}$$

where I_γ is the intensity of the absolute γ transition and ε_γ is the total efficiency of the HPGe at the transition's γ-ray energy determined with calibrations, and it entails the HPGe solid angle. The $\omega_{\beta\gamma}$ factor encompasses β detection efficiency correction to the constant $\Omega_\beta \cdot \varepsilon_\beta$ value associated with the γ-ray of interest, and excludes detection of conversion electrons from that excitation energy of interest. Using the number of observed β-γ coincidences the P_n is:

$$P_n^{\beta\gamma} = \frac{n_{\beta R} \cdot \Omega_\beta \cdot \varepsilon_\gamma \cdot I_\gamma \cdot \omega_{\beta\gamma}}{n_{\beta\gamma} \cdot \Omega_\beta \cdot \Omega_{MCP} \cdot \varepsilon_{MCP} \cdot \omega_{\beta R} \cdot f} = \frac{n_{\beta R} \cdot \varepsilon_\gamma \cdot I_\gamma \cdot \omega_{\beta\gamma}}{n_{\beta\gamma} \cdot \Omega_{MCP} \cdot \varepsilon_{MCP} \cdot \omega_{\beta R} \cdot f}. \tag{6.7}$$

Some of the observed γ's in the trap-full part of the cycle come from decays of untrapped ions, and hence have an unknown detection efficiency. The number of γ's from the untrapped decays is deduced from the observed number of untrapped decays during the trap-empty cycle. The details of achieving a correct subtraction factor is described in Section 6.5.

6.1.4 Obtaining values for the branching ratio calculations

Values from the experimental data

Observed number of counts obtained during the experiment are: n_β, $n_{\beta R}$, $n_{\beta r}$ and $n_{\beta\gamma}$. The details of obtaining each of these values is described in following sections. The basic overview is:

1. $n_{\beta R}$: obtained from the neutron energy spectrum (resulting from the TOF spectrum), after all the corrections are applied.
2. $n_{\beta r}$: can be obtained from the accidental-subtracted TOF spectrum using proper cuts. If isobaric contaminants are present, the recoils within the slow-recoil TOF window

can be plotted against the cycle time, and the species of interest can be counted by fitting the populations using the `BFit2` program.

3. n_β: the number of counts is supplied by the plastic detector. The number of counts vs. cycle time is fit with the `BFit2` code to provide a number free from isobaric contaminants and β's from untrapped species.
4. $n_{\beta\gamma}$: are obtained by counting the γ's in coincidence with β's in the HPGe spectrum, and subtracting contribution from untrapped species.

Values from simulations

In Section 4.2, I described how the ω relative efficiency values used in the branching ratio calculations are obtained with the use of simulations, guided by comparisons with data. These values were determined for each detector combination and each isotope. In this chapter, I discuss the systematic uncertainties in the P_n values arising from the ω values.

Values from calibrations and physical measurements

The solid angle measurements are discussed in Section 3.3.4. Calibrations of the HPGe efficiency ε_γ were described in Section 3.3.2, and the MCP intrinsic efficiency ε_{MCP} was determined in Section 4.3.

Values obtained from literature

Existing information on the isotopes under study contribute to decreasing the uncertainties of our measurement and uncovering systematic effects. Firstly, the fast-ion counts that we detect constitute a fraction of total counts f of the spectrum above our detection threshold equivalent to 100-keV in neutron energy. The f value can be obtained from the existing neutron spectrum measurements.

Information from the known decay scheme is implicated in several areas of the analysis. We use γ-ray intensities for branching ratio calculations, but also to put limits on the amounts of the isobaric contaminants. The relative β branch intensities are important for setting up the simulations and interpreting results. Although for many of the isotopes studied the decay scheme is incomplete, the existing information can constrain the results. By comparing the simulation results from varying the decay scheme, we can deduce the magnitude of uncertainty due to the unknown scheme. The role of the known decay scheme is especially evident in calculating the effective detection efficiency numbers for the low-energy recoil ions (the $\omega_{\beta r}$). Due to their low recoil energy, they are especially sensitive to the perturbation from the RF fields, an effect that is enhanced for higher charge states. The recoil energy distribution, and hence the β branch intensities to excited states, also have an effect on the observed number of decays.

6.2 The number of recoil ions associated with neutron emission (fast recoils)

The number of βn decays can be obtained directly from the corrected neutron energy spectra from Section 5.6. The corrections account for backgrounds due to γ's, CE's, and neutrons triggering the plastic detectors; effects from β scattering and detector efficiency; and electric fields affecting ion trajectories. Collectively, all these effects comprise the $\omega_{\beta R}$ term, and therefore the number of counts obtained from the neutron spectrum can be written as:

$$n^c_{\beta R} = \int_{E_{th}}^{Q-S_n} \frac{n_{\beta R}(E_i)}{\omega_{\beta R}(E_i)} dE_i, \tag{6.8}$$

where the E_{th} is 100 keV in our experimental setup. To obtain the number of βn events occurring, the $n^c_{\beta R}$ has to be divided by the detector solid angles, Ω_{MCP} and Ω_β, the intrinsic MCP efficiency ε_{MCP} (as in Equation 6.1), and multiplied by the deadtime correction. However, different variables cancel out from the P_n equations, and hence the number used in the subsequent tables for P_n calculations is the $n^c_{\beta R}$, as well as $n^{cd}_{\beta R}$, which represents the $n^c_{\beta R}$ multiplied by the deadtime correction.

The $n^c_{\beta R}$ numbers obtained from the neutron energy spectra from Section 5.7 are listed in Tables 6.1, 6.2, 6.3, and 6.4. These numbers are used in the P_n equations in the proceeding sections, where it's indicated whether the deadtime correction has been applied or not (the average deadtime correction values for each dataset are listed in Table 3.1).

In the case of ^{137}I, presence of ^{137}Te contaminated the neutron spectrum. In order to subtract it properly, a subtraction factor was deduced using the β-singles numbers, which contain the ratio of the trapped ^{137}Te to ^{137}I. The ratio also had to be scaled by the ratio in P_n for the two isotopes. The correction factor can also be calculated with: $1 - \frac{N_\beta^{Te} * 0.97}{N_\beta^I + N_\beta^{Te} * 0.97} \times \frac{P_n^{Te}}{P_n^I}$, where N_β^{Te} and N_β^I is the number of β-singles, 0.97 accounts for conversion electrons in the number of detected ^{137}Te β-singles, and P_n are the neutron branching ratios taken from literature. The resulting correction is **0.931(13)**.

6.3 P_n determined from the β-singles numbers

.

The number of β-singles from the precursor of interest was determined in each dataset by fitting the β vs. cycle time spectra with the use of `BFit2` fitting routine, described in 4.1.2. The data gathered from β-singles and β-γ analysis, including main contaminants, is summarized in Table 6.5. The table contains total counts summed over all detectors, and is used to compare relative amounts of contaminants determined with the two methods. The β-singles results per detector are listed in Table 6.6 and Table 6.7 at the end of this subsection.

^{137}I.07 fast-ion counts				
ΔE-MCP	$n^c_{\beta R}$	$n^{cd}_{\beta R}$	Statistical unc.	Systematic unc.
LR	614.8	658.6	31.5	8.0
LT	631.3	676.2	27.8	8.2
BR	639.7	685.2	30.9	8.3
BT	668.9	716.5	30.9	8.7
Isobar subtracted				
LR	564.8	605.0	31.5	8.7
LT	580.0	621.2	27.8	10.0
BR	587.6	629.5	30.9	13.2
BT	614.5	658.2	30.9	9.1

Table 6.1: $n^c_{\beta R}$ and $n^{cd}_{\beta R}$ (corrected for deadtime) counts from the ^{137}I.07 dataset. The isobar-subtracted counts correct the raw counts by a factor of 0.931 to account for ^{137}Te. In the P_n analysis, only the isobar-subtracted counts are used.

ΔE-MCP	$n^c_{\beta R}$	$n^{cd}_{\beta R}$	Statistical unc.	Systematic unc.
^{138}I.06 fast-ion counts				
LR	389.2	419.0	26.5	8.3
LT	435.4	468.8	22.7	2.9
BR	444.4	478.4	25.5	5.3
BT	407.3	438.5	24.7	5.6
^{138}I.07 fast-ion counts				
LR	167.5	178.3	17.6	6.5
LT	139.9	148.9	13.5	4.1
BR	172.9	184.1	15.3	0.4
BT	185.4	197.4	15.9	0.01

Table 6.2: $n^c_{\beta R}$ and $n^{cd}_{\beta R}$ (corrected for deadtime) counts from the ^{138}I.06 and ^{138}I.07 datasets.

^{144}Cs.02 fast-ion counts				
ΔE-MCP	$n^{c}_{\beta R}$	$n^{cd}_{\beta R}$	Statistical unc.	Systematic unc.
LR	306.4	336.0	33.5	14.0
LT	351.8	385.8	26.9	6.8
BR	347.0	380.4	32.8	11.2
BT	337.3	369.9	29.5	9.2

Table 6.3: $n^{c}_{\beta R}$ and $n^{cd}_{\beta R}$ (corrected for deadtime) counts from the ^{144}Cs.02 dataset.

^{145}Cs.02 fast-ion counts				
ΔE-MCP	$n^{c}_{\beta R}$	$n^{cd}_{\beta R}$	Statistical unc.	Systematic unc.
LR	523.7	554.1	31.8	9.6
LT	557.0	589.4	27.6	4.4
BR	516.5	546.5	30.2	9.1
BT	455.5	482.0	29.4	9.5

Table 6.4: $n^{c}_{\beta R}$ and $n^{cd}_{\beta R}$ (corrected for deadtime) counts from the ^{145}Cs.02 dataset.

The results in Table 6.5 show that the only significant contaminant present in the ^{137}I dataset was ^{137}Te. The ^{137}Xe contribution was negligible, as also confirmed by the γ-ray data. CARIBU was not very efficient outputting noble gases at the time, and the remaining ^{137}Xe was eliminated from the beam with the isobar separator. Figures 6.1 and 6.2 show the fits produced with `BFit2`. The fits regressed to a value of about 25s for the trap lifetime. The ^{137}I dataset was taken over the longest cycle time, and hence it was the only dataset significantly affected by the trap lifetime, giving it a 1% systematic uncertainty.

The ^{138}I and ^{144}Cs datasets were free of major contaminants, and hence the TPM model was simple to fit. The β-γ analysis indicated a large number of counts ($\sim$25%) of ^{145}Ba in the ^{145}Cs dataset, possibly due to a nearby contaminating γ-line. The statistics in the β-singles set is much higher than β-γ's, and one would expect very little of trapped ^{145}Ba based on ^{144}Ba absence in the ^{144}Cs dataset, as they are chemically very similar. The details of the β-γ analysis are discussed in the next section.

6.3.1 Systematic uncertainties in the P^{β}_{n} value.

In addition to the systematic uncertainties resulting from the low-TOF background subtraction, the number of fast ions also suffers from the systematic uncertainty due to: (1) the measured MCP solid angle, (2) the MCP intrinsic efficiency deduced from the ^{134}Sb data, and (3) the uncertainty in the f value. The uncertainty in the f value is deduced by varying

Isotope	n_β (1000's)	$n_{\beta\gamma}$ (1000's)	Gamma line (keV)
		^{137}I.07 Dataset	
^{137}Te	445(4)	121(23)	243
^{137}I	1773(8)	1561(166)	1218
		^{138}I.06 Dataset	
^{138}Te	161(7)		
^{138}I	1337(16)	1476(145)	588
^{138}Xe	107(9)	-9(8)	258
		^{138}I.07 Dataset	
^{138}Te	12(2)		
^{138}I	648(6)	638(65)	588
^{138}Xe	0	5(5)	258
		^{144}Cs.02 Dataset	
^{144}Xe	92(34)		
^{144}Cs	3673(25)	4052(497)	200
^{144}Ba	0	31(67)	388
		^{145}Cs.02 Dataset	
^{145}Cs	985(10)	734(107)	175
^{145}Ba	0	273(92)	544

Table 6.5: Summed numbers of detected β-γ's and β-singles, written in thousands, with statistical uncertainty only. The β-γ events have been corrected for the γ detection efficiency and the γ-ray branching ratio, enabling comparison with the β-singles numbers. The main isobaric contaminants are listed for comparison to the isotope of interest, and compared between the two measurement methods. The Information on the relative amounts of contaminants was used to produce detailed fits for each ΔE detector, by incorporating this information into the starting fit parameters.

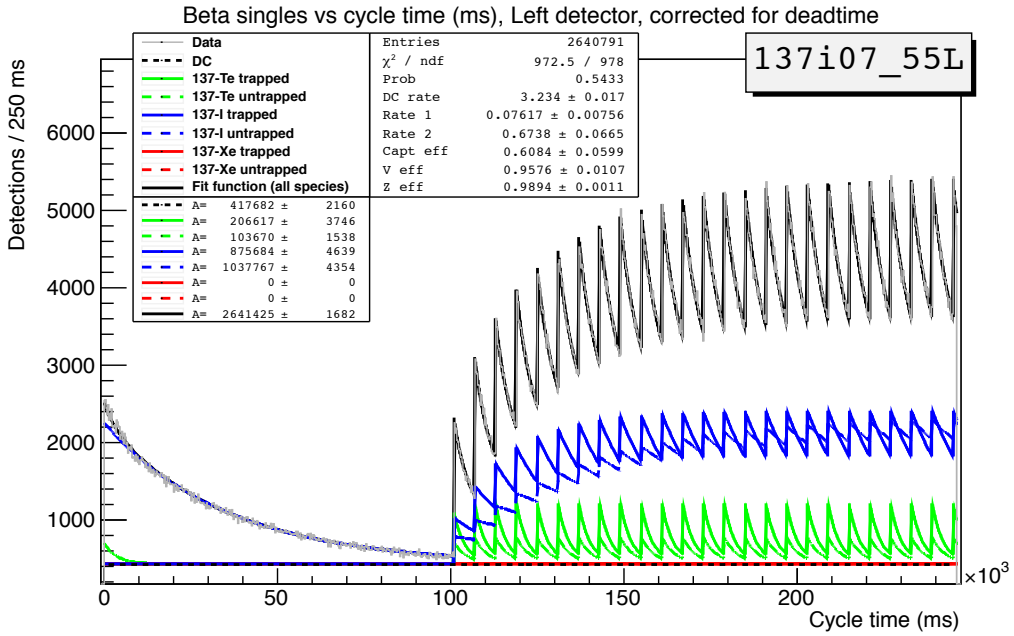

Figure 6.1: β-singles fits for ^{137}I, counts in the left plastic.

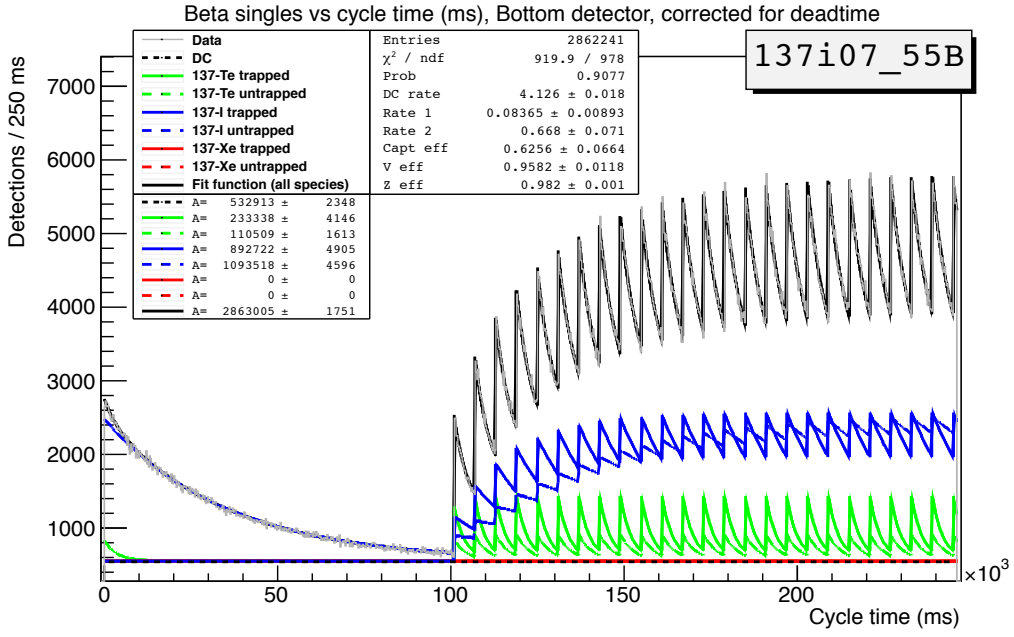

Figure 6.2: β-singles fits for ^{137}I, counts in the bottom plastic.

	^{137}I.07		
Detector	Counts	Statistical unc.	Systematic unc.
Left ΔE	875684	7159	8757
Bottom ΔE	892722	7569	8927

Table 6.6: ^{137}I β-singles results from BFit2 fitting. The systematic uncertainty is a 1% effect from the uncertainty in the trap lifetime and its effect on the fits. The ^{137}I fits were adversely affected by the limited trap lifetime, due to the long length of the measurement cycle. The limited trap lifetime did not affect the $^{144-145}$Cs and ^{138}I fits due to the relative purity of the trap population and the shorter cycle times involved.

Dataset	Counts in Left ΔE	Uncertainty	Counts in Bottom ΔE	Uncertainty
^{138}I.06	826559	2820	801214	2667
^{138}I.07	315294	3730	323449	3983
^{144}Cs.02	1805663	16610	1867865	19347
^{145}Cs.02	502196	7170	484301	6058

Table 6.7: β-singles results from BFit2 fitting.

the 100-keV threshold by the energy resolution of the detector system that was used to make the neutron spectrum measurement derived from literature. The f values and their associated uncertainties are listed in Table 6.8. The MCP solid angles and their uncertainties are listed in Table 3.6, while the MCP intrinsic efficiency and its uncertainty is listed in Table 4.10.

For each isotope, we also have to take into account the systematic uncertainty resulting from the simulated ω_β and $\omega_{\beta R}$ values. The process for obtaining the various ω values was described in Section 4.2. The systematic uncertainty in the P_n^β branching ratio, however, depends on the uncertainty of the ratio $\omega_\beta/\omega_{\beta R}$. The $\omega_{\beta R}$ value is not independent of ω_β value, and hence the uncertainty in the ratio is determined by varying the same systematic effect for both $\omega_{\beta R}$ and ω_β simultaneously, and adding the uncertainty from all the effects in quadrature. The systematic effects studied were:

1. Varying the plastic ΔE detector threshold cut
2. Uncertainty in the characterization of β scattering in the simulation
3. Uncertainty in the MCP relative detection efficiency due to the discriminator threshold

The thresholds for the plastic detectors were characterized as described in Section 3.3.1, and are summarized in Table 4.1. The uncertainty in the $\omega_\beta/\omega_{\beta R}$ ratio due to the plastic

Isotope	f value	Uncertainty	Source
^{137}I	0.960	0.012	Ohm 1980[21]
^{138}I	0.807	0.053	Shalev 1977[48]
^{144}Cs	0.690	0.038	Greenwood 1985[28]
^{145}Cs	0.761	0.033	Greenwood 1985[28]

Table 6.8: The fraction of neutron energy spectrum f above 100 keV, obtained from existing literature results. The systematic uncertainty is derived from an estimate of how much the neutron spectrum could vary below the 100 keV threshold of the recoil-ion data.

threshold effects is established by varying the threshold by $\pm 1\sigma$, and finding the resulting $\omega_{\beta R}$ and ω_β values. The direct neutron detection threshold is much higher than for β's, conversion electrons, or γ's, hence the uncertainties associated with the two thresholds are determined separately.

The detection efficiencies (as in the case of all the ω's) are largely increased by the amount of β scattering. The effect of the uncertainty due to the scattering on the P_n value can be estimated by looking at the difference between the $\omega_\beta/\omega_{\beta R}$ ratio with and without scattering turned on. In the analysis of the simulation, the scattering can be "turned off" by taking the efficiency only for the β events that have the initial momentum vector pointing within the solid angle of the plastic detector. The uncertainty is then assumed to be 15% of that difference in ratios [75].

The MCP efficiency correction is normalized to the absolute MCP efficiency as determined from the slow-ion data in the ^{134}Sb calibration (see Section 4.3). Hence, the uncertainty in the energy-dependent MCP correction (described in Section 5.4) is defined as σ_{MCP}, and is determined from the ratio between the size of the correction due to the MCP relative efficiency for fast and slow recoil ions. The size of the correction for the fast recoil ions is defined as the ratio between the $\omega_{\beta R}$ value obtained with the MCP relative efficiency in place, over the $\omega_{\beta R}$ without the efficiency applied. The size of the correction for the slow ions is defined in the same way, with the ratio of $\omega_{\beta r}$ values. The total σ_{MCP} can be obtained by taking the ratio between the slow and fast corrections, subtracting unity, and multiplying by 0.5 to account for a generous margin of 50% uncertainty in the MCP relative efficiency correction.

The total uncertainty in the $\omega_\beta/\omega_{\beta R}$ ratio due to the three effects consists of the uncertainties from the threshold cuts ($\sigma_{\Delta E}$), scattering (σ_S), and the MCP correction (σ_{MCP}) added in quadrature to produce the total $\sigma(\omega_\beta/\omega_{\beta R})$ uncertainty. The total systematic uncertainty is then the quadratic sum of the relative systematic uncertainties of each value:

$$\frac{\sigma_{P_n^\beta}(Sys.)}{P_n^\beta} = \sqrt{\left(\frac{\sigma_R}{R}\right)^2 + \left(\frac{\sigma_f}{f}\right)^2 + \left(\frac{\sigma_\Omega}{\Omega_{MCP}}\right)^2 + \left(\frac{\sigma_\varepsilon}{\varepsilon_{MCP}}\right)^2 + \left(\frac{\sigma_n}{n_{\beta R}}\right)^2}, \qquad (6.9)$$

	ΔE-MCP			
Systematic Effect	LR	LT	BR	BT
$\sigma_{\Delta E}$	5.4	2.0	2.4	5.4
σ_{MCP}	0.8	3.8	0.7	5.5
σ_S	2.1	1.8	1.8	2.2
σ(low-TOF)	1.4	1.6	2.1	1.4
$\sigma(\Omega_{MCP})$	2.4	2.3	2.4	2.3
$\sigma(\varepsilon_{MCP})$	10.0	10.0	10.0	10.0
$\sigma(f)$	1.3	1.3	1.3	1.3
$\sigma_{P_n^\beta}$(Sys.) for ^{137}I.07	12.0	11.5	11.0	13.1

Table 6.9: Relative contribution from different systematic effects to the total uncertainty in the P_n^β value for the ^{137}I.07 dataset. The uncertainties are given in % relative to each value. The first three rows refer to the contributions to the total uncertainty in the $\omega_\beta/\omega_{\beta R}$ ratio. The low-TOF systematic uncertainty also includes the contribution from the systematic uncertainty due to ^{137}Te fast ions.

where R is the $\omega_\beta/\omega_{\beta R}$ ratio. The relative size of each effect on the total systematic uncertainty in the P_n^β for each isotope is listed in Tables 6.9, 6.10, 6.11, and 6.12.

6.3.2 P_n^β results

The summary of P_n calculated using the β-singles numbers is listed in Tables: 6.13, 6.14, 6.15, 6.16, 6.17. The statistical uncertainty is used to weight the individual P_n results for each detector combination. The total systematic uncertainty for the final P_n value is also a result of weighing each systematic uncertainty by the statistical uncertainty of that detector combination's P_n value.

6.4 P_n determined from recoil ions

The slow recoil ion numbers can be obtained directly from the TOF spectrum or from the inverse recoil ion velocity spectrum, with proper cuts applied and accidentals removed. The inverse velocity spectrum was used in this analysis since it contains information on the impact location and the ion mass.

The standard procedure for subtracting accidentals is to integrate over the counts between 15-20μs in the TOF spectrum corresponding to approximately 0.3-0.4 μs/mm in the v^{-1} spectrum, where the simulations indicate that no recoil ions are expected, and hence the counts are all due to accidentals. The data confirms a flat background rate in that region

	ΔE-MCP			
Systematic Effect	LR	LT	BR	BT
$\sigma_{\Delta E}$	3.8	1.1	0.8	2.9
σ_{MCP}	0.9	2.3	0.5	3.6
σ_S	1.4	1.0	1.3	1.5
σ(low-TOF) for ^{138}I.06	2.0	0.6	1.1	1.3
σ(low-TOF) for ^{138}I.07	3.6	2.7	0.2	0.0
$\sigma(\Omega_{MCP})$	2.4	2.3	2.4	2.3
$\sigma(\varepsilon_{MCP})$	10.0	10.0	10.0	10.0
$\sigma(f)$	6.6	6.6	6.6	6.6
$\sigma_{P_n^\beta}$(Sys.) for ^{138}I.06	13.0	12.5	12.3	13.2
$\sigma_{P_n^\beta}$(Sys.) for ^{138}I.07	13.4	12.8	12.3	13.1

Table 6.10: Relative contribution from different systematic effects to the total uncertainty in the P_n^β value for ^{138}I.06 and ^{138}I.07 datasets. The uncertainties are given in % relative to each value. The first three rows refer to the contributions to the total uncertainty in the $\omega_\beta/\omega_{\beta R}$ ratio.

	ΔE-MCP			
Systematic Effect	LR	LT	BR	BT
$\sigma_{\Delta E}$	2.3	0.2	1.0	1.9
σ_{MCP}	0.0	1.3	0.4	1.5
σ_S	1.2	0.9	0.8	1.0
σ(low-TOF)	4.2	1.8	2.9	2.5
$\sigma(\Omega_{MCP})$	2.4	2.3	2.4	2.3
$\sigma(\varepsilon_{MCP})$	10.0	10.0	10.0	10.0
$\sigma(f)$	5.6	5.6	5.6	5.6
$\sigma_{P_n^\beta}$(Sys.) for ^{144}Cs.02	12.7	11.9	12.1	12.2

Table 6.11: Relative contribution from different systematic effects to the total uncertainty in the P_n^β value for the ^{144}Cs.02 dataset. The uncertainties are given in % relative to each value. The first three rows refer to the contributions to the total uncertainty in the $\omega_\beta/\omega_{\beta R}$ ratio.

	ΔE-MCP			
Systematic Effect	LR	LT	BR	BT
$\sigma_{\Delta E}$	2.6	1.5	2.2	3.1
σ_{MCP}	0.2	1.9	0.1	2.3
σ_S	0.9	0.6	0.5	0.6
σ(low-TOF)	1.7	0.7	1.7	2.0
$\sigma(\Omega_{MCP})$	2.4	2.3	2.4	2.3
$\sigma(\varepsilon_{MCP})$	10.0	10.0	10.0	10.0
$\sigma(f)$	4.3	4.3	4.3	4.3
$\sigma_{P_n^\beta}$(Sys.) for ^{145}Cs.02	11.6	11.4	11.5	12.0

Table 6.12: Relative contribution from different systematic effects to the total uncertainty in the P_n^β value for the ^{145}Cs.02 dataset. The uncertainties are given in % relative to each value. The first three rows refer to the contributions to the total uncertainty in the $\omega_\beta/\omega_{\beta R}$ ratio.

137I.07 Dataset

Det.	$n_{\beta R}^{cd}$	n_β	ω_β	Ω_{MCP}	ε_{MCP}	f	$P_n^\beta(\%)$	$\sigma_{P_n}(stat.)$	$\sigma_{P_n}(sys.)$
LR	605(32)	875684(7159)	1.31	0.051	0.25	0.96	7.51	0.39	0.90
LT	621(28)	875684(7159)	1.31	0.051	0.27	0.96	7.10	0.32	0.81
BR	629(31)	892722(7569)	1.31	0.051	0.25	0.96	7.69	0.38	0.85
BT	658(31)	892722(7569)	1.31	0.051	0.27	0.96	7.40	0.35	0.97
weighted average							7.39	0.18	0.88

Table 6.13: 137I.07 dataset P_n results from β-singles. Statistical uncertainty for the β and βR counts is given in parenthesis.

138I.06 Dataset

Det.	$n_{\beta R}^{cd}$	n_β	ω_β	Ω_{MCP}	ε_{MCP}	f	$P_n^\beta(\%)$	$\sigma_{P_n}(stat.)$	$\sigma_{P_n}(sys.)$
LR	419(27)	826559(2820)	1.35	0.051	0.25	0.81	6.70	0.42	0.87
LT	469(23)	826559(2820)	1.35	0.051	0.27	0.81	6.90	0.33	0.86
BR	478(25)	801214(2667)	1.36	0.051	0.25	0.81	7.94	0.42	0.97
BT	439(25)	801214(2667)	1.36	0.051	0.27	0.81	6.69	0.38	0.88
weighted average							7.02	0.19	0.90

Table 6.14: 138I.06 dataset P_n results from β-singles.

138I.07 Dataset

Det.	$n_{\beta R}^{cd}$	n_β	ω_β	Ω_{MCP}	ε_{MCP}	f	$P_n^\beta(\%)$	$\sigma_{P_n}(stat.)$	$\sigma_{P_n}(sys.)$
LR	178(18)	315294(3730)	1.35	0.051	0.25	0.81	7.48	0.74	1.00
LT	149(14)	315294(3730)	1.35	0.051	0.27	0.81	5.75	0.53	0.73
BR	184(15)	323449(3983)	1.36	0.051	0.25	0.81	7.57	0.64	0.93
BT	197(16)	323449(3983)	1.36	0.051	0.27	0.81	7.47	0.61	0.98
weighted average							6.90	0.31	0.89

Table 6.15: 138I.07 dataset P_n results from β-singles.

144Cs.02 Dataset

Det.	$n_{\beta R}^{cd}$	n_β	ω_β	Ω_{MCP}	ε_{MCP}	f	$P_n^\beta(\%)$	$\sigma_{P_n}(stat.)$	$\sigma_{P_n}(sys.)$
LR	336(33)	1805663(16610)	1.35	0.051	0.25	0.69	2.88	0.29	0.36
LT	386(27)	1805663(16610)	1.35	0.051	0.27	0.69	3.04	0.21	0.36
BR	380(33)	1867865(19347)	1.36	0.051	0.25	0.69	3.17	0.28	0.38
BT	370(29)	1867865(19347)	1.36	0.051	0.27	0.69	2.83	0.23	0.34
weighted average							2.98	0.12	0.36

Table 6.16: 144Cs.02 dataset P_n results from β-singles.

145Cs.02 Dataset

Det.	$n_{\beta R}^{cd}$	n_β	ω_β	Ω_{MCP}	ε_{MCP}	f	$P_n^\beta(\%)$	$\sigma_{P_n}(stat.)$	$\sigma_{P_n}(sys.)$
LR	554(32)	502196(7170)	1.44	0.051	0.25	0.76	16.44	0.97	1.91
LT	589(28)	502196(7170)	1.44	0.051	0.27	0.76	16.09	0.79	1.84
BR	547(30)	484301(6058)	1.46	0.051	0.25	0.76	17.07	0.97	1.96
BT	482(29)	484301(6058)	1.46	0.051	0.27	0.76	13.85	0.87	1.66
weighted average							15.78	0.44	1.83

Table 6.17: 145Cs.02 dataset P_n results from β-singles.

as well. The accidental rate per bin determined in that region is then subtracted from each bin in the entire spectrum.

In some cases, the isobaric contaminants produce a sizable background in the TOF spectrum. In such situations, we can fit the slow-recoils vs. cycle time histogram, and take advantage of the differing half-lives of the two isotopes to separate their contributions to the total activity. Since the β-recoil coincidence ensures that only trapped species are detected, the fits become simpler with only a few trapped populations to account for. In cases with only one contaminant present, the results from the β-singles analysis can be used directly, since they provide the ratio of the contaminant counts to the precursor counts.

The ^{137}I dataset contains ^{137}Te as a large contaminant. The number of ^{137}I slow recoil ions can be derived from the total number of recoil ions within the TOF region of interest by correcting it by: $1 - \frac{(439.5)(0.97)}{1769+(439.5)(0.97)} = 0.806 \pm 0.0046$, where 1769 is the number of ^{137}I β-singles, and (439.5)(0.97) is the number of ^{137}Te β's corrected by 0.97 to account for conversion electrons. There is also an additional $\sim$25% uncertainty associated with the unknown detection efficiency for ^{137}Te slow ions. This correction is consistent with the ratio found by fitting the slow recoil ions vs. cycle time with the `BFit2` program, which resulted in a Te:I ratio of 0.255(9), that corresponds to a correction factor of 0.797. The fit to the slow-recoil ions is shown in Fig. 6.3.

The slow recoil ion counts for all the isotopes and for each detector combination are listed in Table 6.18.

6.4.1 Systematic uncertainty in the P_n^r value

In addition to the systematic uncertainty in the number of fast-ion counts, the P_n^r systematic uncertainty also contains effects from the f value and the (1-P_n) value given by the literature, listed in Table 6.19. In contrast to the the systematic uncertainty in the P_n^β, the MCP solid angle and intrinsic efficiency cancels out in the P_n^r calculation, and hence the associated systematic uncertainties do not affect the final P_n^r value. In the case of 137I.07 dataset, the isobar subtraction contributes a systematic uncertainty of $\sim$2%. Lastly, the contribution

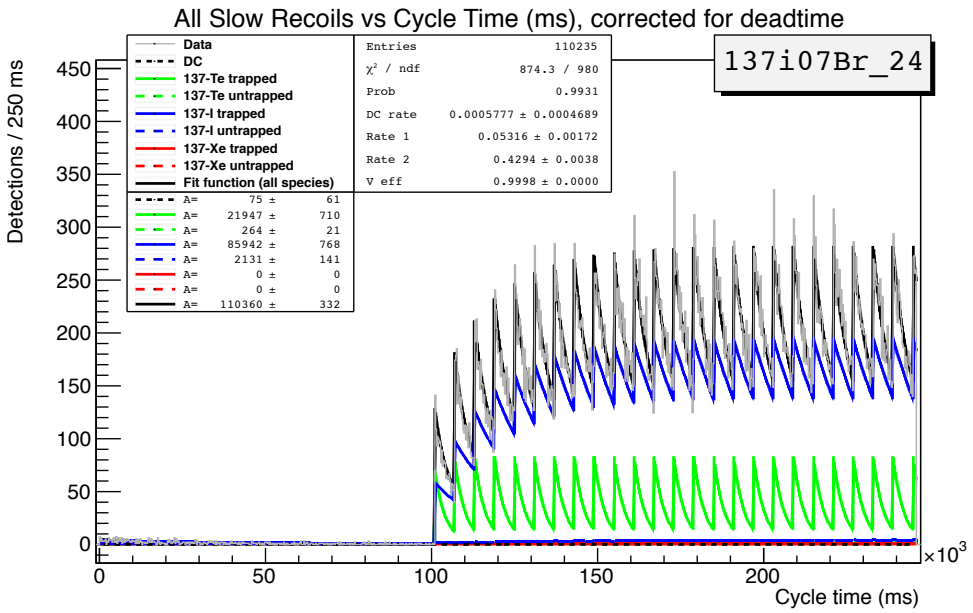

Figure 6.3: Fits to slow recoil ions vs. cycle time for the ^{137}I.07 dataset.

	$n_{\beta r}$				
ΔE-MCP	^{137}I.07	^{138}I.06	^{138}I.07	^{144}Cs.02	^{145}Cs.02
LR	29835(219)	22235(152)	9143(98)	50494(232)	11850(125)
LT	3705(82)	5335(76)	2274(50)	11086(115)	2615(69)
BR	5240(99)	7284(91)	3143(59)	15728(140)	3397(88)
BT	23499(194)	17280(134)	7087(85)	38249(201)	10072(112)

Table 6.18: Slow-recoil ion counts.

Isotope	(1-P_n) value from literature	Uncertainty
^{137}I	0.929	0.002
^{138}I	0.946	0.002
^{144}Cs	0.970	0.001
^{145}Cs	0.853	0.009

Table 6.19: The value of β-delayed neutron branching ratio for each of the isotopes, as evaluated by the IAEA.

	ΔE-MCP			
Systematic Effect	LR	LT	BR	BT
$\sigma_{\Delta E}$	5.4	2.2	2.2	5.4
σ_{MCP}	0.3	12.6	1.7	2.5
σ_S	0.1	9.3	15.0	0.1
σ(low-TOF)	1.5	1.7	2.2	1.5
σ(slow ions)	0.6	0.6	0.6	0.6
$\sigma(f)$	1.3	1.3	1.3	1.3
$\sigma(1-P_n)$	0.2	0.2	0.2	0.2
$\sigma_{P_n^r}$(Sys.) for ^{137}I.07	5.8	15.9	15.5	6.3

Table 6.20: Relative contribution from different systematic effects to the total uncertainty in the P_n^r value for the ^{137}I.07 dataset. The uncertainties are given in % relative to each value. The first three rows refer to the contributions to the total uncertainty in the $\omega_{\beta r}/\omega_{\beta R}$ ratio.

from the $\omega_{\beta r}/\omega_{\beta R}$ ratio has to be taken into consideration.

Estimating the uncertainty in the $\omega_{\beta r}/\omega_{\beta R}$ ratio follows the same procedure as has been done for $\omega_\beta/\omega_{\beta R}$ uncertainty in Section 6.3.1. This includes the uncertainty effects due to the plastic detector threshold, and the β scattering. The $\omega_{\beta r}$ value is weighted by the charge-state distribution determined for that isotope, and utilizes the $a_{\beta\nu}$ correlation value found with the analysis as described in Section 4.2.4. The total relative systematic uncertainties for each isotope, with the various contributions enumerated, are listed in Tables 6.20, 6.21, 6.22, and 6.23. The tables also list total relative systematic uncertainty in the P_n^r value.

6.4.2 P_n^r results

Out of the three methods for calculating P_n, this is the only one independent of the MCP detector intrinsic efficiency, which is uncertain to 10%. However, accounting for the total

	ΔE-MCP			
Systematic Effect	LR	LT	BR	BT
$\sigma_{\Delta E}$	3.9	1.0	0.7	2.9
σ_{MCP}	0.4	4.0	1.0	2.0
σ_S	0.6	1.3	1.9	0.9
σ(low-TOF) for ^{136}I.06	2.1	0.7	1.2	1.4
σ(low-TOF) for ^{136}I.07	3.9	2.9	0.2	0.0
$\sigma(1-P_n)$	0.2	0.2	0.2	0.2
$\sigma(f)$	6.6	6.6	6.6	6.6
$\sigma_{P_n^r}$(Sys.) for ^{138}I.06	7.9	7.9	7.1	7.7
$\sigma_{P_n^r}$(Sys.) for ^{138}I.07	8.6	8.4	7.0	7.5

Table 6.21: Relative contribution from different systematic effects to the total uncertainty in the $P_n^{\beta r}$ value for the ^{136}I.06 and ^{136}I.07 datasets. The uncertainties are given in % relative to each value. The first three rows refer to the contributions to the total uncertainty in the $\omega_{\beta r}/\omega_{\beta R}$ ratio.

	ΔE-MCP			
Systematic Effect	LR	LT	BR	BT
$\sigma_{\Delta E}$	2.3	0.4	0.5	1.9
σ_{MCP}	0.0	4.7	0.7	0.6
σ_S	0.0	1.4	1.6	0.0
σ(low-TOF)	4.6	1.9	3.2	2.7
$\sigma(1-P_n)$	0.1	0.1	0.1	0.1
$\sigma(f)$	5.6	5.6	5.6	5.6
$\sigma_{P_n^r}$(Sys.) for ^{144}Cs.02	7.6	7.7	6.7	6.5

Table 6.22: Relative contribution from different systematic effects to the total uncertainty in the $P_n^{\beta r}$ value for the ^{144}Cs.02 dataset. The uncertainties are given in % relative to each value. The first three rows refer to the contributions to the total uncertainty in the $\omega_{\beta r}/\omega_{\beta R}$ ratio.

	ΔE-MCP			
Systematic Effect	LR	LT	BR	BT
$\sigma_{\Delta E}$	2.0	0.5	1.2	3.1
σ_{MCP}	0.1	6.0	1.3	1.5
σ_S	0.2	1.0	1.2	0.1
σ(low-TOF)	1.8	0.8	1.8	2.1
$\sigma(1-P_n)$	1.1	1.1	1.1	1.1
$\sigma(f)$	4.3	4.3	4.3	4.3
$\sigma_{P_n^r}$(Sys.) for ^{145}Cs.02	5.2	7.6	5.2	6.0

Table 6.23: Relative contribution from different systematic effects to the total uncertainty in the $P_n^{\beta r}$ value for the ^{145}Cs.02 dataset. The uncertainties are given in % relative to each value. The first three rows refer to the contributions to the total uncertainty in the $\omega_{\beta r}/\omega_{\beta R}$ ratio.

detection efficiency of slow recoil ions is complicated by the sensitivity of the $\omega_{\beta r}$ value to the $a_{\beta\nu}$ and the charge-state distribution. The results of the P_n^r calculations, weighted by the statistical uncertainties, are listed in Tables 6.24, 6.25, 6.26, 6.27, and 6.28.

6.5 P_n from β-γ coincidences

The total number of β decays is determined from counting under the γ-ray peaks for transitions in coincidence with a β detection. The β-γ coincident events are free from isobaric contaminants, as the γ transitions are unique for each isotope. However, the efficiency of each HPGe detector is <1%, and so the available statistics are limited. In addition, the untrapped

137I.07 Dataset

ΔE-MCP	$n_{\beta R}^c$	$\omega_{\beta r}$	f	(1-P_n)	$n_{\beta r}$	P_n(%)	$\sigma_{P_n}(stat.)$	$\sigma_{P_n}(sys.)$
LR	572(32)	3.84	0.96	0.93	37025(219)	7.12	0.40	0.41
LT	588(28)	0.48	0.96	0.93	4598(82)	7.39	0.39	1.18
BR	595(31)	0.58	0.96	0.93	6503(99)	6.37	0.35	0.98
BT	623(31)	3.16	0.96	0.93	29162(194)	8.10	0.41	0.51
weighted average						7.18	0.19	0.81

Table 6.24: P_n results, using the number of slow-recoil ions.

138I.06 Dataset

ΔE-MCP	$n^c_{\beta R}$	$\omega_{\beta r}$	f	(1-P_n)	$n_{\beta r}$	P_n(%)	$\sigma_{P_n}(stat.)$	$\sigma_{P_n}(sys.)$
LR	389(27)	2.85	0.81	0.95	22235(152)	5.84	0.40	0.46
LT	435(23)	0.72	0.81	0.95	5335(76)	6.84	0.37	0.54
BR	444(25)	0.86	0.81	0.95	7284(91)	6.12	0.36	0.43
BT	407(25)	2.33	0.81	0.95	17280(134)	6.44	0.39	0.49
weighted average						6.32	0.19	0.48

Table 6.25: P_n results, using the number of slow-recoil ions.

138I.07 Dataset

ΔE-MCP	$n^c_{\beta R}$	$\omega_{\beta r}$	f	(1-P_n)	$n_{\beta r}$	P_n(%)	$\sigma_{P_n}(stat.)$	$\sigma_{P_n}(sys.)$
LR	167(18)	2.85	0.81	0.95	9143(98)	6.97	0.73	0.52
LT	140(14)	0.72	0.81	0.95	2274(50)	5.05	0.50	0.43
BR	173(15)	0.86	0.81	0.95	3143(59)	5.68	0.52	0.38
BT	185(16)	2.33	0.81	0.95	7087(85)	7.86	0.68	0.54
weighted average						5.86	0.28	0.46

Table 6.26: P_n results, using the number of slow-recoil ions.

144Cs.02 Dataset

ΔE-MCP	$n^c_{\beta R}$	$\omega_{\beta r}$	f	(1-P_n)	$n_{\beta r}$	P_n(%)	$\sigma_{P_n}(stat.)$	$\sigma_{P_n}(sys.)$
LR	306(33)	4.59	0.69	0.97	50494(232)	3.92	0.43	0.30
LT	352(27)	0.54	0.69	0.97	11086(115)	2.40	0.18	0.18
BR	347(33)	0.70	0.69	0.97	15728(140)	2.17	0.21	0.15
BT	337(29)	3.80	0.69	0.97	38249(201)	4.71	0.41	0.31
weighted average						2.66	0.13	0.19

Table 6.27: P_n results, using the number of slow-recoil ions.

145Cs.02 Dataset

ΔE-MCP	$n^c_{\beta R}$	$\omega_{\beta r}$	f	(1-P_n)	$n_{\beta r}$	$P_n(\%)$	$\sigma_{P_n}(stat.)$	$\sigma_{P_n}(sys.)$
LR	524(32)	2.92	0.76	0.85	11850(125)	14.46	0.89	0.75
LT	557(28)	0.61	0.76	0.85	2615(69)	14.67	0.83	1.11
BR	517(30)	0.80	0.76	0.85	3397(88)	13.55	0.87	0.71
BT	456(29)	2.33	0.76	0.85	10072(112)	11.81	0.77	0.71
weighted average						13.53	0.42	0.82

Table 6.28: P_n results, using the number of slow-recoil ions.

species also contribute to the β-γ counts, and need to be subtracted. The magnitude of the subtraction can be accomplished by considering the number of β-γ counts as a function of cycle time. During the trap-empty cycle, the activity comes only from untrapped species, and decays with the radioactive half-life of the species, with an initial activity determined by the build-up during the trap-full cycle. Hence, by considering the lengths of trap-empty and trap-full cycles and the species half-life, we can determine the number of untrapped decays during the trap-full cycle from the number of counts during the trap-empty cycle. The two numbers are related by a subtraction factor we refer to as x. The subtraction factor x is defined as:

$$x = \frac{n^F_{U\beta}}{n^E_{U\beta}} = \frac{n^F_{\beta\gamma} - n^F_{T\beta\gamma}}{n^E_{\beta\gamma}}, \tag{6.10}$$

where the F and E superscripts stand for counts integrated over the trap-full or trap-empty cycle, respectively, while the U and T specify the untrapped and trapped populations. With the numbers measured in the β-singles measurement, $n^F_{U\beta}$ and $n^E_{U\beta}$, the number of trapped β-γ's, $n^F_{T\beta\gamma}$, can be found as:

$$n^F_{T\beta\gamma} = n^F_{\beta\gamma} - x n^E_{\beta\gamma}. \tag{6.11}$$

The total β-γ numbers, with the subtraction performed, are summarized in Table 6.29. The table also lists which γ's were used in the analysis.

6.5.1 Systematic uncertainty in the $P_n^{\beta\gamma}$ value

The total systematic uncertainty in $P_n^{\beta\gamma}$ combined the contributions from the systematic uncertainties in the f value, MCP solid angle and intrinsic efficiency, as well as the ratio of the $\omega_{\beta\gamma}$ to $\omega_{\beta R}$. The systematic uncertainty in the $\omega_{\beta\gamma}/\omega_{\beta R}$ ratio is obtained in the same way as was done for both $\omega_{\beta}/\omega_{\beta R}$ and $\omega_{\beta r}/\omega_{\beta R}$ ratios, described in Sections 6.3.1 and 6.4.1. Section 4.2.3 describes how the $\omega_{\beta\gamma}$ value is obtained using the simulations. The resulting $\omega_{\beta\gamma}/\omega_{\beta R}$ relative uncertainties (with its contributions broken down) and the

		Top HPGe			Right HPGe		
Dataset	γ (keV)	$n^T_{\beta\gamma}$	$\sigma_{\beta\gamma}$(stat.)	$\sigma_{\beta\gamma}$(sys.)	$n^R_{\beta\gamma}$	$\sigma_{\beta\gamma}$(stat.)	$\sigma_{\beta\gamma}$(sys.)
^{137}I.07	1218	1598976	68384	162778	1504810	83175	150682
^{138}I.06	588	1499857	29511	146940	1447839	32157	139123
^{138}I.07	588	635062	28783	62217	641991	29484	61689
^{144}Cs.02	200	4509924	74291	367581	3821863	52641	544513
^{145}Cs.02	175	-	-	-	733644	56362	90961

Table 6.29: β-γ counts, with the associated statistical and systematic uncertainties. The γ intensity and the HPGe efficiency have already been taken into account, as have the subtractions of untrapped counts.

remaining systematic uncertainties adding to the total $\sigma(P_n^{\beta\gamma})$ uncertainty value for each isotope are listed in Tables 6.30, 6.31, 6.32, and 6.33.

Another contribution to the $\sigma(P_n^{\beta\gamma})$ value results from the uncertainty in the intrinsic HPGe efficiency, as well as the uncertainty in the γ branching ratio numbers. For most isotope cases studied in this work, this uncertainty is on the order of $\sim$10%. These additional systematic uncertainties, associated only with the γ detectors, are listed separately in Table 6.34.

6.5.2 $P_n^{\beta\gamma}$ results

Although the number of β-γ coincidences is relatively free from isobaric contaminants, these numbers still suffer from the subtraction of the counts due to the untrapped species, as well as generally lower statistics, limited by the low efficiency of the HPGe detectors. The resulting $P_n^{\beta\gamma}$ values are listed in Tables 6.35, 6.36, 6.37, 6.38, and 6.39. These results are presented slightly differently from the other methods: the total number of decays is first found with Equations 6.1 and 6.6. The individual detector combinations are then summed weighted with their statistical uncertainties, as are their systematic uncertainties. The ratio of the $N_{\beta R}$ to the total number of decays given by the β-γ counts N_β, or the $P_n^{\beta\gamma}$ value, is derived using the total numbers.

The summary of all the P_n results from the three methods, and comparisons to the IAEA P_n evaluations, are listed in the next, concluding Chapter 7.

	ΔE-MCP			
Systematic Effect	LR	LT	BR	BT
$\sigma_{\Delta E}$	5.4	2.0	2.5	5.4
σ_{MCP}	0.8	4.1	0.7	6.1
σ_S	2.2	1.8	1.8	2.2
$\sigma(\omega_{\beta r}/\omega_{\beta R})$	5.9	4.9	3.1	8.4
σ(low-TOF)	1.4	1.6	2.1	1.4
$\sigma(\Omega_{MCP})$	2.4	2.3	2.4	2.3
$\sigma(\varepsilon_{MCP})$	10.0	10.0	10.0	10.0
$\sigma(f)$	1.3	1.3	1.3	1.3
$\sigma_{P_n^{\beta\gamma}}$(Sys.) for ^{137}I.07	12.0	11.6	11.0	13.4

Table 6.30: Relative contribution from different systematic effects to the total uncertainty in the $P_n^{\beta\gamma}$ value for the ^{137}I.07 dataset. The uncertainties are given in % relative to each value, and for each detector combination. The first three rows refer to the contributions to the total uncertainty in the $\omega_{\beta\gamma}/\omega_{\beta R}$ ratio.

	ΔE-MCP			
Systematic Effect	LR	LT	BR	BT
$\sigma_{\Delta E}$	3.9	1.0	0.7	2.9
σ_{MCP}	0.8	2.3	0.5	3.6
σ_S	1.5	1.0	1.3	1.5
σ(low-TOF) for ^{138}I.06	2.0	0.6	1.1	1.3
σ(low-TOF) for ^{138}I.07	3.6	2.7	0.2	0.0
$\sigma(\Omega_{MCP})$	2.4	2.3	2.4	2.3
$\sigma(\varepsilon_{MCP})$	10.0	10.0	10.0	10.0
$\sigma(f)$	6.6	6.6	6.6	6.6
$\sigma_{P_n^{\beta\gamma}}$(Sys.) for ^{138}I.06	13.1	12.5	12.3	13.2
$\sigma_{P_n^{\beta\gamma}}$(Sys.) for ^{138}I.07	13.4	12.8	12.3	13.1

Table 6.31: Relative contribution from different systematic effects to the total uncertainty in the $P_n^{\beta\gamma}$ value for the ^{138}I.06 and ^{138}I.07 datasets. The uncertainties are given in % relative to each value, and for each detector combination. The first three rows refer to the contributions to the total uncertainty in the $\omega_{\beta\gamma}/\omega_{\beta R}$ ratio.

	ΔE-MCP			
Systematic Effect	LR	LT	BR	BT
$\sigma_{\Delta E}$	2.3	0.2	0.6	1.7
σ_{MCP}	0.1	1.8	0.4	1.7
σ_S	1.2	0.9	0.8	1.0
σ(low-TOF)	4.2	1.8	2.9	2.5
$\sigma(\Omega_{MCP})$	2.4	2.3	2.4	2.3
$\sigma(\varepsilon_{MCP})$	10.0	10.0	10.0	10.0
$\sigma(f)$	5.6	5.6	5.6	5.6
$\sigma_{P_n^{\beta\gamma}}$(Sys.) for ^{144}Cs.02	12.7	12.0	12.1	12.2

Table 6.32: Relative contribution from different systematic effects to the total uncertainty in the $P_n^{\beta\gamma}$ value for the ^{144}Cs.02 dataset. The uncertainties are given in % relative to each value, and for each detector combination. The first three rows refer to the contributions to the total uncertainty in the $\omega_{\beta\gamma}/\omega_{\beta R}$ ratio.

	ΔE-MCP			
Systematic Effect	LR	LT	BR	BT
$\sigma_{\Delta E}$	2.1	0.1	0.3	3.1
σ_{MCP}	0.2	2.6	0.4	2.5
σ_S	0.0	0.8	0.8	0.7
σ(low-TOF)	1.7	0.7	1.7	2.0
$\sigma(\Omega_{MCP})$	2.4	2.3	2.4	2.3
$\sigma(\varepsilon_{MCP})$	10.0	10.0	10.0	10.0
$\sigma(f)$	4.3	4.3	4.3	4.3
$\sigma_{P_n^{\beta\gamma}}$(Sys.) for ^{145}Cs.02	11.5	11.5	11.3	12.0

Table 6.33: Relative contribution from different systematic effects to the total uncertainty in the $P_n^{\beta\gamma}$ value for the ^{144}Cs.02 dataset. The uncertainties are given in % relative to each value, and for each detector combination. The first three rows refer to the contributions to the total uncertainty in the $\omega_{\beta\gamma}/\omega_{\beta R}$ ratio.

	Systematic Uncertainty (%)	
Isotope	Right HPGe	Top HPGe
^{137}I	10.2	10.0
^{138}I	9.8	9.6
^{144}Cs	8.2	14.2
^{145}Cs	12.4	-

Table 6.34: Relative systematic uncertainty in the $P_n^{\beta\gamma}$ resulting from the uncertainty in the γ branching ratio values and the HPGe efficiency.

		137I.07			
ΔE-MCP	$n_{\beta R}^{cd} \pm \sigma_{stat} \pm \sigma_{sys}$	Ω_{MCP}	ε_{MCP}	f	$N_{\beta R} \pm \sigma_{stat} \pm \sigma_{sys}$
LR	613 ± 32 ± 9	0.051	0.25	0.96	50388 ± 2593 ± 6036
LT	629 ± 28 ± 10	0.051	0.27	0.96	47602 ± 2101 ± 5504
BR	638 ± 31 ± 13	0.051	0.25	0.96	52423 ± 2536 ± 5769
BT	667 ± 31 ± 9	0.051	0.27	0.96	50434 ± 2337 ± 6763
weighted average					49959 ± 1184 ± 5996
HPGe	$n_{\beta\gamma} \pm \sigma_{stat} \pm \sigma_{sys}$	$\omega_{\beta\gamma}$			$N_{\beta\gamma} \pm \sigma_{stat} \pm \sigma_{sys}$
Top	1598976 ± 68384 ± 162778	1.35			592244 ± 25329 ± 60291
Right	1504810 ± 83175 ± 150682	1.35			557366 ± 30807 ± 55811
weighted average					578177 ± 19565 ± 58470
$P_n^{\beta\gamma} = N_{\beta R}/N_{\beta\gamma}$					8.64 ± 0.36 ± 1.36

Table 6.35: P_n results, using the β-γ coincidence number.

138I.06

ΔE-MCP	$n_{\beta R}^{cd} \pm \sigma_{stat} \pm \sigma_{sys}$	Ω_{MCP}	ε_{MCP}	f	$N_{\beta R} \pm \sigma_{stat} \pm \sigma_{sys}$
LR	419 ± 27 ± 8	0.051	0.25	0.81	40953 ± 2591 ± 5347
LT	469 ± 23 ± 3	0.051	0.27	0.81	42157 ± 2040 ± 5266
BR	478 ± 25 ± 5	0.051	0.25	0.81	46763 ± 2488 ± 5773
BT	439 ± 25 ± 6	0.051	0.27	0.81	39435 ± 2223 ± 5201
weighted average					42176 ± 1152 ± 5381
HPGe	$n_{\beta\gamma} \pm \sigma_{stat} \pm \sigma_{sys}$	$\omega_{\beta\gamma}$			$N_{\beta\gamma} \pm \sigma_{stat} \pm \sigma_{sys}$
Top	1499857 ± 29511 ± 146940	1.37			545915 ± 10741 ± 53483
Right	1447839 ± 32157 ± 139123	1.37			526981 ± 11704 ± 50638
weighted average					537259 ± 7914 ± 52173
$P_n^{\beta\gamma} = N_{\beta R}/N_{\beta\gamma}$					7.85 ± 0.24 ± 1.26

Table 6.36: P_n results, using the β-γ coincidence number.

138I.07

ΔE-MCP	$n_{\beta R}^{cd} \pm \sigma_{stat} \pm \sigma_{sys}$	Ω_{MCP}	ε_{MCP}	f	$N_{\beta R} \pm \sigma_{stat} \pm \sigma_{sys}$
LR	178 ± 18 ± 6	0.051	0.25	0.81	17431 ± 1716 ± 2337
LT	149 ± 14 ± 4	0.051	0.27	0.81	13395 ± 1214 ± 1711
BR	184 ± 15 ± 0.3	0.051	0.25	0.81	17998 ± 1500 ± 2213
BT	197 ± 16 ± 0.01	0.051	0.27	0.81	17756 ± 1428 ± 2331
weighted average					16240 ± 716 ± 2089
HPGe	$n_{\beta\gamma} \pm \sigma_{stat} \pm \sigma_{sys}$	$\omega_{\beta\gamma}$			$N_{\beta\gamma} \pm \sigma_{stat} \pm \sigma_{sys}$
Top	635062 ± 28783 ± 62217	1.37			231149 ± 10476 ± 22646
Right	641991 ± 29484 ± 61689	1.37			233671 ± 10731 ± 22453
weighted average					232379 ± 7496 ± 22553
$P_n^{\beta\gamma} = N_{\beta R}/N_{\beta\gamma}$					6.99 ± 0.38 ± 1.13

Table 6.37: P_n results, using the β-γ coincidence number.

144Cs.02

ΔE-MCP	$n_{\beta R}^{cd} \pm \sigma_{stat} \pm \sigma_{sys}$	Ω_{MCP}	ε_{MCP}	f	$N_{\beta R} \pm \sigma_{stat} \pm \sigma_{sys}$
LR	336 ± 33 ± 14	0.051	0.25	0.69	38441 ± 3830 ± 4872
LT	386 ± 27 ± 7	0.051	0.27	0.69	40613 ± 2833 ± 4872
BR	380 ± 33 ± 11	0.051	0.25	0.69	43529 ± 3758 ± 5270
BT	370 ± 29 ± 9	0.051	0.27	0.69	38939 ± 3104 ± 4766
weighted average					40299 ± 1650 ± 4921
HPGe	$n_{\beta\gamma} \pm \sigma_{stat} \pm \sigma_{sys}$	$\omega_{\beta\gamma}$			$N_{\beta\gamma} \pm \sigma_{stat} \pm \sigma_{sys}$
Top	4509924 ± 74291 ± 367581	1.39			1625760 ± 26781 ± 132508
Right	3821863 ± 52641 ± 544513	1.39			1377725 ± 18976 ± 196289
weighted average					1460633 ± 15483 ± 178334
$P_n^{\beta\gamma} = N_{\beta R}/N_{\beta\gamma}$					2.76 ± 0.12 ± 0.48

Table 6.38: P_n results, using the β-γ coincidence number.

145Cs.02

ΔE-MCP	$n_{\beta R}^{cd} \pm \sigma_{stat} \pm \sigma_{sys}$	Ω_{MCP}	ε_{MCP}	f	$N_{\beta R} \pm \sigma_{stat} \pm \sigma_{sys}$
LR	554 ± 32 ±10	0.051	0.25	0.76	57454 ± 3297 ± 6620
LT	589 ± 28 ± 4	0.051	0.27	0.76	56222 ± 2634 ± 6384
BR	547 ± 30 ± 9	0.051	0.25	0.76	56666 ± 3129 ± 6399
BT	482 ± 29 ±10	0.051	0.27	0.76	45983 ± 2804 ± 5518
weighted average					53764 ± 1466 ± 6210
HPGe	$n_{\beta\gamma} \pm \sigma_{stat} \pm \sigma_{sys}$	$\omega_{\beta\gamma}$			$N_{\beta\gamma} \pm \sigma_{stat} \pm \sigma_{sys}$
Right	733644 ± 56362 ± 90961	1.38			265817 ± 20421 ± 32957
$P_n^{\beta\gamma} = N_{\beta R}/N_{\beta\gamma}$					20.23 ± 1.65 ± 3.43

Table 6.39: P_n results, using the β-γ coincidence number.

Chapter 7

Summary and conclusions

The experimental campaign of 2013 was built upon the results of the proof-of-principle experiment, and its main motivation was to demonstrate the limits of the technique and to identify the necessary areas of improvement in a scaled-up setup. For that reason, isotopes studied in this work have been measured previously with other techniques, many to a high precision. The larger statistics accessible in this run (compared with the low-statistics in the proof-of-principle experiment) exposed several challenges and systematic errors, which can now be addressed in future iterations of the experiment.

This concluding chapter summarizes the branching ratio results. The largest sources of systematic uncertainty are discussed, along with plans for future expansion and improvements to the experimental array.

7.1 Summary of results

The P_n results, the outcome of the analysis discussed in great detail in Chapter 6, are summarized in Tables 7.1, 7.2, 7.3, 7.4, and 7.5. The results are also visually displayed in Figures 7.1, 7.2, 7.3, and 7.4. Clearly, the systematic effects are the dominant source of uncertainty for all the methods. Though most of our measurements are precise to within 10%, the β-γ P_n method tends to be uncertain up to 15% in part due to the the $\sim$10% uncertainty in the γ-ray branching ratios obtained from literature. The systematic uncertainties in the ^{137}I dataset contain in addition a contribution from the ^{137}Te contaminant, for both the slow and fast recoil ion numbers, increasing the systematic uncertainty.

The results are consistent with the IAEA evaluation with most P_n values within $\pm$ 1 σ. The method yielding a P_n value with the smallest uncertainty is the slow-recoil method $P_n^{\beta r}$. For $P_n^{\beta r}$, the biggest source of systematic uncertainty is the $\omega_{\beta r}$ value found through simulations, which relies on the knowledge of the decay scheme. However, it is much less sensitive to the MCP intrinsic efficiency.

137I.07 Dataset

Method	P_n (%)	Stat. Unc.	Sys. Unc.	Total Frac. Unc.
P_n^{β}	7.39	0.18	0.88	12%
$P_n^{\beta\gamma}$	8.64	0.35	1.36	16%
$P_n^{\beta r}$	7.18	0.19	0.81	12%
IAEA Eval.	7.14		0.23	3%

Table 7.1: P_n results for ^{137}I, compared to the IAEA evaluation. The total uncertainty consist of the statistical and systematic uncertainties added in quadrature. For the IAEA evaluation, the uncertainty does not distinguish between statistical and systematic, and hence the listed error is the combination of both.

138I.06 Dataset

Method	P_n (%)	Stat. Unc.	Sys. Unc.	Total Frac. Unc.
P_n^{β}	7.02	0.19	0.90	13%
$P_n^{\beta\gamma}$	7.85	0.24	1.26	16%
$P_n^{\beta r}$	6.32	0.19	0.48	8%
IAEA Eval.	5.43		0.22	4%

Table 7.2: P_n results for ^{138}I, dataset 06.

138I.07 Dataset

Method	P_n (%)	Stat. Unc.	Sys. Unc.	Total Frac. Unc.
P_n^{β}	6.90	0.31	0.89	14%
$P_n^{\beta\gamma}$	6.99	0.38	1.13	17%
$P_n^{\beta r}$	5.86	0.28	0.46	9%
IAEA Eval.	5.43		0.22	4%

Table 7.3: P_n results for ^{138}I, dataset 07.

144Cs.02 Dataset

Method	P_n (%)	Stat. Unc.	Sys. Unc.	Total Frac. Unc.
P_n^{β}	2.98	0.12	0.36	13%
$P_n^{\beta\gamma}$	2.76	0.12	0.48	18%
$P_n^{\beta r}$	2.66	0.13	0.19	9%
IAEA Eval.	3.03		0.13	4%

Table 7.4: P_n results for ^{144}Cs.

145Cs.02 Dataset

Method	P_n (%)	Stat. Unc.	Sys. Unc.	Total Frac. Unc.
P_n^{β}	15.78	0.44	1.83	12%
$P_n^{\beta\gamma}$	20.23	1.65	3.43	19%
$P_n^{\beta r}$	13.53	0.42	0.82	7%
IAEA Eval.	14.70		0.90	6%

Table 7.5: P_n results for ^{145}Cs.

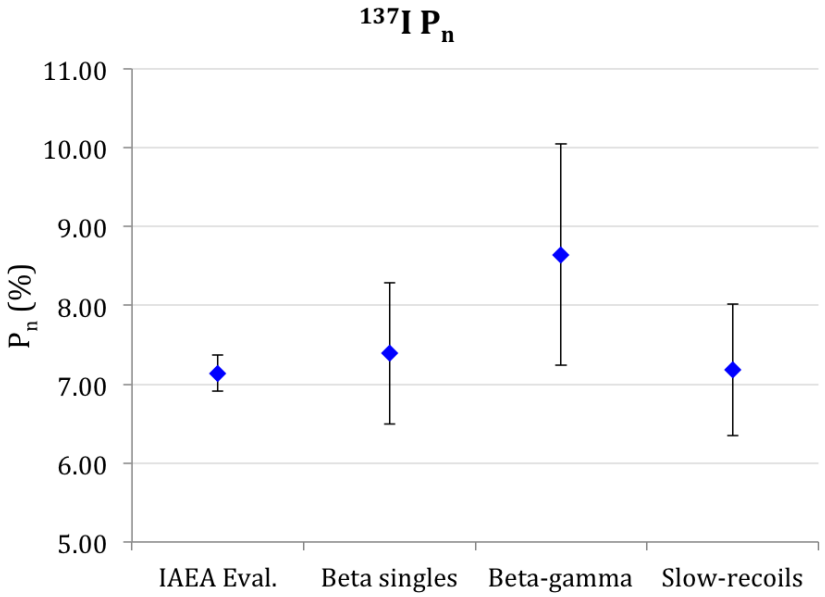

Figure 7.1: ^{137}I P_n results obtained with three different methods, compared against the IAEA evaluation. The error bars contain the combined statistical and systematic uncertainties.

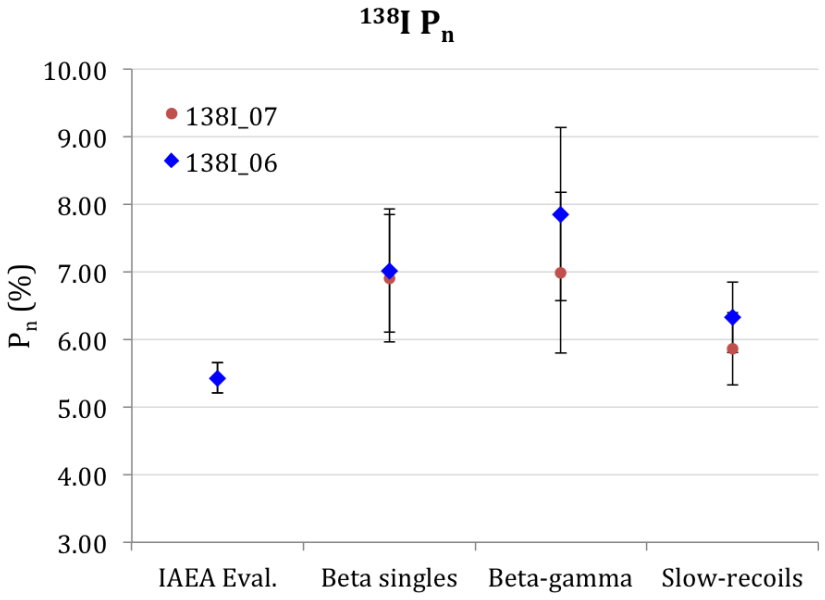

Figure 7.2: ^{138}I P_n results obtained with three different methods for the two datasets taken during the BDN2013 experimental run, compared against the IAEA evaluation. The error bars contain the combined statistical and systematic uncertainties.

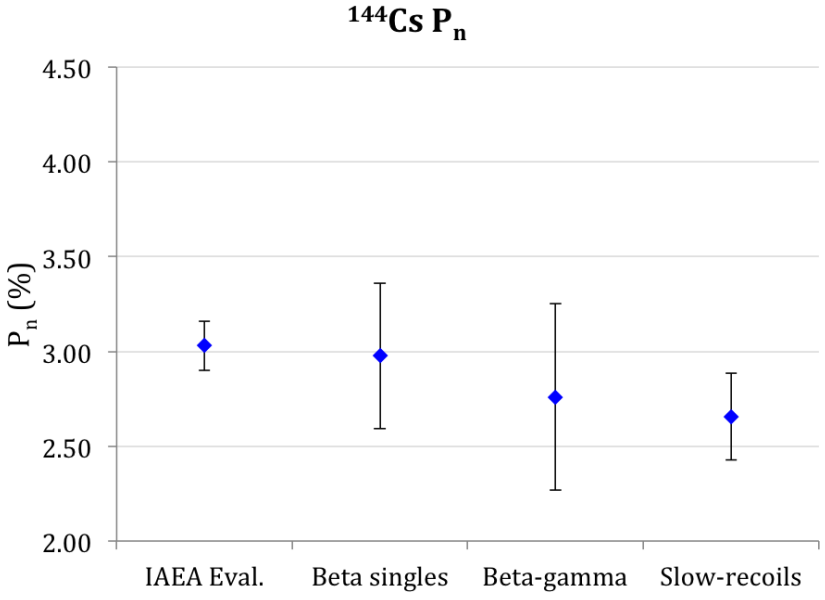

Figure 7.3: ^{144}Cs P_n results obtained with three different methods, compared against the IAEA evaluation. The error bars contain the combined statistical and systematic uncertainties.

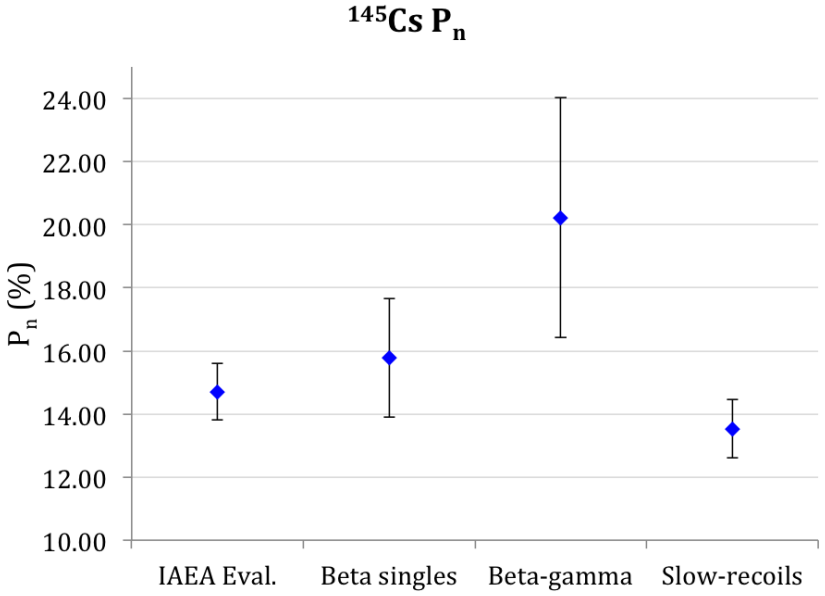

Figure 7.4: ^{145}Cs P_n results obtained with three different methods, compared against the IAEA evaluation. The error bars contain the combined statistical and systematic uncertainties.

^{137}I P_n results

The branching ratio results from the β-singles and slow-recoil analysis agree well with the IAEA evaluation and results from literature. The βn emission of this isotope has been thoroughly studied with various techniques, and its decay scheme is well-known. The close agreement with previous results confirms that the experiment described in this thesis was successful in reproducing results, giving credibility to the remaining isotope measurements.

The P_n value from the β-γ analysis is about 15% higher than the P_n values given by the other methods. Both the statistical and systematic uncertainty for this method are quite high. In addition, right next to the 1218-keV γ-line lies a 1220-keV line with a 3.5% absolute intensity (compared with 12.8% for the 1218-keV line that we use for the analysis). The contamination from the neighboring line increases the uncertainty of the result.

^{138}I P_n results

Both of the ^{138}I datasets show P_n results approximately 1 σ larger than the IAEA evaluation values, for all three methods. The ^{138}I results eliminate the possibility of the P_n to be around 2%, as measured by Perlow et. al. [76], and later by Asghar et. al. [77]. Though IAEA does not include these measurements in their evaluation, it is a confirmation of their invalidity, as demonstrated by the use of an independent recoil ion measurement technique in this work.

^{144}Cs P_n results

P_n results from the three techniques yield a good agreement with the IAEA evaluation. In the case of ^{144}Cs, the decay scheme was incomplete, with unknown β intensities to daughter states. Although in general the sensitivity to the decay scheme does not strongly influence the $\omega_{\beta r}$ value, the effect was pronounced in the $P_n^{\beta r}$ result given the small βn branching ratio.

The low-TOF background was the largest for this isotope. A large contribution to the systematic uncertainties resulted from the uncertainties associated with the specific background subtraction method used. This background will need to be thoroughly investigated and hopefully eliminated in future experiments.

Despite a few challenges relating to the ^{144}Cs measurement, such as its low P_n value, the branching ratio results agree well with previous results. The ^{144}Cs measurement demonstrated that high-quality data could be collected even for isotopes with small P_n values.

^{145}Cs P_n results

The ^{145}Cs slow recoil ion TOF spectrum was influenced by the presence of high charge-states that produced a noticeable increase in counts at lower TOF's than the main population of the slow recoil ions. The amount of conversion electrons, as revealed by comparing data with simulation, was larger than the values found in literature. These two factors contributed to the uncertainty associated with the $P_n^{\beta r}$. In addition, the γ line used in the analysis lies at 175-keV, which is on a rapidly-changing region of the HPGe efficiency curve. The large efficiency uncertainty increases the systematic uncertainty of the $P_n^{\beta\gamma}$ results.

7.2 Addressing the challenges

An obvious area of improvement is reduction in backgrounds. The β-singles method, though containing the largest amount of statistics, was limited by the isobaric contaminants and the contributions from the untrapped species. A better isobaric separation, achievable with the Multireflection Time-of-Flight system (MR-TOF) at CARIBU, should resolve this issue. However, special attention should be paid to verifying optimal ion trap performance, as the reduced trap storage time resulting from a leak during the 2013 campaign encumbered the analysis and decreased the available statistics.

The unexpected background at low-TOF could be studied and characterized more fully by running the trap-empty measurement cycle for a longer time. Reducing the MCP ringing could also resolve this background. Furthermore, if the MCPs were to be placed farther from the trap center, the fast ion signal would be at longer TOF's from the low-TOF background tail, reducing the amount of low-TOF background in the neutron energy spectrum.

Interpreting the 180° detector combination presented several challenges: the sensitivity to the kinematic focusing, the energy correction due to the lepton recoil, and the background in the plastic detectors due to neutrons. Employing other angles between the detectors could

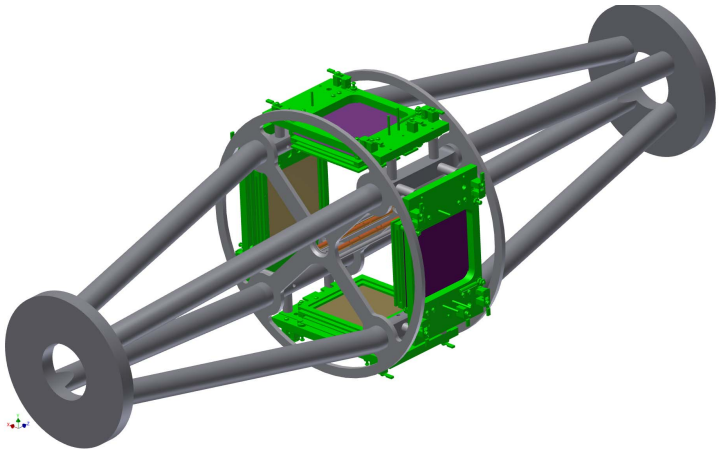

Figure 7.5: One of the planned versions of the new Beta-Paul Trap, surrounded by four MCP's. The new design employs rod electrodes, pictures as orange here. Design by T. Levand.

reduce the uncertainties associated with these challenges. The kinematic focusing can be better characterized with a more detailed knowledge of the decay scheme, which can be supplemented with additional experiments (such as the X-array at CARIBU). Lastly, the neutron signal within the plastic detectors could be better characterized by measuring the neutrons with a dedicated neutron detector.

The derived MCP efficiency from the ^{134}Sb calibration data was unexpectedly low, and the complications arising from the isomer subtraction and incomplete knowledge of the ^{134}Sb decay scheme resulted in a relatively large uncertainty on this value. Future experiments would benefit from an improved calibration, especially now that the challenges involved with using ^{134}Sb have been exposed. Possibly using another calibration isotope, such as ^{92}Rb, would uncover any remaining systematic effects affecting the efficiency value.

7.3 Future experimental plans

The plans for the future experimental campaign include the expansion of the current detector array and the use of higher-intensity fission fragment beams currently available at CARIBU to increase statistics. Challenges encountered in previous experiments will be addressed to decrease the systematic uncertainties. The new detector array is planned to consist of eight ΔE-E plastic scintillators, four MCPs, and four HPGe's. A proposed version of the detector placement around the new BPT chamber is shown in Figures 7.5 and 7.6. The new array will also have different angles between the detectors. The 180° combination proved to be problematic, and avoiding this particular back-to-back detector combination may greatly simplify the analysis.

The MCP response can be improved by employing a 3-plate Z-stack instead of the cur-

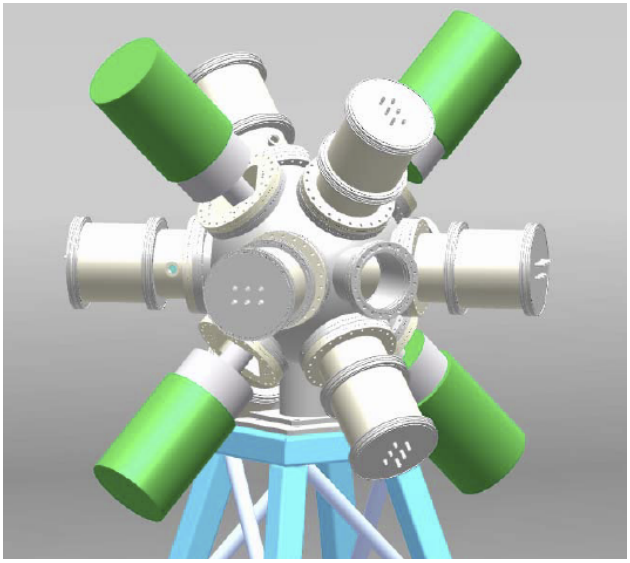

Figure 7.6: Rendition of the new BPT chamber, showing four HPGe's (green cylinders), and eight plastic detectors (grey cylinders). Design by T. Levand.

rently used 2-plate Chevron configuration of the plates. This increases the electron multiplication and the detection efficiency. Additionally, a larger anode would prevent the apodization effect seen in our data, increasing the fiducial area of the detector. Lastly, better care should be taken when setting the gain of the MCPs to ensure that the lower tail of the signal's PHD is above the discriminator threshold. Another systematic effect that complicated the analysis was the ringing seen in the MCP timing signal. An investment in the improvement of the readout electronics and data acquisition to ensure less noise would be worthwhile.

The Beta-Paul Trap itself is planned to undergo improvements. By decreasing the trap radius, lower RF fields can be used, which would decrease the disruption of the slow recoil ions. In the next iteration of the trap, a low-profile rod electrode design will be employed, instead of electrode plates. The lower profile of the electrodes should decrease the amount of β scattering and backgrounds from untrapped species coating the electrodes.

Lastly, the next experimental campaign at CARIBU will take advantage of higher-intensity fission fragment beams from a 1-Ci ^{252}Cf source, and better isobar separation achieved with the newly installed MR-TOF. The isobar separation will be able to eliminate the nearest neighbor isobars, considerably purifying the beam, and therefore reducing systematic uncertainties associated with eliminating the isobar contaminant backgrounds.

The planned improvements will not only simplify the analysis, but also reduce uncertainties from various systematic effects. The higher statistics will push the boundary of our detection ability farther out of the valley of stability, allowing to probe the previously unattainable neutron-rich nuclei, and opening an exciting era in nuclear physics studies.

Appendix A

Glossary

P_n	β-delayed neutron emission branching ratio, deduced from the ratio $N_{\beta R}/N_\beta$.
$N_{\beta R}$	The total number of β-delayed neutrons emitted for the precursor in the dataset.
N_β	The total number of β decays emitted by the precursor in the dataset.
P_n^β	Branching ratio deduced using the total number of β-singles for N_β.
$P_n^{\beta\gamma}$	Branching ratio deduced using the number of γ's coincident with β's.
$P_n^{\beta r}$	Branching ratio deduced using the number of recoil-ions following β-decay without neutron emission.
n_β	Observed number of β's from the precursor of interest.
$n_{\beta\gamma}$	Observed number of β-γ coincidences from the precursor of interest.
$n_{\beta R}$	Observed number of βn decays from the precursor of interest.
$n_{\beta R}^c$	$n_{\beta R}$ number corrected by $\omega_{\beta R}(\mathrm{E}_n)$, where E_n is the deduced energy of the neutron.
$n_{\beta R}^{cd}$	$n_{\beta R}^c$ corrected for deadtime.
f	Fraction of neutron energy spectrum expected above our detection threshold, estimated from literature results.
Ω_{MCP}	MCP detector solid angle.
Ω_β	Plastic detector solid angle.
ε_{MCP}	Intrinsic MCP efficiency.
ε_β	Intrinsic plastic detector efficiency, included within the ω values (listed below).

ω_β Modification from unity to efficiency for detecting β's, averaged over all energies. Includes effects due to scattering, detector thresholds, energy loss through Kapton window, and backgrounds from conversion electrons, γ's and neutrons.

$\omega_{\beta R}$ Modification from unity to efficiency for detecting recoil-ions associated with neutron emission, averaged over all energies. Includes effects due to MCP energy-dependent efficiency in addition to effects associated with β detection.

$\omega_{\beta\gamma}$ Modification from unity for detecting β-γ events, averaged over all energies. Includes effects due to conversion electrons in addition to effects associated with β detection.

$\omega_{\beta r}$ Modification from unity to efficiency for detecting recoil-ions without neutron emission, averaged over all energies. Includes effects due to kinematic focusing, RF field, charge-state distribution and MCP energy-dependent efficiency, in addition to effects associated with β detection.

C_n Correction to the total number of detected recoil ions, due to direct detections of neutrons in the plastic detectors

ε_n Direct neutron detection threshold in the plastic detectors.

K_f Kinematic focusing effect for low-energy recoil-ions (not associated with neutron emission), defined as the number of recoil-ions detected in the 180° detector combination divided by the number detected in the 90° detector combination.

Appendix B

Primer on the Trap Population Model

The short summary of the TPM presented here is based on Shane Caldwell's exhaustive discussion in his thesis [63]. This appendix serves as an overview of the TPM parameters, and description of the populations included.

The model accounts for three species present in the beam, where the species of interest and its nearest neighbors form a β decay chain. Species 1 is a parent of species 2, which in turn is a parent to species 3. Following this convention, species 2 is the actual measured species of interest. The trapped population of each species is defined as $T_i(t)$, and its untrapped component as $U_i(t)$. The end goal of the analysis is to obtain the T_2 component of the population.

The TPM obeys the following assumptions:

1. Trapped ions are only present during the capture part of the measurement cycle, i.e. $T_i(t) = 0$ during the background measurement.
2. The untrapped populations are continuous between the cycles, i.e. $U_i(0) = U_i(t_C)$.
3. Rates of ion injections stay constant during the trapping period (at each capture event).
4. Capture efficiency of the trap is the same for all three species due to their similar masses.
5. Retention efficiency of trapped ions during incoming ion bunch injections is the same for all species.
6. Every radioactive decay species i (trapped or untrapped) produces an untrapped ion of species $i + 1$.

The detection rate $D(t)$ is the sum of all the observed β decays from the species of the entire population, and is related to the height of the histogram bin with a width Δt at a specific time t via:

$$y(t) = N_C D(t) \Delta t. \tag{B.1}$$

The N_C in the above equation denotes the total number of measurement cycles performed over the course of the entire data-taking period. The detection rate of each species is the product of the decay rate (population/lifetime) and the detection efficiency of that population CE (which will vary between trapped and untrapped components):

$$D_i(t) = \varepsilon P_i/\tau_i, \tag{B.2}$$

where P_i is the population of species i (untrapped or trapped), and τ is the radioactive lifetime of species i.The entire population in the BPT then consists of the DC room background (D_0), and the trapped and untrapped species summed over the three species. Rewriting the fit function Eq. B.1 in terms of the detection rates from all the populations (using Eqn B.2), results in the total fit function:

$$\begin{aligned} y(t) = N_C \Bigg[& D_0 + \varepsilon_T \sum_{i=1}^{3} T_i(t)/\tau_i \\ & + \varepsilon_U \sum_{i=1}^{3} (\varepsilon_V V_i(t) + \varepsilon_W W_i(t) + \varepsilon_Z Z_i(t))/\tau_i \\ & + \varepsilon_U \sum_{i=2}^{3} (\varepsilon_X X_i(t) + \varepsilon_Y Y_i(t))/\tau_i \Bigg] \Delta t. \end{aligned} \tag{B.3}$$

The untrapped components are split into five separate populations (V, W, Z, X, Y), each with its own species-independent detection efficiency. The overall untrapped efficiency is set to 1 when all the component efficiencies have their own assigned values, and is included for computational simplicity. The untrapped components consist of the following populations, based on their source terms and dynamics:

V_i: Ions lost immediately following each ion bunch injection due to imperfect capture efficiency (fed by T_i)

W_i: Previously-trapped ions that become untrapped during a capture pulse (fed by T_i)

Z_i: Ions that become untrapped due to finite trap storage time (fed by T_i)

X_i: β decay children of trapped parent isotopes (fed by T_{i-1})

Y_i: β decay children of untrapped parent isotopes (fed by U_{i-1}).

By splitting the populations in this manner, we can apply appropriate dynamics equations to each population, and use appropriate detection efficiencies. The inter-dependance between the different populations is also clearer. All the parameters used in the model are summarized in Table B.1.

Symbol	Description	Value
	Parameters from data	
t_A	Time between captures (s)	5
t_B	Duration of background interval (s)	101
t_C	Duration of the measurement cycle (s)	246
τ_1	Radioactive lifetime of species 1 (s)	3.592
τ_2	Radioactive lifetime of species 2 (s)	35.346
τ_3	Radioactive lifetime of species 3 (s)	330.493
n_C	Number of cycles covered during the data taking period (#)	500
	Model parameters	
R_{DC}	Room background events rate (counts/s)	40
r_1	Rate of species 1 injected into the BPT (ions/s)	100
r_2	Rate of species 2 injected into the BPT (ions/s)	100
r_3	Rate of species 3 injected into the BPT (ions/s)	100
p	Capture efficiency of all species in BPT	0.71349
ρ	Retention efficiency of trapped ions during capture	0.93553
ε_T	Detection efficiency of T population	1
ε_V	Detection efficiency of V population	1
ε_W	Detection efficiency of W population	1
ε_X	Detection efficiency of X population	1
ε_Y	Detection efficiency of Y population	1
ε_Z	Detection efficiency of Z population	1
ε_U	Auxiliary efficiency of all untrapped populations	1
γ_{T1}	Non-radioactive decay rate of trapped species 1 (s^-1)	1/10
γ_{T2}	Non-radioactive decay rate of trapped species 2 (s^-1)	1/20
γ_{T3}	Non-radioactive decay rate of trapped species 3 (s^-1)	1/30
γ_{U1}	Non-radioactive decay rate of untrapped species 1 (s^-1)	1/40
γ_{U2}	Non-radioactive decay rate of untrapped species 2 (s^-1)	1/50
γ_{U3}	Non-radioactive decay rate of untrapped species 3 (s^-1)	1/60

Table B.1: Summary of parameters used in the Trap Population Model, with starting values that were used for the ^{137}I β-singles fits. These parameters need to be adjusted depending on the species of interest and known assumptions.

Having defined all the parameters used in the fitting equation, we can now discuss the source terms necessary to solve the equations. All the dynamics equations are built using the following first-order linear equation:

$$\frac{df}{dt} + \frac{f(t)}{\tau} = g(t). \tag{B.4}$$

This equation can be solved for any integrable function g.The linearity of the equation allows us to decompose the solution to the untrapped components for the two time periods, the "background" cycle and the "trapping" cycle:

$$f(t) = \begin{cases} f_B(t), & 0 \leq t \leq t_B \\ f_B(t) + f_A(t), & t_B < t \leq t_C \end{cases} \tag{B.5}$$

The variety in the solutions for each population is derived from the appropriate source term g applied. For ion injection, we use a δ function at each capture internal:

$$\frac{df}{dt} + \frac{f(t)}{\tau} = A\delta(t - t_1), \tag{B.6}$$

of which the solution is:

$$f(t) = \begin{cases} f(t_0)e^{-(t-t_0)/\tau}, & t < t_1 \\ f(t_0)e^{-(t-t_0)/\tau} + Ae^{-(t-t_1)/\tau}, & t \geq t_1 \end{cases} \tag{B.7}$$

where t_1 is the time in the cycle of the first capture (ion injection). In the full treatment we consider the sum of all the captures.

In case of feeding g by the decay of isotope population h at a rate of $1/\tau_{gh}$, the equation becomes:

$$\frac{dg}{dt} + \frac{g(t)}{\tau_g} = \frac{h(t)}{\tau_{hg}}. \tag{B.8}$$

The solution to the above equation takes the form:

$$g(t) = g(t_0)e^{-(t-t_0)/\tau_g} + h(t_0)\frac{e^{-(t-t_0)/\tau_g} - e^{-(t-t_0)/\tau_h}}{\tau_{hg}\Gamma_h^g}, \tag{B.9}$$

where $\Gamma_h^g \equiv 1/\tau_g - 1/\tau_h$.

The implementation of combinations of appropriate source terms for all the populations, and the resulting solutions are discussed in great detail in Shane Caldwell's thesis [63]. The model and the fit program were validated using a Monte Carlo simulation of the ^{137}I decay, resulting in an excellent agreement between the modeled number of trapped species and the calculated amount using the fitting function with the parameters listed in Table B.1. The comparison between the model and the simulation are shown in Fig. B.1.

In order to effectively use the fitting program, it is important to consider all the populations possibly present in the trap, based on other information derived from the dataset, such as the γ-ray and CPT data. The presence of isobaric contaminants in many cases can be

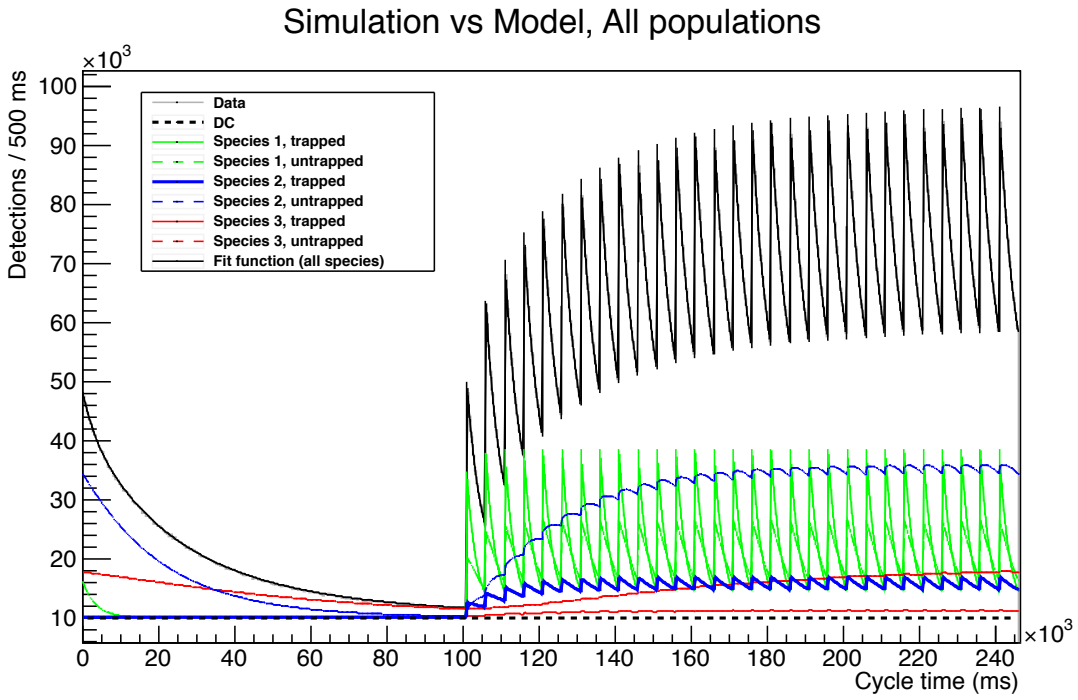

Figure B.1: Data generated with a Monte Carlo simulation for ^{137}I decay, with the fit from BFit2 (colored lines) accounting for all the present populations. The excellent agreement between the simulated numbers and the fit results validates the TPM.

eliminated, and disabled in the fit routine. Certain cuts placed on the data prior to fitting can also be used to cleanly extract parameter values. For example, plotting slow recoil ions vs. cycle time eliminates contributions from untrapped species, simplifying the analysis. Using this histogram, a series of fits can be produced with various values set for the trap storage lifetime. The fit with the best χ^2 value indicates the most probable value for the trap storage lifetime. In summary, using the TPM to analyze each isotope is a unique problem and requires the `BFit2` to be applied thoughtfully.

The `BFit2` is mainly used to extract β-singles number associated with the trapped precursor decay, as well as slow-recoil numbers in cases where isobaric contaminant is present. The fitting routine also helped to find the subtraction factor accounting for the amount of β-γ coincidences due to the untrapped species. Application of the `BFit2` in each specific case is discussed in more detail during the branching ratio discussion in Chapter 6.

Appendix C

Setup diagrams for the detector array

For completeness, this appendix contains diagrams showing how the detectors were set up for the experimental run. The diagrams show the NIM modules involved in signal processing, and the resulting connections into the CAMAC modules.

how all the detectors were wired, and showing all the NIM modules involved in the signal processing.

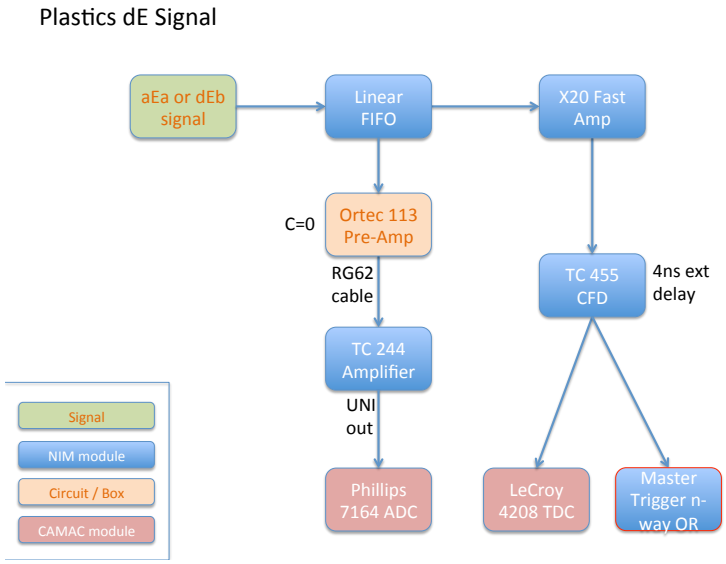

Figure C.1: ΔE plastic scintillator detectors electronics setup.

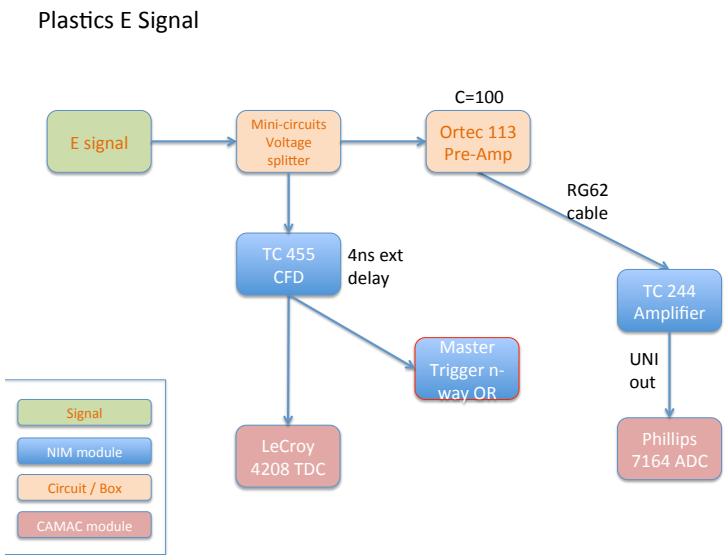

Figure C.2: E plastic scintillator detectors electronics setup.

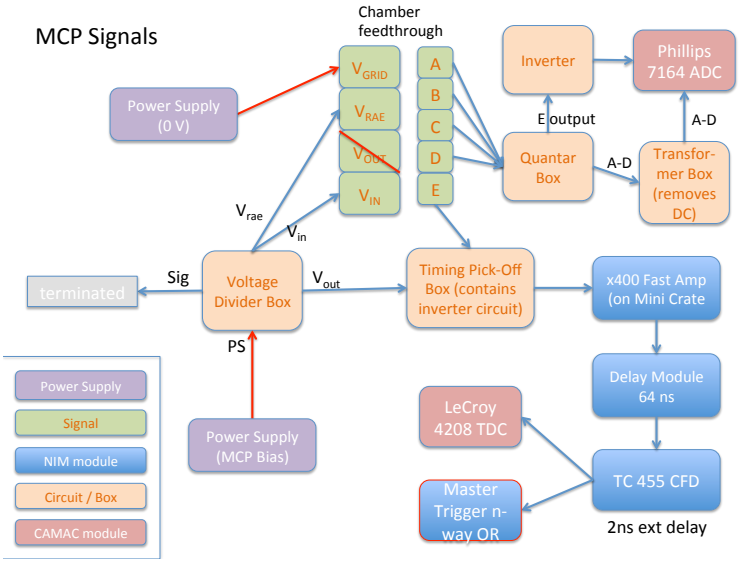

Figure C.3: Electronics setup for the MCP detectors, including modules provided by Quantar.

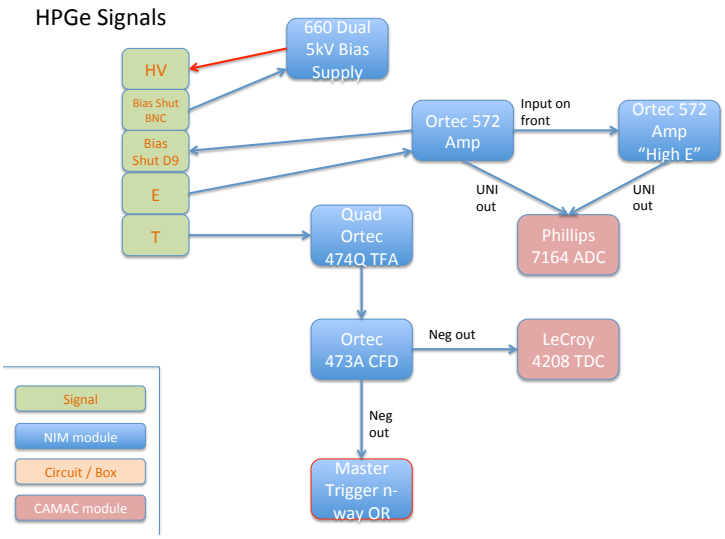

Figure C.4: HPGe electronics setup.

Bibliography

[1] McGeorge Bundy. *Danger and Survival, Choices About the Bomb in the First Fifty Years*. 1st ed. Random House, 1988.

[2] R. B. Roberts, R. C. Meyer, and P. Wang. "Further Observations on the Splitting of Uranium and Thorium". In: *Phys. Rev.* 55 (5 1939), pp. 510–511. DOI: 10.1103/PhysRev.55.510.2. URL: http://link.aps.org/doi/10.1103/PhysRev.55.510.2.

[3] R. B. Roberts et al. "The Delayed Neutron Emission which Accompanies Fission of Uranium and Thorium". In: *Phys. Rev.* 55 (7 1939), pp. 664–664. DOI: 10.1103/PhysRev.55.664. URL: http://link.aps.org/doi/10.1103/PhysRev.55.664.

[4] Niels Bohr and John Archibald Wheeler. "The Mechanism of Nuclear Fission". In: *Phys. Rev.* 56 (5 1939), pp. 426–450. DOI: 10.1103/PhysRev.56.426. URL: http://link.aps.org/doi/10.1103/PhysRev.56.426.

[5] K. S. Krane. *Introductory Nuclear Physics*. 2nd ed. New Jersey: John Wiley and Sons, 1988.

[6] B. Singh D. Abriola and I. Dillmann. *Summary Report of Consultants' Meeting on Beta-delayed neutron emission evaluation*. Tech. rep. INDC(NDS)-0599. Vienna International Centre, Vienna, Austria: International Atomic Energy Agency, 2011.

[7] S. Das. "The importance of delayed neutrons in nuclear research, review". In: *Progress in Nuclear Energy* 28.3 (1994), pp. 209–264. ISSN: 0149-1970. DOI: http://dx.doi.org/10.1016/0149-1970(94)90001-9. URL: http://www.sciencedirect.com/science/article/pii/0149197094900019.

[8] J. A. Winger et al. "Large β-Delayed Neutron Emission Probabilities in the ^{78}Ni Region". In: *Phys. Rev. Lett.* 102 (14 2009), p. 142502. DOI: 10.1103/PhysRevLett.102.142502. URL: http://link.aps.org/doi/10.1103/PhysRevLett.102.142502.

[9] P. Hosmer et al. "Half-lives and branchings for β-delayed neutron emission for neutron-rich Co–Cu isotopes in the r-process". In: *Phys. Rev. C* 82 (2 2010), p. 025806. DOI: 10.1103/PhysRevC.82.025806. URL: http://link.aps.org/doi/10.1103/PhysRevC.82.025806.

[10] R.Q. Wright and R.E. MacFarlane. "Review of ENDF/B-VI fission-product cross sections". In: *Comp. Phys. Eng.* 1 (2008).

[11] R.J. Onega and R.J. Florian. "The implication of sensitivity analysis on the safety and delayed-neutron parameters for fast breeder reactors". In: *Annals of Nuclear Energy* 10.9 (1983), pp. 477–490. ISSN: 0306-4549. DOI: http://dx.doi.org/10.1016/0306-4549(83)90029-4. URL: http://www.sciencedirect.com/science/article/pii/0306454983900294.

[12] E. Kiefhaber. "Influence of Delayed Neutron Spectra on Fast Reactor Criticality". In: *Nucl. Sci. Eng.* 111 (1992), pp. 197–204.

[13] R. M. Yee et al. "β-Delayed Neutron Spectroscopy Using Trapped Radioactive Ions". In: *Physical Review Letters* 110.9 (Feb. 2013), p. 092501. ISSN: 0031-9007. DOI: 10.1103/PhysRevLett.110.092501. URL: http://link.aps.org/doi/10.1103/PhysRevLett.110.092501.

[14] R. Surman et al. "Sensitivity studies for the weak r process: neutron capture rates". In: *AIP Advances* 4.4, 041008 (2014). DOI: http://dx.doi.org/10.1063/1.4867191. URL: http://scitation.aip.org/content/aip/journal/adva/4/4/10.1063/1.4867191.

[15] M. A. Stoyer et al. Tech. rep. COCA-2000-738. LLNL, 2000.

[16] M. A. Stoyer et al. Tech. rep. COCA-2001-54. LLNL, 2001.

[17] M. Guttormsen, T. Ramsoy, and J. Rekstad. "The first generation of γ-rays from hot nuclei". In: *Nuclear Instruments and Methods in Physics Research Section A: Accelerators, Spectrometers, Detectors and Associated Equipment* 255.3 (1987), pp. 518–523. ISSN: 0168-9002. DOI: http://dx.doi.org/10.1016/0168-9002(87)91221-6. URL: http://www.sciencedirect.com/science/article/pii/0168900287912216.

[18] A Schiller et al. "Extraction of level density and γ strength function from primary γ spectra". In: *Nuclear Instruments and Methods in Physics Research Section A: Accelerators, Spectrometers, Detectors and Associated Equipment* 447.3 (2000), pp. 498–511. ISSN: 0168-9002. DOI: http://dx.doi.org/10.1016/S0168-9002(99)01187-0. URL: http://www.sciencedirect.com/science/article/pii/S0168900299011870.

[19] A. Spyrou et al. "Novel technique for Constraining r-Process (n, γ) Reaction Rates". In: *Phys. Rev. Lett.* 113 (23 2014), p. 232502. DOI: 10.1103/PhysRevLett.113.232502. URL: http://link.aps.org/doi/10.1103/PhysRevLett.113.232502.

[20] J. L. Tain et al. "Enhanced γ-Ray Emission from Neutron Unbound States Populated in β Decay". In: *Phys. Rev. Lett.* 115 (6 2015), p. 062502. DOI: 10.1103/PhysRevLett.115.062502. URL: http://link.aps.org/doi/10.1103/PhysRevLett.115.062502.

[21] H. Ohm et al. "Beta-delayed neutrons and high-energy gamma-rays from decay of ^{137}I". English. In: *Zeitschrift f́ur Physik A Atoms and Nuclei* 296.1 (1980), pp. 23–33. ISSN: 0939-7922. DOI: 10.1007/BF01415611. URL: http://dx.doi.org/10.1007/BF01415611.

[22] O. Sorlin and M.-G. Porquet. "Nuclear magic numbers: New features far from stability". In: *Progress in Particle and Nuclear Physics* 61.2 (2008), pp. 602–673. ISSN: 0146-6410. DOI: http://dx.doi.org/10.1016/j.ppnp.2008.05.001. URL: http://www.sciencedirect.com/science/article/pii/S0146641008000380.

[23] T. Kawano, P. Möller, and W. B. Wilson. "Calculation of delayed-neutron energy spectra in a quasiparticle random-phase approximation–Hauser-Feshbach model". In: *Phys. Rev. C* 78 (5 2008), p. 054601. DOI: 10.1103/PhysRevC.78.054601. URL: http://link.aps.org/doi/10.1103/PhysRevC.78.054601.

[24] E. A. McCutchan et al. "Improving systematic predictions of β-delayed neutron emission probabilities". In: *Phys. Rev. C* 86 (4 2012), p. 041305. DOI: 10.1103/PhysRevC.86.041305. URL: http://link.aps.org/doi/10.1103/PhysRevC.86.041305.

[25] K. Miernik. "Phenomenological model of β-delayed neutron-emission probability". In: *Phys. Rev. C* 88 (4 2013), p. 041301. DOI: 10.1103/PhysRevC.88.041301. URL: http://link.aps.org/doi/10.1103/PhysRevC.88.041301.

[26] B. Leist et al. "Neutron capture cross sections for neutron-rich isotopes". English. In: *Zeitschrift fur Physik A Atoms and Nuclei* 322.3 (1983), pp. 531–532. ISSN: 0939-7922. DOI: 10.1007/BF01412093. URL: http://dx.doi.org/10.1007/BF01412093.

[27] K.-L. Kratz et al. "Determination of stellar neutron-capture rates for radioactive nuclei with the aid of beta-delayed neutron emission". In: *Astron. Astrophys.* 125 (1983), pp. 381–387.

[28] R. C. Greenwood and A. J. Caffrey. "Delayed-Neutron Energy Spectra of $^{93-97}$Rb and $^{143-145}$Cs". In: *Nucl Sci Eng* 91 (1985), pp. 305–323.

[29] K. Lodders. "Solar system abundances and condensation temperatures of the elements". In: *The Astrophysical Journal* 591 (2003), pp. 1220–1247.

[30] C. Sneden and J. J. Cowan. "Genesis of the Heaviest Elements in the Milky Way Galaxy". In: *Science* 299 (Jan. 2003), pp. 70–75. DOI: 10.1126/science.1077506.

[31] R. Tribble *et al. The Frontiers of Nuclear Science: A Long Range Plan.* Tech. rep. Nuclear Science Advisory Committee, 2007.

[32] E. Haseltine. "The 11 greatest unanswered questions of physics". In: *Discover Magazine* 23.2 (2002), pp. 36–43.

[33] K.-L. Kratz et al. "Isotopic r-process abundances and nuclear structure far from stability-Implications for the r-process mechanism". In: *ApJ* 403 (Jan. 1993), pp. 216–238. DOI: 10.1086/172196.

[34] Takeshi Kodama and Kohji Takahashi. "R-process nucleosynthesis and nuclei far from the region of stability". In: *Nuclear Physics A* 239.3 (1975), pp. 489–510. ISSN: 0375-9474. DOI: http://dx.doi.org/10.1016/0375-9474(75)90381-4. URL: http://www.sciencedirect.com/science/article/pii/0375947475903814.

[35] M. Arnould, S. Goriely, and K. Takahashi. "The r-process of stellar nucleosynthesis: Astrophysics and nuclear physics achievements and mysteries". In: *Physics Reports* 450.4-6 (2007), pp. 97–213. ISSN: 0370-1573. DOI: http://dx.doi.org/10.1016/j.physrep.2007.06.002. URL: http://www.sciencedirect.com/science/article/pii/S0370157307002438.

[36] K.-L. Kratz, K. Farouqi, and B. Pfeiffer. "Nuclear physics far from stability and r-process nucleosynthesis". In: *Progress in Particle and Nuclear Physics* 59.1 (2007). International Workshop on Nuclear Physics 28th CourseRadioactive Beams, Nuclear Dynamics and AstrophysicsEttore Majorana Center for Scientific Culture, pp. 147–155. ISSN: 0146-6410. DOI: http://dx.doi.org/10.1016/j.ppnp.2006.12.024. URL: http://www.sciencedirect.com/science/article/pii/S0146641006001050.

[37] O. Sorlin. "Report on the first EURISOL User Group Topical Meeting, The formation and structure of r-process nuclei, between N=50 and 82 (including 78Ni and 132Sn areas". In: *Nuclear Physics News* 21.3 (2011), pp. 30–38.

[38] W.C. Sailor and S.G. Prussin. "Calculation of the energy dependent efficiency of gridded 3He fast neutron ionization chambers". In: *Nuclear Instruments and Methods* 173.3 (1980), pp. 511–515. ISSN: 0029-554X. DOI: http://dx.doi.org/10.1016/0029-554X(80)90907-6. URL: http://www.sciencedirect.com/science/article/pii/0029554X80909076.

[39] S. Shalev and J.M. Cuttler. In: *Trans. Am. Nucl. Soc.* 14 (1971), p. 373.

[40] S. Shalev and J.M. Cuttler. In: *Nucl. Sci. Engng.* 51.1 (1973), p. 52.

[41] S. Shalev and G. Rudstam. "Energy spectra of delayed neutrons from separated fission products". In: *Nuclear Physics A* 230.1 (1974), pp. 153–172. ISSN: 0375-9474. DOI: http://dx.doi.org/10.1016/0375-9474(74)90535-1. URL: http://www.sciencedirect.com/science/article/pii/0375947474905351.

[42] H. Franz et al. "Delayed-neutron spectroscopy with ^{3}He spectrometers". In: *Nuclear Instruments and Methods* 144.2 (1977), pp. 253–261. ISSN: 0029-554X. DOI: http://dx.doi.org/10.1016/0029-554X(77)90116-1. URL: http://www.sciencedirect.com/science/article/pii/0029554X77901161.

[43] E.F. Bennett. "Fast Neutron Spectroscopy by Proton-Recoil Proportional Counting". In: *Nucl. Sci. Engng* 27 (1972), pp. 16–27.

[44] G. Fieg. "Measurements of delayed fission neutron spectra of ^{235}U, ^{238}U and ^{239}Pu with proton recoil proportional counters". In: *Journal of Nuclear Energy* 26.12 (1972), pp. 585–592. ISSN: 0022-3107. DOI: http://dx.doi.org/10.1016/0022-3107(72)90008-1. URL: http://www.sciencedirect.com/science/article/pii/0022310772900081.

[45] E.T. Chulick et al. "Energy spectrum of delayed neutrons from the spontaneous fission of ^{252}Cf". In: *Nuclear Physics A* 168.2 (1971), pp. 250–258. ISSN: 0375-9474. DOI: http://dx.doi.org/10.1016/0375-9474(71)90791-3. URL: http://www.sciencedirect.com/science/article/pii/0375947471907913.

[46] G. Savard et al. "The Canadian Penning Trap Spectrometer at Argonne". English. In: *Hyperfine Interactions* 132.1-4 (2001), pp. 221–228. ISSN: 0304-3843. DOI: 10.1023/A:1011986930931.

[47] N. D. Scielzo et al. "Measurement of the $\beta - \nu$ Correlation using Magneto-optically Trapped ^{21}Na". In: *Phys. Rev. Lett.* 93 (10 2004), p. 102501. DOI: 10.1103/PhysRevLett.93.102501. URL: http://link.aps.org/doi/10.1103/PhysRevLett.93.102501.

[48] S. Shalev and G. Rudstam. "Energy spectra of delayed neutrons from separated fission products". In: *Nuclear Physics A* 275 (1977), pp. 76–92.

[49] K.-L. Kratz et al. "Investigation of beta strength functions by neutron and gamma-ray spectroscopy: (I). The decay of ^{87}Br, ^{137}I, ^{85}As and ^{135}Sb". In: *Nuclear Physics A* 317 (1979), pp. 335–362. ISSN: 0375-9474. DOI: http://dx.doi.org/10.1016/0375-9474(79)90486-X. URL: http://www.sciencedirect.com/science/article/pii/037594747990486X.

[50] R. C. Greenwood and K. D. Watts. "Delayed-Neutron Energy Spectra of $^{87-90}$Br, $^{137-139}$I, and ^{136}Te". In: *Nucl Sci Eng* 126 (1997), p. 324.

[51] G. Savard et al. "Development and operation of gas catchers to thermalize fusionâ evaporation and fragmentation products". In: *Nuclear Instruments and Methods in Physics Research Section B: Beam Interactions with Materials and Atoms* 204 (2003). 14th International Conference on Electromagnetic Isotope Separators and Techniques Related to their Applications, pp. 582–586. ISSN: 0168-583X. DOI: http://dx.doi.org/10.1016/S0168-583X(02)02134-1. URL: http://www.sciencedirect.com/science/article/pii/S0168583X02021341.

[52] G. Savard et al. "A new cooling technique for heavy ions in a Penning trap". In: *Physics Letters A* 158.5 (1991), pp. 247–252. ISSN: 0375-9601. DOI: http://dx.doi.org/10.1016/0375-9601(91)91008-2. URL: http://www.sciencedirect.com/science/article/pii/0375960191910082.

[53] N.D. Scielzo et al. "The Paul trap: A radiofrequency-quadrupole ion trap for precision studies". In: *Nuclear Instruments and Methods in Physics Research Section A: Accelerators, Spectrometers, Detectors and Associated Equipment* 681 (2012), pp. 94–100. ISSN: 0168-9002. DOI: http://dx.doi.org/10.1016/j.nima.2012.04.035. URL: http://www.sciencedirect.com/science/article/pii/S0168900212003907.

[54] M.B. Chadwick, M. Herman, P. Obložinský, et al. "ENDF/B-VII.1 Nuclear Data for Science and Technology: Cross Sections, Covariances, Fission Product Yields and Decay Data". In: *Nuclear Data Sheets* 112.12 (2011). Special Issue on ENDF/B-VII.1 Library, pp. 2887–2996. ISSN: 0090-3752. DOI: 10.1016/j.nds.2011.11.002. URL: http://www.sciencedirect.com/science/article/pii/S009037521100113X.

[55] C. N. Davids and D. Peterson. "A compact high-resolution isobar separator for the CARIBU project". In: *Nuclear Instruments and Methods in Physics Research Section B: Beam Interactions with Materials and Atoms* 266.19-20 (2008). Proceedings of the XVth International Conference on Electromagnetic Isotope Separators and Techniques Related to their Applications, pp. 4449–4453. ISSN: 0168-583X. DOI: http://dx.doi.org/10.1016/j.nimb.2008.05.148. URL: http://www.sciencedirect.com/science/article/pii/S0168583X08007544.

[56] G. Savard et al. "The Canadian Penning trap mass spectrometer". In: *Nuclear Physics A* 626 (1997). Proceedings of the Third International Conference on Nuclear Physics at Storage Rings, pp. 353–356. ISSN: 0375-9474. DOI: http://dx.doi.org/10.1016/S0375-9474(97)00557-5. URL: http://www.sciencedirect.com/science/article/pii/S0375947497005575.

[57] J.C. Wang et al. "The Canadian Penning Trap mass spectrometer". In: *Nuclear Physics A* 746 (2004). Proceedings of the Sixth International Conference on Radioactive Nuclear Beams (RNB6), pp. 651–654. ISSN: 0375-9474. DOI: http://dx.doi.org/10.1016/j.nuclphysa.2004.09.044. URL: http://www.sciencedirect.com/science/article/pii/S0375947404009893.

[58] W. Paul. "Electromagnetic traps for charged and neutral particles". In: *Reviews of Modern Physics* 62.3 (1990), pp. 531–540.

[59] J. Ladislas Wiza. "Microchannel plate detectors". In: *Nuclear Instruments and Methods* 162 (June 1979), pp. 587–601. DOI: 10.1016/0029-554X(79)90734-1.

[60] M. Lampton and C. W. Carlson. "Low-distortion resistive anodes for two-dimensional position-sensitive MCP systems". In: *Review of Scientific Instruments* 50 (Sept. 1979), pp. 1093–1097. DOI: 10.1063/1.1135990.

[61] K. Teh. *Data Acquisition at ATLAS.* Tech. rep. Lemont, IL: Argonne National Laboratory Physics Division, 2004.

[62] Glenn F. Knoll. *Radiation Detection and Measurement.* 4th ed. John Wiley and Sons, 2010.

[63] S. Caldwell. "A trapped-ion technique for beta-delayed neutron studies". PhD thesis. University of Chicago, Department of Physics, 2015.

[64] N. D. Scielzo et al. "Recoil-ion charge-state distribution following the β^+ decay of ^{21}Na". In: *Phys. Rev. A* 68 (2003), p. 022716. DOI: 10.1103/PhysRevA.68.022716. URL: http://link.aps.org/doi/10.1103/PhysRevA.68.022716.

[65] J.C. Hardy et al. "The essential decay of pandemonium: A demonstration of errors in complex beta-decay schemes". In: *Physics Letters B* 71.2 (1977), pp. 307–310. ISSN: 0370-2693. DOI: http://dx.doi.org/10.1016/0370-2693(77)90223-4. URL: http://www.sciencedirect.com/science/article/pii/0370269377902234.

[66] C. S. Wu and S. A. Moszkowski. *Beta Decay.* Interscience Publishers, New York, 1966.

[67] G.W. Fraser. "The ion detection efficiency of microchannel plates (MCPs)". In: *International Journal of Mass Spectrometry* 215.1-3 (2002). Detectors and the Measurement of Mass Spectra, pp. 13–30. ISSN: 1387-3806. DOI: http://dx.doi.org/10.1016/S1387-3806(01)00553-X. URL: http://www.sciencedirect.com/science/article/pii/S138738060100553X.

[68] S. Yagi et al. "Relative counting efficiencies of ion charge-states by microchannel plate". In: *Nuclear Instruments and Methods in Physics Research Section B: Beam Interactions with Materials and Atoms* 183.3-4 (2001), pp. 476–486. ISSN: 0168-583X. DOI: http://dx.doi.org/10.1016/S0168-583X(01)00724-8. URL: http://www.sciencedirect.com/science/article/pii/S0168583X01007248.

[69] J Oberheide, P Wilhelms, and M Zimmer. "New results on the absolute ion detection efficiencies of a microchannel plate". In: *Measurement Science and Technology* 8.4 (1997), p. 351. URL: http://stacks.iop.org/0957-0233/8/i=4/a=001.

[70] E. Lienard et al. "Performance of a micro-channel plates position sensitive detector". In: *Nuclear Instruments and Methods in Physics Research Section A: Accelerators, Spectrometers, Detectors and Associated Equipment* 551.2âĂŞ3 (2005), pp. 375–386. ISSN: 0168-9002. DOI: http://dx.doi.org/10.1016/j.nima.2005.06.069. URL: http://www.sciencedirect.com/science/article/pii/S0168900205013811.

[71] A. H. Snell and F. Pleasonton. "The Atomic and Molecular Consequences of Radioactive Decay". In: *The Journal of Physical Chemistry* 62.11 (1958), pp. 1377–1382. DOI: 10.1021/j150569a008.

[72] A. H. Snell and F. Pleasonton. "Charge Spectrometry for ^{133}Xe-^{133}Cs^{133}". In: *Phys. Rev.* 111 (5 1958), pp. 1338–1343. DOI: 10.1103/PhysRev.111.1338. URL: http://link.aps.org/doi/10.1103/PhysRev.111.1338.

[73] Eric Brannen and Garth L. Olde. "The Response of Organic Scintillators to Electron Energy Deposited in Them". In: *Radiation Research* 16.1 (1962), pp. 1–6. DOI: 10.2307/3571123.

[74] R.L. Craun and D.L. Smith. "Analysis of response data for several organic scintillators". In: *Nuclear Instruments and Methods* 80.2 (1970), pp. 239–244. DOI: http://dx.doi.org/10.1016/0029-554X(70)90768-8. URL: http://www.sciencedirect.com/science/article/pii/0029554X70907688.

[75] M. G. Sternberg. "Limits on tensor currents from ^{8}Li decay". PhD thesis. University of Chicago, Department of Physics, 2013.

[76] Gilbert J. Perlow and Andrew F. Stehney. "Halogen Delayed-Neutron Activities". In: *Phys. Rev.* 113 (5 1959), pp. 1269–1276. DOI: 10.1103/PhysRev.113.1269. URL: http://link.aps.org/doi/10.1103/PhysRev.113.1269.

[77] M. Asghar et al. "The P_n values of the $^{235}U(n_{th}, f)$ produced precursors in the mass chains 90, 91, 93-95, 99, 134 and 137-139". In: *Nuclear Physics A* 247.2 (1975), pp. 359–376. ISSN: 0375-9474. DOI: http://dx.doi.org/10.1016/0375-9474(75)90642-9. URL: http://www.sciencedirect.com/science/article/pii/0375947475906429.